Devenir des nanoparticules dans l'environnement : stabilité colloïdale, réactivité chimique et impacts sur le végétal

Edwige Demangeat

Edwige Demangeat. Devenir des nanoparticules dans l'environnement : stabilité colloïdale, réactivité chimique et impacts sur le végétal. Sciences de la Terre. Université de Rennes, 2018. Français. NNT : 2018REN1B050 . tel-02097970

HAL Id: tel-02097970
https://theses.hal.science/tel-02097970

Submitted on 12 Apr 2019

UNIVERSITE ECOLOGIE
BRETAGNE GEOSCIENCES
LOIRE AGRONOMIE ALIMENTATION

UNIVERSITÉ DE RENNES 1

THESE DE DOCTORAT DE

L'UNIVERSITE DE RENNES 1
COMUE UNIVERSITE BRETAGNE LOIRE

ECOLE DOCTORALE N° 600
Ecole doctorale Ecologie, Géosciences, Agronomie et Alimentation
Spécialité : Sciences de la Terre et de l'environnement

Par
Edwige DEMANGEAT

Devenir des nanoparticules de fer dans l'environnement

Stabilité colloïdale, réactivité chimique et impacts sur le végétal

Thèse présentée et soutenue à Rennes, le 10 décembre 2018
Unité de recherche : Géosciences Rennes
Thèse N° :

Rapporteurs avant soutenance :

François Chabaux, Professeur à l'Université de Strasbourg, LHyGeS

Oleg Pokrovsky, Directeur de recherche CNRS, GET Toulouse

Composition du Jury :

François Chabaux, Professeur à l'Université de Strasbourg, LHyGeS

Oleg Pokrovsky, Directeur de recherche CNRS, GET Toulouse

Laurence Denaix, Directrice de recherche INRA, ISPA Villenave D'Ornon

Co-Directeurs de thèse
Aline Dia, Directrice de recherche CNRS, Géosciences Rennes

Francisco-Cabello-Hurtado, Maître de Conférences (HDR), ECOBIO Rennes

Mathieu Pédrot, Maître de Conférences (HDR), Géosciences Rennes

Remerciements

Ce travail a été réalisé au sein de l'équipe NanoBioGéochimie (NBG), à Géosciences Rennes (Université de Rennes1). Mes remerciements vont d'abord à Olivier Dauteuil, directeur du laboratoire, et Anne-Catherine Pierson-Wickman, responsable de l'équipe, pour m'avoir garanti des conditions de travail de qualité, aussi bien en termes d'équipement que du cadre scientifique de travail.

Je remercie tous les membres du jury de m'avoir fait l'honneur de juger cette thèse, et notamment, François Chabaux et Oleg Pokrovsky pour avoir accepté de rapporter le manuscrit, et Laurence Denaix pour avoir pris part à mon jury de soutenance en tant qu'examinatrice.

Je tiens à adresser mes plus sincères remerciements à mes trois directeurs de thèse, Mathieu Pédrot, Francisco Cabello-Hurtado et Aline Dia. Je les remercie pour leur aide et leur soutien tout au long de ces trois années. Merci d'avoir été si patients face à mes fréquents doutes et questions… Je vous remercie aussi pour toute l'expérience que vous m'avez fait partager, les connaissances acquises et l'ouverture scientifique à laquelle vous m'avez permis d'accéder. Je suis heureuse d'avoir débuté à vos côtés.

J'ai eu la chance de travailler au sein d'une équipe dynamique et très humaine, que je souhaite remercier pour tout le soutien dont j'ai bénéficié. Merci à Mélanie Davranche, Julien Gigault, Rémi Marsac et Anne-Catherine Pierson-Wickman. Merci également aux ingénieurs, pour leur profonde implication dans le projet, Martine Bouhnik-Le-Coz, et Patrice Petitjean. Et enfin, merci à mes collègues de bureau, passés et présents, pour tous les moments partagés: Sen Gu, Elaheh Lofti Kalahroodi (« Ellie »), Anthony Beauvois, Caroline Lory,… et plus anciennement, Charlotte Catrouillet, Hélène Guénet, Marie Denis et Sarah Deville.

Le sujet de thèse, interdisciplinaire, m'a également permis de faire connaissance avec de nombreuses personnes que je souhaiterai remercier. Tout d'abord, merci à Stéphanie DeVerbigier, pour son travail, sa patience, et les très bons moments passés ensemble. Je remercie également, Kamagaté Mahamhadou, qui m'a épaulé pendant plusieurs analyses et a gardé sa bonne humeur en toutes circonstances. Merci à Fabien Grasset, Fabienne Gauffre et Kahlil Hanna, pour les rencontres enrichissantes et les discussions scientifiques très constructives que nous avons eues. Et enfin, merci à Pierrick Roperch pour son implication, sa disponibilité, sa curiosité et son ouverture d'esprit vis-à-vis du projet.

Finalement, cette thèse s'est construite sur le soutien de ma famille, qui m'a toujours adressé les bons mots aux bons moments pour aller de l'avant. Merci à mes parents, mes grands-parents, mes deux sœurs et mon frère pour tout leur amour.

Sommaire

Sommaire

Article: *Colloidal and chemical stabilities of iron oxide nanoparticles in aqueous solution: the interplay of structural, chemical and environmental drivers.*

Article soumis: ***Do surface transformations impact the reactivity of iron oxide NPs? Insights from copper binding and iron oxide dissolution***

Article en preparation: ***Magnetite nanoparticles introduction into sunflower plants: Fe-nutrient or toxic compound?***

Annexe 1: Does As(III) interact with Fe(II), Fe(III), and organic matter through ternary complexes ? C. Catrouillet, M. Davranche, A. Dia, M. Bouhnik-Le-Coz, E. Demangeat, & G. Gruau, Journal of Colloid and Inerface Science 470 (2016) 153-161.

Annexe 2: Highlighting the wide variablility in arsenic speciation in wetlands: a new insight into the control of the behavior of arsenic. H. Guenet, M. Davranche, D. Vantelon, M. Bouhnik-Le-Coz, E. Jardé, V. Dorcet, E. Demangeat & J. Jestin.

Annexe 3 : Experimental evidence of REE size fraction redistribution during redox variation in wetland soil. H. Guenet, E. Demangeat, M. Davranche, D. Vantelon, A.-C. Pierson-Wickman, E. Jardé, M. Bouhnik-Le-Coz, E. Lofti, A. Dia & J. Jestin. Science of the Total Environment, 631-632 (2018), 580-588.

Introduction

Introduction

Le nanomonde est celui des nanosciences et des nanotechnologies, il recouvre les objets de taille nanométrique. Le terme émergea en 1959 avec un célèbre physicien dans son discours pour l'American Scientific Society mais, ce n'est qu'avec l'invention du microscope à effet tunnel en 1981, que les nanosciences ont connu leur véritable essor (SCENIHR, 2006). Depuis près d'une trentaine d'années, les techniques et connaissances acquises dans le nanomonde ont initié une véritable révolution technologique. D'ores et déjà, des produits issus des nanotechnologies commencent à peupler notre quotidien : textiles antitaches ou à imperméabilité renforcée, crèmes solaires invisibles et protectrices, huiles anticholestérols, vitres hydrophobes autonettoyantes, etc., la liste, déjà conséquente, est en constante augmentation (Vance, 2015). Au-delà des bénéfices apportés par les innovations scientifiques et technologiques, des conséquences ambivalentes sont toutefois attendues. Les avancées considérables induites par l'utilisation des nanotechnologies, particulièrement celles des nanoparticules (NPs), dans les domaines aussi vastes que l'industrie chimique, la médecine, l'électronique, ou l'environnement, ont accru la production de NPs et souligné le besoin de connaissances qui s'y rapportent, en particulier vis-à-vis des conséquences sanitaires et environnementales attendues (Patil et al., 2018). Si les instances nationales et internationales se mobilisent, celles-ci appuient le besoin de mener des recherches approfondies dans ce domaine, qui reste encore exploratoire.

Les NPs, en tant que « nano-objets », sont des particules dont le diamètre est compris entre 1 et 100 nm (ANSES, 2014) (**Figure 1**). Elles représentent un état de la matière particulier, entre l'atome et la molécule. A cette échelle, les NPs ont un rapport surface sur volume très élevé comparé à leurs analogues macroscopiques ; ce qui leur prodigue une très grande réactivité (rapport surface / volume très élevé) et explique la multiplicité des applications auxquelles elles sont associées. Les NPs sont désormais au centre de nombreuses recherches portant aussi bien sur leurs applications que sur leurs interactions avec les constituants de l'environnement (Vindedahl, 2016 ; Yu, 2018). En effet, une fois libérées dans les eaux et les sols, les NPs entrent en contact avec de multiples espèces naturelles - minéraux et substances humiques insolubles, éléments traces métalliques ou organiques dissous, micro-débris animaux ou végétaux, bactéries, etc. - dont l'interdépendance a un impact majeur sur la dynamique terrestre et sur la vie.

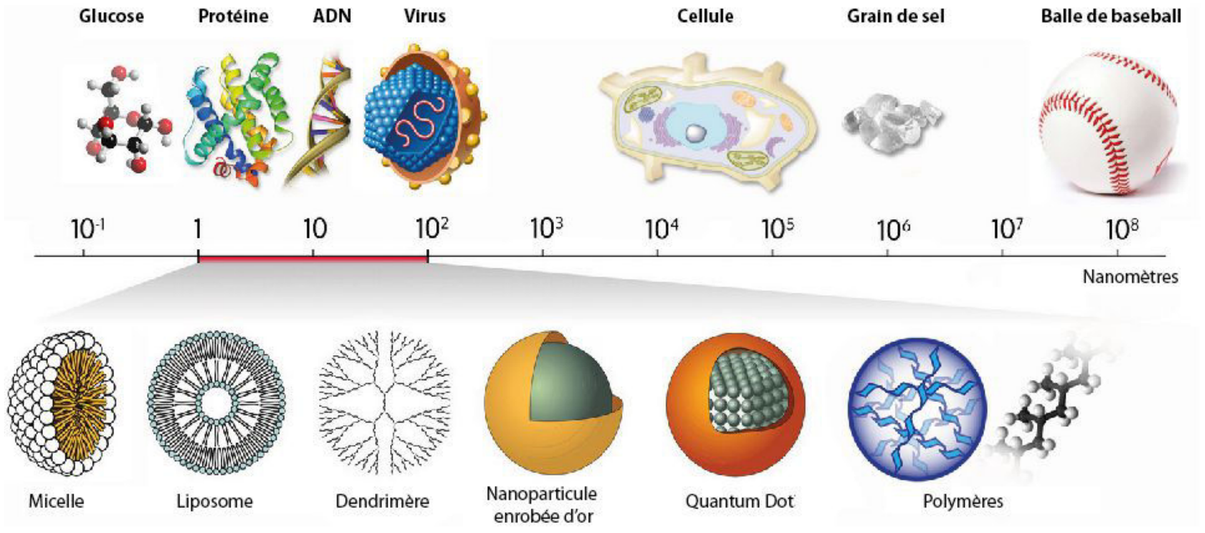

Figure 1 : Les NPs et nano-objets comparés à des substances et objets de taille connue

Qu'elles soient d'origine biogénique ou géogénique, les NPs de fer (NPs-Fe) existent naturellement dans l'environnement, dispersées dans les sols, en suspension dans les eaux de surface ou balayées par les courant atmosphériques (Guo et al., 2013). Leur présence dans les différents compartiments terrestres n'est cependant pas sans conséquences sur la dynamique du milieu qu'elles intègrent. Les particules de fer, de taille nanométrique ou micrométrique, jouent en effet, un rôle clé dans les écosystèmes en catalysant ou en participant à de multiples réactions biogéochimiques. A leur surface, des réactions acido-basiques, d'oxydo-réduction, d'adsorption de surface ou de coprécipitation contrôlent la mobilité et la spéciation des éléments traces (ETs). C'est cette grande réactivité physico-chimique de surface vis-à-vis des constituants organiques et inorganiques qui explique en partie l'essor particulier des NPs de fer (NPs-Fe) parmi l'ensemble des NPs manufacturées (Aitken et al., 2011). Leur utilisation particulièrement prometteuse dans les domaines de l'environnement et de la dépollution concerne essentiellement les NPs de magnétite (Fe_3O_4), de maghémite (ɣ-Fe2O3) et de Fe-zéro valent (nZVI), du fait de leur grande affinité pour les éléments traces métalliques et certains métalloïdes (Tang et Lo., 2013). De nombreux travaux ont montré la capacité de séquestration de métaux à la surface de NPs de magnétite et de maghémite, soulignant leur applicabilité dans les domaines de la remédiation des sols et des eaux polluées (Auffan, 2007 ; Huang et al., 2009 ; Yang et al., 2010). Ces études ont aussi mis en évidence le rôle clé non seulement, des propriétés morpho-structurales et de surface de ces matériaux mais aussi, celui de leur stabilité et de l'impact des conditions du milieu (pH, force ionique, composition chimique de la solution et propriétés des constituants solides présents) sur leur comportement, leur devenir dans les sols et leurs possibles impacts sur le milieu.

Si les NPs-Fe sont capables d'impacter à la fois la mobilité, la disponibilité et la spéciation des ETs dans les sols, l'idée a émergé que les NPs-Fe pourraient être directement conçues à des fins agronomiques. De récents travaux ont ainsi étudié l'utilisation de NPs de fer en tant que nano-fertilisants ou nano-pesticides (Kah et al., 2013). Les effets des NPs sur les plantes soulèvent toutefois encore de nombreuses questions quant aux impacts possibles que les NPs pourraient induire sur les végétaux. Il a en effet, été montré que les NPs pouvaient engendrer des effets néfastes sur certaines espèces. En participant aux réactions de Haber-Weiss et de Fenton dans les cellules par exemple, les NPs-Fe seraient génératrices de ROS (Reactive Oxygen Species). D'autres travaux, ont non seulement prouvé l'innocuité des NPs-Fe sur diverses espèces végétales, et aussi, observé des effets positifs par exemple, sur la production de biomasse végétale (Zhu et al., 2008 ; Salama et al.,2009).

Au regard de ces différentes constatations, parfois contradictoires, il apparaît indispensable de définir les caractéristiques et les limites des systèmes étudiés. Les effets des NPs-Fe sur leur milieu dépendent de nombreux paramètres intrinsèques et extrinsèques, incluant la quantité et les propriétés des NPs-Fe introduites ainsi que les caractéristiques physico-chimiques du milieu. Ces paramètres jouent un rôle majeur dans les interactions des NPs-Fe avec les constituants du milieu et sont également déterminants vis-à-vis des transformations que les NPs subissent dans leur milieu. **L'identification et la hiérarchisation des paramètres impliqués dans ces interactions** devraient permettre de résoudre ou d'apporter des éléments de réponse à plusieurs questions fondamentales parmi lesquelles : **comment se comportent les NPs en solution (stabilité colloïdale) ? Quelles interactions se produisent entre les NPs-Fe et les éléments traces ? Quels sont les impacts du milieu, et celui des plantes, sur les propriétés des NPs-Fe ? Les NPs-Fe ont-elles un impact sur leur milieu ? Quelles sont les interactions NPs-Fe / plantes ?**

Chapitre 1:

Etat de l'art

I.1. Les NPs de fer manufacturées (NPs-Fe)

I.1.1. Définition et contexte d'étude

En 2011, un rapport établi par la Commission Européenne (2011/696/UE) définit le terme « nanomatériau » comme un matériau naturel, formé accidentellement ou manufacturé contenant des particules libres, sous forme d'agrégats ou sous forme d'agglomérat, dont au moins 50% des particules, dans la répartition numérique par taille, présentent une ou plusieurs dimensions externes se situant entre 1 et 100 nm. A ce titre, les « NPs », en tant que « nano-objets », sont des particules dont le diamètre est compris entre 1 et 100 nm (ANSES, 2014). Les NPs dites « manufacturées » sont fabriquées par l'Homme, intentionnellement, à des fins industrielles. Elles se distinguent des NPs naturelles (poussières d'érosion ou d'éruption volcanique, embruns marins, virus) et des NPs incidentelles (produites involontairement par les activités humaines - fumées de combustion de bois ou industrielles, émanations des moteurs diesel). Suivant leur composition, les NPs manufacturées peuvent être classées en trois grands types de NPs : les NPs organiques (fullerènes, « noir de carbone », etc.), les NPs métalliques (Ag, Au, Fe, etc.) et les NPs d'oxydes métalliques (CeO, CuO, Fe_3O_4, TiO_2, ZnO, etc.). Ces dernières, les NPs d'oxydes métalliques, sont les plus employées du fait de leurs propriétés particulièrement intéressantes pour l'industrie (propriétés optiques, conductrices, thermiques, mécaniques, émulsifiantes, dispersantes) (Rahman et al., 2011 ; Vance et al., 2015).

Selon leurs propriétés intrinsèques, les NPs-Fe sont utilisées dans des applications médicales, technologiques ou environnementales:

- Les NPs de maghémite, principalement, sont utilisées comme vecteur de médicaments, agent de contraste lors des IRMs, et pour détruire les cellules cancéreuses (hyperthermie). Leur intérêt réside principalement dans leurs propriétés magnétiques, qui permettent un contrôle « à distance » des particules. En outre, la fonctionnalisation de la surface des NPs de fer est commune et facilement réalisable, ce qui accroît leur biocompatibilité et leur comportement dans les milieux physiologiques (Gupta et Gupta, 2005 ; Wu et al., 2008).

- Les NPs de magnétite, de maghémite et d'hématite possèdent des propriétés conductrices et thermiques qui expliquent leur utilisation dans les applications de stockage de données et comme catalyseurs dans de nombreuses applications industrielles de chimie (Tartaj et al., 2011).

- Dans le secteur de l'environnement, les NPs de magnétite et de maghémite permettent de traiter les eaux contaminées en arsenic ou par certains métaux (Cr, Co, Cu) dans les eaux polluées. Leur forte affinité pour les polluants, leur grande réactivité, et leur rapide cinétique d'adsorption pour les métaux et pour certaines substances organiques toxiques font des NPs-Fe d'efficaces piégeurs de métaux (Tang et Lo., 2013). Les NPs magnétiques sont ainsi utilisées en contexte de drainage acide miniers (Etale et al., 2016). Elles peuvent aussi être facilement récupérées et séparées de leur matrice du fait de leurs propriétés magnétiques (Hiemstra, 2018).
- En agriculture, les NPs de magnétite sont utilisées comme vecteur d'engrais ou de pesticides ; les formulations contenant des NPs présenteraient une meilleure cinétique de libération de pesticides, une diminution de la vitesse de photolyse, ainsi que l'utilisation de quantités plus faibles de substances actives (Khot, et al., 2012 ; Kahet al., 2013). L'utilisation des NPs de fer zéro valent (nZVI) - NPs métalliques - est devenue une pratique répandue pour la remédiation des sols pollués par des composés organochlorés persistants (certains types de pesticides) dans les sols agricoles (Lefevre et al., 2016). Leur application à grande échelle a déjà été réalisée depuis plusieurs années (58 cas d'étude dont 17 en Europe) (Bardos et al., 2011).

La multiplicité des applications ainsi que l'utilisation grandissante des NPs-Fe conduisent à leur libération et à leur dissémination dans les différents compartiments de l'environnement (**Figure 1**). Cette dernière peut intervenir au moment de leur fabrication, au cours de leur utilisation ou lors de leur gestion de fin de vie.

Le comportement et le devenir des NPs-Fe dans les environnements de surface (eau, sol) sont d'une part, influencés par leur mode d'introduction dans le milieu (concentration introduite, formulation) qui affecte la stabilité colloïdale des NPs-Fe en solution, leur agrégation et donc leur mobilité dans l'environnement (les traitements de surface sont fréquents dans plusieurs applications médicales et industrielles, initialement pour améliorer leur dispersion) (Das et al., 2016). Les caractéristiques du sol (texture, composition minéralogique), de la solution de sol (pH, température, force ionique, salinité, composition chimique) et de la biomasse sont aussi déterminantes vis-à-vis de la mobilité et de la biodisponibilité des NPs-Fe qui entrent alors en interaction avec de multiples composants (microorganismes, constituants organiques et inorganiques dissous et/ou particulaires) (Dwivedi et al., 2015 ; Joo et Zhao, 2017). Ces derniers modifient les propriétés des NPs-Fe en réagissant avec leur surface, ce qui peut conduire à différents phénomènes (agrégation, dissolution, adsorption). Enfin, les propriétés intrinsèques des NPs-Fe (taille, surface spécifique, composition chimique, cristallinité) sont directement impliquées dans les interactions entre les NPs-Fe et leur environnement (sections suivantes).

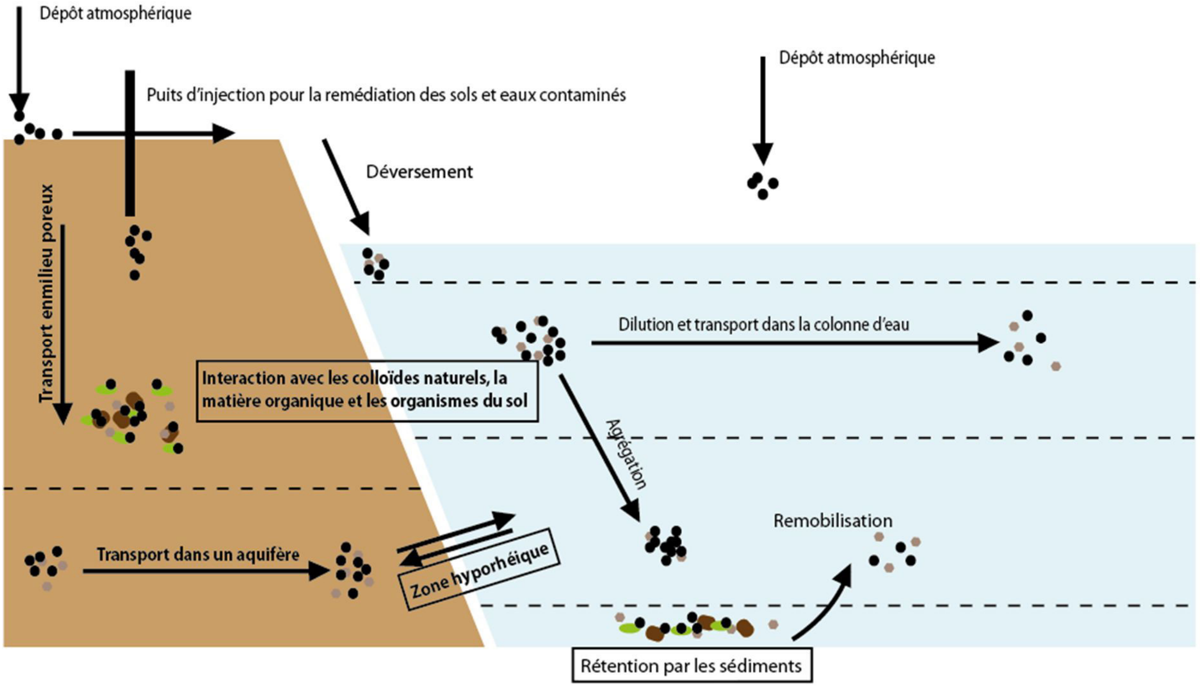

Figure 1 : Schéma illustrant les différentes voies de diffusion des NPs-Fe dans l'environnement.

I.1.2. Propriétés intrinsèques

Les NPs d'oxydes de fer regroupent les oxydes de fer composés de fer ferreux (wüstite), de fer ferreux et de fer ferrique (magnétite) et les oxydes de fer contenant uniquement du fer ferrique dans leur structure (hématite, maghémite).

En termes de structure cristalline, la magnétite (Fe_3O_4) appartient au groupe des spinelles, dont la formule générale est Me(II) Fe_2O_4 (où Me(II) correspond ici à l'ion métallique bivalent Fe(II)). La maille cristalline de la magnétite consiste en un réseau cubique à face centré dans lequel les sites interstitiels accueillent les ions métalliques Fe(II) (sites octaédriques) et Fe(III) (sites octaédriques et tétraédriques) (Cornell et Schwertman, 2000). La magnétite stœchiométrique, avec un rapport Fe(II)/Fe(III) = 0,5, n'est formée que de manière naturelle (biogénique ou géogénique) alors que les magnétites synthétiques ont un rapport Fe(II)/Fe(III) légèrement inférieur à 0,5 lorsqu'elles sont synthétisées en conditions anaérobiques. En conditions aérobiques, la magnétite opère un changement de phase et par oxydation se transforme en maghémite. La maghémite (γ-Fe_2O_3), qui se définit suivant la même structure que la magnétite, ne se distingue de cette dernière que par l'absence de Fe^{2+} dans sa structure. Lorsque la magnétite s'oxyde en maghémite, les atomes de fer situés au cœur de l'oxyde migrent vers la surface pour s'oxyder en Fe^{3+}, créant des lacunes dans la structure (Tartaj et al., 2011). L'hématite (α- Fe_2O_3), dont la formule minérale appartient à celle des corindons, est, elle, constituée d'atomes d'oxygène formant un réseau hexagonal compact dans lequel les ions métalliques trivalents Fe^{3+} occupent deux tiers des sites octaédriques (**Figure 2**). La maghémite et l'hématite représentent les oxydes de fer les plus stables chimiquement. La cristallochimie (structure et la composition chimique) des NPs détermine également d'autres propriétés qui en résultent, telles que la cristallinité, les propriétés magnétiques et la capacité oxydante/réductrice des oxydes de fer (Hiemstra, 2018).

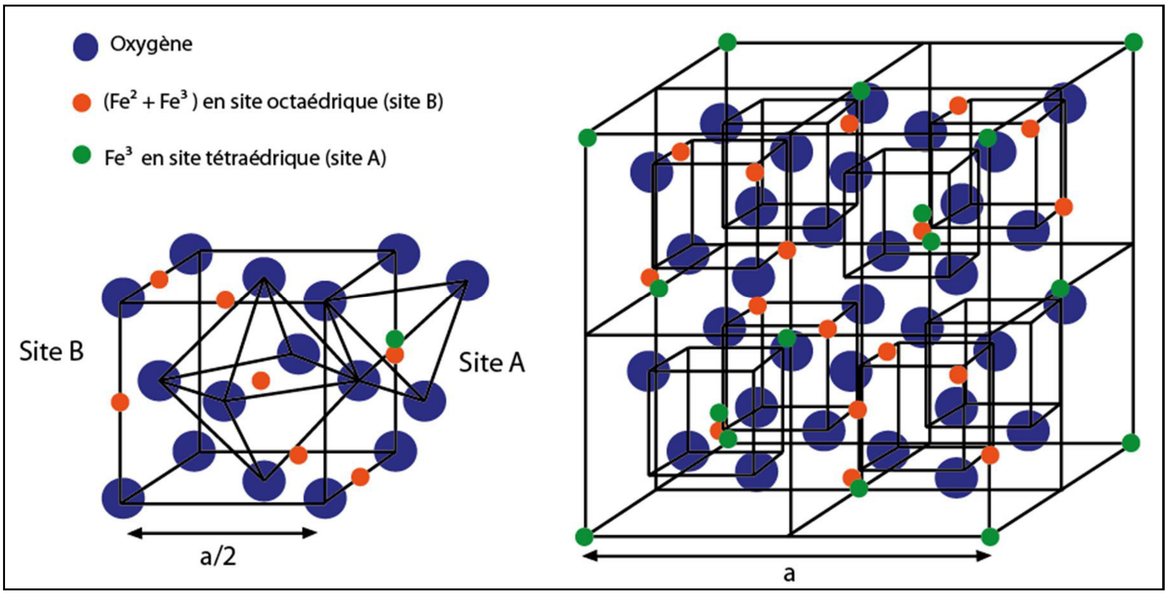

Figure 2 : Maille élémentaire d'une structure spinelle (d'après Mornet, 2002).

Comparées à leurs analogues naturels, les NPs manufacturées ont des propriétés bien spécifiques (taille, morphologie, composition) qui leur confèrent une réactivité chimique et des propriétés physiques distinctes (optiques, catalytiques, conductrices) (Tartaj et al., 2011). Celles-ci sont contrôlées lors de la synthèse, selon différents paramètres qui dépendent de la méthode choisie. La première synthèse de magnétite fut réalisée en 1852 par Le Fort par co-précipitation de sels de fer. Les méthodes par co-précipitation se sont surtout développées à partir de 1938 et pendant près de 40 ans. Les techniques se sont progressivement perfectionnées pour obtenir une répartition de taille homogène et une certaine stabilité des NPs. Divers protocoles ont ainsi été développes, parmi lesquelles les méthodes chimiques (co-précipitation, microémulsion, méthode sol-gel, hydrothermale…) sont plus diversifiées et plus employées que les méthodes par voie physique (pyrolyse laser) ou biologique (incubation microbiologique) (Ali et al., 2016 ; Wu et al.,2008). Ces méthodes permettent de contrôler non seulement, la taille des NPs, les caractéristiques morphologiques, la chimie et la cristallinité des oxydes de fer mais aussi, dans la mesure du possible, la dispersion des tailles et l'état d'agrégation des NPs qui représentent souvent un défi majeur (Zhang et al., 2008). Les propriétés des NPs induites pendant la synthèse sont cruciales car elles influencent le comportement des NPs dans leur milieu (agrégation, réactivité) et sont déterminantes par leurs impacts (notamment la toxicité) sur les constituants en présence.

I.1.3. Réactivité de surface

La taille est une caractéristique majeure des NPs car elle conditionne directement la surface spécifique (unité de surface par unité de masse) d'une particule et donc sa réactivité et sa toxicité (surface de contact). Plus la taille d'une particule diminue, plus le nombre d'atomes se trouvant en surface ou sub-surface augmente. Plus précisément, il existe une relation exponentielle entre le nombre d'atomes présents à la surface d'une nanoparticule et sa taille (**Figure 3**). Ainsi, les NPs ayant un diamètre inférieur à 10 nm sont des objets particulièrement réactifs du fait du rapport surface /volume très élevé (de 30 et 90% de leurs atomes sont présents en surface) (Auffan, 2007). La surface spécifique est l'une des propriétés déterminantes quant à la potentielle réactivité dans le milieu et la toxicité des NPs vis-à-vis des constituants et des organismes en présence.

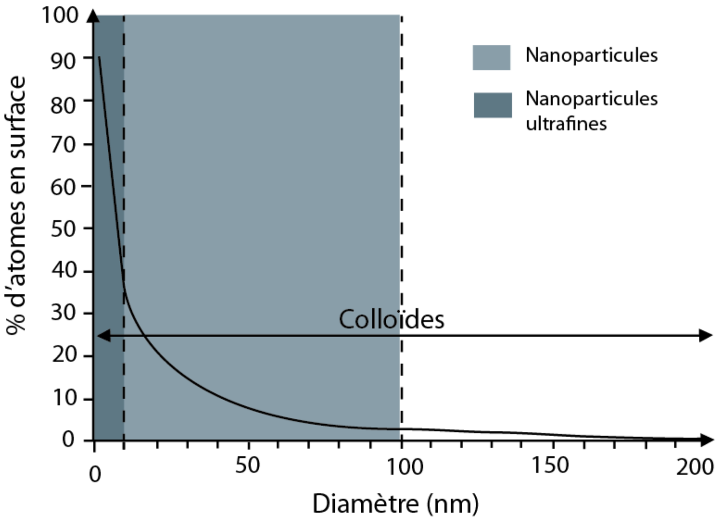

Figure 3 : Fraction d'atomes se situant dans la couche de surface et sub-surface (0,5 nm d'épaisseur) d'une particule en fonction de son diamètre (d'après Auffan, 2007).

A l'échelle atomique d'une nanoparticule, chaque atome situé au cœur du minéral a un degré de coordination optimal alors que les atomes situés en surface ont un degré de coordination incomplet (Auffan, 2007). En réponse à ce déséquilibre de charges de surface, une forte énergie, d'intensité supérieure à l'énergie des couches plus internes de la particule, serait générée en surface de la NPs-Fe. Non seulement, la coordination non-optimale des atomes mais aussi, la forte pression présente en surface des NPs, seraient suffisantes pour provoquer un excès d'énergie à la surface des particules ultrafines. Comparées à leurs analogues macroscopiques, les NPs sont donc considérées comme des objets métastables d'un point de vue thermodynamique. Des modifications structurales sont de plus attendues à la suite de l'évacuation de cet excès d'énergie. La stabilité des phases cristallines, la morphologie des NPs, la croissance cristalline et la réactivité des NPs avec leur environnement seraient toutes reliées à ce phénomène de minimisation de l'énergie libre (Banfield et Navrotsky, 2001).

En solution aqueuse, la minimisation de l'énergie en surface des NPs-Fe peut avoir plusieurs conséquences :

- La forte tension de surface des NPs favorise leur agrégation ;
- L'adsorption d'ions et molécules en surface par les NPs;
- En conditions favorables, la croissance cristalline peut se produire.

Au vu de leur grande réactivité, le comportement des NPs-Fe dans les sols est fortement contrôlé par leurs caractéristiques physico-chimiques et leurs propriétés de surface. Une fois dans l'environnement, ce comportement est toutefois susceptible d'évoluer. La stabilité, la réactivité avec les constituants du sol, ainsi que la mobilité et la biodisponibilité des NPs sont aussi dépendants des propriétés physico-chimiques du milieu dans lequel elles se trouvent.

I.2. Comportements, réactivité et devenir des NPs de fer dans les sols

I.2.1. Propriétés du sol

Le sol, ou « couverture pédologique », est la couche superficielle la plus externe de la croûte terrestre (Gobat et al., 2003). Il est formé de matériaux non consolidés, organiques et minéraux, qui constituent le substrat indispensable à la vie de multiples organismes terrestres. C'est donc un milieu complexe dans lequel transitent et se transforment des composés divers (organiques, et inorganiques, dissous et colloïdaux, vivants). Ces éléments résultent d'une part, de phénomènes physico-chimiques (érosion, altération) et d'autre part, de l'activité biologique induite par les organismes qui s'y trouvent. Le sol est en effet un milieu chimiquement très riche et en constante évolution, dans lequel la partie vivante contribue pour beaucoup à la dynamique géochimique des écosystèmes (« cycles biogéochimiques »). L'équilibre d'un sol repose sur les multiples flux qui s'effectuent entre les différents compartiments du sol : le sol solide, la solution de sol (phase liquide), la phase gazeuse (dont l'interaction avec les NPs est beaucoup plus limitée que les autres phases du sol) et la biomasse (incluse dans la phase solide du sol). Le comportement et le devenir des NPs sont dépendantes des propriétés de ces différents compartiments et des flux qui les relient et, qui peuvent aussi les affecter en retour.

I.2.1.1. Les constituants du sol solide

Le sol se caractérise initialement par sa composition (minérale et organique), qui reflète le matériel parental dont il est issu ainsi que les facteurs environnementaux qui l'ont affecté.

Les principaux minéraux présents dans la plupart des sols incluent : les minéraux de silice (principalement le quartz), les argiles, les oxydes et hydroxydes et les carbonates (Gobat et al., 2003). La proportion dans le sol des différentes fractions granulométriques (sableuse, limoneuse ou argileuse) détermine la texture minérale du sol qui joue un rôle majeur dans le transport et la biodisponibilité des éléments présents. La fraction argileuse (< 2 µm) est particulièrement importante à cet égard. Elle n'influence pas seulement la structure, la porosité et la perméabilité d'un sol, elle contrôle aussi en grande partie sa capacité d'échange cationique (Sparks, 1995). Leur grande surface spécifique (de 15 pour la kaolinite à 800 $m^2\ g^{-1}$ pour la smectite), leur capacité d'adsorption d'eau et de gonflement (hydrophilie) et leur électronégativité jouent un rôle majeur dans les propriétés qu'elles confèrent au sol et dans les interactions qu'elles entretiennent avec les différents constituants qui sont en contact avec elles (complexe argilo-humique).

La fraction organique du sol comprend tous les composés organiques simples ou complexes, isolés ou bien associés entre eux dans des ensembles vivants ou non. Ils incluent : les organismes vivants constituants la biomasse, les organismes morts en voie de dégradation, les composés organiques des chaînes réactionnelles de la minéralisation et les substances humiques (Stevenson, 1982). Les dernières, les substances humiques, sont des polymères naturels complexes et hétérogènes constitués principalement d'oxygène et de carbone (Demirel et al., 2007). Ce sont des molécules organiques aux propriétés chimiques voisines (solubilité, acidité, groupements fonctionnels diversifiés,…). Leurs groupements fonctionnels sont à l'origine de leurs propriétés d'acidité et des interactions multiples auxquelles elles participent. Les acides humiques (HA) et fulviques (FA), lors d'un titrage acide-base, se comportent comme un mélange d'acides faibles avec différents pK (Stevenson, 1982). Cette diversité permet notamment la complexation de divers ions métalliques avec divers ligands, selon leurs affinités, sur une large gamme de pH. Selon Sparks et al. (1995), 25 à 95% de la capacité d'échange cationique d'un sol est développé par la matière organique.

En fonction de leurs proportions respectives dans le sol, leur variabilité spatio-temporelle, et de la vitesse des flux qui les relient, les constituants minéraux et organiques déterminent les propriétés majeures du sol qui sont impliquées dans le fonctionnement global du système. Le sol se caractérise par : sa texture, sa structure, son régime hydrique, son taux d'humidité, sa température (ainsi que le pédoclimat), le complexe argilo-humique, les échanges ioniques, la capacité d'échange, le pH du sol, son potentiel d'oxydo-réduction, sa fertilité.

I.2.1.2. La solution de sol

La phase liquide du sol occupe la porosité du sol avec la phase gazeuse. Elle est composée d'eau et de nombreux éléments dissous qui forment la « solution de sol ». Les éléments dissous sont présents sous de multiples formes allant des ions monoatomiques aux particules colloïdales incluant de nombreuses molécules, ions et complexes de coordination. La composition de la solution de sol est avant tout liée à la nature du substrat avec lequel elle est en contact ainsi qu'à la composition des eaux de pluie et de surface qui l'alimentent. La richesse de la solution du sol résulte principalement des mécanismes d'altération et de solubilisation de la phase solide (Solanki et al., 2015), des produits des activités biologiques et microbiologiques (**cf. section 3.2.1.**) ainsi que ceux liés aux activités anthropiques (activités agricoles, déchets de la sphère urbaine et industrielle). Ces derniers modifient considérablement la composition de la phase liquide et favorisent la dispersion de plusieurs types de NPs.

Dans la solution de sol et dans la plupart des milieux aquatiques, les métaux peuvent être présents sous forme dissoute, colloïdale, et/ou particulaire. La « frontière » entre le soluble et l'insoluble est généralement fixée à 0,2 µm (0,45 µm pour la norme AFNOR). La **Figure 4** propose une description du concept dissous/particulaire et donne quelques exemples de tailles d'entités habituellement rencontrées dans les milieux aquatiques naturels.

En termes de transport et dynamique géochimique, la solution de sol assure les déplacements de matière et permet aux composés réactifs d'interagir avec leur environnement. Le pH de la solution du sol joue à cet égard un rôle particulier puisqu'il détermine l'acidité ou la basicité du sol et peut donc considérablement influencer les réactions chimiques, géochimiques et biochimiques qui s'y produisent (Solanki et al., 2015). La température, la force ionique, la salinité sont aussi des paramètres physico-chimiques de la solution de sol impliqués dans ces réactions. Enfin, la nature chimique des constituants, leur biocompatibilité et biodégradabilité sont des facteurs majeurs vis-à-vis des interactions pouvant se produire entre les NPs et les différents constituants du sol.

La solution du sol joue finalement un rôle agronomique important car les plantes y puisent les éléments nutritifs dont elles ont besoin. Ces éléments sont les espèces présentes sous forme solubilisée généralement désignées par les termes « assimilables » ou « biodisponibles » (**cf. section 3.1.1**).

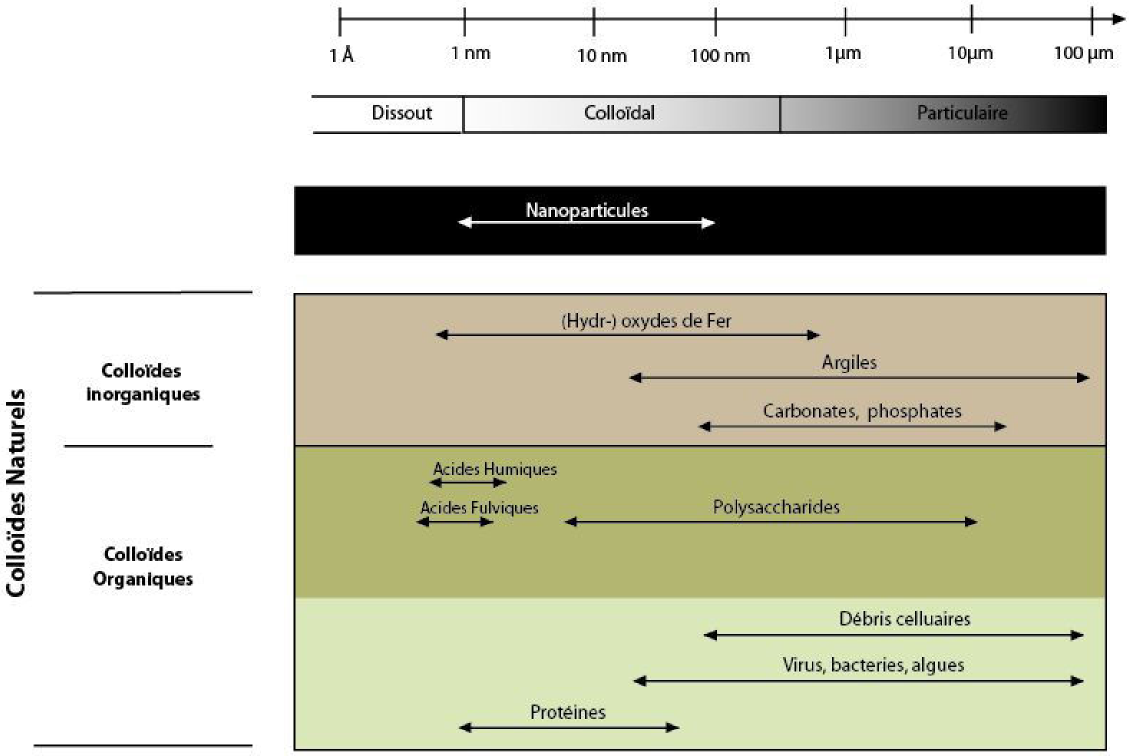

Figure 4 : Principales catégories de colloïdes et NPs présents dans les eaux de surfaces et domaines de tailles auxquels ils appartiennent.

I. 2.2. Interactions des NPs-Fe avec les constituants du sol

I.2.2.1. Stabilité colloïdale

La stabilité colloïdale des NPs est généralement caractérisée par la distribution et la dispersion des tailles des NPs en solution (Hadju, 2009). La stabilité colloïdale des NPs est principalement associée au phénomène d'agrégation, qui est l'un des processus majeurs résultant des interactions entre les NPs-Fe elles-mêmes. Celui-ci provient d'une part de l'attraction qui résulte de la charge de surface des NPs (définie suivant le pH de la solution et le pHzpc propre aux NPs), du nuage électronique induit par la force ionique de la solution, des propriétés de surface des NPs et de leurs propriétés magnétiques (Wang et al., 2016). A cet égard, la théorie DLVO (Derjaguin, Landau, Verwey, Overbeek), est l'une des théories les plus utilisées pour décrire les réactions se produisant à l'interface surface des NPs/solution (Ghosh, 2011). Suivant cette théorie, le bilan des forces aux interfaces varie essentiellement avec les forces de Van der Waals (liées à la composition des particules) et les forces électrostatiques, qui résultent de leur charge de surface et dépendent des caractéristiques du milieu (Ollivier et al., 2016).

Dans les solutions de sol, la stabilité colloïdale des suspensions de NPs-Fe est susceptible d'évoluer fortement. D'une part, les caractéristiques physico-chimiques de la solution (température, force ionique, pH, salinité) affectent les interactions électrostatiques entre NPs et leur agrégation (Joo et Zhao, 2017). D'autre part, les constituants présents dans la solution de sol et en contact avec les NPs sont autant d'agents capables de modifier les propriétés de surface des NPs et qui sont fondamentales dans les réactions d'attraction/répulsion des NPs-Fe entre elles (Dwivedi et al., 2015). Plusieurs études ont notamment montré que l'adsorption d'acides humiques à la surface des NPs favorisait la dispersion des NPs sur une large gamme de pH (>2,3) (Liu et al., 2008 ; Yu et al., 2018). Ainsi, en modifiant la chimie de surface des NPs (par l'encrage de groupes fonctionnels spécifiques), les acides humiques modifient les interactions de surface entre NPs (**Figure 5**) (interactions stériques et électrostatiques). Toutefois, l'enrobage de NPs par des acides humiques ne favorise pas toujours leur dispersion et peut, suivant les conditions du milieu, conduire à leur agrégation. Par exemple, en fonction de la concentration en acides humiques et du pH du milieu, si la quantité d'acides humiques est insuffisante pour recouvrir toute la surface des NPs, cela peut favoriser les forces d'attraction entre particules (partiellement couvertes) du fait des charges opposées qu'elles portent (Hadju et al., 2009).

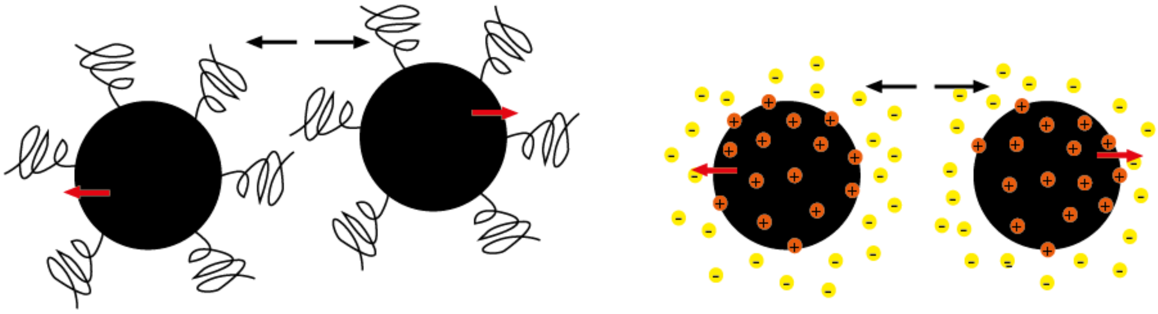

Figure 5 : Les différentes interactions de surface impliquées dans la stabilité colloïdale des NPs en solution. A gauche est illustrée l'interaction stérique résultant de la présence de molécules attachées à la surface des NPs, et à droite sont illustrées les interactions électrostatiques entre particules chargées.

La stabilité colloïdale des NPs-Fe est importante car elle est fortement impliquée dans les interactions NPs-Fe / constituants du sol et de la solution de sol. La taille des agrégats affecte notamment leur capacité à pénétrer les pores du sol ou à s'attacher à la surface des constituants présents, ce qui conditionne directement leur mobilité (cf. section 2.3.2.). Elle est aussi impliquée dans les interactions avec le vivant, aussi bien d'un point de vue de la toxicité des NPs-Fe (les plus petites NPs-Fe peuvent plus facilement pénétrer les pores cellulaires) qu'au niveau de leur biodégradabilité (les plus gros agrégats sont plus longs à solubiliser). Enfin, la stabilité colloïdale pourrait jouer un rôle majeur concernant la réactivité des NPs-Fe et notamment dans les interactions NPs-Fe / métaux, en impactant notamment l'accessibilité aux sites d'adsorption.

I.2.2.2. Réactivité à l'interface NPs-Fe / solution

En milieu aqueux, la surface des oxydes forme des complexes avec l'eau. Des groupements OH^- se forment par dissociation d'un proton et recouvrent la surface pour compléter la coordination des ions métalliques (**Figure 6**). Le mécanisme est alors analogue à une réaction de complexation avec échange de protons (Stumm, 1992).

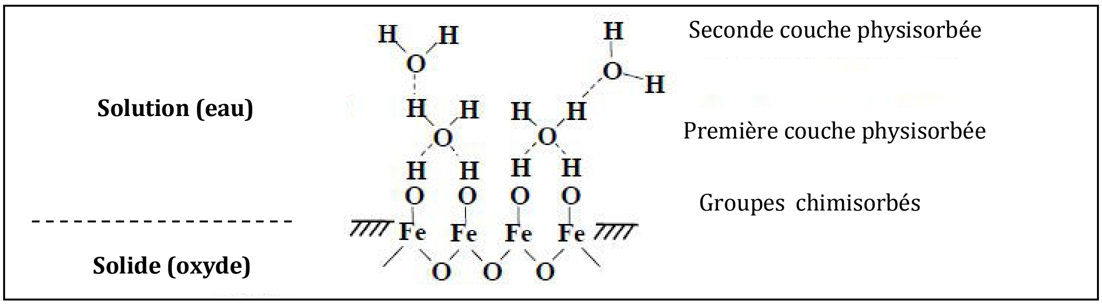

Figure 6 : Représentation schématique de l'adsorption de l'eau à la surface d'un oxyde de fer (modifiée de Stumm et al., 1992).

Les cations métalliques ont une grande affinité pour les oxydes et hydroxydes de fer à la surface desquels ils s'adsorbent. Leur complexation sur les sites de surface hydrolysés est dépendante du pH (**Figure 7**). Les phénomènes de complexation des métaux en solution ou d'adsorption en surface des oxydes de fer sont des mécanismes importants qui contrôlent aussi leur biodisponibilité et leur spéciation (Sparks, 1995). Les métaux sont en général sous forme dissoute dans l'eau, en ions plus ou moins hydratés, ou complexés.

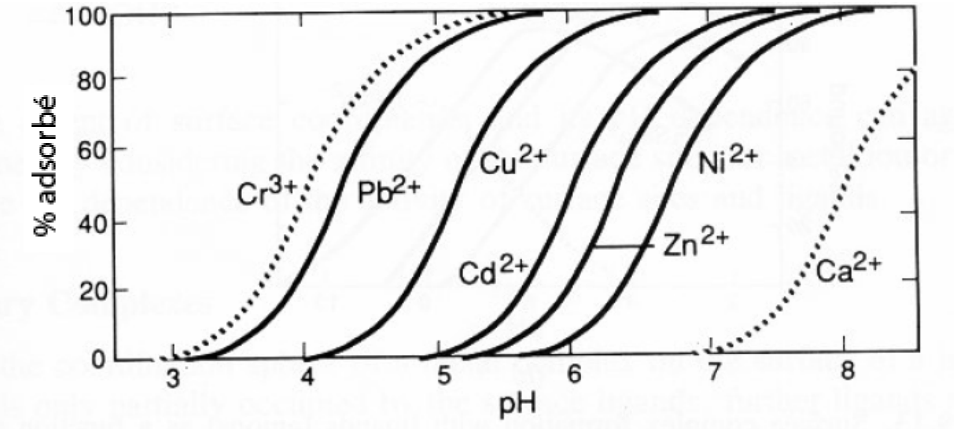

Figure 7 : Formation de complexes de surface de quelques métaux à la surface d'un oxyhydroxyde de fer en fonction du pH (90 mg de FeOOH(s) avec 2.10^{-4} mol de sites de surface par litre, 5.10^{-7} M de métaux et une force ionique de 0.1M $NaNO_3$) (modifié d'après Stumm, 1992).

Des formes complexées organiques ou inorganiques présentes en solution peuvent aussi participer à la réaction de complexation en modifiant le type d'adsorption selon la concentration en métal initialement présente (association Surface – Métal – Ligand lorsque la quantité de métal adsorbé augmente avec le pH, ou association Surface – Ligand – Metal lorsqu'au contraire la quantité de métal adsorbé diminue avec le pH) (Stumm, 1992). Plusieurs molécules organiques tels que les AH, AF ou les acides carboniques, ou d'autres acides de l'environnement forment aussi facilement des complexes avec les métaux, affectant leur biodisponibilité. La matière organique des sols tend à immobiliser les polluants cationiques, adsorbés par des ligands organiques insolubles (Shaker et Albishri, 2014 ; Tipping, 1993 ; Weber et al., 2006). La forme chimique d'un métal (spéciation) est fondamentale puisqu'elle est directement reliée au comportement en solution des espèces, à leur biodisponibilité et à leur toxicité (Weinberg et al., 2011). Ainsi, la complexation d'un métal par des composés inorganiques et organiques, comme par exemple, la matière organique des sols ou des eaux peut entraîner une diminution notable de sa toxicité en diminuant la concentration ionique libre et la biodisponibilité (Aïken et al., 2011). Si la matière organique peut être absorbée par les organismes par ingestion, sa capacité à fixer les métaux devient au contraire un vecteur de la biodisponibilité.

I.2.3. Devenir des NPs-Fe dans les sols

Une fois dans l'environnement, les NPs agissent entre elles et avec leur milieu (matière en suspension ou en solution, communauté microbienne) via divers processus (cf. sections précédentes). Ces interactions affectent non seulement leur devenir et comportement dans les sols (mobilité, biodisponibilité, toxicité) mais aussi, leurs impacts sur le milieu (dynamique géochimique des écosystèmes) (Joo et al., 2017 ; Dinesh et al., 2012).

I.2.3.1. Impacts du milieu sur les propriétés intrinsèques des NPs-Fe

Les conséquences majeures qui résultent des interactions des NPs-Fe avec la solution de sol et les constituants qui y sont dissous peuvent induire les transformations suivantes:

- L'agrégation des NPs, induite par les propriétés du milieu (pH, force ionique) ou par la présence de constituants favorisant leur agrégation/dispersion (**cf. section 2.1.1.**) (Tombacz et al., 2013 ; Vindedahl et al., 2016);
- Les transformations cristallochimiques ; l'oxydation de la magnétite en maghémite est un exemple de transformation structurale spontanée pouvant se produire en conditions naturelles (aérobies) (Frison et al., 2013). Ces transformations sont également fondamentales car elles peuvent modifier les propriétés magnétiques des NPs qui à leur tour affectent leur agrégation, mobilité, réactivité ;
- La complexation d'ions ou de ligands inorganiques ou organiques à la surface des NPs-Fe peut modifier leur état d'agrégation mais aussi le transport, la réactivité, la disponibilité, la spéciation/toxicité et/ou la biodégradabilité des substances adsorbées (Otero-Farina et al., 2015) ;
- La (co-)précipitation ; si les concentrations en métaux et conditions Eh et pH le permettent, certains métaux peuvent précipiter et former une nouvelle phase à partir de l'oxyde initial. Les bactéries peuvent aussi contribuer activement à la précipitation de nouvelles phases cristallines (Pédro, 2007) ;
- La solubilisation des NPs-Fe, qui résulte des conditions Eh et pH de la solution de sol et est favorisée par la présence de molécules organiques comme celles produites par les végétaux et microorganismes (« biodégradations ») pour dissoudre les oxydes et

hydroxydes de fer dans les sols (**cf. section 3.1.2.**) (Dwivedi et al., 2015; Mudunkotuwa et al., 2011).

Ces modifications, qui dépendent avant tout des conditions physico-chimiques du milieu et de leur composition, sont importantes et nécessitent d'être considérées puisqu'elles peuvent affecter la mobilité des NPs, ainsi que leur disponibilité et leur toxicité pour les organismes du sol.

I.2.3.2. Mobilité des NPs-Fe et interactions avec le vivant

La mobilité d'un élément est définie par sa capacité à migrer, à passer d'une forme chimique à une autre ou à changer de phase (Lefevre et al., 2016). Elle dépend directement du régime hydrique du sol, qui repose sur sa texture (détermine les forces de rétention de l'eau), sa structure (influence la circulation de l'eau) et sa porosité (définit le volume du réservoir hydrique du sol). Elle est aussi généralement associée à une durée. Afin d'évaluer la mobilité des NPs dans le milieu naturel, les lois de la dynamique colloïdale (agrégation et/ou dépôt) sont généralement appliquées (Ollivier et al.,2016). Celles-ci permettent de prendre en compte à la fois la composante liée à l'efficacité du transport des NPs et celle liée au bilan des forces qui résulte des interactions avec les composants en présence (attraction/répulsion). Les deux principaux paramètres étudiés en termes de dynamique colloïdale sont la fréquence de collision entre les particules et la surface (qui dépend de la concentration en NPs et leur type de mouvement), et un coefficient d'efficacité de collage α qui varie de 0 (système purement répulsif) à 1 (lorsque chaque collision entraîne le collage des NPs) (Dwivedi et al., 2015).

Les processus strictement physico-chimiques susceptibles d'influencer le comportement des NPs peuvent être divisés en deux groupes : ceux favorisant l'immobilisation (par exemple, l'adsorption des NPs par des ligands organiques insolubles), et ceux favorisant leur mobilité et leur dispersion (par exemple, enrobage de matières organiques) (Grillo et al., 2015 ; Zhang et al., 2009). Ces processus, qui gouvernent la mobilité des NPs-Fe, ont un impact direct sur la disponibilité et la toxicité des NPs-Fe.

Enfin, en plus d'être sous l'influence de leur milieu, les NPs influencent elles-mêmes le devenir des constituants avec lesquels elles interagissent. Elles sont donc susceptibles d'affecter aussi la mobilité, la biodisponibilité et la toxicité de ces constituants.

I.3. Interactions entre les NPs-Fe et les plantes

I.3.1. Nutrition des plantes

Le comportement en solution, la réactivité vis-à-vis des constituants du sol et de la solution de sol et leurs transformations dans le temps, font des NPs des constituants dynamiques qui évoluent avec les changements du milieu dans lequel ils se trouvent, mais aussi qui influencent les propriétés de ce milieu. Il apparaît donc crucial de comprendre les impacts des NPs-Fe sur le sol, puisque ce dernier constitue un support de vie fondamental pour les plantes et les organismes qui s'y développent. Avant d'étudier les impacts potentiels directs associés à la mise en contact des NPs-Fe avec les plantes, nous précisons comment les plantes utilisent leur milieu et s'y développent afin de comprendre en quoi les NPs-Fe pourraient, par leur présence dans le sol, interférer dans le processus fondamental de nutrition des plantes.

I.3.1.1. De la roche aux bioéléments

La lumière du soleil, l'eau, le CO_2, l'O_2 ainsi que de nombreux éléments chimiques sont les principaux constituants dont les plantes ont besoin pour se développer. Environ soixante éléments chimiques sont présents dans un végétal (bien qu'une grande partie de la masse des cellules ne soit composée que des quatre éléments chimiques primaires - azote, hydrogène, carbone et oxygène). Parmi les nombreux éléments absorbés par la plante, dix-sept de ces bioéléments sont considérés actuellement comme des éléments essentiels. Ces éléments incluent neuf macroéléments ($\geq$ 1000 mg Kg^{-1} de masse sèche de la plante) et huit microéléments ou oligo-éléments ($\leq$ 100 mg Kg^{-1} de masse sèche de la plante) (Marschner, 1995). Les « oligo-éléments » désignent les éléments nécessaires à la croissance d'un organisme en faible quantité. Ils incluent plusieurs cations (B, Fe, Mn, Zn, Cu, Mo, Ni) indispensables à la vie cellulaire végétale qui entrent en général dans la structure et la fonction de cofacteurs enzymatiques (**Tableau 1**).

Parmi les éléments absorbés par la plante, une partie entre par les feuilles, via les stomates (NH_3, SO_2…) tandis qu'une autre partie, d'origine minérale, est absorbée par les racines (Mengel et Kirkby, 2001). Ces bioéléments sont initialement présents dans le réseau cristallin des minéraux primaires (les silicates comme les micas, les plagioclases, les pyroxènes, … fournissent - outre la silice - des éléments essentiels tels que Fe, Mg, K, Cl) et des minéraux secondaires (les argiles, oxydes, carbonates… fournissent du Ca, Fe, Cl...). Leur libération est réalisée par divers processus physico-chimiques d'origine géologique (érosion, altération) ou biologique. La baisse du pH du sol, favorisée par l'apport des eaux de pluie et la décomposition de la matière organique, entraîne l'altération et favorise la solubilisation à pH acide des carbonates, sulfates et phosphates qui libèrent des ions (K^+, Mg^{2+}, Ca^{2+} et Mn^{2+}) sous des formes chimiques disponibles pour les plantes. (Solanki et al., 2015). L'action du vivant altère aussi directement les minéraux et provoque leur solubilisation en absorbant des ions. En effet, certains micro-organismes participent indirectement à la corrosion des roches en modifiant leur milieu. Ces changements affectent le pH, la teneur en oxygène et le potentiel redox ainsi que la production de composés organiques capables de complexer des ions minéraux sous forme de chélates. Ainsi, l'attaque acide de minéraux, solubilise les éléments sous une forme ionisée. En conditions aérobies, ce sont principalement les bactéries chimiolithotrophes nitrifiantes et sulfooxydantes qui solubilisent les minéraux en produisant les acides sulfurique et nitrique. Les champignons mycorhizhiens sont aussi d'efficaces solubilisateurs et extracteurs de minéraux. Ils sont capables d'absorber et de minéraliser des composés organo-métalliques et de transférer ces métaux à la plante sous forme d'ions inorganiques. De plus, du fait de leur extension dans le sol, de la surface élevée de leur mycélium extraradiculaire et de leur grande capacité à concentrer les métaux, les champignons mycorhiziens augmentent considérablement le potentiel d'absorption des métaux par les plantes (Gobat et al., 2003). La production d'acides organiques par les microorganismes et les racines joue ainsi un rôle important dans l'altération des minéraux (Jones et al., 2004). Leur action concerne de nombreux métaux bi- ou trivalents (Fe, Al, Cu, Zn, Ni, Mn, Ca, Mg), alors susceptibles de former des complexes avec des di- ou triacides organiques. Les acides oxalique, citrique, 2-cétoglutonique, tartrique, ainsi que des polyphénols (acides salicylique et dihydroxybenzoïque) sont souvent secrétés par divers microorganismes et plantes. Les complexes formés entre les acides organiques et les métaux se présentent sous la forme de cycles incorporant les cations ce qui permet de les stabiliser sous une forme soluble, à travers un large domaine de pH et de potentiel redox. Plusieurs bactéries favorisent la croissance des végétaux en solubilisant des ions nutritifs, y compris des métaux lourds, par acidolyse (Sparks, 1995). Enfin, l'origine des bioéléments dans la solution de sol provient également de l'oxydation de la matière organique libérant ses éléments constitutifs (recyclage).

Lorsqu'ils sont libérés, les ions se fixent sur les complexes argilo-humiques ou sont dissous dans la solution de sol, par échange ionique (Sparks, 1995). Leur disponibilité est ensuite fonction des conditions du milieu, contrôlant notamment leur spéciation. Le taux d'humidité, le pH et le potentiel redox varient temporairement et influencent la solubilité des ions. La baisse du pH (pH < 4), ou son augmentation (pH > 7), induisent la mise en solution de nombreux ions, notamment des métaux qui peuvent s'avérer toxiques (Reeder et al., 2006). D'un autre côté, les modifications saisonnières de la microstructure du sol changent également l'accessibilité de certains sites aux radicelles et au mycélium extraradiculaire des mycorhizes (Gobat et al., 2003).

La spéciation des éléments du sol représente un enjeu majeur vis-à-vis de la nutrition des plantes car elle contrôle leur biodisponibilité. Alors que les NPs-Fe constituent une forme chimique particulière du fer, elles pourraient, par leur présence dans le sol, être une source de fer pour la plante. Avant d'envisager cette hypothèse, les principaux mécanismes biogéochimiques du fer dans les sols seront abordés. Par ailleurs, du fait des interactions fortes pouvant se produire entre NPs-Fe et métaux (cf. section 2.), les interactions métaux/plantes seront également étudiées afin de comprendre comment les NPs-Fe pourraient interférer dans ces interactions.

Tableau 1 : Rôles des principaux cations métalliques du sol dans les plantes.

Elément	**Forme dans le sol**	**Concentrations dans le sol (S) et la plante (P)** (mg kg^{-1} mat. Sèche)	**Rôles principaux dans la plante, carence, toxicité**
Fe	- plus de 20 composés minéraux: magnétite, hématite, goethite, lépidocrocite, etc. - constituant du complexe argilo-humique - chélaté à la matière organique - forme ionique en solution (Fe^{2+} dans les sols anoxiques)	S: jusqu'à 40 000 P: 50 à 1000	- évite la chlorose - effecteur des processus d'oxydoréduction - constituant et activateur d'enzymes - chélaté par les sidérophores, transporteurs cellulaires - régulateur de la réduction des nitrites et la fixation d'azote
Mn	- semblables à celles du fer	S : 200 à 4000 P: 20 à 200	- favorise la croissance et évite la chlorose - carence possible sur les sols basiques et toxicité sur sols acides - constituant et activateur d'enzymes - rôle dans l'oxydoréduction de l'eau lors de la photosynthèse
Cu	constituant de minéraux (ex. chalcopyrite) chélaté à la matière organique	S : 5 à 100 P: 2 à 200 (P cuprophytes: jusqu'à 1600)	- régulateur des processus d'oxydoréduction - constituant d'enzymes assurant la synthèse de la lignine - stimulation de la croissance - toxique à hautes concentrations, sauf pour les plantes adaptées
Zn	constituant de silicates ferromagnésiens très peu de Zn^{2+} en solution	S : 10 à 300 P: 10 à 100	- constituant d'enzymes d'oxydation (oxydases) - synthèse et protection des hormones de croissance - aide à la synthèse de la chlorophylle
Mo	constituant de minéraux MoO_4^{2-} ou $HMoO_4^-$ fixés sur le complexe adsorbant ou libres dans la solution du sol	S: 0,5 à 5 P: 0,2 à 10	- nécessaire au métabolisme de l'azote (constituant de l'enzyme nitrate réductase, ainsi que du complexe de la nitrogénase)
B	constituants des silicates (ex. 3-4% de la tourmaline)	S : 5 à 100 P: 2 à 100	- constituant d'enzymes - aide à la synthèse de la chlorophylle - carences fréquentes, amenant par exemple le pourrissement du cœur de la betterave ou des lésions de l'écorce du pommier
Al	- constituant de base des minéraux, avec Si (8% de la lithosphère) - formes nombreuses en fonction de l'acidité du sol entre $Al(OH)_4^-$, $Al(OH)^{2+}$, et Al^{3+} (ion libre)	S: 50 à 200 P: 2 à 3	- favorise, à de très faibles concentrations, la production d'espèces cultivées - très vite toxique dès que le pH du sol est inférieur à 5,5 - sur sol acide, seules les alumino-tolérantes résistent (ex. Ericacées)
Ni	- présent dans les minéraux des roches magmatiques ultra-basiques. -généralement sous forme ionique en solution : Ni^{2+}	S: 20 à 400 P: 10 à 100	- composant de l'uréase -en cas de carence en Nickel, l'accumulation de l'urée dans les feuilles peut entraîner une nécrose.

I.3.1.2. Biogéochimie du fer

Le fer est le quatrième élément chimique le plus abondant de la croûte terrestre et le deuxième métal le plus abondant (après l'aluminium). Sa position (26ème place) dans le tableau périodique, au milieu de la première série des éléments de transitions (dont l'orbitale d est incomplète), implique que le fer peut se trouver sous différents états d'oxydation. Les deux principales formes chimiques du fer sont Fe^{2+} et Fe^{3+} (Crichton et al., 2001).

Le fer est un bioélément essentiel pour les plantes. C'est un élément redox sensible majeur dans les enzymes faisant partie des cofacteurs (structures moléculaires non protéiques qui participent directement à la réaction catalysée par une enzyme) transporteurs d'électrons ($Fe^{2+} \rightarrow Fe^{3+} + e^-$). Le fer est notamment présent dans les protéines ferrosulfureuses (classe de protéines redox intervenant dans les transferts d'électrons) et les hémoprotéines (classe de protéines redox intervenant dans les transferts d'électrons et dans le transport de l'oxygène) (Kobayashi et Nishizawa, 2012). En plus de faire partie de certains cofacteurs redox, le fer est essentiel pour les plantes du fait de son rôle dans la biosynthèse de chlorophylle, en régulant plusieurs enzymes. Lorsqu'une plante est carencée en fer, la chlorose est le principal symptôme lié à ce déficit, associé selon l'espèce, à une moindre production de biomasse (Briat et al., 2007).

La carence en fer est un symptôme plus répandu que sa toxicité pour le végétal. Elle se produit généralement dans les sols calcaires à pH élevé lorsque la décomposition de la matière organique accroît la précipitation de bicarbonates (augmentant alors la disponibilité en phosphate) (Vose, 1982). L'absorption du fer par la plante est en effet dépendante de celle des autres éléments en présence dans le sol. Il a notamment été démontré qu'un sol avec des teneurs élevées en cuivre (Cu) diminuait considérablement l'absorption du Fe (Xing, 2010). La carence en Fe peut en effet être induite par d'autres éléments (Zn, P, Cu) présents en forte concentration dans les sols. Par ailleurs, la disponibilité du fer est fonction de son état d'oxydation, la forme Fe(II) du fer étant la forme soluble la plus disponible (Uren, 1984).

Le fer utilisé par les plantes est généralement d'origine sédimentaire (hydroxydes et oxydes ferriques) ou bien issu de roches cristallines (fer bivalent à l'exemple de la pyrite) (Colombo et al., 2013). En milieu oxique, le fer n'est solubilisé sous forme d'ions ferriques (Fe(III) libres) qu'en milieu très acide. Lorsque les conditions de pH sont proches de la neutralité, le fer est présent sous sa forme oxydée qui correspond à des composés quasi insolubles (oxydes et phosphates) (Claudio et al., 2017). Dans ce cas, sa solubilisation implique l'intervention de petites molécules capables de chélater le Fe(III). Les substances humiques sont des chélateurs particulièrement actifs dans les podzosols (Pédro, 2007). Certaines bactéries (rhizogènes ou non) et des champignons (mycorhizogènes ou saprophytes) produisent des substances complexantes du fer (acides aliphatiques carboxyliques, acides phénols, acides hydroxamiques…) qui participent à l'altération de minéraux (ferromagnésiens, oxydes) et à la solubilisation d'éléments minéraux (transférés plus abondamment à la solution de sol et aux végétaux). L'oxydation du fer ferreux n'exige pas, quant à elle, la participation d'organismes vivants et peut se faire spontanément avec les conditions Eh et pH du milieu (Ehrlich, 2002). Les bactéries ferrooxydantes (comme par exemple, *Thiobacillus ferrooxidans* en dessous de pH 4 ou *Gallionella ferruginea* à des pH proches de la neutralité) sont néanmoins de puissants catalyseurs du processus. En conditions anoxiques, la réduction des oxydes et hydroxydes de fer et leur solubilisation sous forme d'ions Fe^{2+} nécessite l'activité de microorganismes (Münch et Ottow, 1983). Certaines bactéries, généralement des bactéries hétérotrophes (chimio-organotrophes) utilisent le Fe(III) comme accepteur d'électron pour leur respiration, en parallèle ou en complément de fermentations. Celles-ci réduisent le Fe(III) en solution, mais entraînent aussi la dissolution et l'altération des oxydes et oxyhydroxydes. Le fer, alors disponible sous forme de Fe(II), ne restera soluble qu'en conditions réductrices ou acides (Berthelin et Stemmler, 2004). Les bactéries ferroréductrices spécialisées (par exemple les bactéries du genre *Geobacter* ou *Geotrix*) participent à la réduction du fer lors de l'oxydation de substrats organiques, en particulier dans l'élimination de contaminants organiques dans les aquifères.

I.3.1.3. Interactions plantes / métaux

Les « métaux lourds » désignent les éléments dont la masse volumique est supérieure à 5 g cm^{-1} (Adriano, 2001). La plupart des métaux lourds sont des éléments traces, trouvés en faible quantité (< 100 µg g^{-1}). Les roches magmatiques, qui peuvent par exemple contenir de fortes teneurs en métaux lourds, libèrent par altération les métaux finalement distribués à l'état de traces dans le sol, les végétaux et les eaux (L'Huillier, 1994). Les éléments traces métalliques (ETs) proviennent également de contaminations locales liées à des activités industrielles ou à des apports agricoles concentrés (**Figure 8**). Celles-ci peuvent mener à la présence de métaux en concentrations supérieures aux concentrations naturellement présentes dans l'environnement.

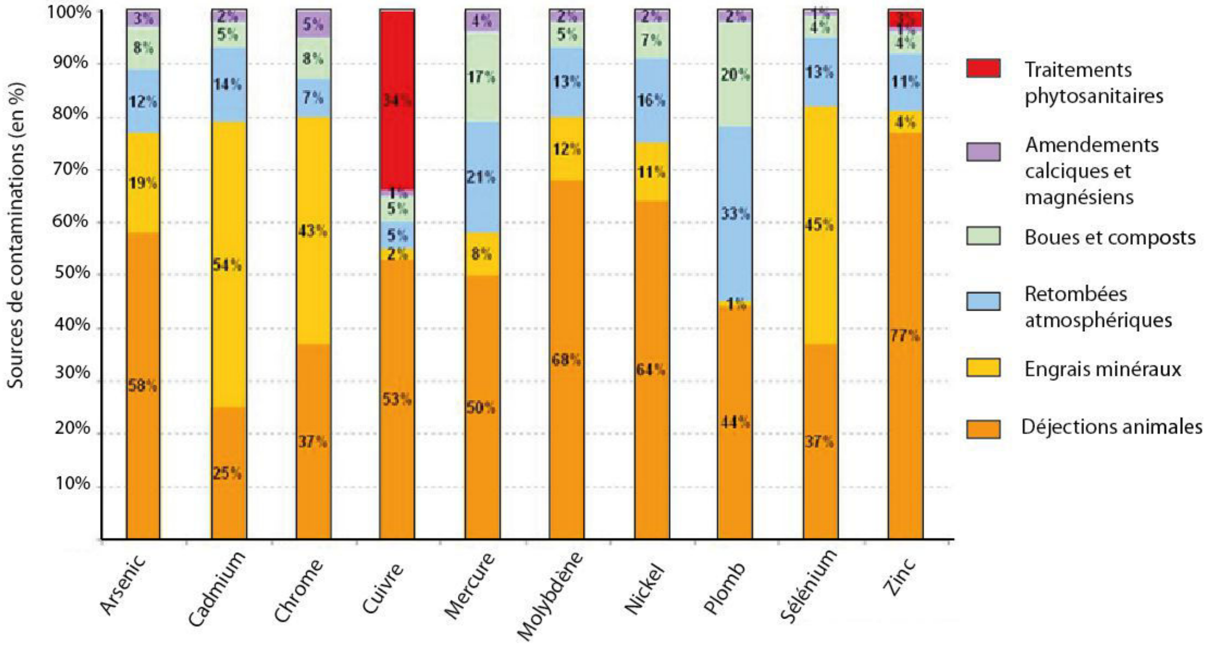

Figure 8 : Proportion des différentes sources de contamination dans l'estimation des quantités totales de métaux et métalloïdes entrant sur les sols agricoles, en % (données : Ademe-Sogreah 2007, 2012)

Chez les plantes, et chez la plupart des organismes vivants, plusieurs ETs ont une fonction biologique bien reconnue dans de faibles quantités, mais avec l'augmentation de leur concentration, ils deviennent toxiques (Marschner, 1995). C'est le cas de plusieurs éléments très répandus dans les sols (Fe, Mn, Cu, Zn, Mo) qui forment de nombreux composés avec les molécules inorganiques ou organiques (notamment les enzymes). D'autres éléments ne sont pas nécessaires pour les organismes et peuvent produire des effets toxiques, même à très faible concentration (c'est le cas par exemple du Pb, Hg et du Cd) (Gobat et al., 2003).

En général, les effets toxiques des métaux sont observés au niveau des racines et sont souvent diversifiés (diminution de la biomasse, changement de morphologie, diminution de l'élongation racinaire, diminution de la densité de poils absorbants, subérification ou lignification accrue, épaississement du méristème, brunissement ou apparition de pigments…) (Ouzounidou, 1994 ; Saad, 2017). L'inhibition de la croissance racinaire est un effet précoce de la toxicité des métaux lourds sur les végétaux (Barcelo et Poschenrieder, 1990). Cet effet est toutefois souvent difficile à observer, de sorte que le principal effet visible est une diminution de la croissance des parties aériennes (il peut y avoir diminution de la croissance sans déformations foliaires, chloroses, nécroses ou colorations particulières). D'autre part, les chloroses, induites par une carence en fer, sont souvent liées à un effet toxique des métaux

(Leskova et al., 2017). Indépendamment des effets physiologiques directs induits aux plantes, la présence de métaux est aussi à l'origine d'une modification de la structure et de la diversité des communautés microbiennes (Brookes et McGarth, 2006) ; ce qui contribue aux impacts physiologiques induits par les métaux aux plantes.

La phytotoxicité des métaux se produit en (a.) altérant les transferts hydriques, aboutissant à un flétrissement de la plante (généralement en dégradant le système racinaire) (Barcelo et Poschenrieder, 1990), (b.) altérant l'intégralité du plasmalemme des cellules du cortex racinaires - soit, par dégradation de la membrane (cas du Cu) induisant des phénomènes de fuites d'ions soit, par fixation du métal sur la membrane (cas de l'Al) par altération des systèmes d'absorption-, (c.) inhibant la mitose au niveau des méristèmes racinaires, (d.) inhibant la photosynthèse et (e.) affectant diverses activités enzymatiques(telle qu'une diminution de l'activité de la Rubisco (cas du Cd, Cu, Pb ou Zn) entraînant une diminution de la fixation photosynthétique du CO_2 (L'Huillier, 1994).

Les principales stratégies mises en place par les plantes pour résister aux métaux lourds sont d'ordre physiologique. Elles relèvent de :

- processus internes d'adaptation mis en place pour évacuer les éléments toxiques ou pour les stocker sous une forme inactive ;
- mécanismes externes capables de ralentir ou d'empêcher l'entrée des cations toxiques (les champignons mycorhiziens, par exemple, peuvent filtrer les flux ioniques avant leur entrée dans la plante).

Finalement, la concentration en métal d'un sol, d'un sédiment et même de l'eau n'est pas suffisante pour déterminer sa toxicité pour les organismes présents. La concentration dans l'eau des pores serait un meilleur critère pour les sols, avec l'hypothèse supplémentaire que le transfert à travers les membranes biologiques soit proportionnel à l'activité de l'ion métallique libre en solution. Plusieurs études suggèrent que l'assimilation est proportionnelle à la concentration en ion libre et non à la concentration totale du métal en solution (Saad, 2017). En outre, la toxicité des métaux est liée à la présence d'une certaine forme des métaux dans la solution de sol, généralement une forme ionique (Jaishankar et al.,2014). La toxicité des métaux est donc souvent limitée d'une part, par leur biodisponibilité et d'autre part par le développement possible de mécanismes de résistance aux métaux de la communauté microbienne (Hoosta et al., 2008).

I.3.2. Absorption des éléments du sol et des NPs-Fe

I.3.2.1. Absorption des éléments dissous

Grâce à leur appareil racinaire, les plantes absorbent des cations (Ca^{2+}, Mg^{2+}, K^{+}, Cu^{2+}, Mn^{2+}, NH^{4+}…) ou des anions (NO^{3-}, $HPO4^{2-}$, H_2PO^{4-}, $SO4^{2-}$…) ainsi que de petites molécules organiques (comme des monosaccharides) et des chélates (par exemple, les sidérophores). La racine (ou appareil racinaire) est le lieu d'échanges entre le sol et la plante vasculaire (**Figure 9**). La racine principale (ou les racines adventives selon les cas), qui assurent l'encrage de la plante dans le sol, se ramifient en racines moyennes (racines latérales ou secondaires) qui pénètrent la porosité du sol et en racines fines (radicelles) qui assurent la nutrition de la plante (Gobat et al., 2003). L'eau et les bioéléments y sont absorbés au moyen de poils absorbants ou de champignons mycorhiziens qui leur sont associés (**Figure 10**). Cette interface représente la rhizosphère. C'est une zone dynamique d'interactions plante-microbes où l'activité biologique intense et la rhizodéposition racinaire impactent considérablement les propriétés physico-chimiques du sol sur lequel elles se développent (Jones et al., 2004).

Avec la libération de composés carbonés et azotés (les rhizodépôts), la rhizosphère contient 10 à 100 fois plus de microorganismes par gramme de sol que le sol non rhizosphérique (Cunningham et Ow, 1996). Dans la « rhizodéposition » se trouvent : les cellules détachées (principalement de la coiffe), sécrétrices d'enzymes et de protéines (avant et après être détachées) ; les lysats (issus de l'autolyse des tissus rhizodermiques et corticaux) ; les mucilages sécrétés par plusieurs zones de la racine (principalement par la coiffe mais aussi, par les poils absorbants); et les exsudats qui forment la part dominante de la rhizodéposition (ce sont des composés organiques solubles qui comprennent des sucres, des acides aminés, des acides organiques, des facteurs de croissance - par exemple les vitamines - et des phyto-hormones). Les mucilages, d'origine mixte végétale ou microbienne, sont des composés gélatineux à base de polysaccharides (ou de pectine au niveau des poils absorbants). Ils sont particulièrement importants pour l'agrégation des microorganismes et des particules du sol (Gobat et al., 2003). Les plantes peuvent également favoriser l'abondance de microorganismes bénéfiques dans la rhizosphère. Certaines bactéries, qualifiées de Rhizobactéries qui Favorisent la Croissance des Plantes (RFCP) ou Plant Growth Promoting Rhizobacteria (PGPR) en anglais (Lugtenberg et Kamilova, 2009), ont reçu beaucoup d'attention en raison de leurs effets bénéfiques sur la croissance des plantes (Beneduzi et al., 2012). Elles représentent 2 à 5% de la totalité des rhizobactéries (Antoun et Kloepper, 2001) et appartiennent à différents genres : *Pseudomonas, Azospirillum, Azotobacter, Bacillus, Burkholderia, Curtobacterium, Rhizobium*...Une bactérie qualifiée de PGPR présente trois caractéristiques principales, telles que : a) la production de métabolites bénéfiques à la croissance des plantes, b) la production de métabolites antagonistes aux agents pathogènes et enfin c) une capacité à coloniser efficacement le système racinaire.

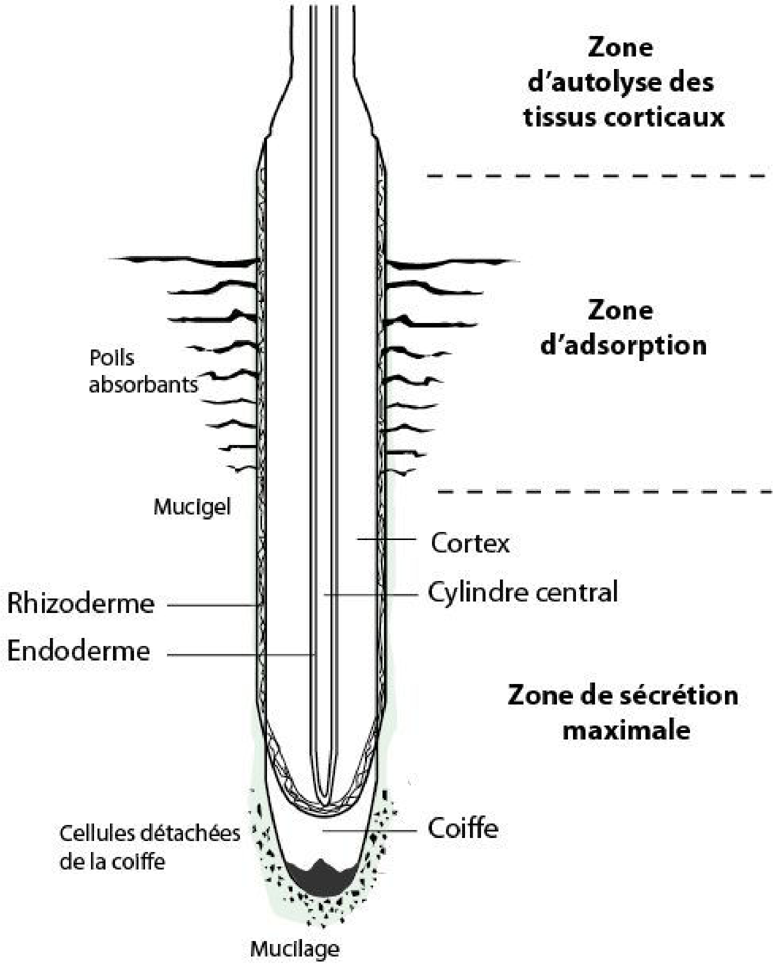

Figure 9 : Coupe longitudinale d'une racine, illustrant les différentes zones d'absorption et les sécrétions libérées au niveau de la rhizosphère (modifié d'après Gobat et al., 2003).

Après solubilisation au sein de la rhizosphère, le transport des éléments du sol vers la plante s'effectue d'abord dans le sol distant et dans les espaces intercellulaires des couches externes de la radicelle (voie apoplastique - cortex racinaire). Dans cette zone, le transport se fait de façon passive par flux de masse (entraînement par l'eau) ou par diffusion (transport d'une substance d'un compartiment où le potentiel électrochimique de la substance est plus fort vers un compartiment où il est plus faible) (Saad, 2017). Le transport des éléments vers l'intérieur la cellule (voie symplastique) a lieu à la limite du cylindre central, au niveau des poils absorbants ou de l'endoderme (**Figure 10**). A cet endroit, le passage des éléments par voie apoplastique est bloqué par des substances hydrophobes, comme la subérine, qui font barrage obligeant les éléments à pénétrer dans le cytoplasme et à emprunter la voie symplastique (Gobatet al., 2003). Un transport actif y est nécessaire pour vaincre le gradient osmotique défavorable et apporter les ions dans des cellules deconcentration saline plus élevée (Krämer et al., 2007 ; Saad, 2017). Plusieurs mécanismes successifs sont alors impliqués. Une « pompe à protons » expulse de la cellule des ions H^+ ; ce qui crée une différence de potentiel électrique et de pH permettant aux cations de pénétrer dans le cytoplasme (dont le potentiel électrochimique est alors plus faible que l'extérieur). Puis, l'intervention d'une protéine de transport, le symporteur (un co-transporteur), permet aux anions de rentrer contre le gradient électrochimique, ce qui rapatrie les protons à l'intérieur de la cellule. Au cours de ce processus, les cations ne sont pas toujours transportés sous forme libre. Ils peuvent en effet être rapidement complexés à des agents chélatants dans le cytoplasme (comme l'acide citrique ou malique, l'histidine ou la nicotianamine) qui permettent par exemple aux métaux d'être convertis en formes moins toxiques (Fushiya et al., 1982). Pour ce qui est des cations métalliques, ils sont ensuite transportés dans différents compartiments cellulaires des parties aériennes comme le mésophylle, l'épiderme ou encore les trichomes au niveau des feuilles. Les cations métalliques se trouvent généralement en forte concentration dans les vacuoles car elles sont moins sensibles aux oxydations que les autres organites (Eapen et D'Souza, 2005). Pour ce qui est de l'absorption du fer, deux stratégies d'absorption ont été proposées correspondant à l'appartenance ou non d'une plante à la famille des poacées (Maschner et Röhmeld et al., 1986). Pour les non-poacées (le cas de cette étude), l'absorption du Fe est d'abord gérée au niveau des racines par la production de protons (ou d'acides organiques) et de porteurs d'électrons qui se chargent de séparer Fe(III) du ligand organique auquel il était associé (forme mobile). Ceci permet d'augmenter la solubilité et la réduction du Fe(III) en Fe(II) (Kobayashi et Nishizawa, 2012). A la surface de la racine, le Fe(III) chélaté est réduit puis absorbé sous forme de Fe(II) à travers la membrane plasmique de la racine (Kobayashi et Nishizawa, 2012 ; Briat et al., 2007). Dans le cas des poacées, les sidérophores ou phytosidérophores, produits parles microorganismeset par les plantes, permettent le transport du fer (sous forme Fe(III)) (Krämer et al., 2007). La production de sidérophores, n'est cependant réalisée qu'en cas de carence en fer, la présence de fer en solution exerçant un effet répresseur sur leur production (Gobat et al., 2003). Ce mécanisme de régulation est fondamental car il permet aux plantes d'éviter les intoxications par le fer à concentrations élevées. En outre, de nombreux types de sidérophores existent, chacun plus ou moins spécifiques des plantes et des divers microorganismes qui les produisent. Ceci peut générer une réelle compétition pour le fer dans certains environnements rhizosphériques (certaines bactéries peuvent par exemple empêcher la germination en privant les plantes de fer).

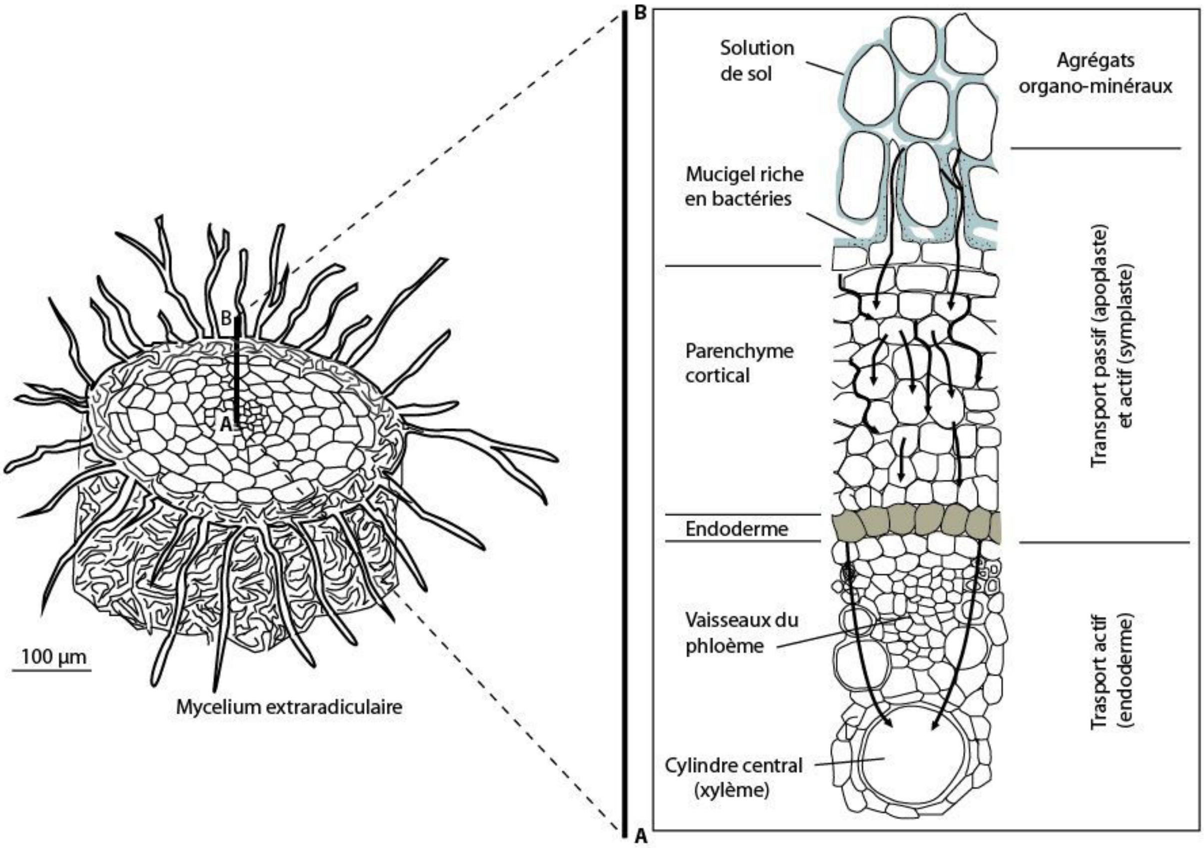

Figure 10 : Transport des bioéléments de la solution de sol vers la plante suivant une coupe transversale d'une radicelle au niveau des poils absorbants.

Enfin, la capacité d'absorption d'un ion par une plante est aussi soumise à la présence et à la concentration des autres éléments à proximité du site d'absorption. Ainsi, les antagonismes entre cations (un ion peut en chasser un autre et diminuer la réserve à moyen terme) modifient leur assimilation (c'est le cas par exemple, entre le calcium et le potassium). Il existe également des interactions ioniques de dépendance (comme entre l'azote et le phosphore) qui favorisent au contraire l'absorption de certains ions. En outre, toutes les plantes n'ont ni, les mêmes capacités d'absorption ni, les mêmes besoins en éléments nutritifs (Marschner, 1995). Des différences s'observent aussi entre individus de même espèce, ayant par exemple un âge différent ou entre radicelles du même individu selon leur situation dans des microsites précis. Le type d'enracinement, son architecture ou sa capacité de régénération sont également cruciaux à cet égard, permettant à la plante de prospecter un plus ou moins large volume de sol (Gobat et al., 2003). Les symbioses entre les plantes et les microorganismes influencent aussi les conditions de la nutrition des végétaux (Jones et al., 2004). Par exemple, si la croissance est limitée par des éléments autres que le carbone, certaines bactéries continuent d'absorber le substrat carboné pour le transformer en métabolites (alcools, acides organiques) qui modifient les conditions du milieu et favorisent la solubilisation de minéraux. Cette solubilisation peut à son tour lever la limitation nutritionnelle du milieu.

I.3.2.2. Absorption, translocation et internalisation des NPs-Fe

Les études actuelles portées sur l'absorption et la translocation de NPs dans les plantes vasculaires ont révélé que les NPs s'accumulaient principalement au niveau des racines, avant de pénétrer dans les parties supérieures de la plante (**Figure11**) (Ma et al., 2010). La localisation dans les tissus foliaires des plantes a mis en évidence l'utilisation du système vasculaire par les NPs (Corredor et al., 2009). Une fois introduites, les NPs circulent dans le phloème et dans le xylème et peuvent s'accumuler dans les différents tissus végétaux (Tripathiet al.,2017 ; Navarro et al., 2008 ; Wang et al., 2012 ; Zhu et al., 2008) ont constaté que des NPs de magnétite de 20 nm de diamètre avaient été absorbées par *Cucurbita maxima* puis transloquées et accumulées dans les différents tissus des plantes. Toutefois, si la plupart des travaux ont observé la pénétration de NPs au niveau racinaire, peu d'entre elles ont révélé leur translocation dans les parties aériennes des plantes. Les principales méthodes utilisées pour mettre en évidence la pénétration et la translocation de NPs-Fe dans la plante se font : a) par observation directe d'un échantillon de plante (MEB ou MET), b) par NanoSIMS (Nunez et al., 2017), ou, pour les NPs-Fe permettant d'enregistrer un signal magnétique fort comme la magnétite, c.) par des méthodes magnétiques (généralement par mesure de l'aimantation rémanente ou de la susceptibilité magnétique du matériel végétal) (Iannoneet al., 2016 ; Zhu et al., 2008). Les mécanismes d'absorption des NPs au niveau des racines soulèvent toutefois encore plusieurs questions, notamment en ce qui concerne la taille et l'état des NPs absorbées pour permettre leur entrée à travers les parois cellulaires. Ces dernières ne permettant le passage que d'objets ayant des dimensions comprises entre 5 et 20 nm (Anjum et al., 2016), l'entrée de NPs agrégées (souvent de plusieurs centaines de nm ou sont même de l'ordre du µm) - telles qu'elles peuvent le devenir sous certaines conditions (pH éloigné de leur pHzpc, force ionique élevée, adsorption des NPs à de plus grandes particules (> 20nm…)) – peut aussi compliquer leur pénétration.

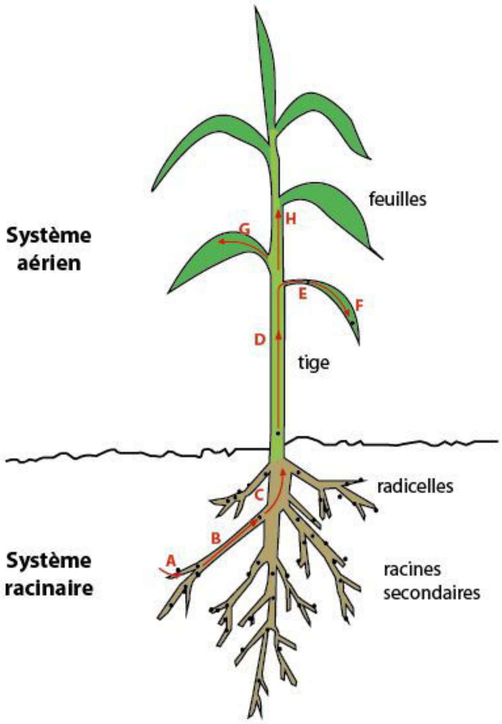

Figure 11 : Translocation des NPs depuis le système racinaire vers le système aérien d'une plante vasculaire.

Plusieurs mécanismes ont été mis en évidence pour expliquer l'internalisation des NPs dans les cellules végétales (**Figure 12**). L'interaction des protéines de transport, aquaporines, canaux ioniques et diverses matières organiques (comme les exsudats racinaires) avec les NPs faciliterait leur absorption cellulaire (Anjum et al., 2016, Navarro et al., 2008). D'un autre côté, il est possible que l'internalisation de NPs, éventuellement agrégées, provoque des dommages au niveau des parois cellulaires, avant d'affecter les constituants internes de la cellule. Le transport et l'absorption de l'eau et des NPs dans les cellules pourraient ainsi être facilités par la création de nouveaux pores cellulaires. (Navarro et al., 2008). Enfin, l'absorption des NPs pourrait être réalisée par endocytose (Ivanov, 2008; Anjum et al., 2016) ; mécanisme au cours duquel les constituants (généralement diverses molécules, ou des virus ou bactéries) sont enveloppés et absorbés par la membrane cellulaire.

Au vu des différents mécanismes impliqués dans l'internalisation cellulaire des NPs, il apparaît fondamental de connaître l'état physique (notamment l'état d'agrégation, la taille -

dissolution partielle -) et la forme chimique (l'état d'oxydation, les modifications de surface - molécules adsorbées - et l'état final) selon lequelles NPs seront absorbées par les plantes pour en comprendre les effets sur la plante.

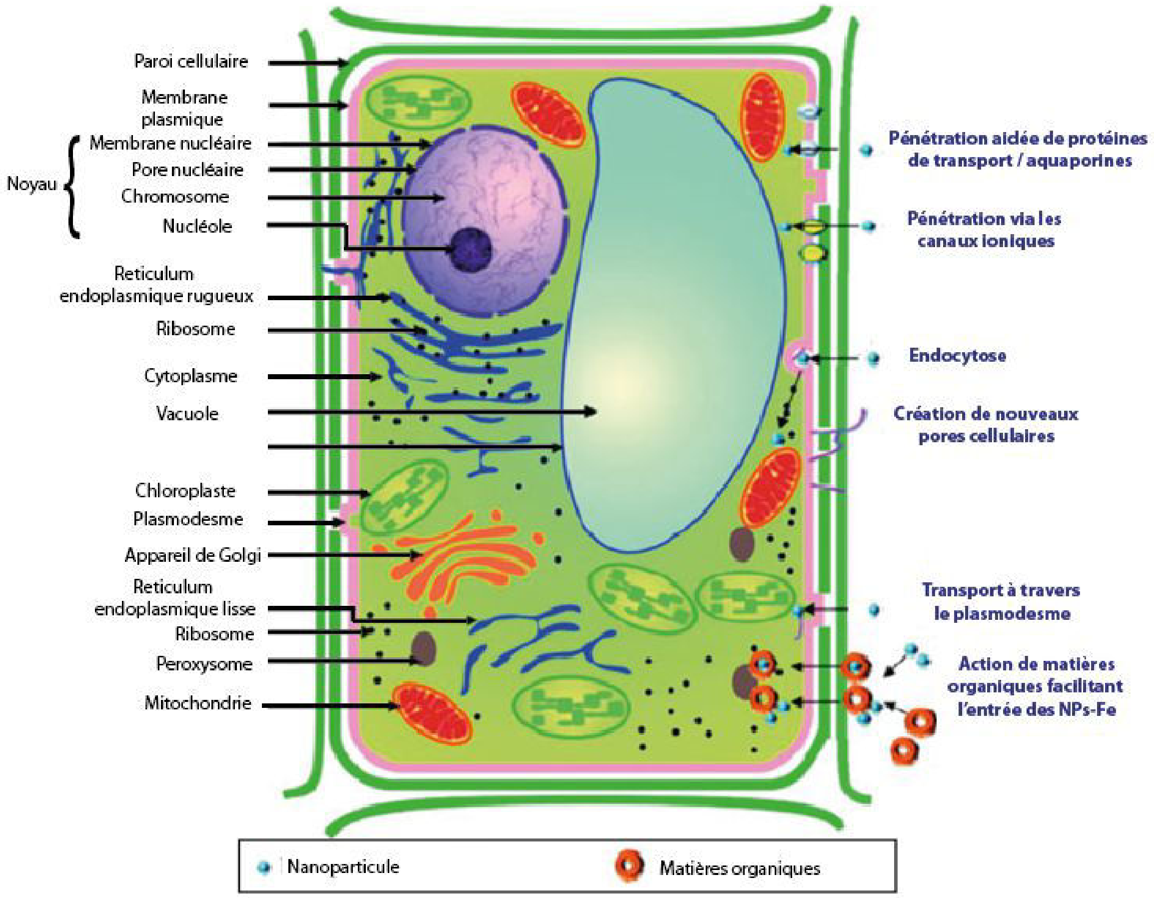

Figure 12: Illustration des différents mécanismes permettant l'entrée des NPs-Fe (et autres NPs) dans une cellule végétale (d'après Rico et al., 2011).

I.3.3. Quels sont les impacts des NPs-Fe sur les plantes ?

Les propriétés intrinsèques des NPs (composition chimique, propriétés de surface), la concentration de NPs dans le milieu, les propriétés du milieu dans lequel sont introduites les NPs, l'espèce végétale exposée, son stade de développement, la durée d'exposition… sont autant de paramètres impliqués dans les interactions NPs/plantes (Amde, 2017). Ceci est à l'origine des résultats souvent contrastés observés dans la littérature en termes de toxicité des NPs (Nair et al., 2010). Des expériences de germination et de culture en hydroponie sur le blé tendre *(Triticum aestivum)* par Iannone et al. (2016) ont mis en évidence l'internalisation de NPs de magnétite (10 nm de diamètre) dans les tissus végétaux et l'absence d'impact toxique aux différentes concentrations d'exposition réalisées (5 à 20 mg L^{-1}). Dans une autre étude conduite sur le maïs (*Zea mays*) (Li et al.,2016), les NPs de maghémite (17,7 nm) introduites aux graines de maïs en concentration de 20 et 50 mg L^{-1} n'ont pas non plus affecté les pousses de maïs alors que l'exposition, à des concentrations égales à 100 mg L^{-1} de NPs de maghémite, a inhibé la germination des graines. D'un autre côté, Pariona et al. (2017) ont récemment montré que l'exposition de graines de maïs (*Zea mays*) à des concentrations de 1 à 6 g L^{-1} de NPs de ferrihydrite et d'hématite avait un impact positif sur le taux de germination des plantes. Le **Tableau 2** résume les résultats des principales études réalisées sur l'exposition de diverses espèces à des NPs-Fe.

Les effets négatifs des NPs-Fe, observés sur diverses espèces concernent principalement l'inhibition de la germination, l'inhibition de la croissance et/ou la baisse de production des chlorophylles (Kim et al., 2014). Ces effets peuvent résulter de plusieurs impacts induits par la présence de NPs dans les tissus végétaux. Les NPs peuvent par exemple, empêcher l'entrée et la sortie des flux nutritifs et sécrétions organiques de la plante (Miralles et al., 2012). En outre, lorsqu'elles parviennent à pénétrer les cellules, les NPs de fer peuvent directement accroître la production de ROS ou la favoriser en interférant avec les chaînes de transport d'électrons mises en place au niveau des mitochondries et des chloroplastes (Sharma, 2015 ; de Souza Pinto et al., 2016). L'augmentation de la production de ROS a des conséquences majeures sur la plante, puisque ces composés sont en interaction avec la plupart des composants cellulaires. La production de ROS peut en effet modifier la structure des protéines, augmenter la peroxidation lipidique et/ ou endommager l'ADN dans le noyau des cellules (Blokhina et al., 2003 ; Salama et El-Betagi, 2009 ; Rastogi et al.,2017). Par ailleurs, l'introduction de NPs-Fe à diverses espèces de plantes a montré des effets bénéfiques en agriculture en réduisant la phytotoxicité de certains métaux (Praveen et al., 2017). Par ailleurs, l'apport en fer induit par les NPs-Fe permettrait de parer à une carence en fer et à ses conséquences sur le métabolisme de la plante (chlorose) (Kokina et al., 2017). Il s'avère qu'elles pourraient aussi être bénéfiques à la croissance des plantes (augmentation de la production de biomasse), à la production de chlorophylles par la plante (Salama et al.,2009) et pourraient favoriser la réponse antioxydante des plantes au stress oxydatif (Iannone et al., 2016). Enfin, les NPs-Fe pourraient aussi montrer un effet bénéfique dans le cadre de sols pollués en métaux lourds, dans le domaine de la phytoremédiation. Dans certaines conditions, les NPs-Fe ont permis de diminuer la toxicité de certains métaux en diminuant leur disponibilité aux plantes (Martinez-Fernandez, 2015).

Les impacts engendrés par l'exposition de NPs-Fe aux plantes, dépend donc de nombreux paramètres qui nécessitent d'être identifiés précisément afin de comprendre les mécanismes et impacts induits par les NPs-Fe. A cet égard, la forme chimique finale sous laquelle les NPs de fer sont absorbées (fer dissout, nanoparticule individualisée ou nanoparticule agrégée) est certainement une étape fondamentale dans la compréhension du problème.

Tableau 2 : Effets observés chezdifférentes espèces végétales exposées à des NPs-Fe dans diverses conditions d'expérimentation.

Nanoparticules	**Concentrations**	**Espèce végétale**	**Culture**	**Durée**	**Effets**	**Référence**
20 nm Fe_3O_4	500 mg L^{-1}	*Cucurbita maxima*	croissance en hydroponie	20 jours	Pas d'effets toxiques visibles	Zhu et al., 2008
9 nm Fe_2O_3 18 nm Fe_2O_3	2 - 20 - 50 mg L^{-1}	*Citrullus lanatus*	*germination puis croissance sur sol sableux*	36h	Augmentation des indices de germination et de croissance L'exposition à 20 mg L-1 a démontré les effets les plus marqués de l'augmentation de l'activité des racines	Li et al., 2013
20 nm Fe_3O_4 (enrobage acide citrique)	5 - 10 - 15 - 20 mg L^{-1}	*Triticum aestivum*	croissance en hydroponie	5 jours	Les NPs n'ont pas affecté le taux de germination, la teneur en chlorophylles et la croissance de la plante et n'ont pas induit de peroxidation lipidique et d'accumulation de ROS Augmentation des activités antioxydantes	Iannone et al., 2016
17.7 nm γ-Fe_2O_3	20 mg L-1	*Zea mays*	germination	36h	L'exposition à 20 mg L^{-1} favorise la croissance des racines et l'index de germination	Li et al., 2016
	50 et 100 mg L^{-1}				L'exposition à 50 mg L^{-1} et 100 mg L^{-1} réduit la taille des racines et des teneurs en chlorophylles et favorise le stress oxydant et la teneur en MDA aux racines.	
3nm-Ferrihydrite 100nm-Hématite	1, 2, 4, et 6 g L^{-1}	*Zea mays*	germination puis croissance	4 jours puis 12 jours	Pas d'impact induit par aucune des deux NPs-Fe sur la germination. Augmentation de la croissance et de la production de chlorophylles (excepté à partir de 6 g L^{-1})	Pariona et al., 2017

I.4. Objectifs et démarche

L’étude du devenir des NPs de magnétite dans l’environnement et leur valorisation par les plantes constitue l’axe central de cette étude abordée via une démarche expérimentale. Afin de répondre aux questions qui s’y rapportent, mon travail s’est ainsi organisé selon deux axes principaux :

I. La caractérisation des NPs et de leur réactivité

Le but de ce volet d’étude est :

- d’identifier les caractéristiques physicochimiques propres aux NPs synthétisées (taille, forme, surface spécifique, cristallochimie),
- de modéliser l’impact d’enrobages naturel (acides humiques, phospholipides) et de l’oxydation de la magnétite (en maghémite) sur la stabilité colloïdale des NPs (état d’agrégation) stabilité chimique (cinétique d’oxydation) et enfin,
- d’évaluer la réactivité des NPs de magnétite en étudiant la capacité d’adsorption d’un élément trace (Cu) en regard des modifications surfaciques apportées en fonction du pH.

II. Impact des NPs de fer sur le développement des plantes

Il s’agit au travers des travaux conduits d’étudier à la fois :

- l’effet positif (nutritionnel) et toxique des NPs sur la croissance et la physiologie des plantes. Cette étude s’est effectuée dans un premier temps via des tests de germination permettant d’étudier les paramètres de croissance de différentes espèces de plantes sans NPs-Fe et avec différentes concentrations de NPs-Fe sur une période courte (1 semaine). Des expériences de culture en milieu hydroponique ont ensuite permis d’évaluer le « potentiel » toxique et / ou nutritionnel des NPs-Fe par des analyses physiologiques et biochimiques des plantes. Les expériences ont été conduites sur différentes espèces végétales d’intérêt agronomique en faisant à nouveau varier les concentrations de NPs administrées.
- Enfin, des expériences de modélisation de systèmes sol-plante en colonne de sol ont permis d’étudier le comportement des NPs-Fe dans un sol, leur impact sur la dynamique géochimique du sol (notamment en présence d’un élément trace (Cu)

présent en excès dans le milieu), mais aussi l'impact de la présence de plantes sur les propriétés physico-chimiques des NPs-Fe et celui des NPs-Fe elles-mêmes sur les plantes après 57 jours d'exposition.

Références :

D.C. Adriano, 2001. Trace elements in terrestrial environments: biogeochemistry, bioavailability and risks of metals. 2nd Springer-Verlag, New York, Berlin, Heidelberg.

G. R. Aïken, H. Hsu-Kim et J.N. Ryan, 2011. Influence of dissolved organic matter on the environmental fate of metals, nanoparticles and colloids. Environmental Sciences and Technology, 45, 3196-3201.

A. Ali, H. Zafar, M. Zia, I. ul Haq, A.R. Phull, J.S. Ali et A. Hussain, 2016. Synthesis, characterization, applications and challenges of iron oxide nanoparticles. Nanotechnology, Science and Applications 9, 49-67.

M. Amde, J.-F. Liu, Z.-Q. Tan et D. Bekana, 2017. Transformation and bioavailability of metal oxide nanoparticles in aquatic and terrestrial environments. A review. Environmental Pollution, 230, 250-267.

N. A. Anjum, M. A. Merios Rodrigo, A. Moulick, Z. Heger, P. Kopel, O. Zitka, V. Adam, A. S. Lukatkin, A. C. Duarte, E. Pereira et R. Kizek, 2016. Transport phenomena of nanoparticles in plants and animals/humans. Environmental Research, 15, 233-243.

ANSES, Evaluation des risqué liés aux nanomatériaux – Avis de l'Anses. Autosaisine n°2012-SA-0273.

H. Antoun et J.W. Kloepper, 2001. Plant growth promoting rhizobacteria. In: Brenner S, Miller JH, editors. Encyclopedia of Genetics. Academic; New York: 2001. pp. 1477-1480.

M. Auffan, 2007. NPs d'oxydes métalliques : relations entre la réactivité de surface et des réponses biologiques. Thèse de doctorat N° : 2007AIX30074. Université Paul Cézanne Aix-Marseille III.

J.F. Banfield, and A. Navrotsky, 2001. Nanoparticles and the environment. Reviews in mineralogy and geochemistry. Mineralogical Society of America, Washington DC.ISBN13 978-0-939950-56-0

J. Barcelo et C. H. Poschenrieder, 1990. Plant water relations as affected by heavy metals stress: a review. Journal of Plant Nutrition, 13, 1-37.

P. Bardos, L. Bakker, H. Slenders et P. Nathanail, 2011. Sustainable remediation. In: Swartjes F.A. (Ed.), Book on Contaminated Sites. From Theory Towards Practical Application, Springer Publishers, Dordrecht. ISBN: 978-90-481-9756-9, 889–948.

R. Barrena, E. Casals, J. Colon, X. Font, A. Sanchez et V. Puntes, 2009. Evaluation of the ecotoxicity of model nanoparticles. Chemosphere, 75, 850-857.

A. Beneduzi, A. Ambrosini et L.M.P. Passaglia, 2012. Plant-growth promoting rhizobacteria (PGPR): their potential as antagonists and biocontrol agents. Geneticsand Molecular Biology 35(4 Suppl): 1044–1051.

J. Berthelin, C. Quantin, S. Stemmler et C. Leyval, 2004. Biodisponibilité Du Fer Dans Les Sols : Rôle Majeur Des Activités Microbiennes.Copyright Académie d'Agriculture de France. Séance du 8 décembre 2004.

O. Blokhina, E. Virolainen et K. Fagerstedt, 2003. Antioxydants, Oxidative Damage and Oxygen Deprivation Stress: a Review. Annals of Botany (91), 179-194.

J.F. Briat, C. Curie et F. Gaymard, 2007. Iron utilization and metabolism in plants. Current Opinion in Plant Biology, 10, 276-282.

P.C. Brookes et S.P. McGarth, 2006. Effect of metal toxicity on the size of the soil microbial biomass. Journal of Soil Science, 35(2), 341-346.

C. Claudio, E. di lorio, Q. Liu, Z. Jiang et V. Barron, 2017. Iron Oxide Nanoparticles in Soils: Environmental and Agronomic Importance. Journal of Nanoscience and Nanotechnology 17, 4449-4460.

C. Colombo, G. Palumbo, J.-Z. He, S. Cesco, 2013. Review on iron availability in soil: interaction of Fe minerals, plants, and microbes. Journal of soil and sediments (14). DOI: 10.1007/s11368-013-0814-z

R.M. Cornell et U. Schwertmann, 2000. Iron Oxides in Laboratory: Preparation and Characterization (second ed.), WILEY-VCH, Weinheim, Germany.

E. Corredor, P.S. Testillano, M.J. Coronado, P. Gonzalez-Melendi, R. Fernandez-Pacheco, C. Marquina, M.R. Ibarra, J.M. de la Fuente, D. Rubiales, A. Perez-de-Luque et C. Risueno, 2009. Nanoparticle penetration and transport in living pumpkin plants: in situ subcellular identification. BMC Plant Biol 9:45.

R.Crichton, R.R. Crichton et J.R. Boelaert, 2001. Inorganic Biochemistry of Iron Metabolism: From Molecular Mechanisms to clinical consequences. Université catholique de Louvain, Belgium. 326pp.

S. D. Cunningham et D. W. Ow, 1996. Promises and Prospects of phytoremediation.Plant Physiology, 110, 715-719.

R.K. Das, S. K. Brar, and M. Verma, 2016. Checking the Biocompatibility of Plant-Derived Metallic Nanoparticles: Molecular Perspectives. Trends in Biotechnology 34(6), 440-449.

C.U. Demirel, M. Bekbol et, et J. Swietlik, 2007. Natural organic matter: Definitions and characterization. Control of Disinfection By-Products in Drinking Water Systems. 253-277.

S. de Souza Pinto, A. E. de Souza, M. A. Oliva et E. Gusmao Pereira, 2016. Oxidative damage and photosynthetic impairment in tropical rice cultivars upon exposure to excess iron. Scientia Agricola 73 (3), 217-226.

R. Dinesh, M. Anandaraj, V. Srinivasan, S. Hamza, 2012. Engineered nanoparticles in the soil and their potential implications to microbial activity. Geoderma 173-174, 19-27.

A.D. Dwivedi, S.P. Dubey, M. Sillanpää, Y.-N. Kwon, C. Lee et R.S. Varma, 2015. Fate of engineered nanoparticles: implications in the environment. Coordination Chemistry Reviews 287, 64-78.

S. Eapen et S. F. D'Souza, 2005. Prospects of genetic engineering of plants for phytoremediation of toxic metals.Biotechnology Advances, 23(2), 97-114.

H.L. Ehrlich, 2002. Geomicrobiology. 4th Edition, Marcel Dekker Publisher, New York.

A. Etale, H. Tutu et D.C. Drake, 2016. Application of maghemite nanoparticles as sorbents for the removal of Cu(II), Mn(II) and U(IV) ions from aqueous solution in acid mine drainage conditions. Applied Water Science, 6, 187-197.

R. Frison, G. Cernuto, A. Cervellino, O. Zaaharko, G. M. Colonna, A. Guagliardi et N. Masciocchi, 2013. Magnetite-Maghemite Nanoparticles in the 5-15 nm range: correlating the core-shell composition and surface structure to the magnetic properties. A total scattering study, Chemistry of Materials, 25, 4820-4828.

S. Fushiya, K. Takahashi, S. Nakatsuyama, V. Sato, S. Nozoe et S. Takagi, 1982. Cooccurrence of nicotianamine and avenic acids in Avena sativa and Oryza sativa. Phytochemistry, 21: 1907–1908.

J.M. Gobat, M. Aragno et W. Matthey, 2003. The living soil: basic pedology - soil biology (2nd edition). Chapman and Hall, London, 569 pp.

S. Ghosh, W. Jiang, J. D. McClements et B. Xing, 2011. Colloidal Stability of Magnetic Iron Oxide nanoparticles: Influence of Natural Organic Matter and Synthetic Polyelectrolytes. Langmuir, 27, 8036-8043.

R. Grillo, A.H. Rosa et L.F. Fraceto, 2015. Engineered nanoparticles and organic matter: a review of the state of the art. Chemosphere, 119, 608-619.

H. Guo et A.S. Barnard, 2013. Naturally occurring iron oxide nanoparticles: morphology, surface chemistry and environmental stability. Journal of Materials Chemistry A, 1, 27-42.

A. K. Gupta, M. Gupta, 2005. Synthesis and surface engineering of iron oxide nanoparticles for biomedical applications. Biomaterials, 26, 3995-4021.

A. Hadju, E. Illés, E. Tombacz et I. Borbath, 2009. Surface charging, polyanionic coating and colloid stability of magnetite nanoparticles. Colloids and Surfaces A: Physicochemical and Engineering Aspects, 347, 104-108.

T. Hiemstra, 2018. Surface structure controlling nanoparticles behavior: magnetism of ferrihydrite, magnetite and maghemite. Environmental Sciences : Nano, 5(3), 752-764 .

T. Hiemstra, W.H. et Van Riemsdijk, 2006. On the relationship between charge distribution, surface hydration and the structure of the interface of metal hydroxides. Journal of Colloid and Interface Science, 301, 1-18.

M.J. Hoosta, M.G. Bidart-Bouzat et J.L. Bouzat, 2008. Local adaptation of microbial communities to heavy metal stress in polluted sediments of Lake Erie**.** FEMS Microbiology Ecology**,** 65(1), 156–168.

S-H. Huang et D-H. Chen, 2009. Rapid removal of heavy metal cations and anions from aqueous solutions by an amino-functionalized magnetic nano-adsorbent. Journal of Hazardous Materials, 163, 174–179

M.F. Iannone, M. D. Groppa, M.E. de Sousa, M. Beatriz Fernandez van Raapet M.P. Benavides, 2016. Impact of Magnetite Iron Oxide nanoparticles on wheat (*Triticum aestivum L.*) development: evaluation of oxidative damage. Environmental and Experimental Botany. 131, 77-88.

A. I. Ivanov, 2008. Exocytosis and endocytosis. Preface.Methods of Molecular Biology,440, v-vi.

M. Jaishankar, T. Tseten, N. Anbalagan, B. B. Mathew etK. N. Beeregow, 2014. Toxicity, mechanisms and health effects of some heavy metals. Interdisciplinary Toxicology 7(2), 60-72.

D.L. Jones, A. Hodge et Y. Kuzyakov, 2004. Plant and mycorrhizal regulation of rhizodeposition. New Phytologist 163, 459-480.

S.H. Joo et D. Zhao, 2017. Environmental dynamics of metal oxide nanoparticles heterogenous systems: a review. Journal of Hazardous Materials 322, 29-47.

M. Kah, S. Beulke, K. Tiede et T. Hofmann, 2013. Nanopesticides: state of knowledge, environmental fate, and exposure modeling. Critical Review. Environmental Science and Technology, 43(16), 1823-1867.

L.R. Khot, S. Sankaran, J.M. Maja, R. Ehsani et E.W. Schuster, 2012. Applications of nanomaterials in agricultural production and crop protection: a review. Crop Prot. 35, 64-70.

A. Kihal, B. Bouzabata, G. Fillion et D. Fruchart, 2009. Magnetic and structural properties of nanocrystalline iron oxide. Physics Procedia 2, 665-671.

J.-H. Kim, Y. Lee, E.-J. Kim, S. Gu, E.-J. Sohn etY.-S. Seo, 2014. Exposure of iron nanoparticles to Arabidopsis thaliana enhances root elongation by triggering cell wall loosening. Environmental Sciences and Technology, 48 (6), 3477-3485.

T. Kobayashi et N.K. Nishizawa, 2012. Iron Uptake, Translocation, and Regulation in Higher Plants. Annual Review of Plant Biology 63, 131-152.

I. Kokina, I. Mickeviča, I. Jahundoviča, A. Ogurcovs, M. Krasovska, M. Jermaļonoka, I. Mihailova, E. Tamanis et V. Gerbreders, 2017. Plant Explants Grown on Medium Supplemented with Fe_3O_4 Nanoparticles Have a Significant Increase in Embryogenesis. Journal of Nanomaterials. Article ID 4587147, 11 pages.

U. Krämer, I.N. Talke et M. Hanikenne, 2007.Transition metal transport. FEBS Special Issue: Plant Ion Channels and Transporters, 1-24.

E. Lefevre, N. Bossa, M.R. Wiesner et C.K. Gunsch, 2016. A review of the environmental implications of in situ remediation by nanoscale zero valent (nZVI): behavior, transport and impacts on microbial communities. Science of the Total Environment 565, 889-901.

A. Leskova, R.F.H. Giehl, A. Hartman, A. Fargasova et N. von Wiren, 2017. Heavy Metals Induce Iron Deficiency Responses at Different Hierarchic and Regulatory Levels. Plant Physiology 174 (3), 1648-1668.

L. L'Huillier, 1994. Biodisponibilité du nickel dans les sols ferrallitiquesferritiques de Nouvelle-Calédonie : effets toxiques de Ni sur le développement et la physiologie du maïs. Thèse de Doctorat, Université de Montpellier II.

J. Li, P.R. Chang, J. Huang, Y. Wang, H. Yuan et H. Ren, 2013. Physiological effects of magnetic iron oxide nanoparticles towards watermelon. Journal of Nanoscience and Nanotechnology, 13, 5516-5567.

J. Li, J. Hu, C. Ma, Y. Wang, C. Wu, J. Huang et B. Xing, 2016. Uptake, translocation and physiological effects of magnetic iron oxide (γ-Fe_2O_3) nanoparticles in corn (*Zea mays* L.). Chemosphere 159, 326-334.

J.-F. Liu, Z.-S. Zhao et G.-B. Jiang, 2008. Coating Fe_3O_4 Magnetic Nanoparticles with Humic Acid for High efficient Removal of Heavy Metals in water. Environmental Science and Technology, 42, 6949-6954.

B. Lugtenberg et F. Kamilova, 2009. Plant-growth-promoting-rhizobacteria. Annual Review of Microbiology, 63, 541-556.

X. Ma, J. Geiser-Lee, Y. Deng et A. Kolmakov, 2010. Interactions between engineered nanoparticles (ENPs) and plants: Phytotoxicity, uptake and accumulation. Science of the Total Environment 408, 3053-3061.

H. Marschner, 1995. Mineral nutrition of higher plants, 2^{nd} edition. Academic, San Diego.

H. Marschner, V. Römheld, and M. Kissel, 1986. Different strategies in higher plants in mobilization and uptake of iron. Journal of Plant Nutrition, 9 (3-7), 695-713.

D. Martinez-Fernandez, M. Vitkova, M.P.Bernal et M. Komarek, 2015. Effects of Nano-maghemite on Trace Element Accumulation and Drought Response of Helianthus annuus L.in a Contaminated Mine Soil. Water Air SoilPollution, 226,101-110.

K. Mengel et E.A. Kirkby, 2001. Principles of plant nutrition, 5th edn. Kluwer Academic Publishers, Dordrecht, 849.

P. Miralles, T. L. Church etA. T. Harris Toxicity, Uptake, and Translocation of Engineered Nanomatrials in Vascular plants, 2012. Environmental Science and Technology, 46, 9224-9239.

S. Mornet, 2002. Synthèse et modification chimique de surface de NPs de maghémite à des fins d'applications biomédicales. Université de Bordeaux I, Bordeaux.

I. A. Mudunkotuwa et V. H. Grassian, 2011. The devil is in the details (or the surface): impact of surface structure and surface energetics on understanding the behavior of nanomaterials in the environment, Journal of Environmental Monitoring, 13, 1135-1144.

J.C. Munch and J.C.G. Ottow, 1983. Environmental Biogeochemistry. Ecological Bulletins, 35, 383-394.

R. Nair, S. H. Varghese, B.G. Nair, T. Maekawa, Y. Yoshida et D.S. Kumar, 2010. Nanoparticulate material delivery to plants. Plant Sciences, 179 (3), 154−163.

E. Navarro, A. Baun, R. Behra, N. B. Hartman, J. Filser, A-J. Miao, A. Qigg, P. H. Santschi et L. Sigg, 2008. Environmental behavior and ecotoxicity of engineered nanoparticles to algae, plants and fungi. Ecotoxicology, 17, 372-386.

J. Nuñez, R. Renslow, J.B. Cliff, and C.R. Anderton, 2017. NanoSIMS for biological applications: Current practices and analyses. Biointerphases 13 (3), 03B301-1 - 03B301-26.

P. Ollivier et J. Labille, 2016. Les NPs manufacturées: innovation et devenir dans l'environnement. Géosciences, 20, 66-73.

A. Otero-Farina, R. Gago, J. Antelo, S. Fiol, F. Arce, 2015. Surface complexation modeling of arsenic and copper immobilization by iron oxide precipitates derived from acid mine drainage. Boletin de la Sociedad Geologica Mexicana, 67, 493-508.

G. Ouzounidou, 1994. Copper induced changes on growth, metal content and photosynthetic function of *Alyssum montanum L.* plants. Environmental and experimental Botany 34 (2), 165-172.

N. Pariona, A.I. Martinez, H.M. Hdz-Garcia, L.A. Cruz etA. Hernandez-Valdes, 2017. Effects of hematite and ferrihydrite nanoparticles on germination and growth of maize seedlings. Saudi Journal of Biological Science, 24, 1547-1554.

R.M. Patil, N.D. Thorat, P.B. Shete, P.A. Bedge, S. Gavde, M.G. Joshi, S.A.M. Tofail et R.A. Bohara, 2018. Comprehensive cytotoxicity studies of superparamagnetic iron oxide nanoparticles. Biochemistry and Biophysics Reports, 13, 63-72.

G. Pédro, 2007. Cycles biogéochimiques et écosystèmes continentaux. Rapport sur la science et la technologie n°27. Institut de France, Académie des Sciences.EDP Sciences.

A. Praveen, E. Khan, S. Ngiimei D., M. Perwez, M. Sadar, M. Gupta, 2017. Iron Oxide Nanoparticles as Nano-adsorbents: A Possible Way to Reduce Arsenic Phytotoxicity in Indian Mustard Plant (Brassica juncea L.). Journal of Plant Growth Regulation. DOI 10.1007/s00344-017-9760-0

M.M. Rahman, S.B. Khan, A. Jamal, M. Faisal et A. M. Aisiri, 2011. Iron Oxide Nanoparticles, Nanomaterials, Prof. Mohammed Rahman (Ed.), ISBN : 978-953-307-913-4.

In Tech, Available from: http://www.intechopen.com/books/nanomaterials/iron-oxide-nanoparticles.

A. Rastogi, M. Zivcak, O. Sytar, H. M. Kalaji, X. He, S. Mbarki and M. Brestic, 2017. Impact of metal and metal oxide nanoparticles on plant: a critical review. Frontiers in Chemistry, 5, 78-94.

R.J. Reeder, M.A.A. Schoonen and A. Lanzirotti, 2006. Metal speciation and its role in bioaccessibility and bioavailability. Reviews in Mineraloggy and geochemistry, 64(1), 59-113.

C.M. Rico, S. Majumdar, M. Duarte-Gardea, J.R. Peralta-VideaetJ.L. Gardea-Torresdey, 2011. Interaction of Nanoparticles with Edible Plants and Their Possible Implications in the Food Chain. Journal of Agricultural and Food Chemistry 59, 3485–3498

V. Römheld et H. Marschner, 1983. Mechanism of iron uptake by peanut plants. I. FeIII reduction, chelate splitting, and release of phenolics. Plant Physiology, 71, 949-954.

R. Saad, 2017. Agromine associant plantes hyperaccumulatrice de nickel et légumineuse, comme service écosystémique des sols ultramafiques. Thèse de Doctorat. Université de Lorraine – Université Libanaise.

Z. Salama et H. El-Beltagi, 2009. Effect of Fe deficiency on antioxidant system in leaves of three flax cultivars. Notulae Botanicae Horti Agrobotanici Cluj-Napoca 37 (1), 122-128.

Scientific Committee on Emerging and Newly Identified Health Risks (SCENIHR). The appropriateness of existing methodologies to assess the potential risks associated with engineered and adventitious products of nanotechnologies. Opinion on adopted by the SCENHIR during the 10th plenary meeting of 10 march 2006 after public consultation, 79 p. *Synthesis report :* http://ec.europa.eu/health/ph_risk/documents/synth_report.pdf

M.A. Shaker et H.M. Albishri, 2014. Dynamics and thermodynamics of toxic metals adsorption onto soil-extracted humic acid. Chemosphere 111, 587-595.

V.K. Sharma, J. Filip, J. Zboril, R.S. Varma, 2015. Natural inorganic nanoparticles - formation, fate and toxicity in the environment. Chemical Society Reviews, 44(23), 8410-8423.

SOGREAH, ADEME, 2007. Bilan des flux de contaminants entrant sur les sols agricoles de France métropolitaine. Rapport final - mai 2007, 329p.

P. Solanki, A. Bhargava, H. Chhipa, N. Jain et J. Panwar, 2015. Nano-fertilizers and their smart delivery system. Nanotechnologies in food and agriculture. Springer International Publishing Cham, 81-101.

D.L. Sparks, 1995. Environmental Soil Chemistry, University of Delaware - Academic Press. ISBN: 0-12-656445-0.

F.J. Stevenson, 1982. Humus Chemistry. Wiley, New-York.

W. Stumm, 1992. Chemistry of the solid-Water interface. Wilez, New-York.

S.C.N. Tang et I.M.C. Lo, 2013.Magnetic nanoparticles: Essential factors for sustainable environmental applications. Water Research, 47, 2613-2632.

P. Tartaj M.P. Morales, T. Gonzales-Carreno, S. Veintemillas-Verdaguer et C.J. Serna, 2011.The Iron Oxides Strike Back: From Biomedical Applications to Energy Storage Devices and Photoelectrochemical Water Splitting. Advanced Materials, 23, 5243-5249.

E. Tipping, 1993. Modeling the Competition between Alkaline Earth cations and Trace Metal Species for Binding by Humic Subtances. Environmental Science and Technology 27, 520-529.

E. Tombacz, I.Y. Toth, D. Nesztor, E. Illes, A. Hadju, M. Szekeres et L. Vékas, 2013. Adsorption of organic acids on magnetite nanoparticles, pH dependent colloidal stability and salt tolerance. Colloids and Surfaces A: Physicochemical and Engineering Aspects 435, 91-96.

D. K. Tripathi, Shweta, S. Singh, S. Singh, R. Pandey, V. P. Singh, N. C. Sharma, S. M. Prasad, N. K. Dubey et D. K. Chauhan, 2017. An overview on manufactured nanoparticles in plants: Uptake, translocation, accumulation and phytotoxicity. Plant Physiology and Biochemistry (110) 2-12.

N.C. Uren, 1984. Forms, reactions and availability of iron in soils, Journal of Plant Nutrition, 7:1-5, 165-176.

M.E. Vance, T. Kuiken, E.P. Vejerano, S.P. McGinnis, M.F. Hochella Jr, D.Rejeski et M.S. Hull, 2015. Nanotechnology in the real world: Redeveloping the nanomaterial consumer products inventory. Beilstein Journal Nanotechnology, 6, 1769-1780.

A.M. Vindedahl, J.H. Strehlau, W.A. Arnold etR. Lee Penn, 2016. Organic matter and iron oxide nanoparticles: aggregation, interactions and reactivity. Environmental Science: Nano, 3, 494-505.

P. B. Vose, 1982. Iron nutrition in plants: A world overview, Journal of Plant Nutrition, 5:4-7, 233-249.

Z. Wang, X. Xie, J. Zhao, X. Liu, W. Feng, J.C. White et B. Xing, 2012. Xylem- and phloem-based transport of CuO nanoparticles in maize (*Zea mays* L.). Environmental Science Technology, 46, 4434-4441.

M. Wang, B. Gao et D. Tang, 2016. Review of key factors controlling engineered nanoparticles transport in porous media. Journal of Hazardous Materials 318, 233-246.

T. Weber, T. Allard, E. Tipping et F. Benedetti, 2006. Modeling iron binding to organic matter. Environmental Science and Technology 40, 7488-7493.

H. Weinberg, A. Galyean et T. Leopold. 2011. Evaluating Engineered Nanoparticles in Natural Waters. Trends in Analytical Chemistry 30 (1), 72-83.

M.A. Wilson, N.H. Tran, A.S. Milev, G.S.K. Kannangara, H.Volk et G.Q. M. Lu, 2008. Nanomaterials in soils. Geoderma 146, 291-302.

W. Wu, Q. He et C. Jiang, 2008. Magnetic Iron Oxide Nanoparticles: Synthesis and Surface Functionalization Strategies. Nanoscale Research Letters, 3, 397-415.

W. Xing, W. Huang et G. Liu, 2010. Effect of excess iron and copper on physiology of aquatic plant Spirodela polyrrhiza (L.) Schleid. Environmental Toxicology, 25(2), 103-115

W. Yang, A.T. Kan, W. Chen, M.B. Tomson, 2010. pH-dependent effect of zinc on arsenic adsorption to magnetite nanoparticles. Water Research, 44, 5693-5701.

S.Yu, J. Liu, Y. Yin, et M. Shen, 2018. Interactions between engineered nanoparticles and dissolved organic matter: a review on the mechanisms and environmental effects. Journal of Environmental Sciences 63, 198-217.

Y. Zhang, Y. Chen, P. Westerhoff, K. Hristovski et J.C. Crittenden, 2008. Stability of commercial metal oxide nanoparticles in water. Water Research 42, 2204-2212.

Y. Zhang, Y. Chen, P. Westerhoff et J. Crittenden, 2009. Impact of natural organic matter and divalent cations on the stability of aqueous nanoparticles. Water Research 43, 4249-4257.

H. Zhu, J. Han, J.Q. Xiao, Y. Jin, 2008. Uptake, translocation, and accumulation of manufactured iron oxide nanoparticles by pumpkin plants. Journal of Environmental Monitoring, 10, 713 -*717.*

Chapitre 2 :

Rôle du pH et des propriétés de surface des NPs-Fe dans le contrôle de leur stabilité colloïdale et chimique

Ce chapitre correspond à un article publié dans la revue : *Environmental Science : Nano* : « Colloidal and chemical stabilities of iron oxide nanoparticles in aqueous solutions: the interplay of structural, chemical and environmental drivers », E. Demangeat, M. Pédrot, A. Dia, M. Bouhnik-le-Coz, F. Grasset, K. Hanna, M. Kamagate and F. Cabello-Hurtado (DOI: 10.1039/c7en01159h).

Colloidal and chemical stabilities of iron oxide nanoparticles in aqueous solution: the interplay of structural, chemical and environmental drivers.

E. Demangeat,[a] M. Pédrot,[a] A. Dia,[a] M. Bouhnik-Le-Coz,[a] F. Grasset,[b] K. Hanna,[c] M. Kamagate[c] and F. Cabello-Hurtado[d]

Abstract

Nanoparticle (NP) stability in aqueous environments is dependent upon many parameters including environmental conditions, NP concentrations as well as NP intrinsic characteristics. In this study, the effects of pH and surface modifications on the colloidal and chemical stabilities of nanosized magnetite (Fe_3O_4), maghemite (γ-Fe_2O_3) and hematite (α-Fe_2O_3) are investigated. Because changes in surface charge affect the size distribution of NP, pH plays a key role in driving the colloidal stability. More NP aggregation is observed at pH values close to the pH of zero point of charge (pHzpc). Coating of magnetite with humic acid (HA) and phosphatidylcholine (PC) affects the electrostatic interactions and then the colloidal behavior of NP. The rapid transformation of magnetite into maghemite through air oxidation results in significant modification of both surface charge and specific surface area of NP. Because the maghemite almost exclusively formed µm-scale aggregates, the colloidal stability of magnetite is expected to be hindered in oxic environments. For hematite, the particle size distribution data emphasize the influence of both pH and intrinsic surface properties in the colloidal stability. These findings may have strong implications for an accurate prediction of the transformation and mobility of Fe-nanoparticles under environmentally relevant conditions and thus their fate in nature.

II.1. Introduction

Understanding the prevailing processes controlling chemical exchanges at soil/water interfaces is an environmental priority with regards to their impacts on both ecosystems and soil services, as well as water resources. Iron (Fe) oxides are ubiquitous minerals constituent of soils, sediments, aquifers and geological materials[1, 2]. Their origin is also anthropogenic as they are increasingly used in various fields such as for industrial, medical and environmental purposes[3-6]. Iron oxides nanoparticles (NP) respective stability, specific surface area, porosity, dissolution rate as well as transformation kinetics are controlled by their mineral structure and determine their fate and behaviour in the environment[7]. Amongst them, iron oxide nanoparticles, which also occur as ubiquitous phases in both soils and waters, play a critical role in the chemical dynamics resulting from environmental condition changes since nano minerals are highly reactive[8, 9]. In the natural conditions only a small fraction of engineered iron oxide NP in its original form[10]. Biotransformation, oxidation/reduction, dissolution, precipitation, sorption and photochemical transformation may occur amongst other biogeochemical driven processes[11, 12]. In turn, this transformation can affect the aggregation, mobility, biointeractions, uptake and fate of iron oxide NP in the environment as well as their impacts on the living environment[13].

Engineered iron oxide NP will become new tools for the treatment of contaminated waters and soils[14, 15]. As compared to conventional macroscale materials, nanomaterials exhibit a high surface-to-volume ratio and high reactivity. Thus, their colloidal size may give them high mobility in porous media and their properties allow them to be particularly suitable for the treatment of contaminated soils or aquifers. Iron oxide NP are involved in (i) the dechlorination of organic solvents (CCl_4, C_2Cl_4), (ii) the detoxification of pesticides (such as Lindane, DDT), (iii) the transformation of fertilizers (NO_3^-), and (iv) the immobilization of metals and metalloids (As, Pb, Cr, etc.)[16-18]. If remediation projects using iron oxide NP are currently focused on local-scale pollution, a scale change is initiated to act against diffuse pollution. Moreover, their use in nano-agrochemistry could be developed in the years ahead and would represent an intentional diffuse source of iron oxide NP within the environment[19]. A widespread use of iron oxide NP for *in situ* remediation or in agriculture also raises the question of their environmental compatibility.

Amongst engineered iron oxide NP of environmental concern, magnetite (Fe_3O_4), maghemite (γ-Fe_2O_3) and hematite (α-Fe_2O_3) are popular engineered iron oxide NP because of their biocompatibility and safety towards living organisms under certain conditions[20-22]. In particular, magnetite has shown an outstanding applicability in many research areas (e.g., semiconductor, magnetic resonance imaging, pigment, biomedicine, drug delivery, heterogeneous catalysis, and environmental remediation)[23, 24, 25] due to its unique magnetic properties and easy manipulation for control of morphologies, particle size, and Fe^{II}/Fe^{III} stoichiometry[26, 27]. However, determination of magnetite compositions which is highly sensitive to the preparation conditions is not a trivial task, particularly for nanoscale particles with a higher surface-to-volume ratio. Magnetite compositions range, without modification of crystal structure, from that of stoichiometric Fe_3O_4, with 8 Fe^{3+} ions in tetrahedral and 8 Fe^{2+} + 8 Fe^{3+} ions in octahedral sites, to that of maghemite γ-$Fe^{III}{}_2O_3$ (considered as an extreme example of a non-stoichiometric magnetite) with only Fe^{3+} ions in both tetrahedral and octahedral sites. As compared to these iron oxides, hematite has only one type of cation, Fe^{3+} in its structure[28, 29].

In aqueous solution, iron oxides (IO) are amphoteric solids that acquire a surface charge in the protonation and deprotonation reactions of Fe-OH surface sites. The ensuing electrostatic, steric or combined stabilization layers that develop at the surface of the particles are significant in driving iron oxide NP colloidal stability[30]. The interfacial equilibrium at the surface of iron oxide NP is thus affected by the adsorption and desorption of the various constituents of the soil and soil solution in addition to the solution pH[31, 32]. The surface charge of iron oxide NP is also dependent upon their own structural organization such as isomorphic substitutions, which give iron oxide NP permanent charges.

As part of the Natural Organic Matter (NOM) occurring within soils and waters, macromolecular polyfunctional humic acid (HA), which displays a particular affinity for metal ions and their various acidic functional groups (carboxylic, phenolic, carbonyl), favours the formation of surface complexes on the Fe-OH sites of iron oxides via chemisorption[33]. As a consequence, interactions between iron oxide NP and HA should be further investigated. Several studies have shown that, in aqueous solution, the HA coating on iron oxide NP likely imparts a negative charge to the nanoparticle surfaces, increasing their surface potential and the ensuing propensity to stabilize iron oxide NP against aggregation[34-36]. Nevertheless, Hadju et al.[37] demonstrated that coating magnetite with HA could either foster or hinder Fe_3O_4-NP colloidal stability depending on the amount of HA present at the mineral surfaces. Other natural constituents such as amphiphilic phospholipids (integral major component of cell membranes) likely affect iron oxide NP stability. Using phospholipids as a coating on pyrite surfaces, Hao et al.[38] demonstrated that surface-bound lipids inhibit the iron core from oxidizing, even in the presence of bacteria, by forming a hydrophobic pocket[38, 39]. In addition, several authors have shown that a phospholipid coating likely decreases nanoparticle size dispersion and favours narrow-sized nanoparticles[40, 41]. Furthermore, the instability of magnetite in air causes NP to undergo a partial oxidation to maghemite (γ-Fe_2O_3), ending up with a core-shell structure in which the thickness of the oxidized layer is a function of the particle size[42, 43]. This phase transformation directly affects the surficial properties and internal characteristics of NP, which are deeply involved in driving iron oxide chemical stability and reactivity[44, 45].

In the environment, soils and soil solutions are prior interfaces for iron oxide NP interactions[46] occurring at mineral surfaces and in water. In addition to particle interactions, NP are prone to various chemical and physical modifications which foster the complexity of the reactions and likely affect both NP stability and reactivity. Electrostatic, steric or combined electrosteric forces can result from these interactions and promote repulsive forces whereas Van der Waals and magnetic dipolar interactions foster attraction between particles that likely aggregate. The intrinsic physicochemical properties of iron oxide NP (size, shape, surface area, chemistry, superparamagnetism, etc.), their ensuing high reactivity, together with the surrounding solution composition (dissolved species, pH, ionic strength, nanoparticle concentration), are the main drivers of iron oxide NP chemical and colloidal stability in aqueous media[47, 48].

Considering the geochemical, biological and technological significance of iron oxide NP[49], understanding the mechanisms of their stability may turn out to be relevant to unravel the fate and behaviour of iron oxide NP in the environment as well as their impacts on living organisms. Therefore, the aim of this work is to investigate the dual colloidal and chemical stability of magnetite NP in order to (i) understand the effects of their intrinsic properties (size, morphology, surface chemistry) and those of the environmental drivers (especially the effect of pH) on their aggregation state, (ii) assess the oxidation kinetics of magnetite, (iii) investigate the link between colloidal and chemical stability of NP, as well as (iv) identify the resulting environmental impacts. Hematite has also been studied to better understand the impact of intrinsic structural properties on iron oxide NP colloidal stability as the structure of hematite differs from both magnetite and maghemite. Indeed hematite NP size and morphology as well as internal crystal structure, generally confer a higher stability and crystallinity to the oxide. Last, the method we chose to study the iron oxide NP aggregation state allowed us to study their size distribution over a wide range of sizes (that spread from one tenth of a nm to µm-scale aggregates) which allowed us to determine NP behavior in a context comparable to those observed in natural waters.

II.2. Experimental

II.2.1. Iron oxide nanoparticles and coated magnetite NP

II.2.1.1. Synthesis of bare iron oxide NP

Magnetite (Fe_3O_4) was prepared by the co-precipitation of iron salts according to the modified literature procedure [50, 51]. In brief, $FeCl_2.4H_2O$ (1.988 g) and $FeCl_3.6H_2O$ (5.406 g) were dissolved in 5 mL HCl (2 M) and 20 mL H_2O, respectively, and then mixed with magnetic stirring to obtain an iron solution with a molar ratio of Fe(II)/Fe(III) = 0.5. Magnetite NP were then precipitated by the dropwise addition of the iron salt solution into a 0.7 M NaOH-$NaNO_3$ base solution (250 mL). The black precipitate was left to settle in anaerobic conditions for a few hours to get rid of the supernatant. Three washings were then conducted in anaerobic conditions with deoxygenated deionized water and 5 10^{-3} M NaCl solution.

Maghemite (γ-Fe_2O_3) was synthesized following the method of Anna et al.[52], through the oxidation of the previously synthesized magnetite by adding 5 wt% NaOCl aqueous solution (16 mL) and sonicating for 2 hours. The solid product was magnetically separated and washed with water.

Hematite (α-Fe_2O_3) was synthesized by the forced hydrolysis of acid Fe(III) salt solutions at 98°C from 0.02 M $Fe(NO_3)_3$ following the protocol described in Schwertmann & Cornell (2003)[1].

II.2.1.2. Coatings with humic acid and phosphatidylcholines

Fe_3O_4-NP were coated with HA (Elliott Soil Humic Acid Standard IV) and PC (1, 2-bis (10, 12-tricosadiynoyl)-sn-glycero-3-phosphocholine - CAS Registry Number: 76078-28-9) to model a natural surface modification. The coating was carried out by physical interactions between the dissolved organic species (HA and PC) and a concentrated fraction of the Fe_3O_4-solution. Humic acid (0.2 g) was dissolved in 10 mL NaOH (1 M) and the obtained HA-solution was completed to 56 mL with deionized water. A similar PC-solution was obtained by dissolution in deionized water and ultrasonication. Fourty-four mL of a 6.0 g L^{-1} Fe_3O_4-NP solution was then added to each organic stock solution and each 100 mL of solution was shaken for 48 hours. At the end of the interaction, five washings were performed to remove the uncoated materials present in the supernatant after centrifugation.

II.2.1.3. Nanoparticle mass concentration measurement

The concentration of the iron oxide NP solution was inferred from the ICP-MS measurements of iron on triplicate samples for the iron oxide NP solutions and then recalculated regarding the total theoretical iron content of the minerals. Each NP sample was digested with sub-boiled nitric acid (14.6 M HNO_3) at 85°C, and then re-solubilized in 0.37 M HNO_3 after complete evaporation before measurement. Major- and trace-element concentrations were determined by ICP-MS (Agilent 7700x), using rhenium and rhodium as the internal standard. The international geostandard SLRS-5 was used to check the validity and reproducibility of the results[53].

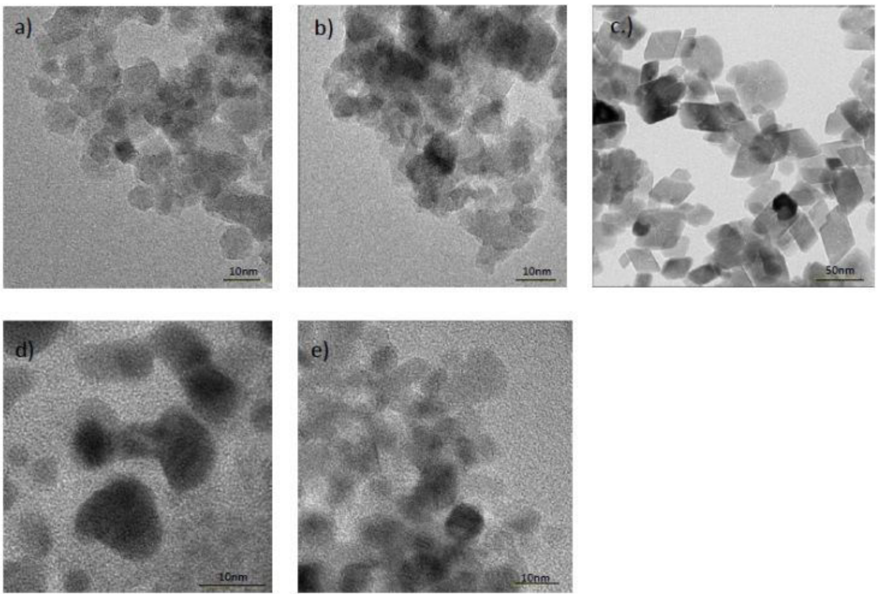

Figure. 1: High Resolution TEM (HRTEM) images of a) Fe_3O_4, b) ɣ-Fe_2O_3, c) α-Fe2O3, d) HA-Fe_3O_4 and e) PC-Fe_3O_4

II.2.2. Characterization

II.2.2.1. Size, morphology and surface properties

The morphology and individual particle size of Fe_3O_4, HA-Fe_3O_4, PC-Fe_3O_4, ɣ-Fe_2O_3 and α-Fe_2O_3 were determined using High Resolution Transmission Electron Microscopy (HR-TEM) with a JEOL2100F (voltage 200 kV). Specimens were prepared by drop-casting diluted Fe-NP suspensions on 300 mesh Au-grids supported with carbon film. The specific surface area of the iron oxides was determined by multipoint N_2–BET (Brunauer Emmett Teller) analysis using a Coulter (SA 3100) surface area analyzer. The pH of zero point of charge was determined by potentiometric titrations, which were conducted with 1 and 2 g L^{-1} of solid at three ionic strengths (10^{-2}, 5.10^{-2}, and 10^{-1} M of NaCl). The suspension was purged with nitrogen gas to remove CO_2 in a double-walled Pyrex cell, which was kept at constant temperature by circulating water from thermostat. Titrations were conducted from 4 to 10 by addition of titrant solutions (HCl or NaOH). Synthesized NP were characterized using X-ray powder diffraction (XRD). XRD data were collected with a Johanson monochromator using CuK_{α} radiation ($\lambda = 1.5406$ A). The X-ray diffractograms were found to be identical with the expected oxides. Laser particle size analyses allowed the characterization of the size distribution of magnetite, maghemite, hematite and HA- and PC- coated magnetite to study the colloidal stability and, conversely, their aggregation behaviour. Assuming measurements on spherical particles, the technique provided sizes amongst the 100 size classes detected, which spread from 0.04 µm to 2500 µm. Analyses were performed by the laser diffraction technique on a Cilas1180 analyzer. Measurements were taken on each bare iron oxide (Fe_3O_4, γ-Fe_2O_3 and α-Fe_2O_3) and coated magnetite (HA-Fe_3O_4 and PC-Fe_3O_4) at five different pH values (pH = 3, 4, 5, 6, 7.5). Then, the pH was equilibrated with HCl and NaOH solutions (0.1 M and 0.1 M to 1.0 M, respectively) until the target pH was reached.

Table 1: Physicochemical properties of a) Fe_3O_4, b) γ-Fe_2O_3 and c) α-Fe_2O_3 obtained from TEM, BET analyses and potentiometric titration.

NP	TEM (nm)	BET ($m^2 g^{-1}$)	pHzpc
Magnetite	7 ± 2	115	5.8
Maghemite	6 ± 2	131	7 - 8.4
Hematite	28 ± 5 39 ± 5	49	8.2

II.2.2.2. ATR-FTIR

Attenuated total reflectance-Fourier transform infrared (ATR-FTIR) spectra were recorded in the 780 - 1800 cm^{-1} region on an IS50 Nicolet spectrometer equipped with a KBr beam splitter and a liquid Nitrogen cooled MCT (Mercury Cadmium Telluride) detector. A nine-reflection diamond ATR accessory (Durasampl*IR* ™, SensIR Technologies) was used for acquiring spectra of wet samples. The resolution of the single beam spectra was 4 cm^{-1}. Prior to ATR-FTIR analyzes, tubes containing coated NP were centrifuged at 4110 RCF for 30 min. Wet mineral pastes were directly and uniformly applied to the diamond ATR crystal then covered with a lid of a flow-through cell to prevent the evaporation of water. ATR-FTIR spectra were then recorded immediately.

To monitor potential dissolution of NP, aliquots were collected at each pH value, centrifuged and the supernatants were filtered using 5 KDa ultrafiltration cells (from

Sartorius) in order to stop NP on the filter. ICP-MS was then performed to measure total iron concentration.

II.2.2.3. Oxidation kinetics

A NP suspension (2.5 g L^{-1}), prepared in anoxic conditions, was placed outside the glove box under air ambient environment to monitor the oxidation. The total Fe(II)/Fe(III) ratio in suspension was then analyzed versus time over nine days. For each sampling, two aliquots were placed in an anaerobic chamber: the first aliquot contained bulk solution and the second was filtered (0.2 µm, Whatman). NP suspension was dissolved during 12h using 0.6N HCl while filtered NP were directly dissolved. Dissolved Fe(II) and Fe(III) concentrations were then determined using the phenanthroline method[54, 55] and the bulk Fe(II) content turned out to be very close to that determined by acid digestion on the filtered solid. The amount of magnetite bound-Fe(II) ([Fe(II)] bound = [Fe(II)]tot – [Fe(II)]aq) was used to calculate the effective Fe(II)/Fe(III) ratio (denoted as (Fe(II)/Fe(III)) bound) in magnetite which was shown to vary with pH, as reported in Cheng et al.[56]. [Fe(II)]tot is the total concentration of Fe(II) in the suspension (solid + solution) and [Fe(II)]aq is the dissolved concentration of Fe(II), measured after filtration (0.2 µm, Whatman) of the magnetite suspension.

II. 3. Results and discussion

II.3.1. Iron oxide NP physicochemical properties

HR-TEM analyses provided images to assess the individual sizes and shapes of the nanoparticles (Fig. 1). Magnetite and maghemite oxides both displayed rounded shapes and similar sizes with average diameters of 7 ± 2 nm and 6 ± 2 nm (Table 1), suggesting that the oxidation of magnetite to maghemite did not impact the particle size. Accordingly, BET surface area for maghemite (131 m^2g^{-1}) is relatively close to that of magnetite (115 m^2g^{-1}) (Table 1). Hematite displayed different morphologies with rhombohedral shapes measuring 28 nm-wide and 39 nm-long on average, with a surface area of 49 m^2g^{-1} (Table 1). No significant changes were reported for neither HA- nor PC-coated magnetite from TEM images, suggesting that the coating process did not modify the morphology of magnetite. Although the surface area was not determined for coated materials, no significant modification is expected, according to previous findings[57].

II.3.2. ATR-FTIR spectroscopy

The IR spectrum recorded for of Fe_3O_4, HA-Fe_3O_4 and PC-Fe_3O_4 showed successful coating of HA and PC on magnetite surfaces (Fig. 2). In the spectra of HA-Fe_3O_4, the presence of an acid carboxylic group was proven by the vibrational bands at 1410 cm^{-1} and 1614 cm^{-1} [58-60]. In the spectra of PC-Fe_3O_4, the absorption bands at 1239 cm^{-1}, 1088 cm^{-1} and 970 cm^{-1} were assigned to the presence of the PO_4^{3-} group, suggesting that PC was coated on the magnetite surface[61, 62].

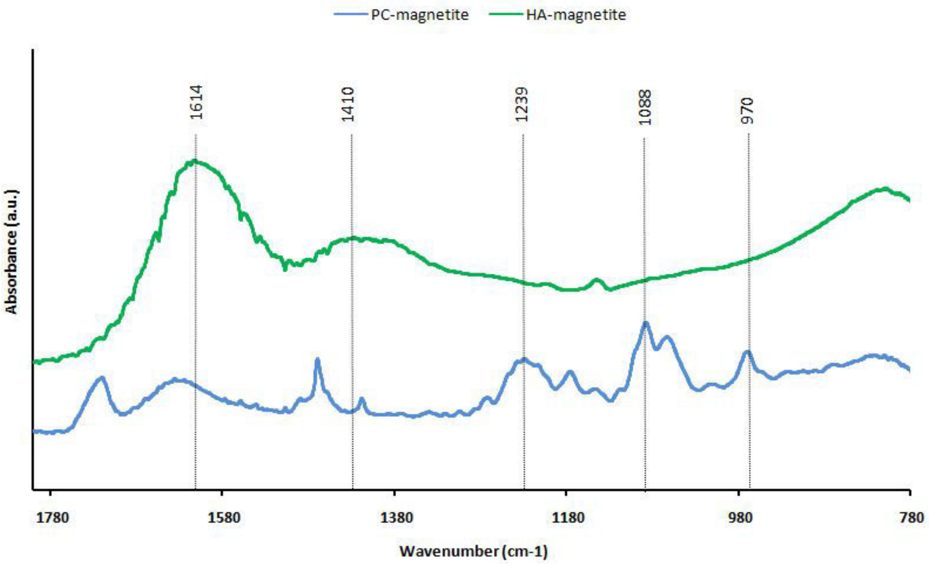

Figure 2: ATR-FTIR spectra of HA-magnetite and PC-magnetite in the range 780-1800 cm^{-1} obtained from 0.5 g L^{-1} NP suspensions at pH= 6.

II.3.3. Oxidation kinetics

The variation of total Fe(II)/Fe(III) ratio versus time for magnetite suspension exposed to air is characterized by a two-steps' behavior. Over the four first days (0-96 h), a sharp decrease in total Fe(II)/Fe(III) ratio was observed (from 0.46 to 0.09). During this first stage, the bound Fe(II)/Fe(III) ratio was also decreased for magnetite as represented by red symbols in Figure 3. Then, the total Fe(II)/Fe(III) ratio slightly decreased beyond 5 days to reach 0.09 at the end of the experiment (236 h). As expected from the magnetite solubility at pH = 7.5[1], very little difference was observed between the total and bound Fe(II)/Fe(III) ratios.

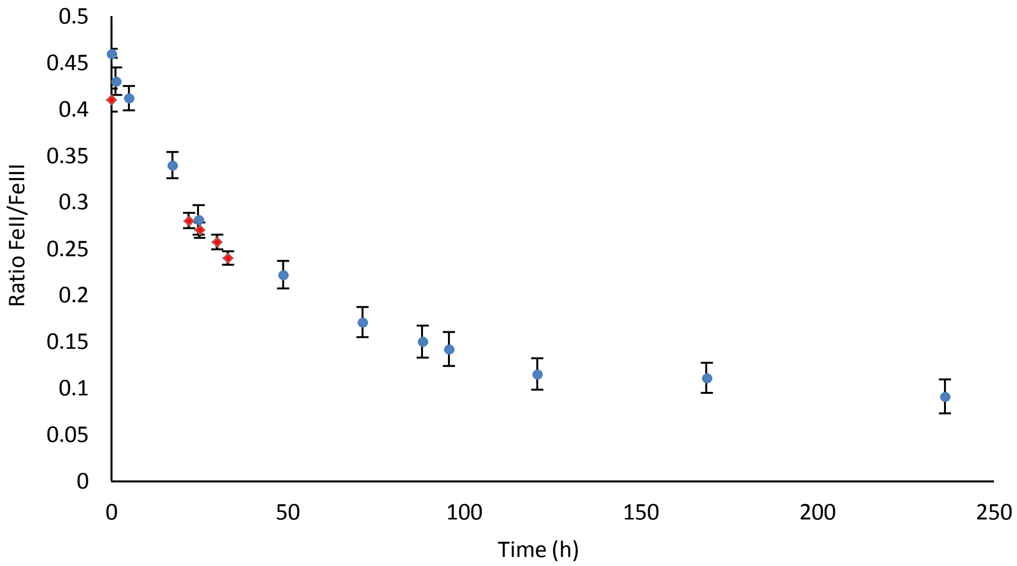

Figure 3: Evolution of the total Fe(II)/Fe(III) ratio (blue circles) and bound Fe(II)/Fe(III) ratio (red diamond) as a function of time. The reaction was performed with 2.5 g L^{-1} magnetite NP at pH = 7.5 in oxic conditions.

II.3.4. Aggregation state

To assess the effect of pH and the effects of coating, laser diffraction analyses were performed on each iron oxide (Fe_3O_4, HA-Fe_3O_4, PC- Fe_3O_4, ɣ-Fe_2O_3 and α-Fe_2O_3) at five different pH values. For all experiments, the aggregation state was associated with the size distribution of the NP, which was described by considering the evolution of the sizes (based on number analyses) with the pH, occurrence rate and the polydispersity of the sizes (PDI, size range, mode and mean) of each iron oxide NP.

	Magnetite		**HA-Magnetite**		**PC-Magnetite**			**Maghemite**			**Hematite**	
pH	6	5	4	3	7.5	5	4	7.5	6	5	7.5	5
Range (µm)	0.04 - 0.4; 1.6 - 32	0.04 - 0.4; 1.6 - 32	0.04 - 18	0.04 - 0.4; 1.1 - 19	0.04 - 0.4; 1.2 - 45	0.04 - 0.4; 1.1 - 40	0.04 - 0.4; 1.6 - 56	0.04 - 0.4; 1.6 - 28	0.04 - 0.4; 1.6 - 28	0.5 - 0.7; 1.1 - 28	0.04 - 6	0.04 - 0.4; 1.1 - 12
Mode (µm)	0.04	0.04	0.04	0.04	0.04	0.04	0.04	0.04	0.04	8	1.4	0.04
Mean (µm)	1.3	0.9	0.4	0.6	1.1	0.8	1.3	4.1	1.1	6.8	1.3	0.5
Median (µm)	0.07	0.04	0.04	0.07	0.07	0.04	0.07	0.2	0.04	7	1.2	0.04
PDI	1.38	2.74	13	5	1.9	3.4	1.3	0.56	2.06	0.72	4.8	7.6

Table 2: Size distribution characteristics of each NP at some typical pH (aggregation state versus colloidal stability). The table shows the size-range, mode, mean size, median value and the PDI (polydispersity index) of magnetite, HA-coated magnetite, PC-coated magnetite, maghemite and hematite. High PDI have values up to 1.0 and very high PDI are up to 2.0.

II.3.4.1. Effects of pH

The impact of pH on particle size distribution provides valuable information that could be used to distinguish the colloidal stability from the aggregation state of the various NP (Table 2). The different pH-dependent configurations highlighted the role of pHzpc in controlling NP aggregation through electrostatic interactions (Fig. 4). The effect of pH was studied by considering the evolution of the size distributions into four size classes (Fig. 4). The fractions were defined with regards to the most common sizes (representability) and depending on the way they vary with pH. However, it should be noted that fractions are not fully comparable to one another, as they were not spread out equally (i.e. fraction >0.4 µm (µm-scaled size class) as compared to 40-100 nm fraction (nm-scaled sizes)). The full-size distribution diagrams obtained from laser particle analyses as well as the precise occurrence rates (detectors) are provided in the Electronic Supporting Information (ESI).

It is worth noting that the total dissolved iron content was only detected in magnetite suspension at pH = 3 and pH = 4 (90 and 23 µmol L^{-1} respectively). These values correspond to 1.4 % and 0.4 %, respectively, of the total iron amount in NP suspension. For HA- and PC-magnetite samples, no dissolved iron was detected regardless of the investigated pH.

Magnetite. The NP size distribution displayed two size distribution configurations: at pH = 5, 4 and 3, magnetite NP showed colloidal stability as compared to their size distribution at pH = 6 and 7.5. Magnetite size distribution at acidic pH was characterized by a high proportion of small NP (≤0.04 µm), and the occurrence of few dispersed µm-scaled aggregates (with sizes ranging between 1.6 µm and 32 µm). Such distribution allowed a large amount of NP not to sediment, as defined by Buffle et al.[63]. When the pH increased to 6 and 7.5, the number of coarser 100-400 nm and 40-100 nm-sized aggregates all increased as the proportion of small aggregates decreased. This is consistent with the measured pHzpc = 5.8 (in accordance with previously published values[4]), since aggregation is commonly favoured at pH close to the pHzpc. Therefore, particles exhibiting negative charges likely formed coarser aggregates when the pH approached the pHzpc because of favorable electrostatic interactions[64].

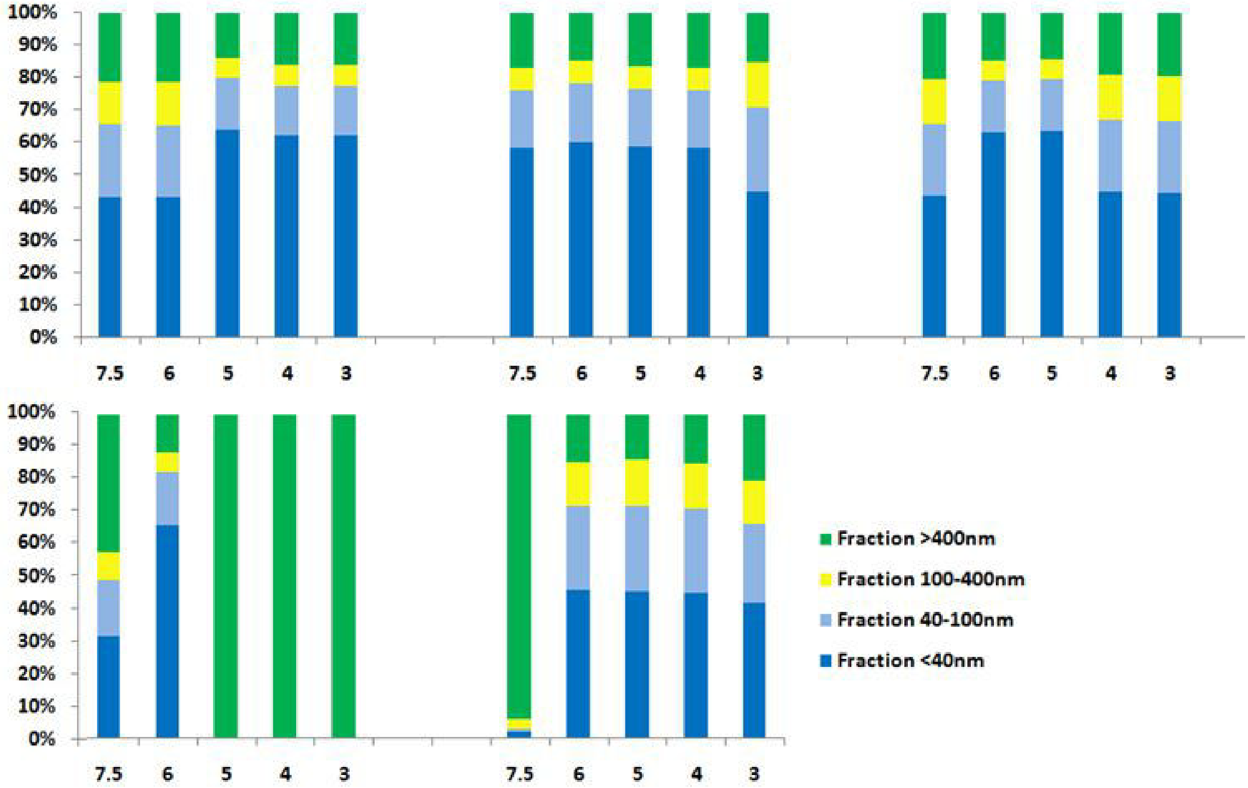

Figure 4: Evolution of the size-class proportion with pH for a) magnetite, b) HA-magnetite, c) PC-magnetite, d) maghemite and e) hematite.

HA-Magnetite. HA-magnetite nanoparticles displayed both a continuous size distribution (pH = 4 to pH = 7.5) and a dual size distribution (pH = 3). In both cases, fraction below 0.04 µm was more important but their proportion decreased as the pH decreased from pH = 4 to 3. This decrease was accompanied by a slight increase in 40–100 nm-sized fraction and an increase in the proportion of coarser intermediate 100-400 nm NP size-class, which appeared to be more dependent upon pH than other fractions. The occurrence rate of the coarse aggregate fraction (> 0.4 µm and > 1.1 µm) remained constant regardless of the pH, hence a lower pH implied a moderated aggregation with small (≤ 0.04 µm) particles aggregating in only slightly coarser (0.05-0.4 µm) aggregates. Thus in HA-coated iron oxide NP, HA appeared to be an effective organic stabilizer towards iron oxide NP as previously demonstrated[65, 66].

PC-Magnetite. PC-magnetite nanoparticles highlighted two size distributions depending on the pH. At pH = 6 and 5, the size distribution was similar to that of bare magnetite at acidic pH (pH = 3 and pH = 4) where the colloidal stability displayed its maximum. At pH = 7.5, 4 and 3, Fe_3O_4-PC showed a similar size distribution to bare magnetite at pH > 6, when it aggregated. When the pH decreased to pH = 4 and pH = 3, small aggregates (≤ 0.04 µm) were still the most common but in a lower proportion which was compensated by a higher amount of the three other coarser size fraction~~s~~ (in order: 40-100 nm; >1.6 µm and 100-400 nm). Although 100-400 nm-sized aggregates were still the least common, this fraction was the most sensitive to pH as its proportion more than doubled from pH 6 and 5 to pH 4 and 3.

Maghemite. The size distribution displayed three configurations as distinct fractions whose proportions were strongly controlled by the pH. At a weak basic pH (pH = 7.5), the distribution was highly polydispersed and made up of coarse aggregates (> 0.4 µm), which spread over a large size range. Maghemite NP displayed colloidal stability at pH = 6 with a size distribution similar to that of magnetite. However, when the pH decreased to a more acidic pH (pH = 5, 4 and 3), small-sized NP and NP aggregates disappeared to form much coarser aggregates with almost exclusively µm-scale sizes (>1 µm). Thus, the maghemite size distribution would be in good agreement with a high pHzpc close to 7.5[67, 68], as it became coarser than at pH = 6, but the high aggregation observed from pH = 3 to 5 suggested the possible implication of parameters other than electrostatic interactions to drive maghemite colloidal stability.

Hematite. The hematite size distribution showed two pH-dependent size distribution patterns. At pH = 7.5, the sizes were continuously distributed with a unique narrow size range composed of coarse homogeneous sizes displaying high polydispersity (multimodal distribution centered on 1.4 µm). When the pH decreased to pH = 6 and lower, the pH drastically modified the hematite size distribution to a more stable aggregation state[69] characterized by a monomodal distribution (0.04 µm) and higher abundance of finer particles (< 0.4 µm). In accordance with the hematite pHzpc at pH = 8.2, hematite NP tended to aggregate when the pH reached pH = 7.5.

II. 3.4.2. Effects of coating

The physico-chemical characteristics obtained from the combination of HR-TEM and ATR-FTIR showed that HA have been successfully coated onto magnetite NP. According to HR-TEM images, HA coating on magnetite did not affect the original morphology and size of the precursor NP. As the surface modification with HA provided primarily acidic functional groups, the HA-coated magnetite pHzpc likely decreased to a lower pH (pHzpc = 2.3). Accordingly, magnetite-HA promoted colloidal stability from pH = 7.5 to pH = 4 because of repulsive electrostatic interactions. The aggregation observed at pH = 3 - close to the new pHzpc - would then be explained by the lack of negative surface sites to compensate for the protonation induced by the H^+ concentration increase in the aqueous solution. Both HA and bare magnetite evidenced that the proportion of their size- fractions was strongly controlled by the pH, which induced either colloidal stability or aggregation. Nevertheless, HA coating promoted smaller-sized aggregates as well as a narrower size distribution and more homogeneous stable sizes (especially for coarser particles (>0.4 µm)) compared to bare magnetite (Table 2). This enhanced stabilization may stem from a HA steric barrier that helped maintain a space between the particles to prevent the aggregation of NP[70, 71].

Similar to the HA coating, the PC surface modification did not affect the size and morphology of magnetite. Magnetite coated with PC displayed a different colloidal behaviour as compared to bare magnetite. As PC imparted both negative and positive surface groups on the surfaces of the NP (glycerophosphate group, trimethylethanolammonium group), and because of the complex and heterogeneous surface structures that are generated by adsorbed PC[72], PC-coated nanoparticles likely displayed variable colloidal behaviours. As compared to magnetite, PC-NP showed similar size proportions and repartition although the magnetite-PC coarse fraction displayed a few large aggregates (hence its wider size range, see Table 2) regardless of the pH. PC-NP were thus probably able to form highly contrasted structures (according to their size) suggesting that PC-coated magnetite did not entirely depend on electrostatic interactions but also on steric forces[72].

II. 3.4.3. Effects of iron oxide intrinsic physicochemical properties

The oxidation of magnetite (Fe_3O_4) to maghemite (γ-Fe_2O_3) did not change morphology and particle size. Maghemite still displayed a higher surface area (131 $m^2\ g^{-1}$) than magnetite (115 $m^2\ g^{-1}$) and oxidized NP very likely yielded intrinsic compositional differences. These modifications probably resulted in a higher surface potential thereby explaining the variable size distributions observed as the pH changed. Maghemite NP aggregation was favoured at acidic pH (equal or below 5), which would be in good agreement with their high surface potential. Indeed, the tendency to form large aggregates at these pH values likely resulted from a high energetic barrier that had to be overcome at the mineral surfaces[73]. Indeed, increasing NP surface to volume ratio leads to a higher surface energy which induces aggregation between particles. As hematite displayed a much lower surface area, the higher colloidal stability observed over a wide pH range may result from a lower energetic barrier at the surface of the particles in accordance with NP having a relatively lower surface potential. Hematite stability would thus be related, in part, to its smaller surface area and surface potential. However, the typical aggregation behaviour of hematite NP displaying coarse aggregates with homogeneous sizes suggests that other mechanisms are involved at basic pH. Further investigations are thus needed to fully assess iron oxide NP colloidal stability[74-76].

II.3.4.4. Environmental perspectives

Aggregation and stabilization have significant effects on the mobility, reactivity and environmental fate of NP. Once released in surface waters, unstable particles tend to agglomerate, sediment or flocculate or they preferentially adsorb onto bigger particles or surfaces[77]. As a result, aggregated NP that form larger colloids with a possible smaller surface area are less easy to transport and do not get through the soil as easily as smaller particles[78]**.** As aggregated NP become less mobile, they may become more ineffective in acting as nutrient carriers[79]. It is also more difficult for these colloids to be taken up by plants and living organisms as they are less soluble than their smaller counterparts[80]. The dissolution of NP induces the mobilization of ions which are likely complexed with molecules that foster their absorption by plants and animals. In addition, depending on their concentration and speciation as well as on the physiology of the organism that absorbs it, metal atoms or ions can be either positive nutrients or toxic elements. On the other hand, aggregation may directly affect NP toxicity towards living organisms since smaller NP have been shown to penetrate the cell walls of certain species more easily[81, 82].

Considering the pH effect, the physicochemical properties of the soil solution have to be considered in order to accurately assess the fate of NP in the environment. NP intrinsic properties, such as their surface chemistry, are also of prime importance since they are involved in both electrostatic and steric interactions, which may impact their dispersion, bioavailability and biocompatibility[83].In natural waters and surficial aerobic environments, NP likely undergo many surficial modifications and become embedded in matrixes or functionalized with specific molecules[84]. As a result, these attached molecules can both passivate and/or confer their own properties to mineral surfaces; e.g. polyanionic HA coating on magnetite, resulting in a lower pHzpc and enhanced colloidal stability. In addition, HA coating - as well as PC covering - might passivate iron oxide NP surfaces to yield a steric barrier that prevents Fe leakage from mineral surfaces and the ageing of the magnetic core by oxidation. HA, which are ubiquitous in most aquatic systems, display a specific affinity for iron oxide NP as well as trace elements and therefore HA-iron oxide NP complexed structures may also enhance ETM adsorption to NP. However, although natural coatings demonstrated improved iron oxide NP stability and reactivity, their effects depend upon the amount and chemical composition of the substances[4].

The rapid oxidation of magnetite into maghemite is important since iron plays an active redox catalytic role in many energy transfer and electron transfer processes[85-87]. The iron oxide redox state also plays a key role in specific anaerobic environments where Fe(II) and Fe(III) are used as energetic catalysts for bacteria[88, 89]. Finally, the transformation of magnetite into maghemite is also relevant considering its adsorption capacity towards environmental compounds[90]. Several questions are raised from these environmental considerations, especially, what are the impacts of these modifications regarding iron oxide NP reactivity?

II. 4. Conclusions

The pH appears to be a key driver in controlling iron oxide NP colloidal behaviour as resulting from protonation and deprotonation reactions of surface hydroxyl-groups. Surface modifications also implied considerable effects on iron oxide NP colloidal stability as they promoted electrostatic interactions. In contrast to PC, HA was shown to be particularly efficient in enhancing magnetite colloidal stability. Magnetite seems to be highly unstable in aerobic conditions. The oxidation of magnetite into maghemite modified its surface chemistry and surface area, and these modifications resulted in higher aggregation at most pH values. Compared to maghemite, hematite appeared to be less sensitive to pH and displayed a lower surface area and surface potential. Both hematite and maghemite displayed high aggregation size distributions at different pH values.

Considering the widespread use of iron oxide NP and their subsequent release in the environment, their fate and behaviour in soils and natural waters raise many environmental questions not only in terms of their possible impacts on living organisms but also for their mobility and fate in ecosystems. Therefore, more attention should be paid for the understanding of colloidal and chemical stabilities of iron oxide NP as it is likely involved in many major interactions within the environment.

Acknowledgements

We are thankful to François Pustoc'h for the time as well as the thorough advices he gave us to conduct laser particle analyses at the CReAAH (University of Rennes1). Dr Patricia Benard-Rocherullé and Dr Vincent Dorcet (ISCR, University of Rennes1) are deeply acknowledged for DRX and MET studies, respectively. Dr Fabienne Gauffre is thanked for her kind help to perform NTA measurements. Last, Dr S. Mullin is acknowledged for post-editing the English style (http://www.proz.com/profile/677614). This study was funded by both the CNRS-INSU/INEE EC2CO and the Interdisciplinarity Mission programs through 'NanoOrgaTraces' and 'ALIEN' projects, respectively both awarded to Mathieu Pédrot and the University Rennes 1 through 'Défis Scientifiques Emergents' program awarded to Aline Dia.

References:

1 R. M. Cornell and U. Schwertmann, 2nd edition, *http://trove.nla.gov.au/version/36973177*, 2003, Edited by Wiley-VCH, 664p.

2 M. F. Hochella Jr, S. K. Lower, P. A. Maurice, R. L. Penn, N. Sahai, D. L. Sparks and B. S. Twining, *Science*, 2008, **139,** 1631.

3 A. Afkhami, M. Saber-Tehrani and H. Bagheri, *Desalination*, 2010, **263**, 240.

4 M. A. Ahmed, S. M. Ali, S. I. El-Dek and A. Galal, *Materials Science and Engineering B,* 2013,**178**, 744.

5 A. K. Gupta and M. Gupta, *Biomaterials,* 2005,**26**, 3995.

6 S. Laurent, J.-L.Bridot, L. Van der Elst and R. N. Muller, *Future Medicinal Chemistry,* 2010, **2(3)**, 427.

7 H. Guo and A. Barnard, *Journal of Materials Chemistry A*, 2013, **1**, 27.

8 M. Schindler and M. F. Hochella Jr., *Geology*, 2016, **44**, 515.

9 S. C. Löhr, D. T. Murphy, L. D. Nothdurft, R. Bohlar, S. Piazolo and C. Siegel, *Geochimica and Cosmochimica Acta*, 2017, **200**, 25.

10 C. W. Isaacson, M. Kleber and J. A. Field, *Environmental Science & Technology*, 2009, **43**,6463.

11 B. Nowack and T.D. Bucheli, *Environmental Pollution*, 2007, **150**, 5.

12 M. Auffan, J. Rose, J.-Y.Bottero, G. V. Lowry, J.-P.Jolivet and M.-R.Wiesner, *Nature Nanotechnology*, 2009, **4**, 634.

13 G. V. Lowry, K. B. Gregory, S. C. Apte and J. R. Lead, *Environmental Science & Technology*, 2012, **46**, 6893.

14 S. C. N. Tang, I. and M. C. Lo, *Water Research*, 2013, **47**, 2613.

15 M. Vitkova, S. Rakosova, Z. Michalkova, M. Komarek, *Journal of Environmental Management*, 2017, **186**, 268.

16 P. N. Dave and L. V. Chopda, *Journal of Nanotechnology*, 2014, **2014**, 1.

17 A. Aftabtalab, H. Sadabadi, CH. Shilpa Chakra, K. V. Rao, S. Shaker and E. Privilege Mahofa, *International Journal of Scientific & Engineering Research*, 2014, **5(1)**,1419.

18 S. R. Chowdhury and E. K. Yanful, *Journal of Environmental Management*, 2013, **129**, 642.

19 L. R. Khot, S. Sankaran, J. M. Maja, R. Ehsani and E. W. Schuster, *Crop Protection*, 2012, **35**, 64.

20 E. Navarro, A. Baun, R. Behra, N. B. Hartmann, J. Filser, A-J.Miao, A. Quigg, P. H. Santschi and L. Sigg, *Ecotoxicology*, 2008,**17**, 372.

21 A. Valdiglesias, N. Fernandez-Bertolez, G. Kiliç, C. Costa, S. Costa, S. Fraga, M. J. Bessa, E. Pasaro, J. P. Texeira and B. Laffon, *Journal of Trace Elements in Medicine and Biology*, 2016, **38**, 53.

22 R. Podila and J. M. Brown, *Journal of Biochemical and Molecular Toxicology*, 2013, **27(1)**, 50.

23 W. Wu, Z. Wu, T. Yu, C. Jiang and Woo-Sik Kim, *Sci. Technol. Adv. Mater.*, 2015, **16**, 023501.

24 O. Veiseh, J. W. Gunn, M. Zhang, Advanced Drug Delivery Review, 2010, **62**, 304.

25 Y. Ju-Nam and J. R. Lead, *Science of the Total Environment*, 2008, **400**, 414.

26 A-H. Lu, E.L. Salabas and F. Schüt, Angew. Chem. Int. Ed., 2007, **46**, 1244.

27 D. Maity and D.C. Agrawal, *Journal of Magnetism and Magnetic Materials*, 2007, **308**, 46.

28 M. M. Can, M. Coskun and T. Firat, *Journal of Alloys and Compounds*, 2012, **542**, 241.

29 A. Lassoued, M. S. Lassoued, B. Dkhil, A. Gadri and S. Ammar, *Journal of Molecular Structure*, 2017, **1141**, 99

30 S. C. Pang, S. F. Chin and M. A. Anderson, *Journal of Colloid and Interface Science*, 2007, **311**, 94.

31 L. Peng, P. Qin, M. Lei, Q. Zeng, H. Song, J. Yang, J. Shao, B. L. and J. Gu, *Journal of Hazardous Materials*, 2012,**209-210**,193.

32 E. Tombacz, Z. Libor, E. Illès, A. Majzik and E. Klumpp, *Organic Geochemistry*, 2004, **35,** 257.

33 A. M. Vindedahl, J. H. Strehlau, W. A. Arnold and R. L. Penn, *Environmental Science: Nano, Critical Review*, 2016, **3**, 1.

34 M. Baalousha, *The Science of the Total Environment*, 2009, **407**, 2093.

35 E. Illes and E. Tombacz, *Journal of Colloid and Interface Science,* 2006, **295**,115.

36 E. Tombacz, I.Y. Toth, D. Nesztor, E. Illés, A. Hadju, M. Szekeres and L. Vékas, *Colloids and Surfaces A: Physicochemical and Engineering Aspects*, 2013,**435**, 91.

37 A. Hajdú, E. Illés, E. Tombácz and I. Borbáth, *Colloids and surfaces A: Physicochemical and Engineering Aspects*, 2009, **347**, 104.

38 J. Hao, C. Cleveland, E. Lim, D. R. Strongin and M. A. A. Schoonen, *Geochemical Transactions*, 2006, **7:8**, 1.

39 X. V. Zhang, T. A. Kendall, J. Hao, D. R. Strongin, M. A. A. Schoonen and S. T. Martin, *Environmental Science & Technology*, 2006, **40**, 1511.

40 J. Giri, S. G. Thakurta, J. Bellare, A. K. Nigam and D. Bahadur, *Journal of Magnetism and Magnetic Materials*, 2005, **293**, 62.

41 S. Chatterjee, M. Krikorian, H. D. Gafney and B. Gersten, *Material Research Society*, 2011, **1061**, MM09-08.

42 R. Frison, G. Cernuto, A. Cervellino, O. Zaaharko, G. M. Colonna, A. Guagliardi and N. Masciocchi, *Chemistry of Materials*, 2013, **25**, 4820.

43 U. S. Khan, Amanullah, A. Manan, N. Khan, A. Mahmood and A. Rahim, *Material Science-Poland*, 2015, **33(2)**, 278.

44 I. Nedkov, T. Merodiiska, L. Slavov, R.E. Vandenberghe, Y. Kusano and J. Takada, *Journal of Magnetic Materials*, 2006, **300**, 358.

45 H. Shokrollahi, *Journal of Magnetism and Magnetic Materials*, 2017, **426**, 74.

46 L. Charlet G. Morin, J. Rose, Y. Wang, M. Auffan, A. Burnol and A. Fernandez-Martinez, *ComptesRendus Geoscience*, 2011, **343**, 123.

47 L. Chekli, S. Phuntsho, M. Roy, E. Lombi. E. Donner and H. K. Shon, *Water Research*, 2013, **47**, 4585.

48 W. Li, J. Wu, C. Kim and J. D. Fortner, *Environmental Science & Technology*, 2014, **48(20)**, 11892.

49 A. Navrotsky, L. Mazeina and J. Majzlan, *Science*, 2008, **319**, 1635.

50 R. Massart, *IEEE Transactions on Magnetics*, 1981, **17**,1247.

51 S. E. Khalafalla and G. W. Reimers, *IEEE Transactions on Magnetics*, 1980, **16(2)**, 178.

52 Z. B. Anna, B. Patricyja, J. Petr, E. Petrovsky, B. Pavel, H. Daniel, *Colloids and Surfaces B: Biointerfaces,* 2016, **141**, 389.

53 D. Yeghicheyan, C. Bossy, M. Bouhnik Le Coz, C. Douchet, G. Granier, A. Heimburger, F. Lacan, A. Lanzanova, T. C. C. Rousseau, J.L. Seidel, M. Tharaud, F.

Candaudap, J. Chmeleff, C. Cloquet, S. Delpoux, M. Labatut, R. Losno, C. Pradoux Y. Sivry and J. E. Sonke, *Geostandards and Geoanalytical Research*, 2013, **37(4)**, 449.

54 C. A. Gorski and M. M. Sherer, *American Mineralogist*, 2010, **95**, 1017.

55 P. Komadel and J. W. Stucki, *Clays and Clay Minerals*, 1988, **36(4)**, 379.

56 W. Cheng, R. Marsac and K. Hanna, *Environ. Sci. Technol.*, 2018, **52 (2)**, 473.

57 J. Lohdia, G. Mandarano, N. J. Ferris, P. Eu and S. F. Cowell, *Biomedical Imaging and Intervention Journal*, 2010,**6(2)**, 1.

58 H. Niu, D. Zhang, S. Zhang, X. Zhang, Z. Meng and Y. Cai, *Journal of Hazardous Materials*, 2011, **190**, 559.

59 J.-F. Liu, Z.-S. Zhao and G.-B.Jiang, *Environmental Science & Technology*, 2008, **42**, 6949.

60 S. Koesnarpadi, S. J. Santosa, D. Siswanta and B. Rusdiarso, *Procedia Environmental Sciences* 30 (2015, 103.

61 S. Debnath, D. B. Hausner, D. R. Strongin and J. Kubicki, *Journal of Colloids and Interface Sciences*, 2010, **341**, 215.

62 Q.-C. Le, M.-H. Ropers, H. Terrisse and B. Humbert, *Colloids and Surfaces B: Biointerfaces*, 2014, **123**, 150.

63 J. Buffle, K. Wilkinson, S. Stoll, F. Montserrat, Z. Jingwu, *Environmental Science & Technology*, 1998, **32(19)**, 2899.

64 A. Kraynov and T. E. Müller, In *Applications of Ionic Liquids in Science and Technology*, 2011, Edited by Prof. S. Handy (516 pages), 235.

65 M. Pédrot, A.L. Boudec, M. Davranche, A. Dia, O. Henin, *Journal of Colloid and Interface Science*, 2011, **359**, 75.

66 D. Palomino and S. Stoll, *Journal of Nanoparticle Research*, 2013, **15(2)**, 1428.

67 N. Fauconnier, J. N. Pons, J. Roger and A. Bee, *Journal of Colloid and Interface Science*, 1997,**194**, 427.

68 L. Vayssieres, *J. Phys. Chem. C,* 2009, **113**, 4736.

69 K. Shimizu, S. V. Sokolov and R. G. Compton, *Colloid and Interface Science Communications*, 2016, **13**, 19.

70 S. Ghosh, W. Jiang, J. D. McClements and B. Xing, *Langmuir*, 2011*,* **27**, 8036.

71 S. F. Meideros, J. O.C. Filizzola, V. F.M. Fonseca, P. F.M. Oliveira, T. M. Silva, A. Elaissari and A. M. Santos, *Materials Letters*, 2015, **160**, 522.

72 R. Michel and M. Gradzielski, *International Journal of Molecular Science*s, 2012, **13**, 11610.

73 K. A. D. Guzman, M. P. Finnegan and J. F. Banfield, *Environmental Science & Technology*, 2006, **40**, 7688.

74 M. D. Carvalho, F. Henriques, L. P. Ferreira, M. Godinho and M. M. Cruz, *Journal of Solid State Chemistry*, 2013,**201**, 144.

75 E. Alp and N. Aydogan, *Colloids and Surfaces A: Physicochemical and Engineering Aspects*, 2016, **510**, 205.

76 D. Dickson, G. Liu, C. Li, G. Tachiev and Y. Kai, *The Science of the Total Environment*, 2012, **429**, 170.

77 A. M. Badawy, A. A. Hassan, K. G. Scheckel, M. T. Suidan and T. M. Tolymat, *Environmental Science and Technology*, 2013, **47**, 4039.

78 M. Komarek, A. Vanek and V. Ettler, *Environmental Pollution*, 2013, **172**, 9.

79 C. Claudio, E. di Iorio, Q. Liu, Z. Jiang, V. Barron, *Journal of Nanoscience and Nanotechnology*, 2017, **17(7)**, 4449.

80 I. A. Mudunkotuwa and V. H. Grassian, *Journal of Environmental Monitoring*, 2011, **13(5)**, 1135.

81 J. Bauman, J. Köser, D. Arndt and J. Filser, *The Science of the Total Environment*, 2014, **484**, 176.

82 K. Powers, M. Palazuelos, B. M. Moudgil and S. M. Roberts, *Nanotoxicology*, *2007,***1 (1)**, 42.

83 R. K. Das, S. K. Brar and M. Verma, *Trends in Biotechnology*, 2016, **34(6)**, 440.

84 D. Lin, S. D. Story, S. L. Walker, Q. Huang, W. Liang and P. Cai, *Environmental Pollution*, 2017, **228**, 35.

85 K. S. Siddiqi, A. ur Rahman, Tajuddin and A. Husen, *Nanoscale Research Letters*, 2016, **11**, 498.

86 H. Wu, J. J. Yin, W. G. Wamer, M. Zeng and Y. M. Lo, *Journal of Food and Drugs Analysis*, 2014, **22**, 86.

87 S. K. Chaudhuri, J. G. Lack, J. D. Coates, *Applied and Environmental Microbiology*, 2001, **67**, 2844.

88 M. Posfai, T. Kasama, E. T. Simpson, R. K. K. Chong and R. E. Dunin-Borkowski, *ActaCrystallica*, 2006**, 62**, 39.

89 J.-Y. Bottero, M. Auffan, J. Rose, C. Mouneyrac, C. Botta, J. Labille, A. Masion, A. Thill and C. Chaneac, *ComptesRendus Geoscience*, 2011, **343**, 168.

90 M. Davranche, A. Dia, M. Fakih, B. Nowack, G. Gruau, G. Ona-Nguema, P. Petitjean, S. Martin and R. Hochreutener, *Chemical Geology*, 2013,**335**, 24.

Supporting Information

Figure S1 - Size distribution diagrams from laser particle analyses

- **Magnetite**

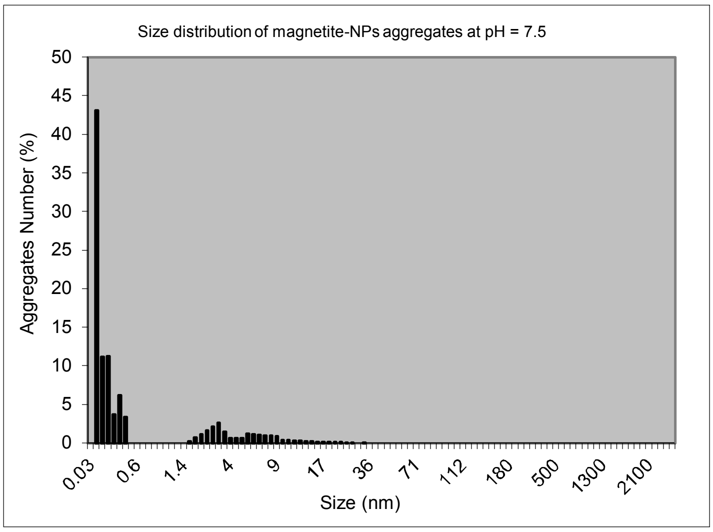

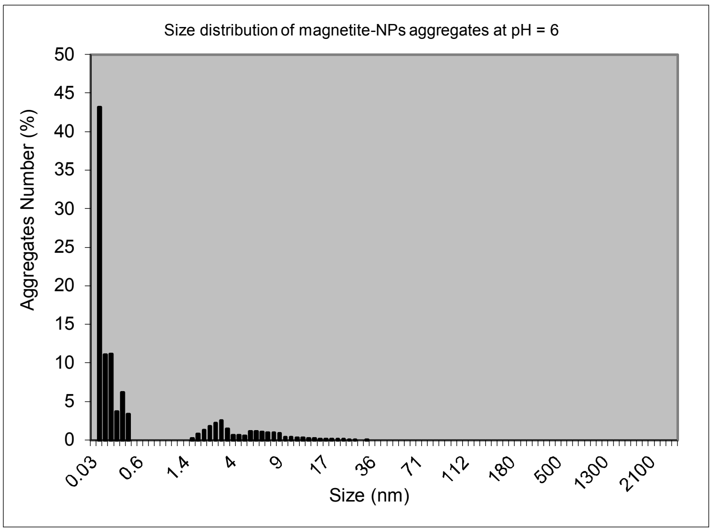

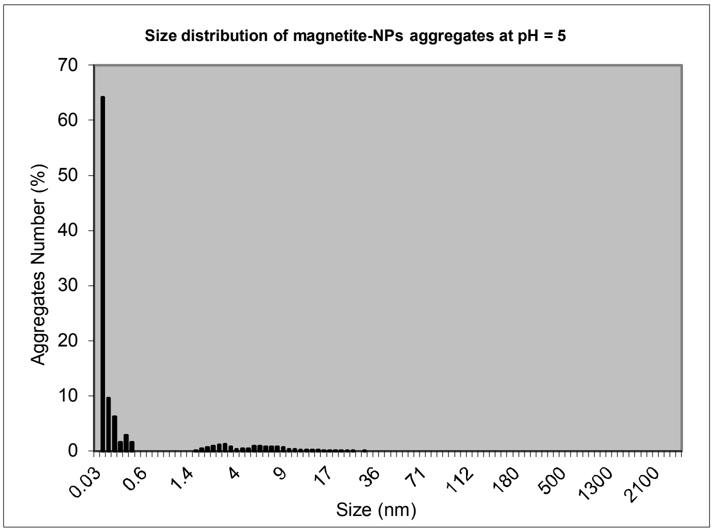

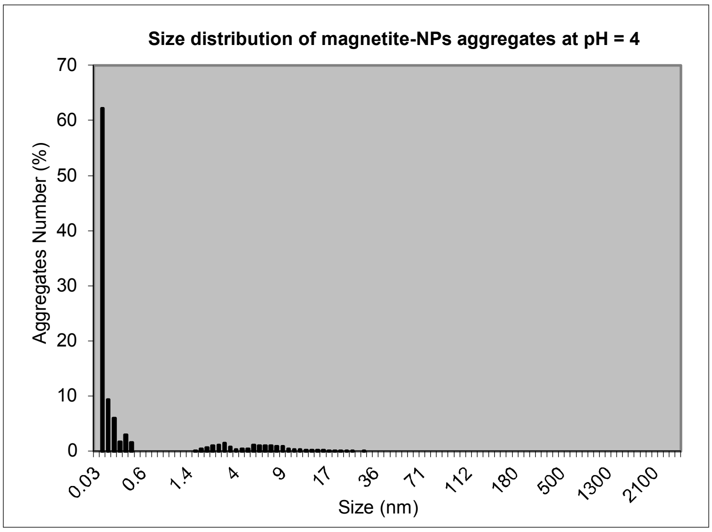

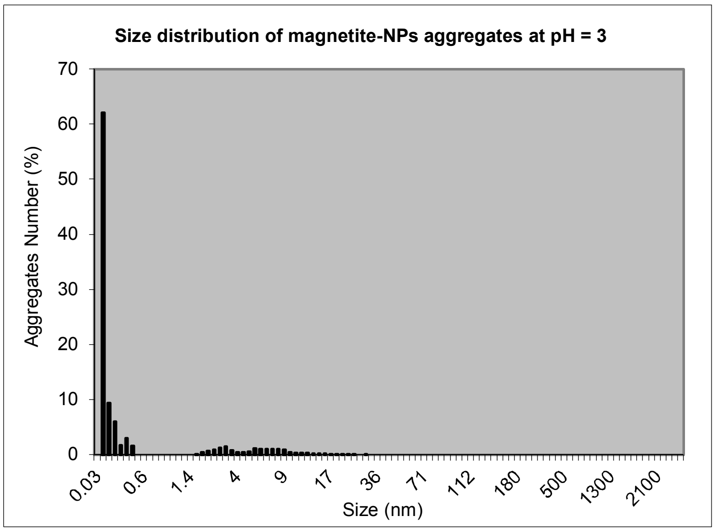

- **Magnetite-HA**

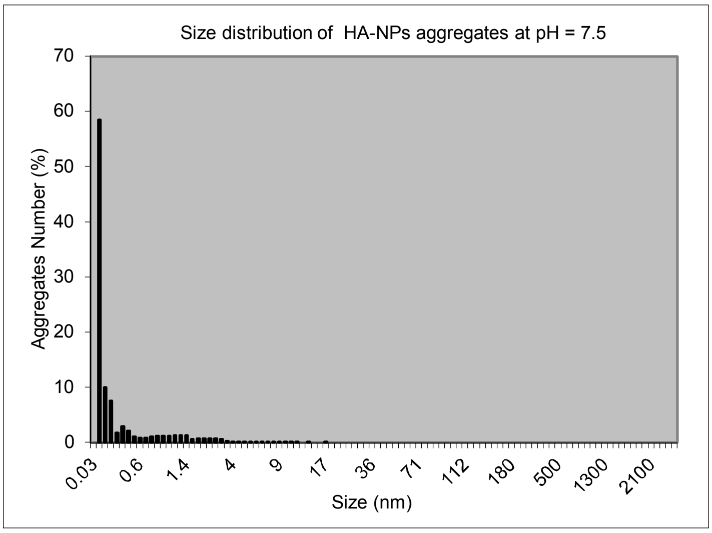
Size distribution of HA-NPs aggregates at pH = 7.5

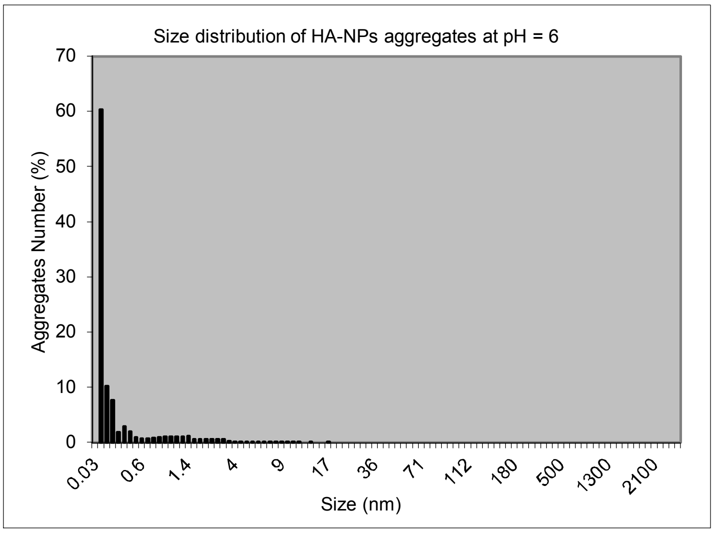
Size distribution of HA-NPs aggregates at pH = 6

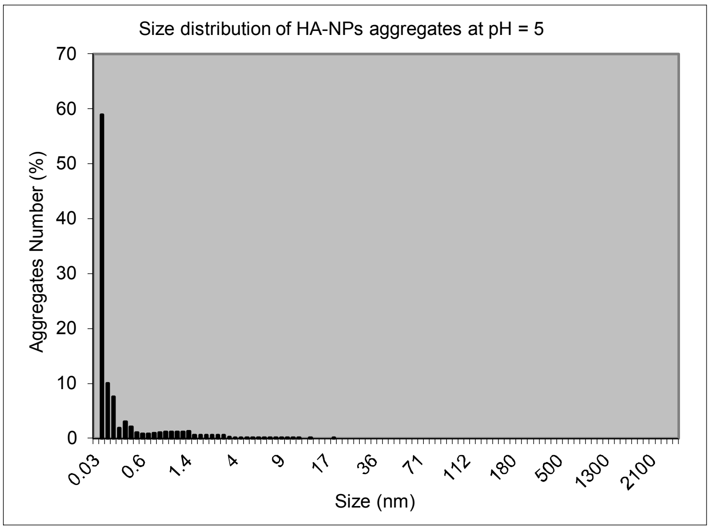
Size distribution of HA-NPs aggregates at pH = 5

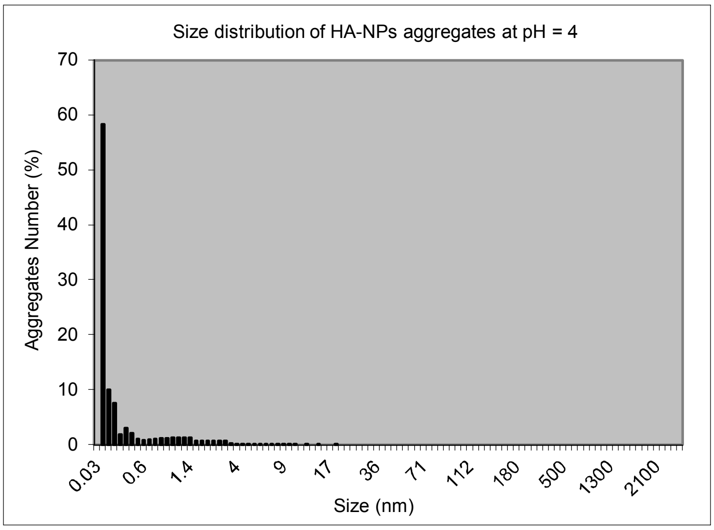
Size distribution of HA-NPs aggregates at pH = 4

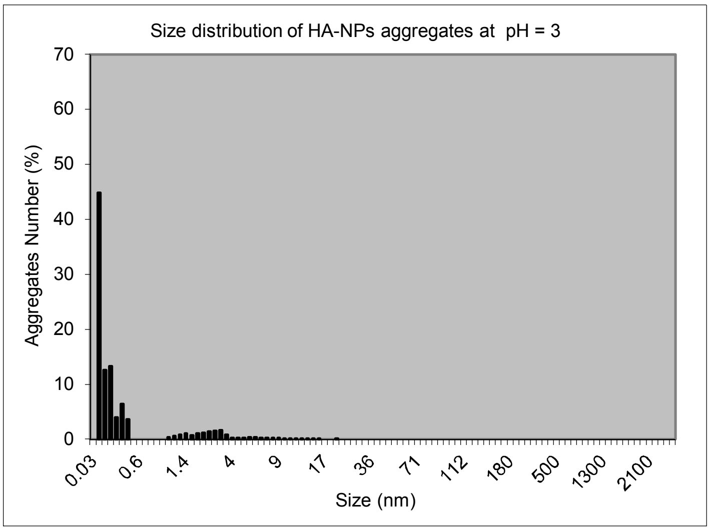
Size distribution of HA-NPs aggregates at pH = 3

- **Magnetite-PC**

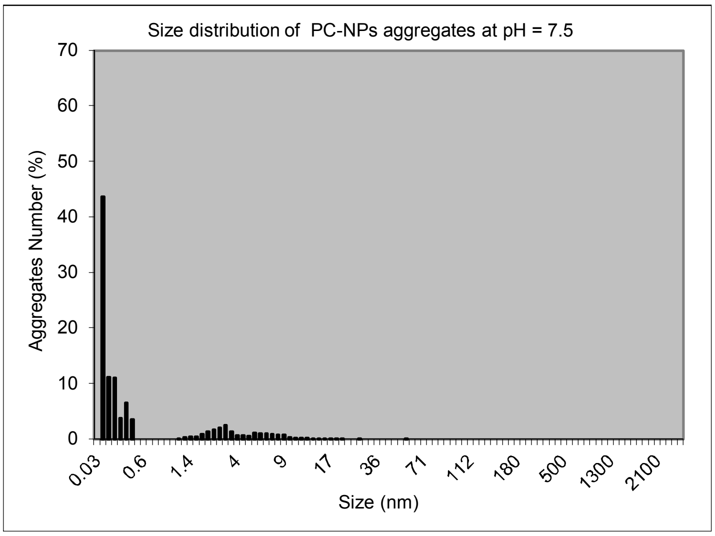
Size distribution of PC-NPs aggregates at pH = 7.5

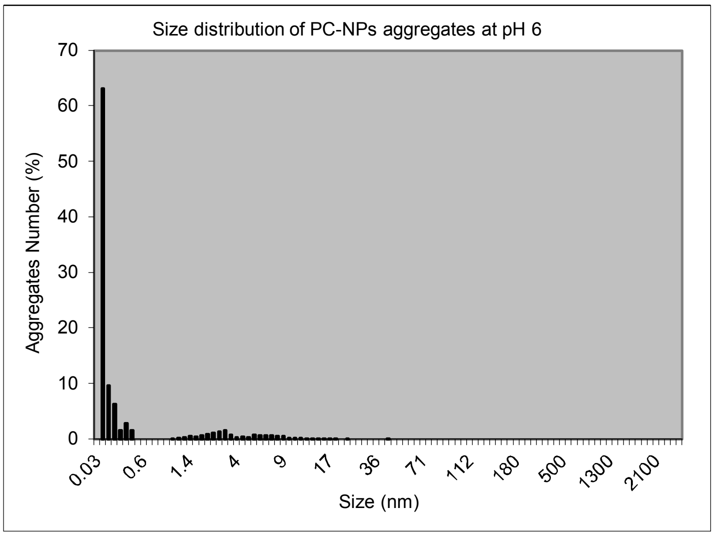
Size distribution of PC-NPs aggregates at pH 6

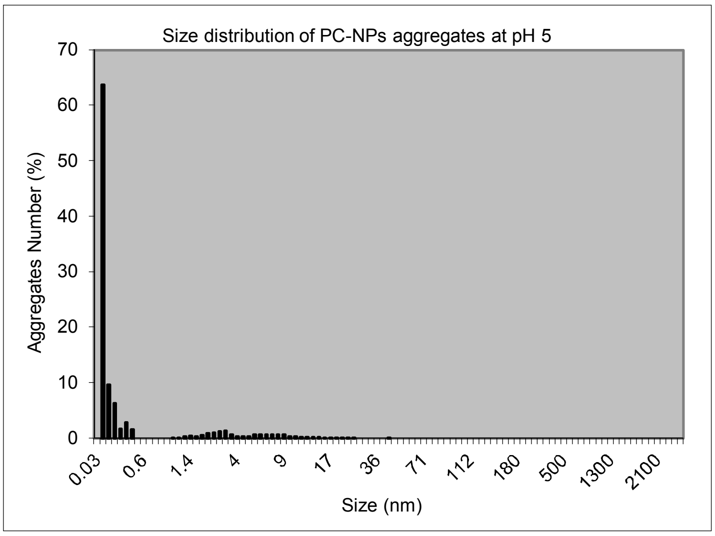
Size distribution of PC-NPs aggregates at pH 5

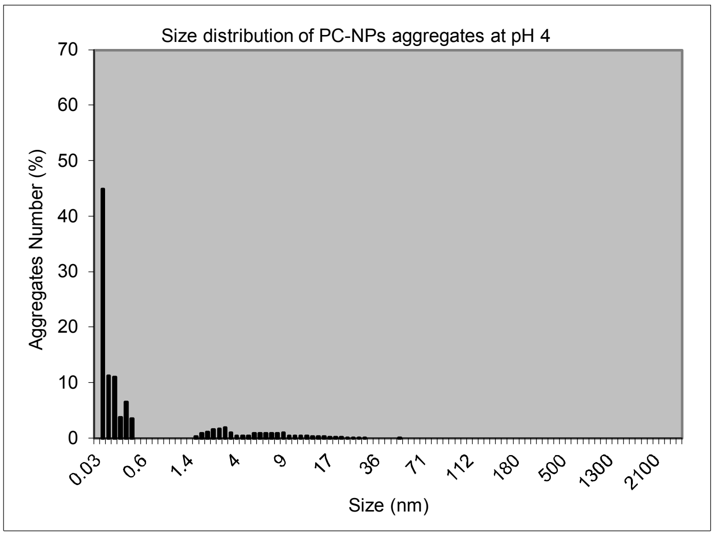
Size distribution of PC-NPs aggregates at pH 4

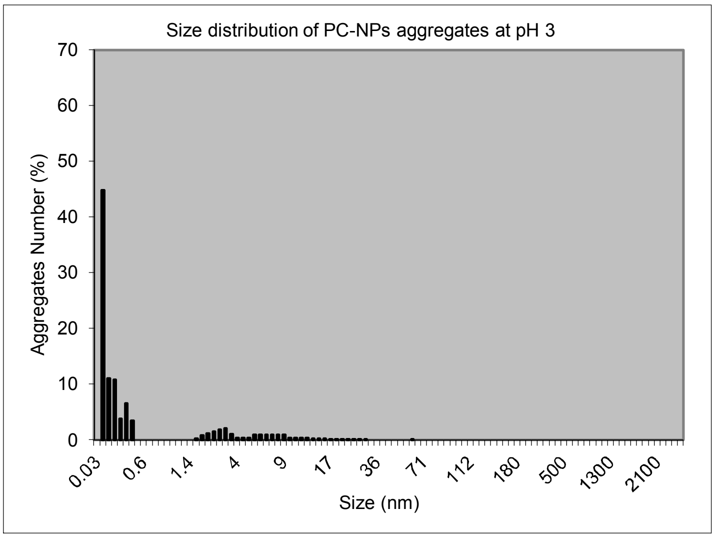
Size distribution of PC-NPs aggregates at pH 3

- **Maghemite**

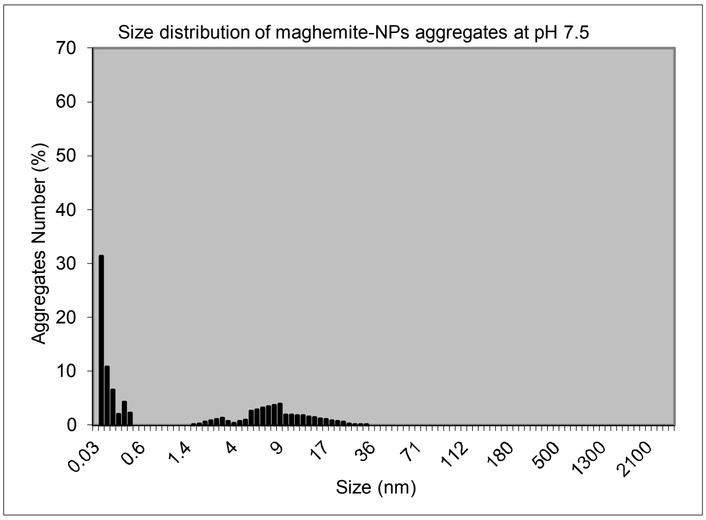
Size distribution of maghemite-NPs aggregates at pH 7.5

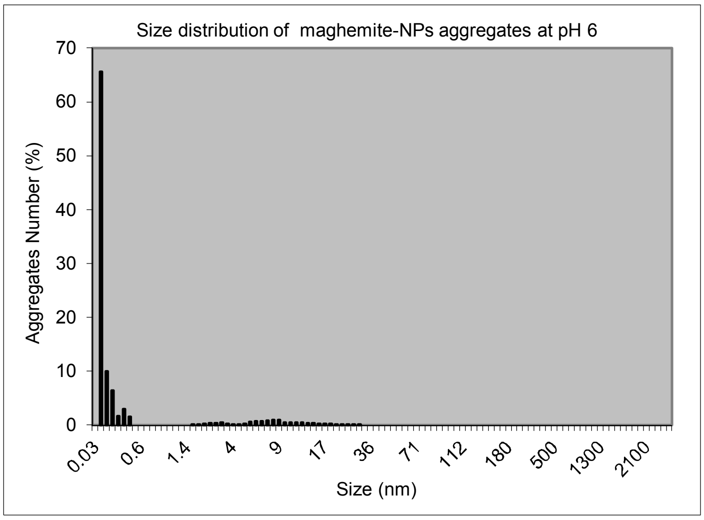
Size distribution of maghemite-NPs aggregates at pH 6

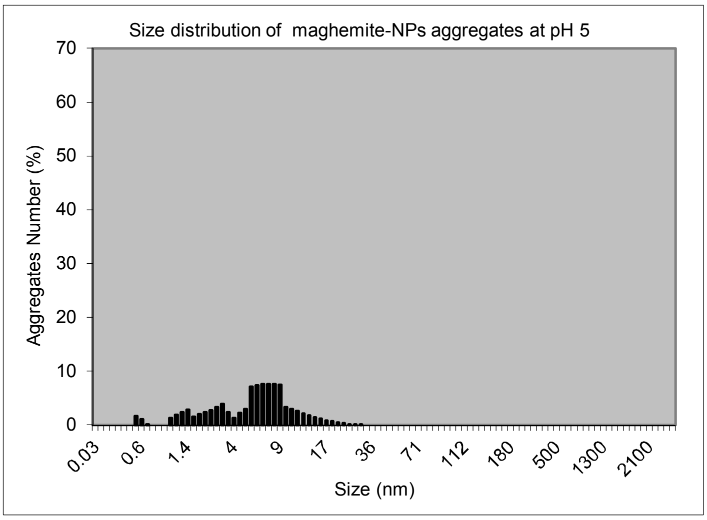
Size distribution of maghemite-NPs aggregates at pH 5

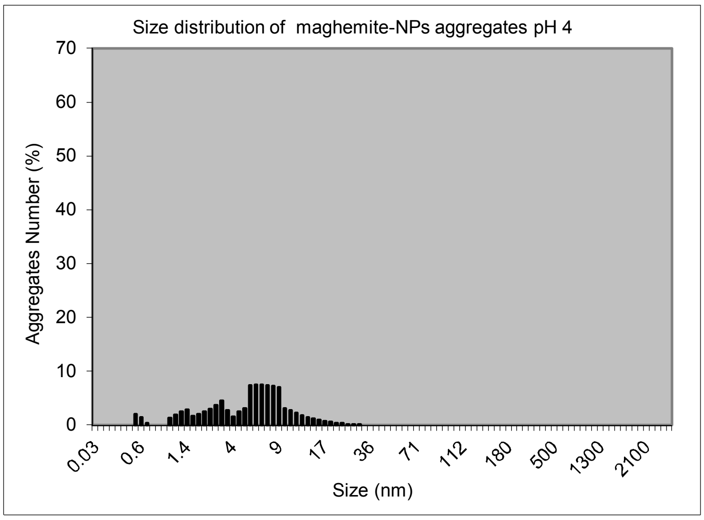
Size distribution of maghemite-NPs aggregates pH 4

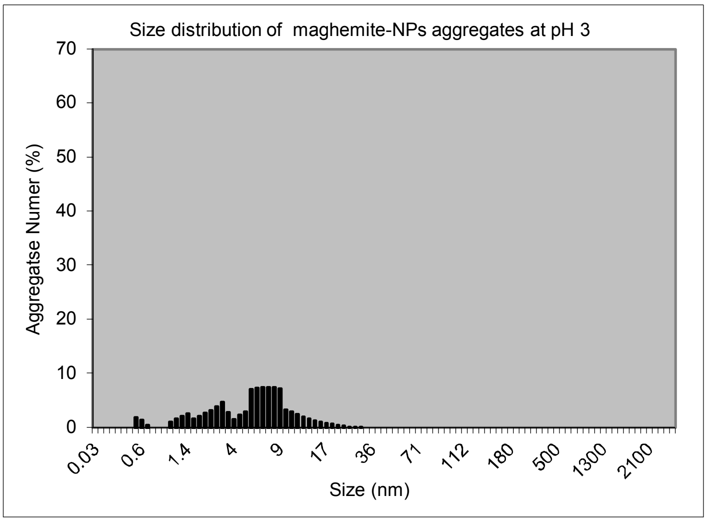
Size distribution of maghemite-NPs aggregates at pH 3

- **Hématite**

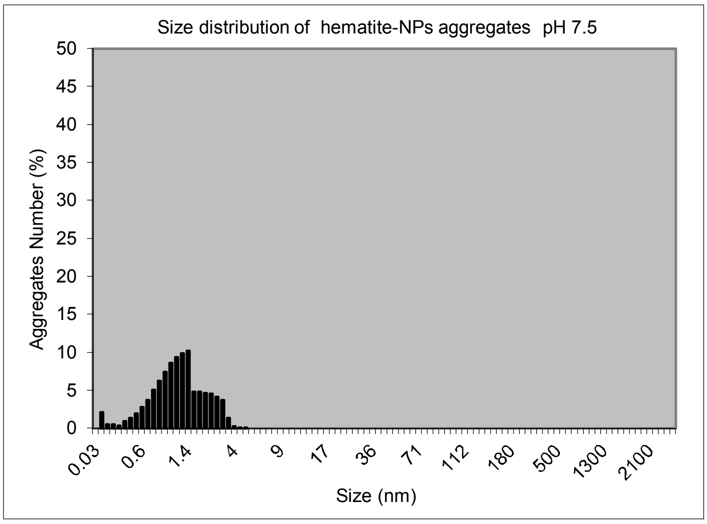
Size distribution of hematite-NPs aggregates pH 7.5

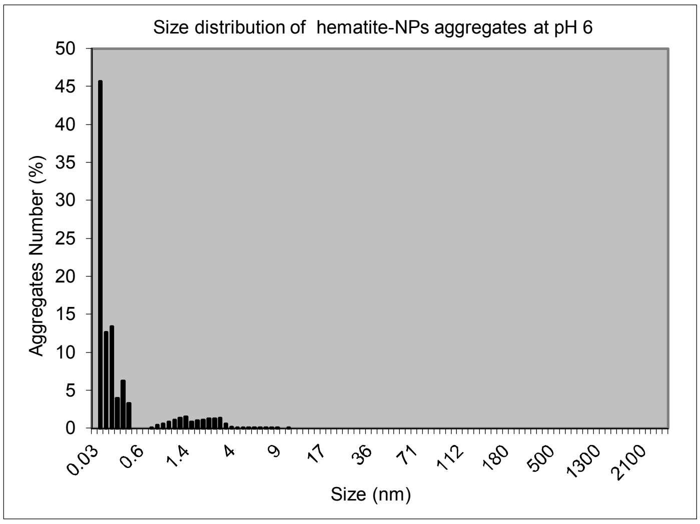
Size distribution of hematite-NPs aggregates at pH 6

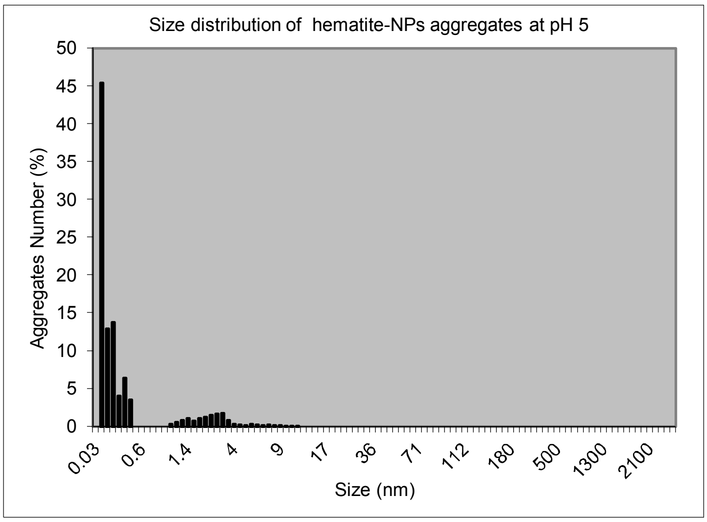
Size distribution of hematite-NPs aggregates at pH 5

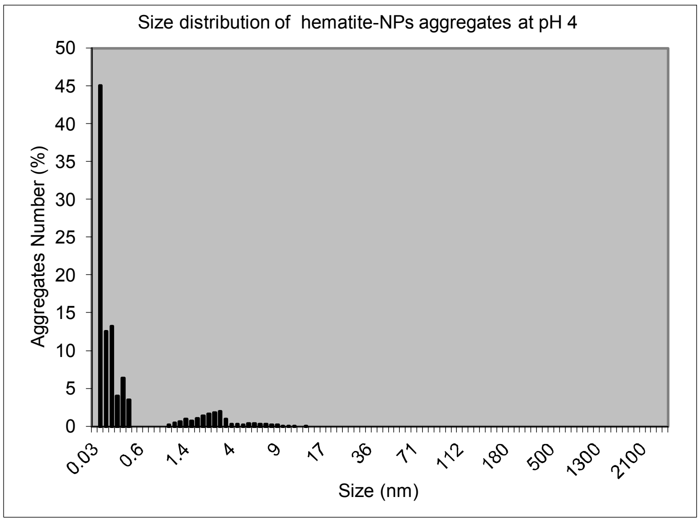
Size distribution of hematite-NPs aggregates at pH 4

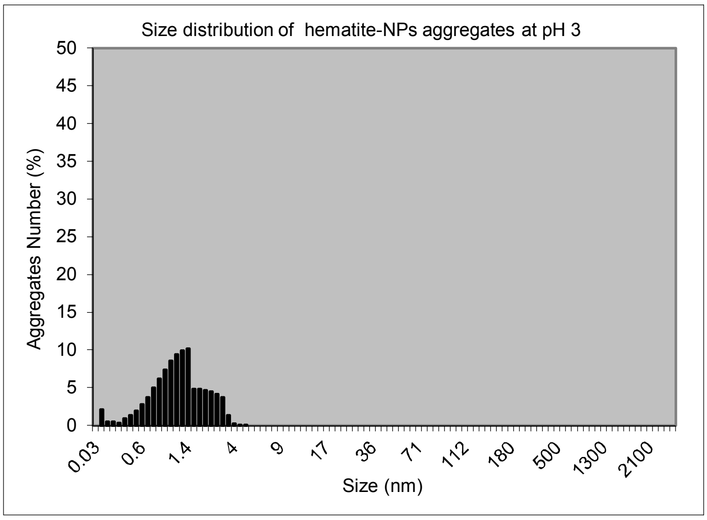
Size distribution of hematite-NPs aggregates at pH 3

Tables S1: Occurrence rates measured on each detector from laser particle size analyses

Caption:

■ >5%
▨ >1%
░ 0.1-1%
□ <0.1%

Magnetite

size (µm)	0.04	0.07	0.1	0.2	0.3	0.4	0.5	0.6	0.7	0.8	0.9	1	1.1	1.2	1.3	1.4	1.6	1.8	2	2.2	2.4	2.6	3
pH 7.5	43.16	11.17	11.26	3.72	6.24	3.38	0.00	0.00	0.00	0.00	0.00	0.00	0.00	0.00	0.00	0.00	0.21	0.73	1.17	1.68	2.16	2.62	1.49
pH 6	43.25	11.11	11.16	3.70	6.23	3.35	0.00	0.00	0.00	0.00	0.00	0.00	0.00	0.00	0.00	0.00	0.28	0.84	1.32	1.78	2.19	2.58	1.44
pH5	64.20	9.69	6.23	1.68	2.95	1.61	0.00	0.00	0.00	0.00	0.00	0.00	0.00	0.00	0.00	0.00	0.14	0.44	0.69	0.89	1.11	1.32	0.76
pH4	62.29	9.39	5.98	1.68	3.02	1.64	0.00	0.00	0.00	0.00	0.00	0.00	0.00	0.00	0.00	0.00	0.16	0.50	0.73	1.00	1.195	1.48	0.85
pH3	62.18	9.37	5.98	1.69	3.05	1.65	0.00	0.00	0.00	0.00	0.00	0.00	0.00	0.00	0.00	0.00	0.16	0.48	0.73	0.97	1.23	1.48	0.85

size (µm)	4	5	6	6.5	7	7.5	8	8.5	9	10	11	12	13	14	15	16	17	18	19	20	22	25	28	32
pH 7.5	0.64	0.68	0.61	1.23	1.12	1.07	1.00	0.97	0.92	0.41	0.39	0.32	0.31	0.25	0.22	0.19	0.15	0.16	0.11	0.12	0.03	0.02	0.00	0.02
pH 6	0.61	0.62	0.59	1.15	1.12	1.03	1.00	1.02	0.92	0.41	0.39	0.32	0.31	0.25	0.22	0.19	0.15	0.16	0.11	0.12	0.03	0.02	0.00	0.023
pH5	0.35	0.42	0.41	0.91	0.90	0.83	0.84	0.80	0.74	0.34	0.32	0.24	0.23	0.20	0.17	0.14	0.1	0.11	0.11	0.06	0.03	0.00	0.03	0.00
pH4	0.39	0.48	0.50	1.11	1.04	1.08	1.01	0.98	0.93	0.42	0.37	0.34	0.26	0.28	0.17	0.18	0.15	0.10	0.11	0.06	0.06	0.00	0.03	0.00
pH3	0.41	0.51	0.52	1.11	1.08	1.076	1.01	1.03	0.93	0.42	0.37	0.31	0.30	0.24	0.17	0.18	0.15	0.10	0.11	0.06	0.06	0.00	0.03	0.00

Magnetite-HA

size (µm)	0.04	0.07	0.1	0.2	0.3	0.4	0.5	0.6	0.7	0.8	0.9	1	1.1	1.2	1.3	1.4	1.6	1.8	2	2.2	2.4	2.6	3
pH7.5	58.55	9.99	7.54	1.85	2.98	2.09	1.07	0.84	0.86	1.08	1.15	1.23	1.23	1.32	1.32	1.34	0.68	0.69	0.69	0.73	0.69	0.68	0.32
pH6	60.37	10.23	7.66	1.86	2.99	2.04	0.97	0.72	0.73	0.92	1.01	1.05	1.09	1.13	1.15	1.16	0.57	0.60	0.64	0.61	0.63	0.61	0.28
pH5	58.98	10.10	7.66	1.87	3.02	2.11	1.09	0.83	0.85	1.02	1.11	1.18	1.18	1.22	1.25	1.27	0.61	0.64	0.66	0.67	0.66	0.64	0.30
pH4	58.39	10.04	7.63	1.87	3.01	2.13	1.11	0.86	0.90	1.09	1.15	1.20	1.27	1.25	1.32	1.30	0.66	0.67	0.69	0.70	0.69	0.68	0.30
pH3	44.90	12.62	13.37	4.06	6.47	3.61	0.00	0.00	0.00	0.00	0.00	0.00	0.41	0.64	0.90	1.15	0.76	1.06	1.24	1.48	1.62	1.72	0.87

	4	5	6	6.5	7	7.5	8	8.5	9	10	11	12	13	14	15	16	17	18	19
pH7.5	0.09	0.08	0.07	0.11	0.12	0.13	0.09	0.1	0.05	0.06	0.03	0.03	0.00	0.04	0.00	0.00	0.05	0.00	0.00
pH6	0.08	0.07	0.05	0.11	0.12	0.09	0.09	0.1	0.05	0.03	0.03	0.03	0.00	0.04	0.00	0.00	0.05	0.00	0.00
pH5	0.08	0.08	0.07	0.11	0.12	0.09	0.09	0.1	0.1	0.03	0.03	0.03	0.00	0.04	0.00	0.00	0.00	0.05	0.00
pH4	0.09	0.08	0.07	0.11	0.12	0.13	0.09	0.1	0.05	0.06	0.03	0.00	0.04	0.00	0.04	0.00	0.00	0.05	0.00
pH3	0.31	0.26	0.23	0.41	0.35	0.33	0.25	0.27	0.23	0.09	0.07	0.07	0.04	0.04	0.05	0.05	0.00	0.00	0.06

Magnetite-PC

size (µm)	0.04	0.07	0.1	0.2	0.3	0.4	0.5	0.6	0.7	0.8	0.9	1	1.1	1.2	1.3	1.4	1.6	1.8	2	2.2	2.4	2.6	3
pH7.5	43.69	11.13	11.08	3.78	6.50	3.56	0.00	0.00	0.00	0.00	0.00	0.00	0.00	0.11	0.27	0.46	0.49	0.92	1.33	1.73	2.11	2.49	1.39
pH6	63.10	9.63	6.30	1.65	2.86	1.61	0.00	0.00	0.00	0.00	0.00	0.00	0.09	0.24	0.37	0.57	0.45	0.71	0.94	1.16	1.38	1.57	0.84
pH5	63.10	9.63	6.30	1.65	2.86	1.61	0.00	0.00	0.00	0.00	0.00	0.00	0.09	0.24	0.37	0.57	0.45	0.71	0.94	1.16	1.38	1.57	0.84
pH4	44.93	11.23	11.07	3.81	6.56	3.52	0.00	0.00	0.00	0.00	0.00	0.00	0.00	0.00	0.00	0.00	0.28	0.88	1.19	1.54	1.76	1.99	1.05
pH3	44.80	11.10	10.86	3.79	6.57	3.53	0.00	0.00	0.00	0.00	0.00	0.00	0.00	0.00	0.00	0.00	0.30	0.90	1.24	1.57	1.86	2.06	1.09

size (µm)	4	5	6	6.5	7	7.5	8	8.5	9	10	11	12	13	14	15	16	17	18	19	20	22	25	28	32
pH7.5	0.63	0.67	0.614	1.17	1.05	0.99	0.87	0.77	0.76	0.29	0.23	0.21	0.15	0.13	0.09	0.1	0.051	0.05	0.06	0.00	0.00	0.02	0.00	0.00
pH6	0.34	0.39	0.36	0.75	0.73	0.65	0.70	0.59	0.58	0.26	0.22	0.21	0.15	0.12	0.09	0.09	0.1	0.05	0.00	0.06	0.00	0.00	0.00	0.00
pH5	0.34	0.39	0.36	0.75	0.73	0.65	0.7	0.59	0.58	0.26	0.22	0.21	0.15	0.12	0.09	0.09	0.1	0.05	0.00	0.06	0.00	0.00	0.00	0.00
pH4	0.40	0.42	0.43	0.90	0.89	0.91	0.92	0.93	0.98	0.44	0.43	0.39	0.39	0.34	0.27	0.29	0.21	0.22	0.17	0.12	0.03	0.02	0.03	0.00
pH3	0.41	0.45	0.44	0.93	0.92	0.95	0.96	0.97	0.98	0.44	0.42	0.39	0.39	0.29	0.32	0.24	0.20	0.16	0.17	0.12	0.03	0.02	0.03	0.00

size (µm)	36	38	40	45	50	53	56
pH7.5	0.00	0.00	0.00	0.00	0.00	0.05	0.00
pH6	0.00	0.00	0.06	0.00	0.00	0.00	0.00
pH5	0.00	0.00	0.06	0.00	0.00	0.00	0.00
pH4	0.00	0.00	0.00	0.00	0.03	0.00	0.00
pH3	0.00	0.00	0.00	0.00	0.00	0.00	0.06

Maghemite

size (µm)	0.04	0.07	0.1	0.2	0.3	0.4	0.5	0.6	0.7	0.8	0.9	1	1.1	1.2	1.3	1.4	1.6	1.8	2	2.2	2.4	2.6	3
pH7.5	31.44	10.85	6.55	2.02	4.31	2.31	0.00	0.00	0.00	0.00	0.00	0.00	0.00	0.00	0.00	0.00	0.11	0.31	0.56	0.83	1.14	1.33	0.80
pH6	65.68	9.97	6.45	1.70	2.96	1.63	0.00	0.00	0.00	0.00	0.00	0.00	0.00	0.00	0.00	0.00	0.07	0.18	0.26	0.38	0.42	0.50	0.28
pH5	0.00	0.00	0.00	0.00	0.00	0.00	1.67	1.12	0.19	0.00	0.00	0.00	1.28	1.90	2.43	2.87	1.63	2.00	2.41	2.77	3.33	3.96	2.35
pH4	0.00	0.00	0.00	0.00	0.00	0.00	2.07	1.45	0.36	0.00	0.00	0.00	1.32	1.96	2.49	2.92	1.64	2.03	2.49	2.95	3.66	4.50	2.76
pH3	0.00	0.00	0.00	0.00	0.00	0.00	1.86	1.35	0.41	0.00	0.00	0.00	1.03	1.60	2.13	2.61	1.58	2.10	2.66	3.22	3.94	4.72	2.78

4	5	6	6.5	7	7.5	8	8.5	9	10	11	12	13	14	15	16	17	18	19	20	22	25	28	32
0.41	0.69	0.99	2.60	2.87	3.19	3.45	3.76	3.90	1.93	1.90	1.85	1.76	1.57	1.44	1.23	1.10	0.91	0.78	0.68	0.23	0.1	0.07	0.02
0.12	0.18	0.23	0.65	0.74	0.80	0.90	0.96	1.02	0.49	0.51	0.46	0.46	0.41	0.35	0.28	0.30	0.21	0.17	0.18	0.032	0.02	0.03	0.00
1.37	2.28	2.96	7.16	7.45	7.61	7.68	7.65	7.50	3.35	3.00	2.59	2.21	1.82	1.48	1.17	0.91	0.73	0.54	0.43	0.13	0.04	0.02	0.00
1.62	2.57	3.16	7.39	7.51	7.54	7.45	7.29	7.03	3.09	2.71	2.28	1.86	1.50	1.20	0.96	0.74	0.58	0.44	0.33	0.1	0.03	0.01	0.00
1.53	2.36	2.96	7.06	7.29	7.42	7.45	7.40	7.23	3.24	2.89	2.46	2.04	1.66	1.33	1.08	0.85	0.67	0.50	0.38	0.12	0.03	0.02	0.00

Hematite

size (µm)	0.04	0.07	0.1	0.2	0.3	0.4	0.5	0.6	0.7	0.8	0.9	1	1.1	1.2	1.3	1.4	1.6	1.8	2	2.2	2.4
pH7.5	2.11	0.55	0.50	0.35	0.94	1.39	1.98	2.81	3.75	5.05	6.25	7.42	8.63	9.40	9.92	10.22	4.87	4.86	4.71	4.55	4.19
pH6	45.69	12.69	13.40	3.97	6.24	3.36	0.00	0.00	0.00	0.15	0.42	0.65	0.89	1.13	1.35	1.55	0.88	1.03	1.15	1.27	1.28
pH5	45.38	12.89	13.73	4.08	6.42	3.56	0.00	0.00	0.00	0.00	0.00	0.00	0.35	0.61	0.87	1.11	0.77	1.09	1.29	1.49	1.67
pH4	45.04	12.56	13.25	4.02	6.40	3.53	0.00	0.00	0.00	0.00	0.00	0.00	0.24	0.45	0.69	1.01	0.73	1.11	1.39	1.64	1.84
pH3	42.05	11.76	12.41	3.84	6.22	3.50	0.00	0.00	0.00	0.00	0.00	0.00	0.53	0.83	1.13	1.48	0.99	1.33	1.61	1.84	2.09

size (µm)	2.6	3	4	5	6	6.5	7	7.5	8	8.5	9	10	11	12	13	14	15
pH7.5	3.75	1.40	0.26	0.09	0.02	0.00	0.00	0.00	0.00	0.00	0.00	0.00	0.00	0.00	0.00	0.00	0.00
pH6	1.35	0.62	0.19	0.15	0.09	0.12	0.09	0.09	0.051	0.05	0.06	0.00	0.03	0.00	0.00	0.00	0.00
pH5	1.73	0.85	0.29	0.22	0.18	0.33	0.27	0.19	0.20	0.16	0.12	0.06	0.03	0.04	0.00	0.00	0.00
pH4	2.04	1.00	0.35	0.32	0.25	0.41	0.40	0.33	0.30	0.22	0.23	0.06	0.069	0.04	0.00	0.04	0.00
pH3	2.27	1.16	0.44	0.42	0.38	0.70	0.59	0.59	0.49	0.46	0.38	0.18	0.1	0.11	0.04	0.04	0.04

Chapitre 3 :

Etude de la réactivité chimique des NPs-Fe via des expériences d'adsorption du cuivre

Ce chapitre correspond à un article soumis dans la revue *Journal of Hazardous Materials* : « Do surface transformations impact the reactivity of iron oxide nanoparticles? Insights from copper binding and iron oxide dissolution », E. Demangeat, M. Pédrot, A. Dia, M. Bouhnik-le-Coz, M. Davrancheet F. Cabello-Hurtado.

Do surface transformations impact the reactivity of iron oxide nanoparticles? Insights from copper binding and iron oxide dissolution

E. Demangeat[a], M. Pédrot[a,*], A. Dia[a], M. Bouhnik-Le-Coz[a], M. Davranche[a]

and F. Cabello-Hurtado[b]

[a] Univ. Rennes, CNRS, Géosciences Rennes - UMR 6118 - Av. General Leclerc - F-35042 Rennes Cedex, France

[b] Univ. Rennes, CNRS, Ecobio - UMR 6553 - Av. General Leclerc- F-35042 Rennes Cedex, France

Abstract

The oxidation of magnetite into maghemite as well as natural organic coatings are common changes that affect the reactivity of iron (Fe) oxide nanoparticles (IONPs) in aqueous environments, particularly in terms of the adsorption of trace elements (TEs). Consequently, certain ubiquitous natural organic constituents such as humic acids (HA) and phosphatidylcholine (PC), displaying a high affinity for both TEs and IONPs, could play a critical role in the interactions involved between both compounds. The adsorption of copper (Cu) onto four different IONPs was studied: magnetite nanoparticles (magnNPs), maghemite NPs (maghNPs), HA- and PC-coated magnetite NPs (HA-magnNPs and PC-magnNPs). According to the results, the percentage of adsorbed Cu (Cu%) increases with increasing pH, irrespective of the IONPs. The impact of pH on Cu sorption highlights the role of protonation/deprotonation reactions in Cu adsorption. Contrary to the other IONPs studied, HA-magnNPs increase adsorbed Cu% at most pH values tested (pH= 3 to 7). The Freundlich adsorption isotherm provides the highest sorption constant K_F (bonding energy) and n value which supports a heterogeneous sorption process on HA-magnNPs. This heterogeneous behavior highlights the existence of different sorption sites and/or different complexes formed at the surface of magnNPs, which are relevant to understanding the speciation of TEs with IONPs and different environmental organic constituents.

Keywords: magnetite, oxidation, surface coating, copper, adsorption, speciation

---

* Corresponding author: mathieu.pedrot@univ-rennes1.fr Phone (+33)2 23 2360 83

Highlights:

- HA and PC coatings modified the surface chemistry of pristine NPs (surface chemistry, surface charge) and the oxidation of magnetite NPs into maghemite impacted its surface area and the Fe(II)/Fe(III) ratio.
- Adsorption of copper onto pristine magnetite and modified IONPs followed the Freundlich isotherm which is a multilayer adsorption model and reversible adsorption process.
- HA-coated magnetite (HA-magnNPs) displayed the largest Cu removal efficiency showing that HA provided high affinity binding sites for Cu onto magnNP surfaces.
- The models obtained using Visual Minteq3.1 were consistent with the experimental data (%Cu adsorbed) in modelling Cu speciation in the presence of IONPs at different pH values.
- Magnetite and maghemite NPs underwent dissolution at acidic pH (3 and 4), whereas both PC and HA-coated NPs prevented iron release from the coated oxides.

Graphical abstract:

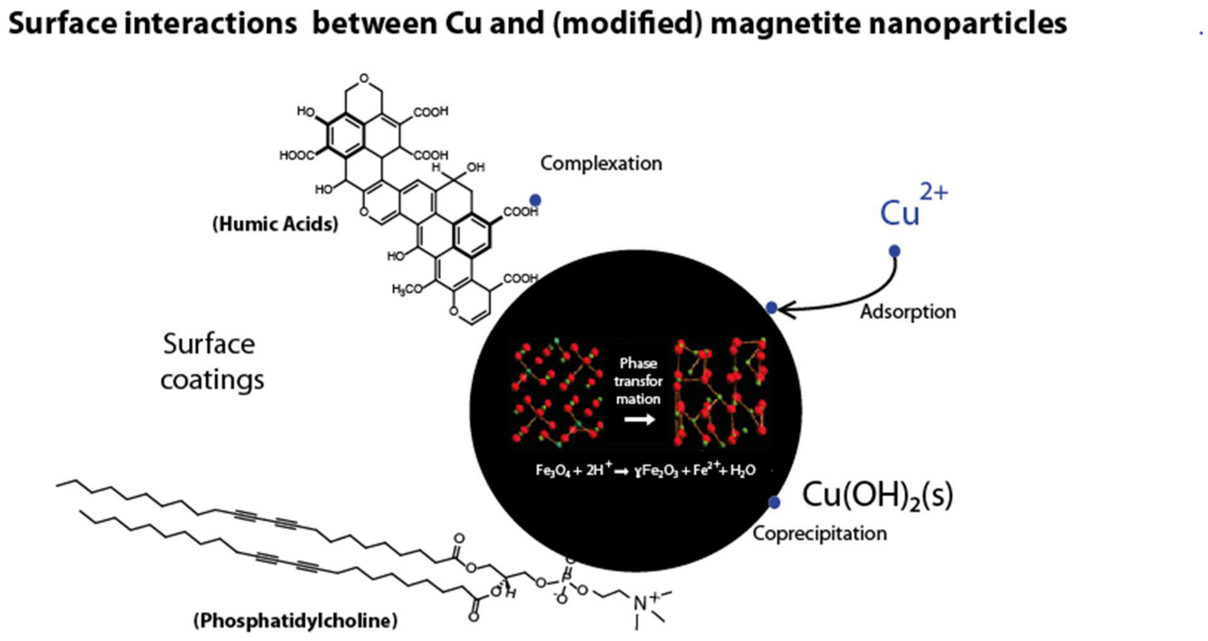

III.1. Introduction

For almost two decades, engineered nanoparticles (NPs), one of many nanomaterials, have been revolutionary tools for human kind. Due to their nano-scale size, NPs display a high surface to volume ratio and ensure high reactivity which provides them with promising properties in many areas [1-3]. With their increasing production and widespread applications, NPs are thus expected to enter the environment and possibly induce some concerning health and environmental issues [4, 5].

More specifically, engineered iron oxide NPs (IONPs) display high reactivity, magnetic properties and biocompatibility, which allow their use in many technical fields and applications requiring a high degree of accuracy. Examples of these uses range from medical therapies (cell labeling, drug delivery) [6, 7], imaging and recording technologies to remediation methods and agricultural uses [8, 9]. In the environment, IONPs exist in various forms, including magnetite, maghemite and hematite, which are the most common mineral species [10].

Whether these materials are engineered or occur naturally, IONPs undergo various modifications in surface ecosystems [11]. Phase transformations, affecting the whole mineral structure, can stem from dissolution, precipitation, oxidation-reduction reactions, photochemical transformations or other internal structural changes [12, 13]. In addition, co-precipitation, sorption (ion exchange, complexation) and certain biotransformations can also affect the interactions occurring at the surfaces of the IONPs and thus modify their reactivity [14]. These transformations appear critical in determining the fate and behavior of IONPs in the environment (i.e. aggregation, mobility, reactivity, biodegradability), as well as their impacts on living organisms (bioavailability or toxicity) [15, 16].

IONP surfaces are the prime interface for the interactions that occur between IONPs and the surrounding aqueous compounds, including solid minerals, organic debris, microorganisms as well as soluble organic constituents and inorganic dissolved species (such as trace elements, TEs). In aqueous environments, IONPs are amphoteric solids that acquire a surface charge in response to the protonation and deprotonation reactions of the Fe-OH surface sites [17]. Consequently, dissolved cationic species are attracted to IONPs at pH values higher than their pHzpc (point of zero charge), where the surfaces of the IONPs are negatively charged. Several studies have highlighted the affinity of TEs - such as Ni^{2+}, Cu^{2+}, Zn^{2+}, Pb^{2+}, Cd^{2+} and Co^{2+} - for IONPs [18-20]. According to Hu and coworkers [21], metal ion adsorption by magnetite involved both electrostatic attraction and ligand exchange at various pH conditions. However, the investigation of the mechanisms controlling IONP and TE interactions requires the full consideration of the studied system since the adsorption of TEs onto IONPs is dependent upon several geochemical parameters such as pH, ionic strength, temperature and soil solution chemistry including the initial TE concentration and the adsorbent (IONPs) concentration [22].

In addition, the specific properties of IONPs (especially their size, surface area, morphology, and surface chemistry) do play a key role in cation adsorption [23]. These intrinsic properties are likely changed when IONPs are released in natural environments because of the numerous transformations that IONPs undergo as well as the interactions that occur with many natural constituents and living organisms |24]. Once released into ecosystems, nanomaterials may be coated with organic substances due to the pervasiveness of these compounds in natural aqueous systems [25]. HA (humic acids) in particular display a high affinity for magnetite, and the adsorption of HA onto magnetite NPs has been proven to largely impact both the colloidal stability of IONPs [26-29] and their interactions with soil solution species including several TEs [30-32]. Phospholipids, another ubiquitous organic compound (integral major component of cell membranes) may also cover the surfaces of the IONPs and interfere in the interactions between the TEs and IONPs. In aqueous medium, phospholipids likely form lipid bilayers on mineral surfaces because of their amphiphilic character and they can form various structures depending on the specific properties of the phospholipid molecules [33]. Phospholipid coating can therefore impact the surface structure of the IONPs and the ensuing interactions with molecules and metal ions via electrostatic and hydrophobic interactions and/or hydrogen bonding [34]. In addition to surface coatings, magnetite is also chemically unstable. The oxidation of magnetite NPs into maghemite NPs has been extensively studied [35, 36] because of the ensuing structural and induced chemical changes (especially, the Fe(II)/Fe(III)molar ratio), which are of great concern for TE adsorption [37].

The surface of the IONPs is a critical interface for TE dynamics. To understand the behavior of TEs and iron NPs is a major issue because of the possible applications and environmental and societal impacts associated with it [38]. TE and IONP interactions raise major environmental issues such as water safety, soil (de-)contamination, sustainable agriculture (plant nutrition, breeding), and more globally, the preservation of natural areas [39, 40].

In this study, the adsorption capacity of four different IONPs was investigated using copper (Cu) as a model metal contaminant. The IONPs included magnetite NPs (magnNPs) and its oxidized form, maghemite NPs (maghNPs). Pristine magnNPs were coated with HA (HA-magnNPs) and PC (PC-magnNPs) to model natural surface transformations. Therefore, the main objectives of the study were to: (i) discern the possible impact(s) of magnNPs transformations in an aqueous environment, (ii) assess the role of surface properties in IONP reactivity, (iii) provide details about Cu(II) adsorption onto bare magnNPs and modified IONPs, and (iv) investigate the relationships that possibly exist between IONP surface properties, their colloidal and chemical stabilities and Cu adsorption capacity.

III. 2. Materials and methods

III.2.1. IONP synthesis and modifications

III.2.1.1. Magnetite-NPs: preparation and oxidation into maghemite

Magnetite (Fe_3O_4) nanoparticles were prepared according to modified literature procedures [41, 42] via the anaerobic co-precipitation of Fe salts. Iron Chloride, $FeCl_2.4H_2O$ (1.988 g) and $FeCl_3.6H_2O$ (5.406 g) were dissolved in 5 mL HCl (2 M) and 20 mL H_2O and then stirred to obtain a Fe solution at a Fe(II)/Fe(III) molar ratio = 0.5. MagnNP precipitation was achieved by the dropwise addition of the Fe salt solution into a 0.7 M NaOH-$NaNO_3$ base solution (250 mL). The black precipitate was left to settle under anaerobic conditions (Jacomex glovebox) for several hours to get rid of the supernatant. Three washings were conducted with deoxygenated deionized water and 5 10^{-3} M NaCl solution before storage under anaerobic conditions.

Maghemite (γ-Fe_2O_3) was synthesized following the method of Anna et al. [43] through the oxidation of the previously synthesized magnetite by adding 5 wt% NaOCl aqueous solution (50% weight/volume) and sonicating for 2 h. The solid product was magnetically separated and washed with deionized water.

III.2.1.2. Surface coatings

MagnNPs were coated with HA (Elliott Soil Humic Acid Standard IV - IHSS) and PC (1, 2-bis (10, 12-tricosadiynoyl)-sn-glycero-3-phosphocholine – Avanti Polar Lipid, CAS Registry Number: 76078-28-9) to model that surface modifications that could occur in natural areas. At first, HA (0.2 g) was dissolved in 1 M NaOH and the obtained HA solution was completed to 56 mL with deionized water. A similar PC solution was obtained via the dissolution of PC **(Fig. 1)** in deionized water and ultrasonication. A 6 g L^{-1} concentrated magnNP suspension (44 mL) was then added to each organic stock solution and each 100 mL of mixed solution was shaken for 48 h. At the end of the coating, three washings were performed with deionized water to remove the uncoated materials present in the supernatant after centrifugation. Each HA-magnNP and PC-magnNP suspension was diluted in NaCl 5.10^{-3} M to perform sorption experiments.

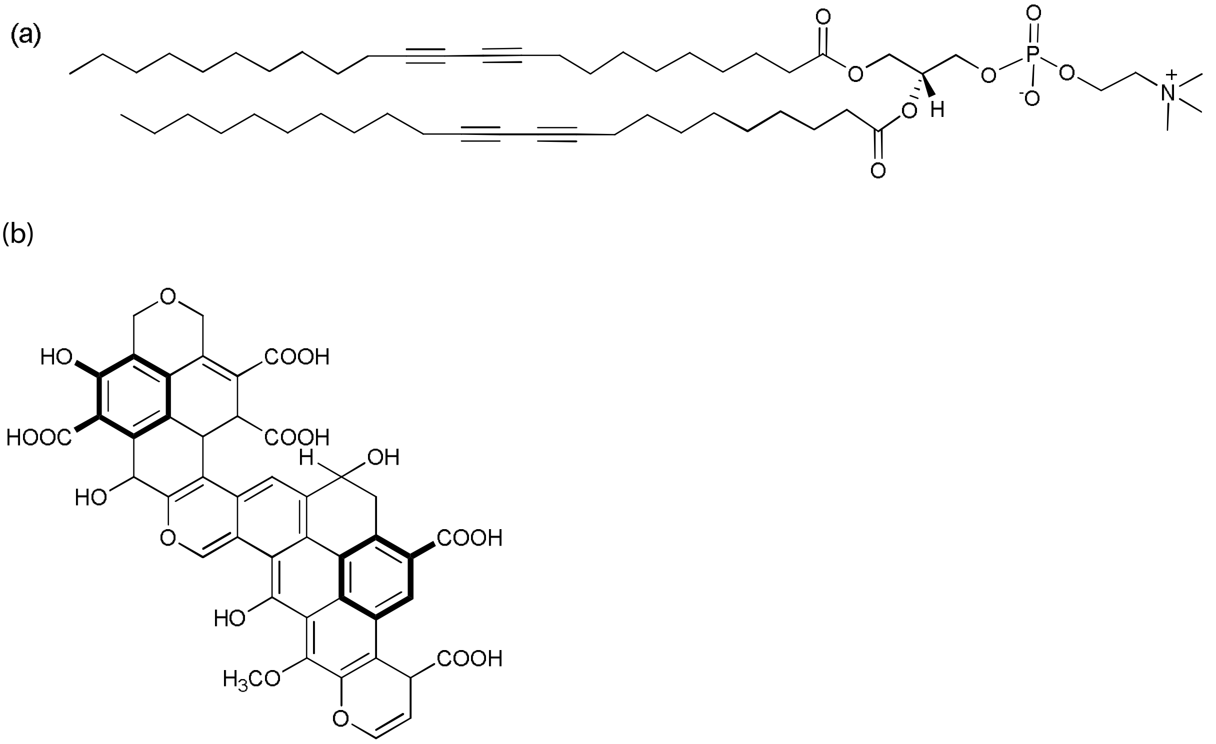

Figure 1: Chemical structure of the two organic coatings (a)1, 2-bis (10, 12-tricosadiynoyl)-sn-glycero-3-phosphocholine and (b) proposed humic acid configuration [43] with possible ion binding sites in bold characters.

III.2.2. Characterization methods

High Resolution Transmission Electron Microscopy (HR-TEM) was carried out with a JEOL2100F electron microscope (voltage 200 kV). Specimens were prepared by drop-casting diluted IONP suspensions on 300 mesh Au-grids supported with carbon film. The specific surface area of the IONPs was determined by the multipoint N_2–Brunauer Emmett Teller (BET) technique using a Coulter (SA 3100) surface area analyzer. The XRD data were recovered from a Johansonmonochromator using CuK_α radiation (λ = 1.5406 A). Attenuated Total Reflectance-Fourier Transform InfraRed (ATR-FTIR) spectra were recorded in the 780 - 1800 cm^{-1} region on an IS50 Nicolet spectrometer equipped with a KBr beam splitter and a liquid Nitrogen cooled MCT (Mercury Cadmium Telluride) detector. A nine-reflection diamond ATR accessory (DuraSamplIR™, SensIR Technologies) was used to acquire spectra for the wet samples. The resolution of the single beam spectra was 4 cm^{-1}.

III.2.3. Batch reactions

The adsorption experiments investigated the affinity of copper (Cu) for bare magnetite NPs (magnNPs), HA coated magnetite NPs (HA-magnNPs), PC coated magnetite NPs (PC-magnNPs) and maghemite NPs (maghNPs). Three experiments were conducted to investigate (i) the Cu adsorption kinetics, (ii) the effect of pH on the Cu adsorption capacity and (iii) the Cu adsorption capacity for the four IONPs studied.

III.2.3.1. Experimental set-up

Cu adsorption kinetic experiments were conducted to determine the equilibration time prior to the Cu adsorption experiments, performedat different pH values and variable Cu concentrations. The kinetic experiments were performed in triplicate for each IONP in a 0.5 ± 0.05 g L^{-1} solution (400mL) at pH = 6 with constant Cu = 0.05 mM. The solutions were shaken for 48 h and for each replicate, 10 samples were collected through time. The samples (1mL) were digested with sub-boiled nitric acid (14.6 M HNO_3) at 95°C, and then re-solubilized in 0.37 M HNO_3, after complete evaporation. The accurate total Cu and IONP concentrations were controlled for each experiment. Major- and trace-element concentrations were determined by ICP-MS (Agilent 7700x), using rhenium and rhodium as an internal standard. The international geostandard SLRS-5 was used to check the validity and reproducibility of the results [44]. Other aliquots were filtrated at 2 kDa using ultrafiltration cells made of cellulose nitrate membrane filters (from Sartorius). ICP-MS analyses were performed to provide the concentrations of the dissolved species. Dissolved Cu was considered as non-adsorbed Cu and dissolved Fe was monitored to highlight possible Fe dissolution, which was expected to occur at acidic pH. The results showed that equilibration was achieved within 15 min. All of the following experiments, which lasted several hours, were therefore performed at equilibrium.

To investigate the effect of pH on the Cu adsorption capacity of the IONPs, the initial Cu concentration wasset to 0.05 mM by diluting a 250 ppm Cu stock solutionin tubes containing 20 mL of 0.5 g L^{-1} IONP suspension. The pH was adjusted using 0.1M NaOH or HCl to reach the targeted pH (pH 3, 4, 5, 6 and 7). Five samples were performed in triplicate for each IONPs. After shaking under anaerobic conditions for 18 h, each sample was split into two aliquots to perform the total and dissolved ICP-MS analyses, as previously described.

In the last experiment, Cu was added to 20 mL of 0.5 g L^{-1} IONP suspension in appropriate amounts to obtain concentrations of Cu = 0.5 mM, Cu = 0.1 mM, Cu = 0.05 mM, Cu = 0.01 mM and Cu = 0.005 mM. The pH was adjusted to pH = 6 ± 0.1 using 0.1 M NaOH and the solutions were shaken for approximately 18 h under anaerobic conditions. ICP-MS analyses were also conducted on both the dissolved and total 1 mL IONPs samples.

III.2.3.2. Adsorption isotherms

The amount of adsorbed Cu on the four investigated IONPs was calculated according to the following equation:

$$\text{Removal efficiency (\%)} = C_0\text{-}C_e/C_0*100 \quad (1)$$

where C_0 (mgL^{-1}) and C_e(mgL^{-1}) are the initial concentrations of Cu and the aqueous concentration of metal ions after adsorption, respectively. The equilibrium adsorption capacity, Q_e (mg g^{-1}) represents the adsorbed Cu per g of IONPs and was calculated using the following mass balance equation:

$$Q_e= (C_0\text{-}C_e)V/m \quad (2)$$

where V (L) is the sample volume, and m (g) is the mass of adsorbent.

To parameterize the adsorption behavior of Cu(II) onto the IONPs, the Langmuir and Freundlich isotherms were tested. The Freundlich model was chosen as it provided the best fit regarding the experimental results for all of the IONPs investigated. The Freundlich isotherm is a well-known relationship describing non-ideal and reversible adsorption. This isotherm remains on a multilayer adsorption model and emphasizes a non-uniform distribution of adsorption heat and affinities over a heterogeneous surface [45]. The adsorption data were fitted with the Freundlich adsorption equation to determine the adsorption parameters and the consistency with the model. The Freundlich isotherm is represented as follows:

$$Q_e=K\times[C_e]^{1/n} \quad (3)$$

where C_e is the concentration of the solute at equilibrium (mg L^{-1}), Q_e is the mass of the contaminant adsorbed per unit weight of the adsorbent (mg g^{-1}) and K and n are constants, which must be evaluated for each solute and temperature, and are related to the adsorption capacity and adsorption energy. When it is expressed in the logarithmic form, Equation (3) gives:

$$\log Q_e = \log K + (1/n) \log C_e \quad (4)$$

The adsorption data were plotted according to Equation (4). The adsorbent concentrations in the solutions were set to the same pH, with initial adsorbent concentrations of 0.5 g L^{-1} and the pH adjusted to pH = 6.

III.2.4. Cu speciation

Cu speciation in the presence of IONPs was investigated using Visual Minteq 3.1. In particular, the concentration of the different Cu species was calculated relative to the pH in our experimental conditions (25°C, 0.005 M NaCl). The model considered the presence of IONPs (0.5 g.L^{-1}) including the properties of magnNPs determined from the BET analyses and potentiometric titration (i.e. number of adsorption sites, pKa1 and pKa2). The sorption constant was fitted using the experimental datasets of the adsorption isotherm experiments. The best fit was validated by the calculation of the RMSE. Calculations were performed at pH values ranging from 3 to 8 to obtain the concentrations of the significant Cu species (Cu^{2+}, $CuOH^+$, $Cu(OH)_2(aq)$, $Cu(OH)^{3-}$, $Cu_3(OH)_4^{2+}$, $Cu(OH)_2(s)$) as well as the saturation index of the possible Cu solids ($Cu(OH)_2(s)$, Tenorite). The adsorption of Cu onto HA-magnNPs and PC-magnNPs was not modeled because Visual Minteq3.1 considers HA and PC as additional ligands instead of surface materials.

III.3. Results and discussion

III.3.1. What are the impacts of magnNP modifications?

As determined from the HR-TEM analyses, magnNPs, HA-magnNPs and PC-magnNPs were all essentially spherical in shape and had a mean diameter close to 7± 2 nm. Neither the HA nor PC coatings induced any significant size change, indicating that the modification was somewhat localized at the surface of the IONPs [46-48]. The surface chemical modifications induced by the two organic coatings were investigated using ATR-FTIR spectroscopy. The IR spectra and detailed absorption bands are presented in **Fig.2**. According to the obtained IR spectra, HA provided primarily carboxylic functional groups, whereas PC implied that the phosphate groups were anchored onto the surface of magnNPs. These surface chemical modifications also likely lowered the pHzpc of pristine magnetite because of these acidic oxygen-containing functional groups. Thus, HA has been reported to decrease magnetite pHzpc to pH = 2.3 [31].

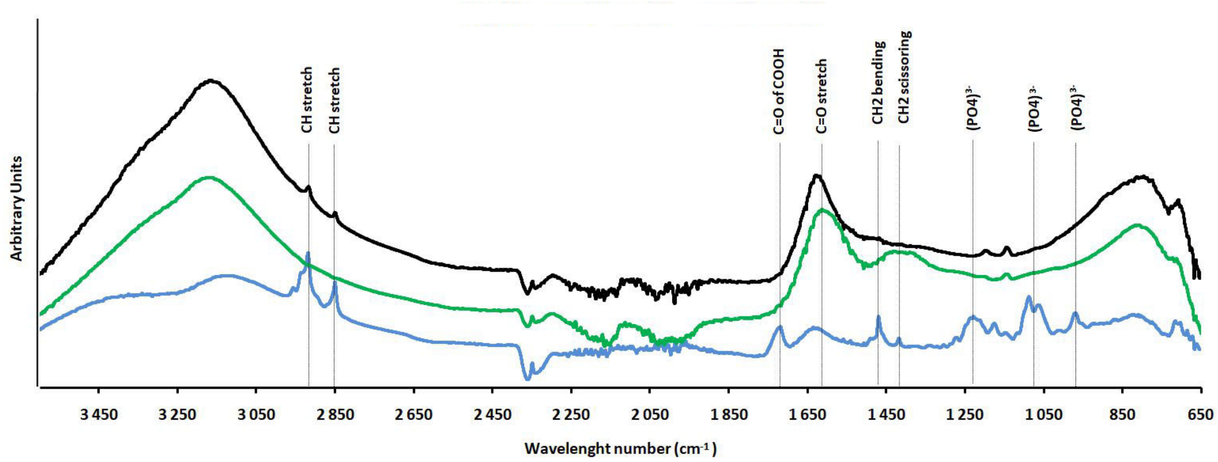

Figure 2: ATR-FTIR spectra of bare magnNPs (black), HA-magnNPs (green) and PC-magnNPs (blue) in the range 780-3600 cm^{-1} obtained from 0.5 g L^{-1} NP suspensions at pH= 6 and ionic strength (IS) = 0.005M NaCl. Large vibration bands recorded at approximately 3150 cm^{-1} refer to hydroxyl groups from H_2O.

The transformation of magnNPs into maghNPs did not show any change in either shape or size **(Table 1)**. The average diameter of the maghNPs was close to 7 ± 2 nm, as determined from the HR-TEM images. The BET measurements highlighted a change in the surface area of magnNPs, which increased from 115 ± 4 m^2 g^{-1} before oxidation to 130 ± 4 m^2 g^{-1} after oxidation (maghNPs). This increase in the surface area has already been observed from magnetite oxidation and it may influence TE interactions as it likely provided increased surface contact for the TEs to bind with the IONPs [49]. It has been demonstrated that maghemite has a disordered crystal structure in which vacancies could favor cation scavenging. As magnetite is very unstable and oxidizes rapidly, it was expected that the surface of magnNPs would be similar to that of maghemite, in response to surface passivation [49, 35]. The transformation of magnNPs into maghNPs was thoroughly described (oxidation kinetics) in a previous study [36] and this experiment was used to characterize magnNP stoichiometry. Hence, in this study, we determined that the starting Fe(II)/Fe(III) ratio of magnNPs is equal to 0.33. The Fe(II)/Fe(III) ratio is also worth considering as it has an influence on the interactions with the surrounding dissolved species, as Fe(II) likely facilitates the transfer of electrons [50].

Table 1: Properties resulting from magnetite oxidation into maghemite NPs.

	IONPs FeII/FeIII ratio	TEM (nm)	BET(m^2 g^{-1})	pHzpc
Magnetite	0.33	7 ± 2	115 ± 4	6.3
Maghemite	0	7 ± 2	130 ± 4	7[51]

III.3.2. Cu adsorption onto IONPs

III.3.2.1. Adsorption isotherms

The Freundlich adsorption isotherm model was used to investigate Cu adsorption onto magnNPs, HA-magnNPs, PC-magnNPs and maghNPs. The calculated linear regression coefficients (R^2) for the logarithmic plots displayed in **Table 2** are higher than 0.95 suggesting a strong linear relationship between log Q_e and log C_e (SI). The obtained K_F and n values are comparable to the Freundlich parameters reported in previous studies [52, 53]. The K_F data highlight the highest affinity of Cu to HA-magnNPs (in the following order of affinity: HA-magnNPs >> maghNPs> PC-magnNPs = magnNPs). The values decreased in the range usually reported for the adsorption of trace metals onto nanomaterials in solution [54]. For the n parameter, the values lie between 1 and 10, indicating a favorable and specific adsorption (chemisorption) of Cu to the IONPs. The isotherm for HA-magnNPs displays the highest n value. As the isotherm is highly deviated from n=1 (**Fig. 3**), there is a high heterogeneity in the process of Cu sorption to HA-magnNPs [55, 56]. Metals, including Fe and Cu, can be held by very strong binding sites on humic substances. It was reported [57] that the sorption between HA and metals could occur through the formation of multidendate complexes with either the carboxylic and phenolic groups of HA or through specific binding between metals and the N and S groups of HA. Therefore, the heterogeneous adsorption between HA-magnNPs and Cu can be explained by both the diversity of the binding sites provided by HA and the formation of multidendate complexes between Cu and some HA functional groups.

Table 2: Freundlich parameters from Cu(II) adsorption isotherms for magnNPs, HA-magnNPs, PC-magnNPs and maghNPs.

	R^2	n	K_F
magnNPs	0.98	1.72	12.62
PC-magnNPs	0.99	1.44	12.64
HA-magnNPs	0.97	2.01	130.32
maghNPs	0.98	1.8	13.37

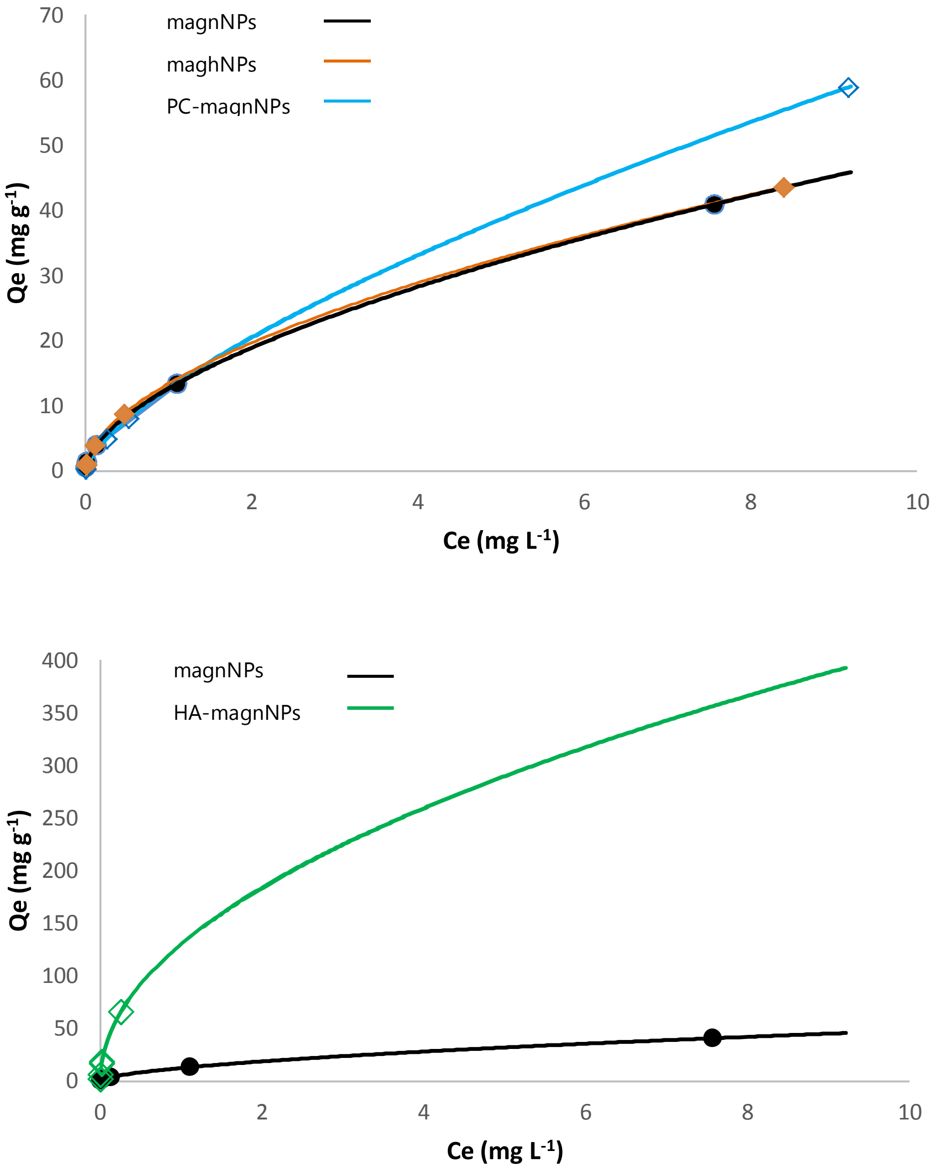

Figure 3: Adsorption isothermsfor (a.) magnNPs, maghNPs and PC-magnNPsand for (b.) HA-magnNPs and magnNPs. The experimental data are represented by dots while the solid lines indicate calculated data. The calculated isotherms were plotted using the Freundlich equation (3) with the calculated parameters (K_F, n) obtained after linearization.

III.3.2.2. pH-adsorption edges

For bare magnNPs, the adsorbed Cu% increased with the increasing pH **(Fig. 4)**. In compliance with the measured pHzpc (determined by potentiometric titration, pHzpc = 6.3), the adsorbed Cu% values at pH > pHzpc (at pH 6 and 7) were high - almost 100% - compared to the weak adsorbed Cu% at acidic pH values (pH 3 and 4). At pH > pHzpc, the IONP surfaces became negatively charged resulting from deprotonation reactions. The decreasing protons concentration at magnetite surface favors cation attraction and allows Cu^{2+} to complex onto the FeO^- surface sites [58, 59].

The results for PC-magnNPs showed that Cu adsorption started frompH = 4 (4% Cu adsorbed). The percentage ofadsorbed Cu reached 100 at pH = 6, similar to that of bare magnNPs. The pH-dependency of Cu adsorption onto PC-magnNPs may have been influenced by the zwitterionic head group in PC (containing a positively charged trimethylethanolammonium group and a negatively charged glycerophosphate group), which likely created a dipole, impacted the surface hydration of the NPs and thus the interaction with Cu [60]. In addition, Cu could coordinate with the oxygen in the carbonyl group deeper in the bilayer. For instance, it has been reported that Zn^{2+} was covalently bound to the electronegative oxygen in the carbonyl group of a lipid membrane [61]. Furthermore, cation binding is expected to occur more or less close to the phosphate group (or to the glycerol group) possibly depending on the size of the ion. Divalent Ca^{2+} was found to coordinate and bind electrostatically with oxygen molecules on four adjacent lipid molecules, while Mg^{2+} bound closer to the phosphate group and coordinated with wateroxygens [62]. Thus, the PC coating does not necessarily represent a barrier to metals and therefore Cu could bind to some of the PC functional groups. Nevertheless, it is still difficult to specify the interaction between Cu and PC-magnNPs as it is not known whether PC encapsulated the whole surface of magnNPs or if it formed patchy coatings around the magnNPs (leaving some of the magnNP surfaces lipid-free).

Cu adsorbed (%) on magnNPs coated with HA increased with the increasing pH. The HA pHzpc is close to pH = 2.3 [31], therefore Cu^{2+} is more adsorbed onto HA-magnNPs when the pH increases (the surface of HA-magnNPs becomes negatively charged thereby promoting cation attraction). Furthermore, the percentage of adsorbed Cu to HA-magnNPs was high even at acidic pH **(Fig.1).** The high removal capacity of HA-magnNPs suggests that HA provided a high density of deprotonated sites. The large number of ionizable functional groups in HA (mainly phenolic and carboxylic groups), allows the formation of stable complexes and chelates with heavy metals [63; 55]. The adsorption induced by HA to HA-magnNPs supports the occurrence of strong complexes, with a covalent character, thatcannot be easily dissociated and are stable in terms of proton exchanges. Several studies have highlighted that most Cu species were bound to HA by forming inner-sphere complexes with HA acidic functional groups although binding through hydrated outer-sphere surface complexes is also expected [64, 65, 56].

Copper adsorption onto maghNPs is quite similar to that of magnNPs, with Cu adsorption increasingwith the increasing pH. Therefore, magnetite and maghemite displayed similar surface properties and only the oxidized surface of magnetite is expected to be involved in Cu adsorption. Magnetite stoichiometry is likely not a key parameter in the adsorption capacity of IONPs. In addition, since no improvements in Cu sorption onto maghemite were observed, the surface area increase observed after oxidation did not enhance the adsorption of Cu although the density of the surface sites was expected to increase. To address this issue, Jarbling et al. [66] proposed that the increased surface area was related to the microporous surface structure of maghemite, which includes non-active surface sites. Therefore, Cu adsorption would not be restricted to the surface area measured by the BET analyses alone. The specific reactive surface sites and the net transport of aqueous ions to IONP surfaces should be considered further.

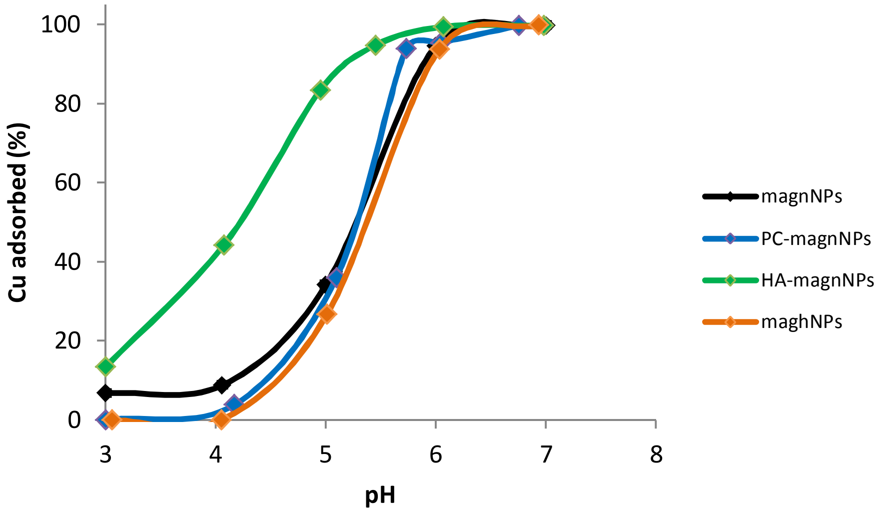

Figure 4: Percentages of adsorbed Cu (%) versus pH on the four IONPs (magnNPs, maghNPs, PC-magnNPs and HA-magnNPs), starting with the same initial Cu concentration (Cu = 0.05 mM) and ionic strength= 5 10^{-3} M NaCl. The error bars (from the experiments performed intriplicate) are within the markers.

III.3.2.3. Cu speciation

The parameters used to yield the Cu speciation models for magnNPs were mainly recovered from our experimental data. The surface area was 115 m^2 g^{-1} (although as we used the BET data, this may be underestimated due to the aggregation and singular behavior of magnNPs as the measurement was made on its dry powder). From the potentiometric titration experiment conducted at NaCl = 0.005M, we calculated pKa1=5.08 and pKa2=-8.7. The surface site density was estimated from the literature, considering magnetite nanoparticles with similar properties as those used in this study (Ns=3.8 sites per nm²) [67]. The stability constant was estimated with Cu at logK= 0.9. For the maghNPs, the surface area was $130 m^2 g^{-1}$ (BET), pKa1=5.4 and pKa2=-9.3, and Ns= 3.8 sites per nm^{-2}. Cu speciation was studied relative tothe pH.For magnNPs, three Cu concentrations were tested (Cu = 0.05 mM, Cu=0.1 mM and Cu = 0.5 mM). For the lowest Cu concentration (Cu = 0.05 mM), dissolved Cu^{2+} was the predominant species up to pH = 5. Beyond this pH, most of the Cu was bound to the surface of the IONPs **(Fig.5)** while most dissolved Cu species occurred in minor amounts (< 1.10^{-5} mM). When the initial Cu concentration increased up to Cu = 0.5 mM, Cu^{2+} was the dominant species until pH = 6.5. Copper adsorption occurred from pH 4 to 6.5. Cu precipitation was expected as the pH reached 6.5, as observed in previous studies [68-70].

Several conclusions can be drawn from the speciation calculation and the present results:

- the pH edges obtained for magnetite at Cu = 0.05 mM turned out to be consistent with our results showing an increasingadsorbed Cu% with the increasing pH (pH > 4);
- the decreasing adsorbed Cu%, observed with the increasing Cu concentrations, was not related to the precipitation of Cu but rather to the surface site saturation.
- no Cu precipitation was expected for Cu = 0.05 mM, whereas the increasing Cu concentration up to Cu = 0.5 mM induced saturation and precipitation at pH values above 6.5;
- the models displayed a high level of consistency with our experimental results and therefore the use of the DLM (diffuse layer surface complexation model), along with the characteristics of the IONPs, could be used to predict Cu dynamics in the presence of IONPs.

(a)

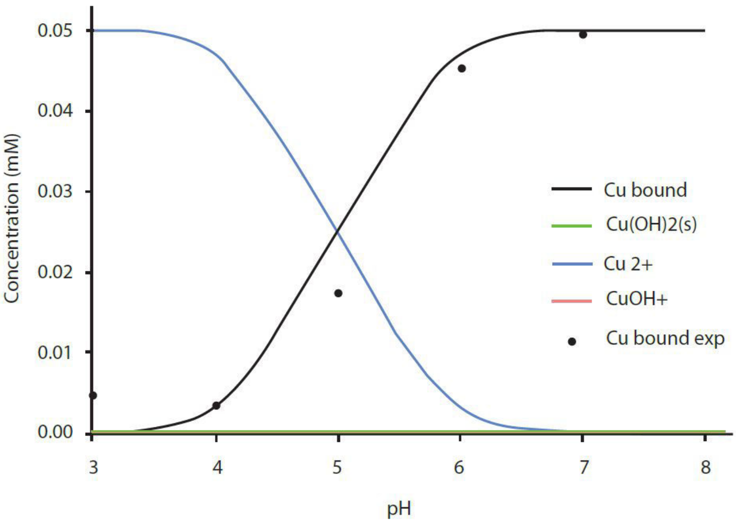
Concentration (mM)
0.05
0.04
0.03
0.02
0.01
0.00
3
4
5
6
7
8
pH
Cu bound
Cu(OH)2(s)
Cu 2+
CuOH+
Cu bound exp

(b)

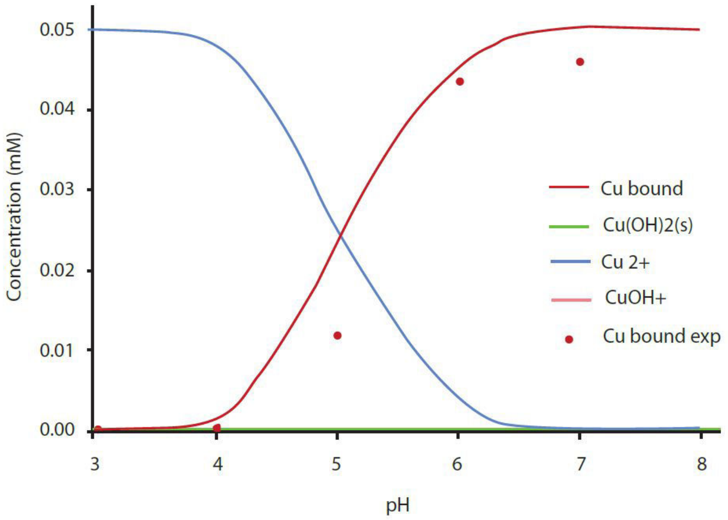
Concentration (mM)
0.05
0.04
0.03
0.02
0.01
0.00
3
4
5
6
7
8
pH
Cu bound
Cu(OH)2(s)
Cu 2+
CuOH+
Cu bound exp

(c)

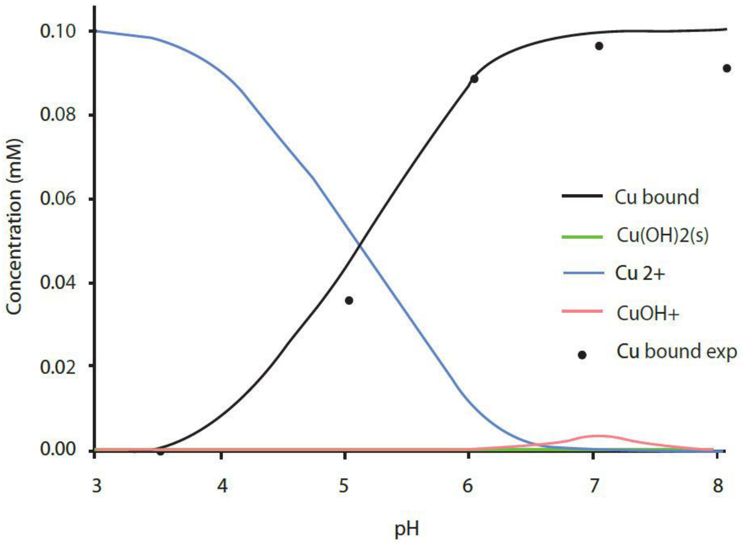
Concentration (mM)
0.10
0.08
0.06
0.04
0.02
0.00
3
4
5
6
7
8
pH
Cu bound
Cu(OH)2(s)
Cu 2+
CuOH+
Cu bound exp

(d)

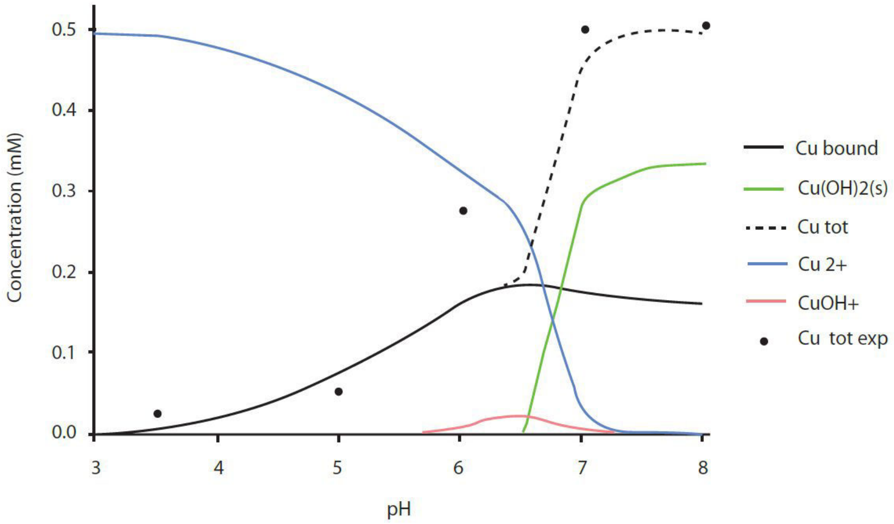

Figure 5: Speciation of Cu with 0.5 g L^{-1} IONPs at a temperature = 25°C and ionic strength = 0.005 mM NaCl.The Cu concentrationsof the different species were calculatedusing Visual Minteq3.1 (solid lines) and determined from our experimental data for(a) 0.05mM Cu and 0.5 g L^{-1} magnNPs, (b) 0.05mM Cu and 0.5 g L^{-1} maghNPs, (c) 0.1 mM Cu and 0.5 g L^{-1} magnNPs and (d) 0.5 mM Cu and 0.5 g L^{-1} magnNPs.The black lines, referred to as “Cu bound”,denotethe Cu concentrations adsorbed onto magnNPs and the blackdots, called “exp data”, refer to the amounts of Cu adsorbed onto magnNPs from our experimental data (Cu >2KDa = adsorbed and/or precipitated Cu species).

III.3.3. Further implications

III.3.3.1. Chemical stability

The increased Fe concentrations (dissolved Fe measurements) highlighted the preferential dissolution of IONPs at acidic pH **(Table 3).** Dissolved Fe accounted for 1.5% of the total Fe content in magnNPs at pH = 3 and decreased to 0.4% when the pH increased to pH = 4. These values appeared to be consistent with the previously reported dissolved Fe concentrations in similar experimental conditions [71]. MaghNPs displayed a lower amount of released Fe than magnNPs, from 0.43% at pH = 3 to 0.09% at pH = 4. The decrease in released Fe between magnNPs and maghNPs stemmed from the different compositions of both Fe oxides. Stoichiometric magnetite (Fe_3O_4), with eight Fe(III) in tetrahedral sites and eight Fe(II) + eight Fe(III) in the octahedral sites, contains Fe(II) in its structure, a much more soluble species, while maghemite only contains Fe(III) [72, 73]. Magnetite was therefore prone to higher leaching than maghemite. The dissolved Fe concentrations were negligible for PC-magnNPs and HA-magnNPs at acidic pH (< 0.002% for PC-magnNPs and < 0.001% for HA-magnNPs) indicating that dissolution was almost ineffective at these pH values. From these observations, we inferred that PC and HA yield comparable protecting effects against

IONP dissolution, probably related to the presence of an efficient barrier at the surface of magnNPs [74]. Furthermore, another possibility is that the surface coatings can bind dissolved Fe which would therefore limit the measured total dissolved Fe [75].

Within a broader context, dissolution can result in the release of metal that can generate either toxic impacts or beneficial effects (nutrient bioavailability) on plants and living organisms [76]. From the nanoparticle perspective, dissolution of the IONPs would result in the formation of NPs with a smaller size and the resulting intrinsic properties would be modified as compared with pristine particles. As a result, this feature impacted their behavior in solution (e.g. the aggregation state or reactivity) [77]. For instance, reduced NP aggregate size, induced by the dissolution of the IONPs, could make it easier for them to be internalized into cells and interact with cellular compounds [78]. Although not yet fully understood, these issues appeared critical with respect to the fate and behavior of the TEs (mobility, transport, bioavailability and toxicity) and also considering the interactions between the IONPs and their surrounding living environment.

Table 3: Fe (mgL^{-1}) released from magnNPs, maghNPs, PC-magnNPs and HA-magnNPs relative to the pH. The experiment was conducted at 0.5g L^{-1} IONPs suspension and with an ionic strength of 5.10^{-3} M NaCl. Values below the limit of quantification for Fe (0.12 µg L^{-1}) were denoted <LQ.

pH	MagnNPs	MaghNPs	PC-magnNPs	HA-magnNPs
3	5. 228	1.634	0.009	0.006
4	1.344	0.325	0.001	<LQ
5	0.005	<LQ	<LQ	<LQ
6	<LQ	<LQ	<LQ	<LQ
7	<LQ	<LQ	<LQ	<LQ

III.3.3.2. Is there any link between IONP colloidal stability and Cu adsorption?

In a previous work [50], we showed that IONPs colloidal stability was dependent upon the surface properties of the IONPs. More precisely, we inferred that, in addition to pH, the surface area and surface chemistry (HA and PC coatings) turned out to be key drivers in controlling the aggregation of IONPs, resulting mainly from electrostatic and combined electrosteric interactions. The observations of Cu adsorption onto IONPs showed that adsorption was likely dependent upon the available active sites for Cu. The distribution, densityand surface binding geometries may vary with the morphology of the aggregates [79]. Therefore, the aggregation of IONPs was expected to control Cu adsorption. Nevertheless, although adsorption experiments showed that increasing pH lead to increasing Cu adsorption, the aggregation study highlighted that larger magnNP aggregates were formed. Hence, instead of diminishing the available reactive surface, aggregation did not prevent Cu from being adsorbed onto those bigger particles. We hypothesized that the aggregation of IONPs would instead remain on weak attraction forces and result in the formation of loosely packed aggregates.

Although no direct link was established considering the impact of IONPs colloidal behavior on Cu adsorption capacity, IONP colloidal stability may still have an impact on Cu dynamics. It was stated that less aggregation yields lower rates of sedimentation and increased mobility [80]. Consequently, rather than being involved directly within the adsorption step, IONPs colloidal stability could play a key role in Cu transport, mobility, bioavailability and toxicity [81]. Furthermore, it would also be interesting to examine the impact of cation adsorption onto IONPs colloidal stability as Cu adsorption is expected to modify the bulk charge of adsorbed particles and the ensuing interparticle interactions.

III.4.Conclusion

IONPs, which either result from magnetite oxidation or stem from HA and PC natural organic coatings, can undergo many changes in natural waters and soils. In this study, we provided evidence that surface coatings with natural organic constituents (such as HA and PC) primarily modified the surface chemistry, including the pHzpc of magnNPs. Maghemite formed from magnetite oxidation also induced a change in pHzpc in addition to increasing the surface area of magnNPs. These changes appeared relevant for Cu adsorption onto IONPs since Cu-IONP interactions remained primarily on protonation/deprotonation reactions at the hydrated interface of the IONPs. These interactions notably accounted for the high pH-dependency observed for Cu adsorption onto IONPs. Bare and modified IONPs adsorption behaviors were consistent with the Freundlich isotherm which accounted for a heterogeneous multilayered binding model for metal adsorption. Comparing the adsorption capacity of the IONPs, HA-magnNPs displayed a higher proportion of adsorbed Cu (%) over a wide pH range even at acidic pH. The structural and chemical diversity of HA, providing a large amount of hydrophobic and heteroaliphatic functional groups, likely favoredthe formation of surface complexes at the surface of HA-magnNPs. Contrary to HA-coating, PC-coating did not favor Cu adsorption onto magnNPs, especially at acidic pH where most Cu(II) remained in solution. In addition to metal binding interactions, HA and PC surface coatings prevented

Fe release from the surface of magnNPs, particularly at low pH (pH = 3 and pH = 4) where dissolution was favored. The impact of oxidation onto magnNPs provided also evidence that Fe(II)/Fe(III) did not impact Cu adsorption. Magnetite and maghemite nanoparticles displayed similar adsorption behaviors. As a result, it was emphasized that Cu adsorption was mainly dependent upon IONPs interfacial properties. Furthermore, maghNPs were less affected by dissolution than magnNPs, thereby suggesting that Fe(II) is likely the preferred dissolved Fe species. Colloidal stability was also discussed as being possibly involved in driving Cu adsorption although no direct relationship was established. It was instead proposed that the aggregation state would be secondarily involved in determining the fate and behavior of the TEs adsorbed to IONPs by impacting IONPs/TE mobility and TE solubility. This study could therefore have strong implications at a large scale, investigating the fate and behavior of IONPs in the environment (mobility, biodegradability and toxicity).

Acknowledgments

We are highly thankful to A. Beauvois for his kind help to perform potentiometric titrations. R.Marsac is also gratefully acknowledged for the thorough advice he gave to build the models. This study was funded by both the CNRS-INSU/INEE EC2CO and the Interdisciplinary Mission programs through the 'NanoOrgaTraces' and 'ALIEN' projects, awarded to M. Pédrot and the University of Rennes1, respectively, through the "DéfisScientifiquesEmergents" program awarded to A. Dia. Dr S. Mullin is acknowledged for post-editing the English style (http://www.proz.com/profile/677614).

References

[1] A. K. Gupta, M. Gupta, Synthesis and surface engineering of iron oxide nanoparticles for biomedical applications, Biomaterials 26 (2005) 3995-4021.

[2] S. Laurent, J.-L. Bridot, L. Vander Elst, R. N. Muller, Magnetic iron oxide nanoparticle for biomedical applications, Future Medicinal Chemistry 2(3) (2010) 427-449.

[3] W. H. Suh., K. S. Suslick, G. D. Stucky, Y.-H.Suh, Nanotechnology, nanotoxicology and neuroscience, Progress in Neurobiology, 87 (2009) 133-170.

[4] R. Podila, J. M. Brown, Toxicity of engineered nanomaterials: a physicochemical perspective, Journal of Biochemical and Molecular Toxicology 27(1) (2013) 50-55.

[5] V. Valdiglesias, N. Fernandez-Bertolez, G. Kiliç, C. Costa, S. Costa, S. Fraga, M. J. Bessa, E. Pasaro, J. P. Texeira, B. Laffon, Are iron oxide nanoparticles safe? Current knowledge and future perspectives, Journal of Trace Elements in Medicine and Biology 38 (2016) 53-63.

[6] W. Wu, Z. Wu, T. Yu, C. Jiang, W-S. Kim, Recent progress on magnetic iron oxide nanoparticles: synthesis, surface functional strategies and biomedical applications, Science and Technology of Advanced Materials 16 (2015) 023501 - 023544.

[7] J. Lodhia, G. Mandarano, N. J. Ferris, P. Eu, S. F. Cowell, Development and use of iron oxide nanoparticles: Synthesis of iron oxide nanoparticles for MRI, Biomedical Imaging and Intervention Journal 6(2) (2010) e12.**doi: 10.2349/biij.6.2.e12.**

[8] P. Sabbatini, F. Yrazu, F. Rossi, G. Thern, A. Marajofsky, M.M. Fidalgo de Cortalezzi, Fabrication and characterization of iron oxide ceramic membranes for arsenic removal, Wat. Res. 44 (2010) 5702-5712.

[9] L. R. Khot, S. Sankaran, J. M. Maja, R. Ehsani, E. W. Schuster, Applications of nanomaterials in agricultural production and crop protection: a review, Crop Protection 35 (2012) 64-70.

[10] R. M. Cornell, U. Schwertmann, The iron oxides: structure, properties, reactions, occurrences and uses, Second edition, *http://trove.nla.gov.au/version/36973177*, Wiley-VCH, 2003.

[11] M. Amde, J.-F. Liu, Z.-O. Tan, D. Bekana, Transformation and bioavailability of metal oxide nanoparticles in aquatic and terrestrial environments, A review, Environ. Poll. 230 (2017) 250-267.

[12] S. C. N. Tang, I. M. C. Lo, Magnetic nanoparticles: Essential factors for sustainable environmental applications,Wat. Res. 47 (2013) 2613-2632.

[13] S. C. Löhr, D. T. Murphy, L. D. Nothdurft, R. Bohlar, S. Piazolo, C. Siegel,Maghemite soil nodules reveal the impact of fire on mineralogical and geochemical differentiation at the Earth's surface, Geochim. Cosmochim. Acta 200 (2017) 25-41.

[14] B. Nowack, T. D. Bucheli, Occurrence, behavior and effects of nanoparticles in the environment, Environ. Poll.150 (2007) 5-22.

[15] R. D. Handy, F. von der Kammer, J. R. Lead, M. Hassellöv, R. Owen, M. Crane, The ecotoxicology and chemistry of manufactured nanoparticles, Ecotoxicology 17 (2008) 287-314.

[16] S. Wagner, A. Gondikas, E. Neubauer, T. Hofman, F. von der Kammer,Spot the Difference: Engineered and Natural Nanoparticles in the Environment - Release, Behavior and Fate, Angew. Chem. Int. 53 (2014) 12398-12419.

[17] S. C. Pang, S. F. Chin and M. A. Anderson, Redox equilibria of iron oxides in aqueous-based magnetite dispersions: Effect of pH and redox potential, J. Colloids Interf. Sci. 311 (2007) 94-101.

[18] L. Wang, J. Li, Q. Jiang, L. Zhao,Water-soluble Fe_3O_4 nanoparticles with high solubility for removal of heavy-metal ions from waste water, Dalton Transactions 41 (2012) 4544-4551.

[19] M.A. Ahmed, S.M. Ali, S.I. El-Dek, A. Galal, Magnetite-hematite nanoparticles prepared by green methods for heavy metal removal from water,Material Science and Engineering B 178 (2013) 744-751.

[20] B. Pan, H. Qiu, B. Pan, G. Nie, L. Xiaio, L. Lv, W. Zhang, Q. Zhang, S. Zheng, Highly efficient removal of heavy metals by polymer-supported nanosized hydrated Fe(III) oxides: behavior and XPS study,Wat. Res. 44 (2010) 815-824.

[21] J. Hu, G. Chen, I. M. C. Lo, Selective removal of heavy metals from industrial wastewater using maghemite nanoparticles: performance and mechanisms,Journal of Environmental Engineering 132 (2006) 709-715.

[22] W. Stumm, Chemistry of the Solid-Water interface. Processes at the Mineral-Water and Particle-Water interface in natural systems, Wiley-VCH,1992.

[23] G. S. Parkinson, Iron oxides surfaces, Surface Science Reports 71(1) (2016) 272-365.

[24] S. H. Joo, D. Zhao, Environmental dynamics of metal oxide nanoparticles in heterogeneous systems: a review,J. Hazard. Mater. 322 (2017) 29-47.

[25] W-W. Tang, G-M. Zeng, J-L. Gong, J. Liang, P. Xu, C. Zhang, B-B. Huang, Impact of Humic/fulvic acid on the removal of heavy metals from aqueous solutions using nanomaterials: A review,Sci. Tot. Environ.468-469 (2014) 1014-1027.

[26] S.Ghosh, W. Jiang, J. D. McClements, B. Xing, Colloidal Stability of Magnetic Iron Oxide nanoparticles: Influence of Natural Organic Matter and Synthetic Polyelectrolytes, Langmuir 27 (2011) 8036-8043.

[27] A. Hadju, E. Illès, E. Tombacz, I. Borbath, Surface charging, polyanionic coating and colloid stability of magnetite nanoparticles,Colloids and Surfaces A: Physicochemical Engineering Aspects 347 (2009) 104-108.

[28] R. Grillo, A. H. Rosa, L. F. Fraceto, Engineered nanoparticles and organic matter: A review of the state-of-the-art, Chemosphere 119 (2015) 608-619.

[29] E. Tombacz, I. Y. Toth, D. Nesztor, E. Illés, A. Hadju, M. Szekeres, L. Vékas, Adsorption of organics on magnetite nanoparticles, pH dependent stability and salt tolerance, Colloids and Surfaces A: Physicochemical and Engineering Aspects 435 (2013) 91-96.

[30] A. M. Vindedahl, J. H. Strehlau, W. A. Arnold, R. L. Penn, Organic matter and iron oxide nanoparticles: aggregation, interactions and reactivity,Environmental Science: Nano, Critical Review 3 (2016) 494-505.

[31] J.-F. Liu, Z.-S.Zhao, G.-B.Jiang, Coating Fe_3O_4 nanoparticles with humic acid for high efficient removal of heavy metals in water, Environ. Sci. Technol. 42 (2008) 6949-6954.

[32] S. Yu, J. Liu, M. Y. Yin, M. Shen, Interactions between engineered nanoparticles and dissolved organic matter: A review on mechanisms and environmental effects, Journal of Environmental Sciences 63 (2018) 198-217.

[33] W. J. Mulder, G. J. Strijkers, G. A. F. van Tilborg, A. W. Griffioen, K. Nicolay, Lipid-based nanoparticles for contrast-enhanced MRI and molecular imaging, NMR Biomed. 19 (2006) 142-164.

[34] C. Solis-Calero, J. Ortega-Castro, J. Frau, F. Munoz,Non-enzymatic reactions above phospholipid surfaces of biological membranes: reactivity of phospholipids and their oxidation derivatives, Oxidative Medicine and Cellular Longevity 15 (2015) 1-22.

[35] Frison, G. Cernuto, A. Cervellino, O. Zaaharko, G. M. Colonna, A. Guagliardi, N. Masciocchi, Magnetite-Maghemite Nanoparticles in the 5-15 nm range: correlating the core-shell composition and surface structure to the magnetic properties. A total scattering study, Chemistry of Materials 25 (2013) 4820-4828.

[36] E. Demangeat, M. Pédrot, A. Dia, M. Bouhnik-le-Coz, F. Grasset, K. Hanna, M. Kamagaté, F. Cabello-Hurtado, Colloidal and Chemical stabilities of iron oxide nanoparticles in aqueous solutions: the interplay of structural, chemical and environmental drivers, Environmental Science: Nano 5 (2018) 992-1001.

[37] J.Hu, G. Chen, I. M. C. Lo, Removal and recovery of Cr(VI) from wastewater by maghemite nanoparticles,Wat. Res. 39 (2005) 4528-4536.

[38] G. R. Aiken, H. Hsu-Kim, J. N. Ryan, Influence of Dissolved Organic Matter on the environmental Fate of Metals, Nanoparticles, and Colloids, Environ. Sci. Technol. 45 (2011) 3196-3201.

[39] E. Navarro, A. Baun, R. Behra. N. B. Hartmann, J. Filser, A-J. Miao, A. Quigg, P. H. Santschi, L. Sigg,Environmental behavior and ecotoxicity of engineered nanoparticles to algae, plants, and fungi,Ecotoxicology 17 (2008) 372-386.

[40] L. Goswani, K-H. Kim, A. Deep, P. Das, S. S. Bhattacharya, S. Kumar, A. A. Adelodun, Engineered nanoparticles: Nature, behavior, and effect on the environment,Journal of Environmental Management 196 (2017) 297-315.

[41] S. E. Khalafalla, G. W. Reimers, Preparation of dilution-stable aqueous magnetic fluids, IEEE Transactions on Magnetics 16(2) (1980) 178-183.

[42] R. Massart, Preparation of aqueous magnetic liquids in alkaline and acidic media,IEEE Transactions on Magnetics 17 (1981) 1247-1248.

[43] Z. B. Anna, B. Paricja, J. Petr, E. Petrovsky, B. Pavel, H. Daniel,Magnetoconductive maghemite core/polyaniline shell nanoparticles: Physicochemical and biological assessment, Colloids and Surfaces B: Biointerfaces (2016).

[44] D. Yeghicheyan, C. Bossy, M. Bouhnik Le Coz, C. Douchet, G. Granier, A. Heimburger, F. Lacan, A. Lanzanova, T. C. C. Rousseau, J.L. Seidel, M. Tharaud, F. Candaudap, J. Chmeleff, C. Cloquet, S. Delpoux, M. Labatut, R. Losno, C. Pradoux Y. Sivry, J. E. Sonke,Geostandards and Geoanalytical Research 37(4) (2013) 449-467.

[45] L. Sigg, P. Behra, W. Stumm, Aquatic chemistry, 5th edition, 2011.

[46] S. Koesnarpadi, S. J. Santosa, D. Siswanta, B. Rusdiarso, Synthesis and characterization of magnetite nanoparticles coated humic acid (Fe_3O_4/HA), Procedia Environ. Sci. 30 (2015) 103-108.

[47] M. Meng, C. Shibao, Removal of Cd, Pb and Cu from Water Using Thiol and Humic Acid Functionalized Fe_2O_3 Nanoparticles, Advanced Materials Research 518-523 (2012) 1956-1963.

[48] L. P. Lingamdinne, Y.-Y.Chang, J.-K.Yang, J. Singh, E.-H. Choi, M. Shiratani, J. R. Koduru, P. Attri, Biogenic reductive preparation of magnetic inverse spinel iron oxide nanoparticles for the adsorption removal of heavy metals,Chemical Engineering Journal 307 (2017) 74-84.

[49] C. A. Gorski J. T. Nurmi, P. G. Tartneyk, T. B. Hofstetter, M. M. Sherer, Redox behaviour of magnetite: implications for contaminant reduction, Environ. Sci. Technol. 44 (2010) 55-60.

[50] M. Auffan, W. Achouak, J. Rose, M.- A. Roncato, C. Chanéac, D. T. Waite, A. Masion, J. C. Woisik, M. R. Wiesner, J.-Y. Bottero, Relation between the redox state of iron-based nanoparticles and their cytotoxicity toward Escherichia coli,Environ. Sci.Technol. 42 (2008) 6730-6735.

[51] L. Vayssieres, On the effect of Nanoparticle Size on Water-Oxide Interfacial Chemistry, The Journal of Physical Chemistry Letters C 113 (2009) 4733-4736.

[52] B. Kakavandi, R. R. Kalantary, Ahmad J. Jafari, S. Nasseri, A. Ameri, A. Esrafili, A. Azari, Pb(II) Adsorption Onto a Magnetic Composite of Activated Carbon and Superparamagnetic Fe_3O_4 Nanoparticles: Experimental and Modeling Study,CLEAN– Soil, Air, Water 43 (8) (2015) 1157-1166.

[53] H. Karami, Heavy metal removal from water by magnetite nanorods, Chemical Engineering Journal 219 (2013) 209-216.

[54] L. L. Vatta, R. D. Sanderson, K. R. Koch, Magnetic nanoparticles: properties and potential applications,Pure Applied Chemistry 78 (2006) 1793-1801.

[55] I. Kostic, T. Andelkovic, R. Nikolic, A. Bojic, M. Purenovic, S. Blagojevic, D. Andelkovic, Copper(II) and lead (II) complexation by humic acid and humic-like ligands, Journal of the Serbian Chemical Society 76 (9) (2011) 1325-1336.

[56] C.-L Li, F. Ji, S. Wang, J-J. Zhang, Q. Gao, J-G. Wu, L-P. Zhao, L-C. Wang, L-R. Zheng, Adsorption of Cu(II) on humic acids derived from different organic materials,Journal of Integrative Agriculture 14(1) (2015) 168-177.

[57] E. Tipping, Cation binding to humic substances, Cambridge University Press,2002.

[58] A. S. Madden, M. F. Hochella Jr, T. P. Luxon, Insights for size-dependent reactivity of hematite nanomineral surfaces through Cu^{2+} sorption, Geochim. Cosmochim. Acta 70 (2006) 4095-4104.

[59] S.-H. Huang, D.-H. Chen, Rapid removal of heavy metal cations and anions from aqueous solutions by an amino-functionalized magnetic-adsorbent, J. Hazard. Mater. 163 (2009) 174-179.

[60] W. Shinoda, Permeability across lipid membranes, Biochim. Biophys. Acta 1858 (2016) 2254-2265.

[61] R. J. Alsop, R. M. Schober, M. C. Rheinstädter, Swelling of phospholipid membranes by divalent metal ions depends on the location of the ions in the bilayers, Soft Matter 12 (2016) 6737-6748.

[62] A. Melcrová, S. Pokorna, S. Pullanchery, M. Kohagen, P. Jurkiewicz, M. Hof, P. Jungwirth, P. S. Cremer, L. Cwiklik,The complex nature of cation interaction with phospholipid bilayers,Scientific Reports 38035 (6) (2016) 1-12.

[63] N. Senesi, G. Sposito, J.P. Martin, Copper and iron complexation by soil humic acids: an IR and ESR study, Sci. Tot. Environ. 55 (1986) 351-362.

[64] Z. R. Komy, A. M. Shaker, S. E. M. Heggy, M. E. A. El-Sayed, Kinetic study for copper adsorption onto soil minerals in the absence and presence of humic acid, Chemosphere 99 (2014) 117-124.

[65] A. Otero-Farina, R. Gago, J. Antelo, S. Fiol, F. Arce, Surface complexation modelling of Arsenic and Copper Immobilization by Iron oxide precipitates derived from Acid Mine Drainage, Boletin de la Sociedad Geologica Mexicana 67 (3) (2015) 493-508.

[66] M. Jarbling, L. Gunneriusson, B. Hussmann, W. Forsling, Surface complex characteristics of synthetic maghemite and hematite in aqueous suspensions, J. Colloid Interf. Sci. 285 (2005) 212-217.

[67] Z. Pan, W. Li, J. D. Fortner, D. E. Giammar,Measurement and surface complexation modeling of U(VI) adsorption to engineered iron oxide nanoparticles, Environ. Sci. Technol. 51 (2017) 9219-9226.

[68] L. Hidmi and M. Edwards, Role of temperature and pH in Cu $(OH)_2$ solubility,Environ. Sci. Technol.33 (15)(1999)2607–2610.

[69] M. Balintova and A. Petrilakova, Study of pH Influence on Selective Precipitation of Heavy Metals from Acid Mine Drainage, Chemical Engineering Transactions 25 (2011) 345-350.

[70] C.Boukhalfa, A. Mennour, L. Reinert, M. Dray, L. Duclaux, Removal of copper from aqueous solution by coprecipitation with Hydrated Iron Oxide, Asian Journal of Chemistry 19 (6) (2007) 4267-4276.

[71] T. Missana, U. Alonso, A. C. Scheinost, N. Granizo, M. Garcia-Gutierrez, Selenite retention by nanocrystalline magnetite: role of adsorption, reduction and dissolution/co-precipitation processes, Geochim. Cosmochim. Acta 73 (2009) 6205-6217.

[72] D. Maity, D. C. Agrawal, Synthesis of iron oxide nanoparticles under oxidizing environment and their stabilization in aqueous and non-aqueous media, Journal of Magnetism and Magnetic Materials, 308 (2007) 46-55.

[73] R. Jolstera, L. Gunneriusson, A. Holmgren, Surface complexation modeling of Fe_3O_4–H^+ and magnesium (II) sorption onto maghemite and magnetite, J. Colloids Interf. Sci. 386 (2012) 260-267.

[74] A-H. Lu, E. L. Salabas, F. Schuth,Magnetic Nanoparticles: Synthesis, Protection, Functionalization, and Application,Angew. Chem. Int. Ed., 46 (2007) 1222 -1244.

[75] C. Catrouillet, M. Davranche, A. Dia, M. Bouhnik-Le Coz, R. Marsac, O. Pourrret, G. Gruau, Geochemical modeling of Fe(II) binding to humic and fulvic acids, Chem. Geol. 372 (2014) 109-118.

[76] A. Bour, F. Mouchet, J. Silvestre, L. Gauthier, E. Pinelli, Environmentally relevant approaches to assess nanoparticles ecotoxicity: a review, J. Hazard. Mater. 283 (2015) 764-777.

[77] I. A. Mudunkotuwa, V. H. Grassian, The devil is in the details (or the surface): impact of surface structure and surface energetics on understanding the behavior of nanomaterials in the environment, J. Environ. Monitor.13 (2011) 1135-1144.

[78] I. Bhatt, B. N. Tripathi, Interaction of engineered nanoparticles with various components of the environment and possible strategies for their risk assessment,Chemosphere 82 (2011) 308-317.

[79] B. Gilbert, R. K. Ono, K. A. Ching, C. S. Kim, The effects of nanoparticles aggregation processes on aggregates structure and metal uptake, J. CollloidsInterf. Sci., 339 (2009) 285-295.

[80] Y. Ju-Nam, J. R. Lead, Manufactured nanoparticles: An overview of their chemistry, interactions and potential environmental implications, Sci. Tot. Environ. 400 (2008) 396-414.

[81] J. Baumann, J. Köser, D. Arndt, J. Filser, The coating makes the difference: Accute effects of iron oxide nanoparticles on Daphnia magna, Sci. Tot. Environ. 484 (2014) 176-184.

Supporting Information

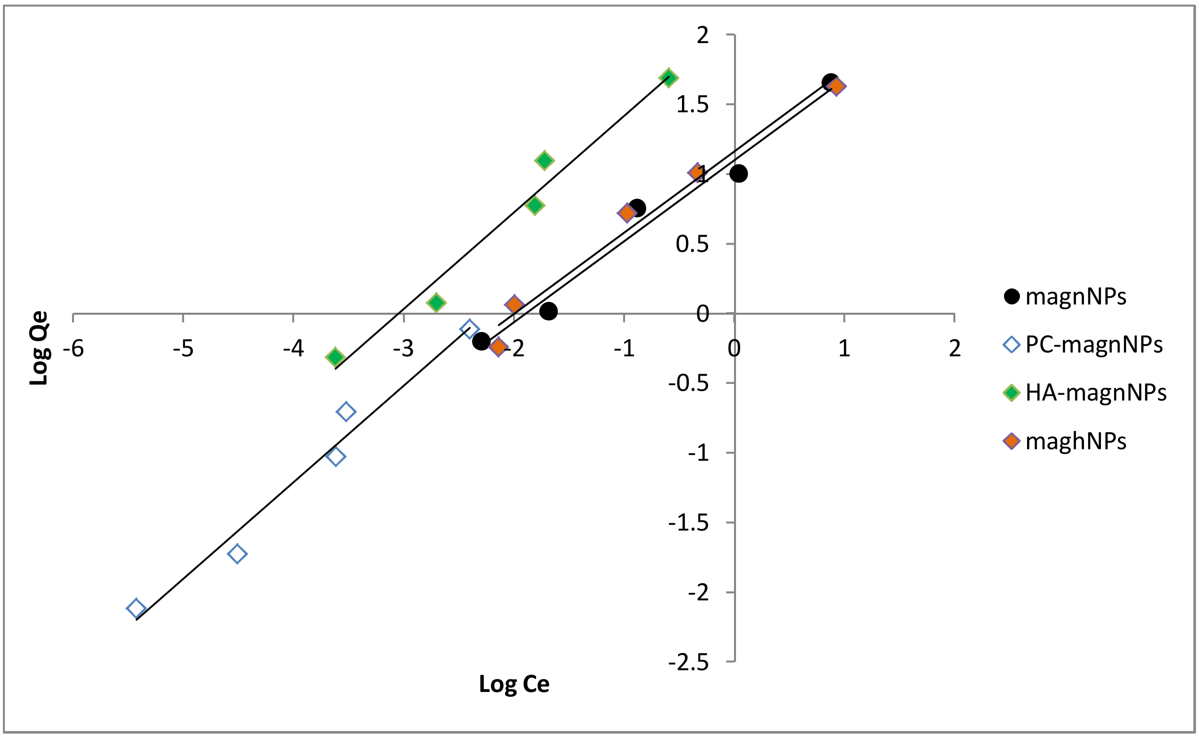

The Freundlich adsorption isotherms of Cu onto the IONPs. The isotherms were carried out at constant pH = 6, with an adsorbent concentration of 0.5 g L^{-1} IONPs.

Chapitre 4 :

Etude des interactions NPs-Fe / plantes : approches géochimiques et biologiques

Magnetite nanoparticles introduction into sunflower plants: Fe-nutrient or toxic compound?

[a] E. Demangeat, [a]M. Pédrot, [a]A. Dia, [a] G. Compaoré,[a] P. Roperch, [a] P. Petitjean, [a]M. Bouhnik-Le-Coz, [a]M. Deneuve, [b]F. Cabello-Hurtado

[a] Univ. Rennes, CNRS, Géosciences Rennes - UMR 6118 - Av. General Leclerc - F-35042 Rennes Cedex, France

[b] Univ. Rennes, CNRS, Ecobio - UMR 6553 - Av. General Leclerc - F-35042 Rennes Cedex, France

Abstract

Iron oxide nanoparticles (IONPs), including magnetite (Fe_3O_4) nanoparticles (magnNPs) have recently been used for agricultural purposes because of their possible biocompatibility and potential beneficial effects on plant growth.

In this work, physiological effects and possible cell internalization of synthesized magnNPs (7 nm) on sunflower (*Helianthus annuus*) germination (7 days) and growth (in both hydroponic conditions and soil columns) were studied. The effects on plants of different magnNPs doses (5 and 1000 or 5000 mg L^{-1}) and their capacity for supplementingiron (Fe) in Fe-deficient cultures were studied in germination and hydroponic experiences. A similar experiment, intended to study the impact of a long-term exposure to magnNPs under hydroponic conditionson plant growth, was also conducted on bean (*Phaseolus vulgaris*). MagnNPs bioavailability and its possible remediation effect in a Cu-polluted soil were eventually investigated in soil column experiments using sunflower (*Helianthus annuus*).

Visualization of root fragments by scanning electron microscopy highlighted that magnNPs deposited at the surface of plant roots by forming aggregates. Magnetic susceptibility measurements performed on roots, stems, leaves and flowers/fruits evidenced that magnNPs were translocated from the roots to the aerial parts of the plants. Much less magnNPs were detected in organs of plants grown in soil columns compared to hydroponically grown plants as it was likely retained in the soil.

MagnNPs neither inhibited the germination of sunflower nor decreased the growth parameters both in hydroponically- and soil- grown plants. Moreover, magnNPs capacity to generate an oxidative stress showed that magnNPs did not provoke any oxidative damage and could protect plants against lipid peroxidation. In the Fe-deficient culture, magnNPs prevented Fe deficiency symptoms at both low and high magnNPs concentrations (5 and 1000 mg L^{-1}). In

Cu-contaminated soils, magnNPs slightly decrease Cu accumulation in the aerial parts of the plants and reduce but did not prevent Cu toxicity, resulting in growth retardation and chlorosis. The presence in excess, of Cu, further decreased magnNPs uptake. These results show that the as-administered magnNPs are not phytotoxic to sunflower, suggesting that they could potentially be useful for agricultural uses, to complement Fe deficiency or to scavenge Cu, although the growth medium should be taken into account to assess the potential effects of magnNPs introduction.

Last, geochemical analyses performed on soil solution leachates evidenced that higher Cu amounts were retained in the soils where magnNPs were present than in Cu-polluted soil without magnNPs. Although in this experience, Cu concentration was likely too high for magnNPs to sequester much Cu, magnNPs ability to retain Cu could show great potential for soil remediation and/ or phytotoxicity applications.

Keywords: magnetite nanoparticles; *Helianthus annuus*; NPs translocation; Fe-deficiency; copper toxicity; soil.

Highlights

- Effects of magnNPs on sunflower growth are dose dependent;
- MagnNPs can prevent sunflower from Fe-deficiency;
- MagnNPs do not provoke any oxidative damage and could protect plants against lipid peroxidation;
- Cu toxicity in sunflower plants was reduced by magnNPs;
- Uptake of magnNPs occurs from roots to shoots and is favored in hydroponic cultures rather than in soils.
- MagnNPs adsorb some of the Cu in the soils thereby reducing Cu uptake.

IV.1. Introduction

Iron oxide nanoparticles (IONPs) are produced from geogenic and biogenic processes, the instigators of their natural distribution over oceans, surface waters, soils and sediments for millions of years (Hochella et al., 2008). The increasing production of engineered IONPs, along with their increasing use, has become an important source of a new material within the environment (Nowack and Bucheli, 2007). The unique properties of IONPs, particularly their high reactivity (high surface to volume ratio), has attracted specific attention for their employment in technologic, medical and environmental fields (Wang et al., 2012; Podilaet al., 2013; Suhet al., 2009), and considerable research is also devoted to understand the interactions between IONPs and their surroundings after their release in the environment (Goswani, 2017; Navarro, 2008; Sharma, 2012). IONPs could represent a threat towards living organisms or lead to unexpected environmental hazards as they are highly reactive and can penetrate cells (Barhoumiand Dewez, 2013; Navarro et al., 2008). Cellular production ofreactive oxygen species (ROS) resulting from nanoparticles'internalization, is a major effect as ROS interact with almost all cellular components producing protein modifications, lipid peroxidation, and damage to DNA (Rastogi et al., 2017).

Direct entry in surface waters, aerial deposition, inputs from spray drift of agrochemicals, utilization of remediation technologies in soils, application of protection products to plants, and excretion of nano-medicines in veterinary products, are some of the many sources that can disperse IONPs amongst water bodies and soils (Batley et al., 2013). IONPs raises particular concerns on the possible impacts resulting from their interaction with plants, especially since plants play a central role within the ecosystems (i.e. trophic chain).In agriculture, smartly designed nanoparticles are already used to raise the crop production, as growth stimulators, nanopesticides, nanofertilizers, soil improving agents, or sensors for monitoring different agricultural parameters in the field (Khot et al., 2012; Kah et al., 2013; Solanki et al., 2015).

Plants are in continuous interaction with air, soil and water, all of which provide routes for IONPs to reach plants. IONPs own properties (size, specific surface area, zeta potential), their concentration, the nature and composition of the medium and some associated environmental physico-chemical factors (temperature, salinity, pH, ionic strength, etc.) are key parameters thatdetermine the fate and behavior of IONPs in the environment (Hiemstra and van Riemsdijk, 2006; Joo and Zhao, 2017). IONPs mobility, their bioavailability and toxicity for plants strongly depend on their own chemical and colloidal stabilities and their reactivity with soil components and microorganisms (Aiken et al., 2011). These properties also drive the composition of the growth medium. For instance, release of metals resulting from engineered nanoparticles (NPs) dissolution has been reported for diverse NPs (Batley et al., 2013; Demangeat et al., 2018).

Effect of different metal and metal oxide NPs on different plants has been observed to be variable and ranged from positive to lethal impacts (Barrena et al., 2009). Most studies evidenced that metal and metal oxides NPs in excess are harmful to plants, whereas, when present in traces some of them could be beneficial for plants. As an example, germination and hydroponic experiments showed that exposure of *Triticum aestivum* to 10nm-sized IONPs (5 to 20 mg L^{-1} Fe_3O_4 NPs), would not alter the germination, plant growth and chlorophyll content of the plants (Iannone et al., 2016). In that study, plants exposed to IONPs showed a favorable response to prevent oxidative damage. Furthermore, another study performed on*Zea mays* using IONPs (maghemite NPs-17.7nm), still showed a positive impact on the germination of the plants using 50 mg L^{-1} IONPs, whereas exposure to 100 mg L^{-1} decreased the germination index (Liet al., 2016).

The entering of NPs in plant tissues still raised several questions, and various mechanisms have been proposed regards to NPs internalization routes (especially, regarding how they can pass cell walls). A recent study revealed that metallic NPs are able to penetrate into plant cells, move through the xylem and the phloem to the aerial parts of vascular plants and accumulate (Tripathi et al., 2017). Zhu et al. (2008) also evidenced the uptake, translocation and accumulation of 20-nm Fe_3O_4NPs in different tissues of pumpkin plants after their absorption from a 500 mg L^{-1} aqueous suspension. Once in the cell, nanoparticles can interfere with electron transport chain of mitochondria and chloroplast, which may results into the oxidative burst, observed by the increase in ROS concentration (Rastogi et al., 2017).

In most natural mediums, Fe bioavailability depends upon the soil properties (redox potential and soil pH) and plant specificities that dictate Fe absorption or alter its metabolic use (Joo and Zhao 2017; Morrissey and Guerinot, 2009). Despite its abundance in the Earth's crust, iron in aerobic soils is found mostly in the form of insoluble Fe^{3+} oxides or hydroxides, which are less available to plants than dissolved Fe^{2+} (Claudio et al., 2017; Marschner et al., 1986). Iron (Fe) deficiency in plants is rather not caused by Fe scarcity in the soil. Under certain conditions, Fe deficiency can occur and lead to leaf chlorosis and inhibited growth (Briat et al., 2007). Iron (Fe) is an essential nutrient for plants, playing important physiological roles as a component of enzyme cofactors that catalyze redox reactions in fundamental metabolic processes (de SouzaPinto et al., 2016). Thus, IONPs introduction to plants has been studied to be used as a nanofertilizer in the context of Fe deficiency as it could provide supplementary iron to plants (Kim et al., 2014). However, the same redox properties that make Fe suitable in many metabolic reactions (for instance, in the cellular electron transfer) or can become toxic when it is present in excess because of ROS overproduction (Salama et al., 2009). The ability of Fe to donate and accept electrons means that Fe can act as pro-oxidant, in the catalysis of free radical generation, such as the generation of $OH^{\cdot}$ radical through Fenton's reaction (Birben et al. 2012; Rout and Sahoo, 2015; Pouran et al., 2012).

IONPs can also impact plant metabolism indirectly. In particular, IONPs can react with dissolved compounds in soilsand soil solution, such as metals, pesticides and other organic wastes, and thus modify the transport, availability and toxicity of these elements.In recent years, Cu pollution in agricultural soils has raised a major concern for sustainable agriculture production, especially in developing countries, resulting from the arbitrary use of pesticides, fungicides, industrial effluents and wastewater irrigation (Adrees et al., 2015).Cu-rich pig and poultry slurries are also important sources of livestock grazing pasture contamination (Legros et al., 2010). In Europe, the application of the Bordeaux mixture has drastically increased the Cu pollution in vineyards soils with Cu concentrations ranging from 200 to 500 mg kg^{-1} soil (Michaud et al., 2007), while in unpolluted soils, Cu concentrations range between 3 and 100 mg kg^{-1} (Marschner, 1995). Although Cu is an essential micronutrient incorporated in many proteins and enzymes of plants, Cu phytotoxicity generally results in growth inhibition (particularly root growth) and leaf chlorosis. Cu toxicity in plants also induces a decreased uptake and accumulation of other mineral nutrients, thus altering important biochemical processes in plants. In particular, Cuwas found to prevent Fe uptake as compared to other nutrients, which highlighted an antagonistic relationship between Fe and Cu. Moreover, the bioavailability of Cu depends upon the total Cu content in soil, soil pH and CEC (Adrees et al., 2015). And much of the Cu present in soils occurs in forms, which are not readily available to plants because of the strong binding of Cu^{2+} by organic matter and other soil colloids (Li et al., 2016). Several studies have evidenced Cu adsorption and affinity for IONPs (Liu et al., 2008) and thus the presence of both compounds could change their mobility and modify the expected phytotoxicity of Cu in a polluted soil.

The environmental interactions between IONPs and plants have been the subject of different researches, with implications for agricultural practices. To exploit the benefits of IONPs as for crop production, issues including IONPs biocompatibility, availability and behavior in the growth medium need answers. In this context, the objectives of this work were to determine the effects of IONPs on the geochemistry of a plant-containing medium and also to define whether IONPs, especially magnetite nanoparticles (magnNPs) had toxic effects on sunflower plants through their entire life cycle in order to thrust aside potential toxic effects on plants and evaluate environmental risks, considering that these nanomaterials could serve as iron source and/or depolluting agents in Cu polluted-soils.

IV.2. Materials and methods

IV.2.1. Nanoparticle synthesis and properties

IV.2.1.1 Synthesis procedure

Magnetite (Fe_3O_4) nanoparticles were prepared according to modified literature procedures (Massart, 1981; Khallafalla and Reimers, 1980) by the anaerobic co-precipitation of Fe salts. Iron chloride, $FeCl_2.4H_2O$ (1.988 g) and $FeCl_3.6H_2O$ (5.406 g), were dissolved in 5 mL HCl (2 M) and 20 mL H_2O and then stirred to obtain an Fe solution at an Fe(II)/Fe(III) molar ratio = 0.5. MagnNPs precipitation was achieved by the dropwise addition of the Fe salt solution into a 0.7 M NaOH-$NaNO_3$ base solution (250 mL). The black precipitate was left to settle under anaerobic condition (Jacomex glovebox) for a few hours to get rid of the supernatant. Three washings were conducted with deoxygenated deionized water and 5 10^{-3} M NaClsolution before storage under anaerobic conditions.

Based on ICP-MS measurements (see Materials and Methods **section4.**), the concentration of Fe_3O_4NPs was calculated to allow further dilutions and reach the expected concentrations accurately. Thus, the magnNPs stock solution allowed for the preparation of diluted magnNPs solutions, using 5 10^{-3} M NaCl, in the concentrations range expected.

IV.2.1.2. Characterization

High Resolution Transmission Electron Microscopy (HR-TEM) was performed with a JEOL2100F (voltage 200 kV). Samples were prepared by drop-casting diluted magnNPs suspensions on 300 mesh Au-grids supported with carbon film. The specific surface area of magnNPs was determined by multipoint N_2-Brunauer Emmett Teller (BET) technique using a Coulter (SA 3100) surface area analyzer.

IV.2.2. Plant growth conditions and treatments

IV.2.2.1. Germination experiments

The experiments were conducted onsunflower (*Helianthus annuus*), bean (*Phaseolus vulgaris*), maize (*Zea mays*) and wheat (*Triticum aestivum*) during 7 days. Data related to bean, maize and wheat germination are displayed in Supporting Information (S.I. A., **Figure S1**). Seeds were sowed under sterile conditions on Petri dishes (90mm diameter, with 6 seeds per Petri dish) on half strength Hoagland's nutrient solution (Hoagland and Arnon, 1950) whether or not containing magnNPs (see below). Before sowing, seeds were surface sterilized with 3% (v/v) sodium hypochlorite (NaOCl) for 3 min and then rinsed 12 min with distilled water for 5 times. They were eventually soaked in distilled water for 45 min in a laminar flow hood. The dishes containing seeds were sealed with parafilmand placed in a growth chamber for germination and growth of the plants at 24 °C and 70% moisturein the dark.

Nutrient solutions were prepared full strength according to the Hoagland solution protocol, which allowed further dilutions with magnNPs stock solutions or0.01 M NaCl to obtain a final half strength (0.5x) Hoagland solution with appropriate magnNPs concentration and NaCl = $5\ 10^{-3}$ M. The pH was adjusted to pH = 5.8 using KOH anhydrous pellets. Hoagland solutions eventually contained 560 ppb Fe (the concentration of the other elements is available in S.I.). When necessary, the same protocol was followed to make a Hoagland solution with no iron (1x) ("Fe-deficient") and eventually reach the 0.5x - Hoagland solution, without iron, after dilution with either magnNPs or NaCl solutions. The solutions were stored in glass bottles and autoclaved for 20 min at 120°C, with bottles of distilled water.

MagnNPs stock solution (2 or 10 g L^{-1}) or 5 mM NaCl for controls was mixed with the appropriate Hoagland solutions (1x) to obtain the six treatments expected (6 mL): Fe-deficient (ø) Hoagland (0.5x) control; Hoagland (0.5x) control; Fe-deficient (ø) Hoagland (0.5x) with 5 mg L^{-1} magnNPs; Hoagland (0.5x M) with 5 mg L^{-1} magnNPs; Fe-deficient (ø) Hoagland (0.5x) with 5000 mg L^{-1} magnNPs; Hoagland (0.5x) with 5000 mg L^{-1} magnNPs. Each experiment was conducted three times, i.e. three Petri dishes containing six seedlings each.

After 7 days, the plantlets were harvested. The Petri dishes were open one at time, and plantlets were placed in a flat glass container to allow taking pictures. Each plantlet was cut accurately to separate the aerial parts from the roots and make fresh weight measurements. The plant samples were eventually wrapped in annotated aluminium paper and immersed in liquid nitrogen to preserve the tissues. Samples were then stored at -40°C until lyophilisation.

IV.2.2.2. Hydroponics

Hydroponic experiments were performed in rectangular boxes (30 x 16 x 3.6 cm) containing interior bags. The bags were made, by tailoring plastics sac to adequate sizes by thermobounding. The bags were, beforehand, washed with 0.5 M HNO_3 solution for 1 night, rinsed with distilled water 3 times and again washed with distilled water for several hours. The interior bags were then filled with 175/175 mL of Hoagland solution (1x) and either distilled water (ionic strength 5.10^{-3}M NaCl) or magnNPs suspensions (0.01 or 2 g L^{-1} solution). The experiment has been conducted on sunflower, bean and maize. Data related to bean and maize hydroponic cultures are displayed in Supporting Information (S.I. –B., **Figure S2**). The six treatment solutions (350 mL) included: Fe-deficient Hoagland (0.5x) control solution; Hoagland (0.5x) control solution; Fe-deficient Hoagland solution (0.5x) containing 5 mg L^{-1} magnNPs; Hoagland solution (0.5x) containing 5 mg L^{-1} magnNPs; Fe-deficient Hoagland solution (0.5x) containing 1000 mg L^{-1} magnNPs; Hoagland solution (0.5 M) containing 1000 mg L^{-1} magnNPs. Two hydroponic boxes, each containing 5 seedlings, were prepared per treatments, so that 6 boxes (one per treatment) were placed in the incubator on upper shelf and 6 other boxes (same 6 treatments) were placed on bottom shelf.

Beforehand, a total of 100 seeds (either sunflower, bean or maize) were surface sterilized with 3% (v/v) sodium hypochlorite (NaOCl) for 3 min and then rinsed 12 min with distilled water for 5 times. They were eventually soaked in distilled water for 45 min in a laminar flow hood. Once washed, the seeds were distributed in Petri dishes in 6 mL Hoagland solutions (0.5x) that were sealed with parafilm and gathered in the incubator at 22°C in an opaque box. After 7 days, the plantlets were counted and sorted out over the 12 systems to ensure homogenous plant sizes at the beginning of the experiment. The plantlets were placed vertically in plastic tubes (about 3 cm high and 0.7 cm diameter) to allow the growth off roots downwards and that of stems and leaves upwards. The tubes with plantlets were then inserted in the systems through holes pierced at the top of the systems, in the lid of the boxes. Hydroponic systems containing seedlings were put in a growth chamber with a 70% relativehumidity, a day/night temperature of 22/18 ºC, a photoperiod of 16 h of light and a photosynthetic photon flux density of 160 µmol $m^{-2}s^{-1}$.

The treatment solutions were continuously aerated using air pumps. Their volumes were regularly adjusted to 350 mL with autoclaved distilled water added in the systems through smaller holes in the boxes lid using syringes of 10, 20 and 50 mL (previously washed with HNO3 and distilled water). In the same holes, 10 mL syringes (assembled with 6 cm long needles) were used to sample 12 mL of the hydroponic solution in each system. At the end the experiment, 6 samples per system were collected through time.

After 25 days growth (7 days in Petri dish and 18 days in hydroponic systems), the plants were harvested. Each system was brought out of the incubator and the plants were briefly placed in distilled water in a plate glass container to take pictures. The roots were washed several times with distilled water to remove the magnNPs adsorbed on the roots surface. The plants were then cut to separate the aerial parts from the roots. Each part of each plant was weighted, wrapped in aluminum paper and immediately plunged in liquid nitrogen. Plant samples were eventually stored in a freezing compartment at -40 °C.

In addition to the 25-days hydroponic experiments, long-term hydroponic cultures were implemented with beans for a 63 days duration. The experiment was set up similarly as the short terms experiences and only the six treatments were slightly different and included: Fe-deficient Hoagland (0.5x) control solution; Hoagland (0.5x) control solution; Fe-deficient Hoagland solution (0.5x) containing 5 mg L^{-1} magnNPs; Hoagland solution (0.5x) containing 5 mg L^{-1} magnNPs; Fe-deficient Hoagland solution (0.5x) containing 2500 mg L^{-1} magnNPs; Hoagland solution (0.5 M) containing 2500 mg L^{-1} magnNPs.

IV.2.2.3. Soil column experiments

The experiments were performed in soil columns (250 mL PP measuring cylinders, from VWR - 612-4404BTU) allowing the growth of 1 plant per column. Introducing a circular drilled holes plate (3.7 cm diameter) covered with a nylon filter in the cylinder, the soil was hold from the middle of the column over a height of 13 cm (120g of dry soil). An aperture was also pierced at the bottom of the cylinder to allow soil solution leakage and to perform regular samplings (S.I. - C., **Figure S3**). The external column walls were eventually packed with aluminum paper to hide the medium from light and prevent the development of algae.

The soil used in the experiment (**Table 1**) was collected in an inventoried zone (ZA Armorique), in the area of Pleine-Fougères (Brittany, France), in the 0 - 20 cm first horizon. The soil was dried and sieved through a 2.0 mm mill before its use. Soils were deposited in the columns after the treatments were applied. Twenty aliquots of soil (120 g) were weighted and individually spread onto aluminum papers to constitute the five replicates of each ofthefour experimental conditions: control soil (unmodified soil), soil containing 1% magnNPs, soil polluted with Cu and soil polluted with Cu containing 1% magnNPs. Cu-polluted soils were contaminated with 5.5 M $CuSO_4$ solution (for an input of 480 ppm of Cu in the soil) by dispensing the preparation dropwise over a grid pattern. Similarly, magnNPs solution (12 g L^{-1}) was added into magnNPs containing soils (whether or not containing copper) to reach 1% magnNPs in the soil (1.2 g magnNPs per soil).

Table 1: Physico-chemical characteristics of soils sampled from Pleine-Fougères (ISAE, Analytical laboratory, Combourg, France).

pH	**CEC**	**MO**	**C/N**	**Cd**	**Cr**	**Cu**	**Ni**	**Pb**	**Zn**
-	meq/100g	%	-	ppm	ppm	ppm	ppm	ppm	Ppm
5,4	15,6	5,75	10,1	0,29	84,30	20,26	30,32	21,95	73,62
SiO_2	**Al_2O_3**	**Fe_2O_3**	**MnO**	**MgO**	**CaO**	**Na_2O**	**K_2O**	**TiO_2**	**P_2O_5**
%	%	%	%	%	%	%	%	%	%
64,89	12	4,03	0,03	0,96	0,39	1	1,85	0,71	0,15

Sunflower seeds were placed for germination directly in the soils. A total of 60 seeds were previously surface sterilized with 1.5% (v/v) sodium hypochlorite (NaOCl) for 3 min and then rinsed 12 min with distilled water for 5 times. They were eventually soaked in distilled water for 45 min in a laminar flow hood. 3 seeds per column were sowed, to ensure enough plants would germinate, but only one seedling per column was maintained. The columns were placed in a growth chamber which provided cyclic growth conditions, with 16 h light at 22 °C and 8 h in the dark at 18°C, a photosynthetic photon flux density of 160 µmol m^{-2} s^{-1}, and a relative humidity of 70%.

For plant watering, a modified Hoagland solution (containing only macronutrients compounds except iron) or a 2 10^{-3} M NaCl solution was alternately poured into the soils at field capacity every 2 days. This steady sprinkling kept the soil moist, while increased volumes of the nutrient solution were given to allow sampling of the soil solution every 3 and 5 days. For each column, about 25 mL of soil solution were collected and further mixed with that of another similar column (originating from the same type of soil) using a peristaltic pump at 1 mL min^{-1}. The last column, which was similarly watered, was used for pH and Eh measurements during sampling.

After 57 days growth, 4 over 5 sunflower plants for each treatment were harvested to allow biological assays. Pictures and fresh weight measurements were taken after separating the roots, the aerials parts and the flower of the plants. However, the whole roots were not precisely and equally recovered from one soil to another, hence the root weights were not provided in the results. Plant samples were frozen in liquid nitrogen and stored under -40°C. A fifth plant, for each treatment, was harvested 38 days later to allow sampling for scanning electron microscopy (SEM) analyses and magnetic measurements and study the translocation efficiency by estimating the distance along which magnNPs were transported inside the plant. Regards to the height of the plant from ground to above, aerial parts of the plants were cut into 3 sections: lower mid-height ("AP1"), upper mid-height ("AP2") and sunflower head ("AP3"). For roots (R) and soils (S), three equal sections were made in the 13-cm-height soil and also numbered from 1 to 3 with increasing depth.

IV.2.3. Biological assays

All the following experiments were conducted on dry plant material obtained after lyophilization (Christ ALPHA 1-2LDplus). Each frozen sample of plants was placed into the chamber of the freeze dryer for a primary long drying (0.09 Pa for 72 h), followed by a secondary drying stage for about 24 h (0.001 Pa). The dry samples were immediately sealed and preserved in a cold room. Before each analyze, the material was gently ground with a mortar and a pestle hence providing fine powders of dry plants.

IV.2.3.1. Chlorophyll content

For chlorophyll determination, 5 mg DW (dry weight) of sunflower leaves were incubated in 500 µL acetone (80 %) at 4°C, for at least 12 h until complete bleaching. Centrifugation at 12000 *g* was realized to recover the clean supernatant in new tubes. 30 µL of each supernatant was diluted in 270 µL of acetone (80 %) in a microplate well. Chlorophyll content was determined spectrophotometrically, by reading the absorbance at 470, 645 and 663nm (spectrophotometer SAFAS FLX-Xenius - PLAY analytical platform of University of Rennes 1).

Pigments contents were eventually calculated (µg mg^{-1} DW) according to the equations of Lichtenthaler and Wellburn (1983):

$Ca = 12.21 * DO_{663} - 2.81 * DO_{645}$, *Chlorophyll a*

$Cb = 20.13 * DO_{645} - 5.03 * DO_{663}$, *Chlorophyll b*

$C = Ca + Cb$, *Chlorophylls (total)*

$K = (1000 * DO_{470} - 3.27 * Ca - 104 * Cb) / 229$, *Carotenoids (xanthophylls + carotenes)*

IV.2.3.2. Determination of lipid peroxidation

The measurement of lipid peroxidation products was achieved bymeasuring the amount of TBARS (thiobarbituric acid reactant species) produced by the thiobarbituric acid (TBA) reaction, according to the corrected TBA method as described by Hodges et al. (1999) and expressed in terms of malondialdehyde equivalents (MDAeq). For each sample, 1 mL ethanol (80%) was added to 15 mg dry shoot to react for 25 min at room temperature in a rotating wheel. After centrifugation at 10 000 g for 10 min, the supernatant was collected in a new tube. Two aliquots of 200 µL were mixed with TBA+ (20.0% trichloraceticacid (p / v), 0.65% (p/v) TBA et 0.01% (w/v) butyl-hydroxytoluene) and two other with TBA-(20.0% trichloracetic acid (p/v) et 0.01% (w/v) butyl-hydroxytoluene). The samples were eventually heated to 95°C for 25 min, rapidly cooled down to room temperature and immediately centrifuged at 10 000 g for 10 min. The supernatants were recovered in new tubes and 300 µL were sampled and placed in a microplate. The absorbance of the supernatants was recorded at 440, 532 and 600 nm spectrophotometrically using a microplate reader (SAFAS FLX-Xenius).

Results are finally expressed in MDAeq per gram of DW following the equations of Hodges et al. (1999):

1) $[(\text{Abs } 532_{\text{TBA+}}) - (\text{Abs } 600_{\text{TBA+}}) - (\text{Abs } 532_{\text{TBA-}} - \text{Abs}600_{\text{TBA-}})] = \text{A}$

2) $[(\text{Abs } 440_{\text{TBA+}} - \text{Abs } 600_{\text{TBA+}})\ 0.0571] = \text{B}$

3) MDA equivalents (nmol ml^{-1}) = $(\text{A-B}/157\ 000)\ 10^{6}$

IV.2.3.3. Soluble protein extraction and quantification

Plant homogenates were prepared in 50 mM phosphate buffer (pH 7.5) containing 1 mM EDTA, 1 g PVP, and 0.1 % (w/v) Triton X-100. About 50 mg of plant shoot (DW) reacted with 1.5 mL of the buffer for 1 h in a rotative wheel at 4°C. The samples were centrifuged twice for 12 min at 12000 *g* and the supernatant was collected in new tubes. Several aliquots were prepared and plunged in liquid nitrogen to perform activity assays of guaiacol peroxidase (POD) and superoxide dismutase (SOD) antioxidant enzymes.

Soluble protein spectrophotometric quantification was performed according to the Bradford's method (1976). For each sample, 10 µL of soluble protein extract was deposited in a microplate, in duplicates, and 250 µL of Bradford reactant were added. The reaction was run for 15 min and the absorbance was read at 595 nm. Calculation of the protein content was determined based on bovine serumalbumin (BSA) calibration solutions (0.1 to 1.4 mg L^{-1}).

IV.2.3.4. Analysis of POD activity

Guaiacol peroxidase (POD) activity was assayed according to the method of Putter (1974) and Cakmak and Marschner (1992) with some slight modifications. For each sample, the reaction mixture (300 µL) was prepared in microplates by adding the following reactants: 190 µL deionized ultrapure water, 30 µL phosphate buffer (1 M, with pH adjusted to pH = 6.5), 30 µL guaiacol (150.06 mM) and 20 µL of soluble protein extract. The reaction was initiated by adding 30 µL H_2O_2 (161.8 mM). The enzymatic activity was determined from the maximum rate of tetraguaiacol formation by monitoring the increase in absorbance at470 nm ($\mathcal{E}_{\mathrm{Tetragaiacol}}$ = 26.6 mM^{-1} cm^{-1}) during 6 min (1 measure every 40 sec). One unit (U) of POD is the amount of enzyme that reduced 1 µmol of H_2O_2 min^{-1} under the assayed conditions.

IV.2.3.5. Analysis of SOD activity

Superoxide dismutase (SOD) activity was assayed by measuring its capacity of inhibiting the photochemical reduction of nitro blue tetrazolium (NBT), following the method of Giannopolis and Ries (1977) with few modifications. For each analysis, the reaction mixture was prepared by adding the following reactants: 180 µL deionized ultrapure water, 30 µL phosphate buffer (500 mM, pH = 7.8), 30 µL methionine (130 mM), 30 µL NBT (750µM) and 10 µL of soluble protein extract. 30 µL riboflavine (20 µM) were eventually added to initiate the reaction. The analyses were performed on 2 parallel microplates - with duplicates on each - one exposed to light and the other hidden in the dark. A pre-read absorbance at 560 nm was realized for each plate before launching the reaction. Riboflavine was then added (30 µL) and the samples were exposed, to light (first plate) and then to obscurity (second plate), 8 min each. Immediately after, the absorbance was read at 560 nm. For calculations, pre-read was first subtracted to the final absorbance measurement. SOD activity was expressed as U mg^{-1} protein, U (a unit) being the amount ofenzyme causing 50 % inhibition of the NBT reduction to blue Formazan observed in the absence of enzyme.

IV.2.4. Geochemical analyses

Major- and trace-element concentrations were determined by ICP-MS (Agilent 7700x), using rhenium and rhodium as internal standard. The international geostandard SLRS-5 was used to check the validity and reproducibility of the results (Yéghicheyan et al., 2013). Samples were prepared in clean room in pre-washed (24h in nitric acid (1.5MHNO_3) at 45°C, 24h in deionized distilled water at 45°C - repeated twice) digestion vessels (Savillex), and further diluted in pre-washed (24h in nitric acid (1.5M HNO_3) at 45°C, 24h in deionized distilled water at 45°C) 50-mL tubes. For magnNPs and soil solutions, samples were first digested with sub-boiled nitric acid (14.6 M HNO_3) for 16 h at 95°C and subsequently heated until complete evaporation of the solvent. The samples were eventually re-solubilized in 0.37 M HNO_3 with appropriate dilution(s) regards to ICP-MS quantifications limits. For plant tissues samples (shoots and roots), lyophilized material (50mg) was digested 5 times in sub-boiled nitric acid (14.6 M HNO_3), with or without hydrogen peroxide (H_2O_2) (10 drops for the two first digestions), with about 8 hours evaporation (95°C) each time. Root samples were digested for longer periods and 2 more digestion-evaporation steps were carried out because of insoluble organic matter and minerals. Final solids obtained after the last evaporation were re-solubilized in 0.37 M HNO_3 with appropriate dilution(s) regards to ICP-MS quantifications limits.

IV.2.5. SEM analyses

SEM and EDS analyses were conducted at the CMEBA (University of Rennes) on a JEOL JSM 7100 F EDS EBSD Oxford. Segments (1 cm length) were taken from the roots of beans (hydroponic culture, long term experience) and sunflowers (soil column experiment) exposed to magnNPs to visualize the magnNPs in plant tissues. Fresh samples were prefixed in 2.5% glutaraldhehyde (diluted with 0.1 M phosphate buffer at pH = 7.2) at 4°C for 48 h, washed in 0.1 M phosphate buffer (3 baths of 10 min) and eventually dehydrated in successive bath of ethanol (60%, 70%, 80%, 90%, 95% and 100%), 10 min each.

IV.2.6. Magnetic susceptibility measurements

Magnetic susceptibility was used to trace the occurrence of magnNPs in soils and estimate the magnNPs uptake in plant tissues. The method has already been used to evidence magnetite occurrence in various environments (Maxbauer et al., 2017).

The measurements were performed with a susceptibilimeter (AGICO KLY3). For sample preparation, the different parts of the plants (aerial parts, roots and stems) harvested from hydroponics (bean) and soil column experiment (sunflower) were stored in plastic containers and lyophilized. Plant and soil sections collected from soil columns experiments (95-days old sunflowers), were dried in an oven and stored in the same plastic containers. Analyses were performed directly on the containers (same for all the samples). Blank (containers without plants) measurements were acquired at the beginning of the experiment and also every three measurements, to account for the possible deviation occurring along with the analyses. Blanks and sample analyses were repeated 10 times to ensure the validity of the measurements. Analyses provided volume susceptibilities to which blank correction were applied. Mass susceptibilities (m^3 kg^{-1}) were then obtained by considering the actual weight of the sample (without container) and the density of the material. Estimation of magnNPs content in the samples was made using the blank-corrected susceptibility of a dry sample of magnNPs (known concentration and weight) and correcting the sample from the contribution of the magnNPs uncontaminated matrix (control plants or control soils).

IV.2.7. Statistical analysis

All data presented are the mean values of at least two independent set of experiments. Each value was presented as means ± standard errors means (SEM), with a minimum of two replicates. Statistical analyses were carried out by one-way ANOVA using the Tukey test to evaluate the significance of the means, taking $p < 0.05$ as significant.

IV.3. Results and discussion

IV.3.1. Highlighting the role of the growth medium in driving magnNPs/plant interactions

IV.3.1.1. Characterization of magnNPs

TEM analyses, potentiometric titration and BET analyses were conducted on magnNPs in aqueous solution. The main properties are summarized in **Table 2**. It is worth noting that magnNPs are not stable objects and their behavior is strongly influenced by the environmental conditions in which they evolve. MagnNPs have previously been characterized regarding their colloidal and chemical stabilities (Demangeat et al., 2018), which highlighted that pH played a key role in driving their aggregation state and dissolution rate. Magnetite is also prone to oxidation and transformation into maghemite, a more stable iron oxide with only Fe^{3+} in its structure (Cornell and Schwertman et al., 2003). In this study, Fe(II)/Fe(III) measurements evidenced that oxidation occurred. After being introduced in the aqueous mediums, the IONPs displayed a Fe(II)/Fe(III) of 0.35 ± 0.02. Furthermore, surface coating with either humic acid or phospholipids (natural constituents found in soil and surface waters) was investigated (Demangeat et al., 2018) and it was evidenced that HA was particularly efficient in enhancing magnNPs colloidal stability and could protect against dissolution at acidic pH

(Vindedahl et al., 2016). Thus magnNPs transformation is expected to play a key role towards magnNPs uptake and toxicity (Amde et al., 2017).

Table 2: Main properties of magnNPs from TEM, BET and potentiometric titration. Data are the mean ± standard error of the mean (SEM) of two independent experiments.

	size (nm)	surface area (m^2/g)	pHzpc
magnNPs	7 ± 2	115 ± 0.4	6.2

IV.3.1.2. Fate, uptake and translocation of magnNPs under hydroponic culture of bean plants

SEM analyses evidenced the deposits of magnNPs aggregates (see Supporting Information: S.I - D.) onto the surface of roots. EDS analyses (S.I - D., **Figures S4, S5 and S6**) evidenced strong peaks of iron and oxygen (iron oxide composition) on the observed particles as compared to EDS analyses in unoccupied areas (volumes analyzed by EDS - targeted EDS points - consisting in cubes of 1µm x 1µm x 1µm). These deposits probably also include organic matter (as evidenced by the carbon peaks in the EDS spectrums – S.I D.) likely resulting from the roots activity. At the root level, magnNPs high reactivity and specific surface area would play an important role, which allowed the adsorption of magnNPs onto the physical interface. Electrostatic adsorption, mechanical adhesion or hydrophobic affinity can allow the accumulation of magnNPs in epidermis or their adherence onto the surficial tissues as single particles and/or aggregates (Anjum et al., 2016). Nevertheless, the adsorption of magnNPs on the root surface cannot be regarded as their actual uptake as some ions and surfactants, usually in the soil solution, can compete with magnNPs or modulate their behavior thereby favoring magnNPs desorption from the roots (Solanki et al., 2015). Moreover, the presence of a mixture of mucilage and roots exudates (composed of a number of organic acids and amino acids) released by plant roots could induce NPs dissolution (Peng et al., 2015; Liu et al., 2016; Perrault et al., 2013).

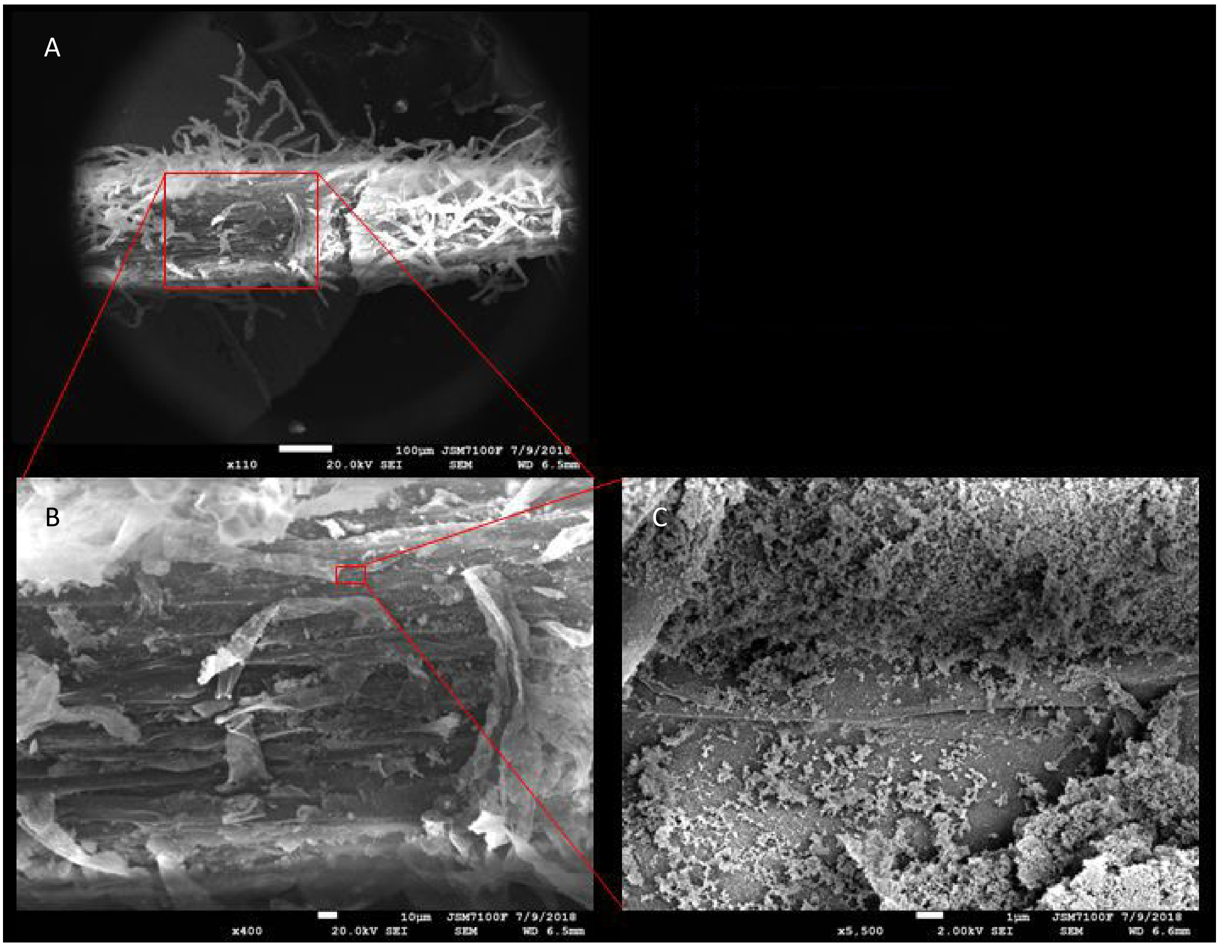

Figure 1: SEM images showing deposits of magnNPs aggregates at a root surface (bean root, after 63 days in hydroponic culture with 2500 mg L^{-1} NPs). Microscope images have been taken at x 110 (A), x 400 (B) and x 5 500 (C) magnifications.

Geochemical results did not evidence a significant Fe release from magnNPs dissolution in the Fe-deficient Hoagland solutions at the end of the experiment (soluble Fe contentsarein the range of quantification limits therefore, results arenot presented). In consistence with our previous study performed in NaCl 510^{-3} M during 48h (Demangeat et al., 2018), magnNPs dissolution was not observed. Indeed, we previously demonstrated that Fe dissolution decreased to less than 0.01% at pH 5 and 6; which correspond to the pH condition observed in the present experience (pH 5.5). Furthermore, in that past experiment, MagnNPs dissolution only occurred at pH 3 and 4 leading to a 1.5 and 0.4% Fe release, respectively (Demangeat et al., 2018). In addition, magnNPs coating with organic materials such as humic acids (HA) and phospholipids prevented the dissolution of magnNPs, and HA considerably improved magnNPs colloidal stability. Thus, it is expected that only few Fe could be dissolved within the conditions of the current experiment, despite the possible implication of roots activity (for instance, the absence of dissolved iron could results from increased plant uptake or, from magnNPs aggregation, inducing decreased root activity).

MagnNPs detection in the plant tissues (using magnetic susceptibility) evidenced that plants are able to absorb magnNPs through the roots before being translocated in the aerial parts of the plants. Magnetic measurements conducted on 63-days-old bean plants further evidenced that magnNPs occurrence increased with increasing magnNPs concentration (**Table 3**). MagnNPs were still detected in the plants exposed to 5 mg L^{-1} magnNPs, although the magnetic susceptibilities were about 10 times lower than that obtained in the plants exposed to 1000 mg L^{-1} NPs. In both cases, however, the distribution of magnNPs highlighted the prime accumulation of magnNPs in(/on) the roots and their progressive distribution into stems and, possibly, into the leaves of bean plants. The transfer and accumulation of magnetite NPs from roots to shoots has been evidenced in several works (Iannone et al., 2016). The most accepted explanation for NPs translocation suggests that NPs can move intra- and/or extra-cellularly through tissues until they reach the xylem. Previous studies conducted on magnetic nanoparticles showed an easy penetration of the root, through entering into the vascular cylinder and access to the aerial parts of the plants via moving the xylem vessels using the transpiration stream (CiFuentes et al., 2010). Several hypotheses are still under considerations but, it is accepted that magnNPs transportation could occur via three main routes that include the cell wall pores (vide supra), the apoplastic pathway (transport on the surface between the cell wall and the plasma membrane), or the symplastic pathway through plasmodesmata (channels of approximately 40-nm-diameter connecting adjacent cells).

Table 3: Magnetic susceptibilities (m^3 kg^{-1}) measured in the different parts of bean plants (stems, leaves, roots) and estimated concentrations of magnNPs in the tissues (mg g^{-1} DW). Bean plants were exposed for 63 days to different concentrations of magnNPs (5 and 1 000 mg L-1) in hydroponic culture. Data represent mean ± standard error of the mean (n=2 to 4). Magnetic susceptibilities were calculated based on raw magnetic susceptibilities (volumic) and regards to the mass of the samples (± 0.7g).

	Stem		**Leaves**		**Roots**	
	MagSuscept	NPs (mg g^{-1})	MagSuscept	NPs (mg g^{-1})	MagSuscept	NPs (mg g^{-1})
Control	-1,0E-09	u.a.b.	2,2E-08	u.a.b.	1,3E-07	u.a.b.
5 ø Fe	7,2E-09	0,01 ± 0,009	3,2E-08	0,02 ± 0,02	5,9E-06	9,9 ± 3,5
1000 ø Fe	5,8E-08	0,1 ± 0,05	4,5E-08	0,04 ± 0,02	7,0E-05	121,2 ± 43,2

*u.a.b.: used as blank to remove the diamagnetic component induced by the plant itself.

IV.3.1.3. Mobility and bioavailability of magnNPs and trace metals in Cu-polluted soils

Magnetic susceptibility measurements evidenced that magnNPs primary accumulated both into the roots of the plants, and in the soils (**Table 4**). In both cases, the measurements are more than two orders of magnitude higher than control plants and soils, meaning that magnNPs occurred in significant amounts in those mediums. On another hand, the aggregation of NPs also usually decreases NPs bioavailability by preventing NPs to penetrate the cells (Amde et al., 2017). At the root cellular level, magnNPs have to interact with plant cell wall before their penetration into cell and subsequent intracellular transportation (Anjun et al., 2016). Cell wall consists in a network of cellulose microfibrils cross-linked with hemicellulose and lignin, and further impregnated by pectin that offers a range of distinct active sites and also represents a semipermeable barrier that allows the passage of small molecules (Navarro et al., 2008). Cell wall contains pores with diameter that ranges from 5 to 20 nm. Thus, the entry of aggregated magnNPs is expected to be restricted to the pores size. Nevertheless, the interaction between NPs and cells could result in the formation of wounds or new pores, which might be bigger than the common pores and thus favor the passage of magnNPs through the cell wall (Iannone et al., 2016; Navarro et al., 2008). Furthermore, the interaction of nanoparticles with carrier proteins, aquaporins, ion channels, and organic chemicals has been proposed to allow the entry of NPs into the plant cells (Anjun et al., 2016; Hu et al., 2018). In that case, cell penetration would occur under the symplastic route, known as an important and highly regulated pathway for the nanoparticle-transportation into major crops (Rico et al., 2011). Endocytosis pathway has also been considered as a significant alternative to allow the internalization of magnNPs (Miralles et al., 2012). In the aerial parts, however, magnetic susceptibilities indicated that magnNPs were not translocated in the two upper levels of the plants (magnetic susceptibilities are negative and close to that of controls) although in the first, close-to-ground section, the positive signals might be correlated with the occurrence of very few magnNPs.

Table 4: Magnetic susceptibilities (m^3 kg^{-1}) measured in the different parts of the plants (aerial parts - fragments including stems and leaves -, roots) and in the soils (initially 1% magnNPs) with estimated concentrations of magnNPs detected. Sunflower plants were exposed for 57 days to 1% magnNPs and / or Cu (500ppm) in soil columns. Data represent mean ± standard error of the mean (n= 4). Magnetic susceptibilities were calculated based on raw magnetic susceptibilities (volumic) and regards to the mass of the samples (± 0.7g). In each column, three sections (samples) were made regards to the height of the aerial parts (increasing height from AP1 to AP3) and depth (increasing depth from 1 to 3) for roots and soils.

		Control	**NPs**		**Cu**	**NPs-Cu**	
		MagSuscept	MagSuscept	NPs (mg g^{-1})	MagSuscept	MagSuscept	NPs (mg g^{-1})
A.P.	**AP3**	-1.0E-08	-2.8E-08	n.d.	-5.8E-09	-3.3E-08	n.d.
	AP2	-7.1E-09	-1.2E-08	n.d.	-4.5E-09	-5.7E-09	n.d.
	AP1	-1.1E-08	1.4E-08	0.04 ± 0,025	-2.4E-09	-1.5E-09	n.d.
Roots	**R1**	-1.7E-09	9.3E-07	2.3 ± 0.4	6.1E-10	1.7E-07	1.6 ± 0.7
	R2	1.9E-09	6.3E-07	2.8 ± 0.6	1.9E-09	1.4E-07	1.1 ± 0.6
	R3	5.2E-09	3.8E-07	2.5 ± 0.5	4.2E-09	5.8E-07	0.7 ± 0.6
Soils	**S1**	7.1E-08	5.9E-06	10.1 ± 0.2	6.8E-08	7.3E-06	11.5 ± 0.2
	S2	6.8E-08	5.5E-06	9.4 ± 0.4	6.8E-08	6.7E-06	10.7 ± 0.3
	S3	6.8E-08	5.8E-06	10.0 ± 0.2	6.9E-08	6.4E-06	10.1 ± 0.2

*n.d.: not detected

According to ICP-MS measurements (**Figure 2**), higher iron content was measured in the aerial parts (AP1+AP2+AP3) of magn NPs and magnNPs-Cu plants (as compared with control and Cu plants, respectively), suggesting that magnNPs were able to reach the aerial parts of the plants. In particular, roots' exudates (organic acids, amino acids, fatty acids, proteins, and sugars) may induce transformations of magnNPs into more bioavailable forms (e.g. phytosiderophores), by increasing magnNPs solubility and/or mobility (Uren, 1984). Furthermore, ICP-MS measurements of dissolved trace elements (< 0.2µm) in the solution after 57 days leaching (**Figure 2**) evidenced a significant Fe release from the soils (especially magnNPs - containing soils), which was likely associated with Fe reduction occurring in the first days of the experiment. Indeed, under anoxic conditions, Fe(III) is readily reduced either, by inorganic chemical reactions (driven by Eh and pH conditions) or, by microbial processes (Colombo et al., 2014). This process was quickly reversed and aerobic conditions prevailed in the following days of the experiment along with iron oxidation (**Figure 3**). On another hand, the total iron content measured in the shoots of magnNPs and magnNPs-Cu plants was significantly different than those treatments (**Figure 2**); therefore, Cu might play an important role in regulating Fe uptake. Furthermore, in Cu contaminated soils, the amount of Fe released was almost similar between magnNPs-Cu and Cu soils and they were lower than the amounts of Fe released from control soils. Thus, although magnNPs-Cu soil was likely enriched in magnNPs (consistently with magnetic susceptibility measurements), access to magnNPs bioavailable pool of Fe might have been decreased because of Cu contamination.

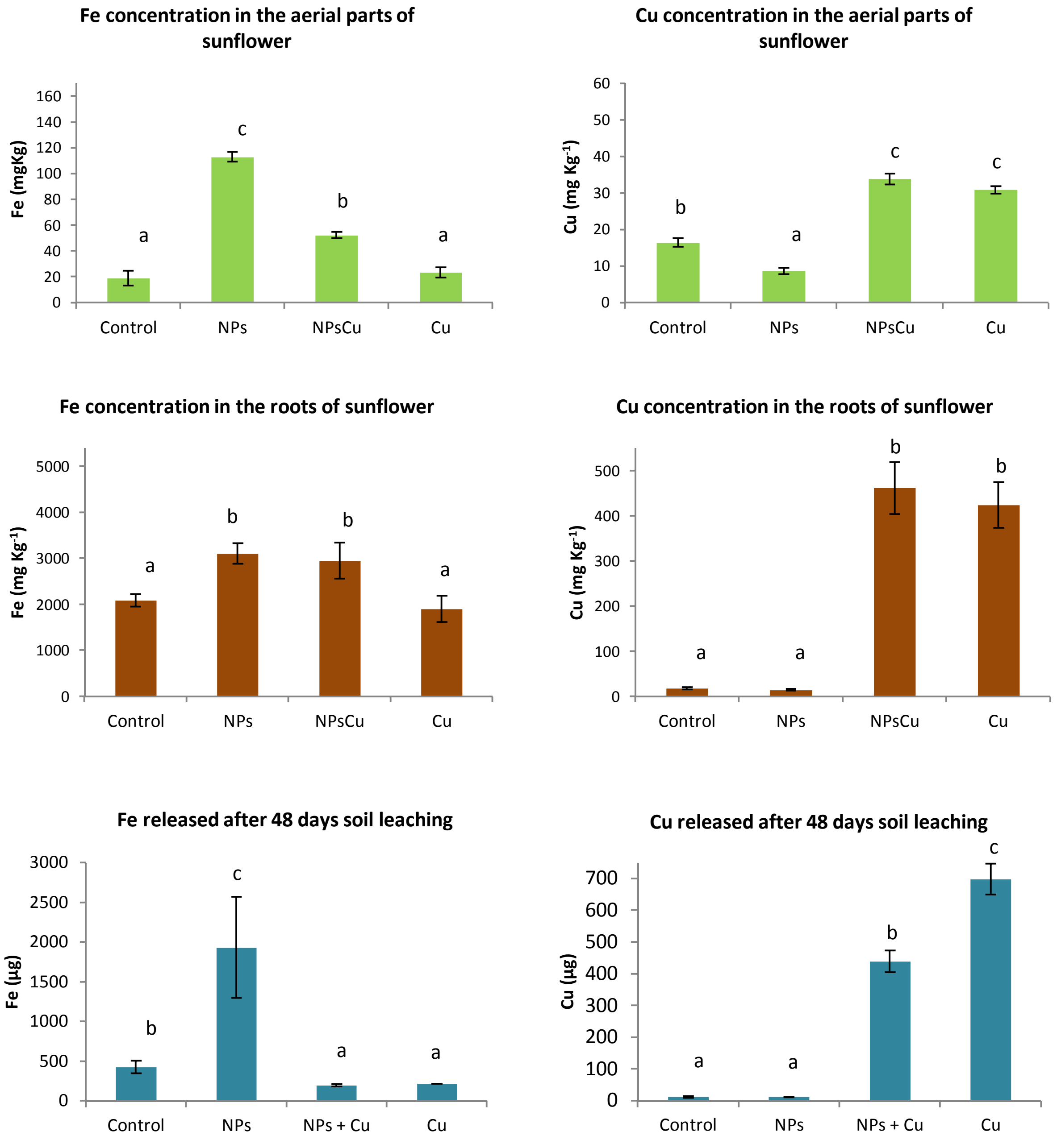

Fe concentration in the aerial parts of sunflower

Cu concentration in the aerial parts of sunflower

Fe concentration in the roots of sunflower

Cu concentration in the roots of sunflower

Fe released after 48 days soil leaching

Cu released after 48 days soil leaching

Figure 2: ICP-MS concentrations (mg Kg^{-1} DW) of Fe and Cu measured in the plant issues (aerial parts, roots) of sunflowers from soil column experiment. Data represent mean ± standard error of the mean (n=3 or 4). Different letters above bars indicate statistical significance (p< 0.05) at each condition.

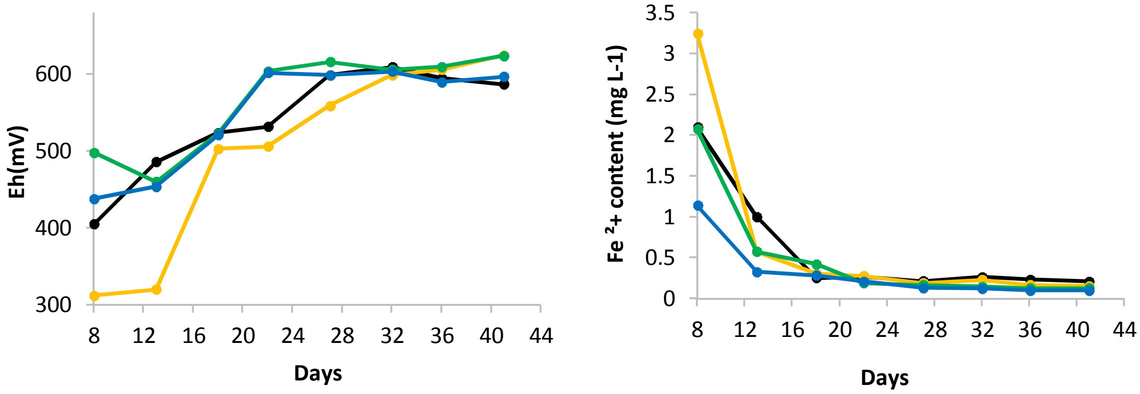

Figure 3: Evolution of the redox potential (left graph) and the content of reduced iron (Fe^{2+}) (right graph) as a function of time in the different columns: control (black), magnNPs (yellow), magnNPsCu (blue) and Cu (green).

As expected from the initial Cu inputs, Cu concentrations were much higher in plants grown in Cu contaminated soils than in control plants and NPs soils (**Figure 3**). The introduction of magnNPs into Cu contaminated soil yet decreased the accumulation of Cu in both the roots and aerial parts of the plants. Moreover, plants exposed to magnNPs alone, without Cu contamination (500 ppm), displayed a lower Cu content in both the roots and the aerial parts as compared to the control plants. Thus, magnNPs may scavenge Cu and decrease Cu bioavailability. In addition, lower amounts of Cu were measured in the final leaching solution from magnNPs-Cu soils as compared to Cu amount measured in the solution from Cu contaminated soils without magnNPs. Thus, the magnNPs occurrence likely decreased the amount of Cu leached by retaining Cu onto magnNPs surface and into the soil. On another hand, the increased natural organic matter (NOM) release occurred in soils containing either magnNPs, magnNPs and Cu, or Cu alone, as evidenced by the distribution of the dissolved organic carbon (DOC) amounts displayed in **Figure 4**. As Cu and NOM display high affinity and easily form chelates (Li et al., 2016), stabilization of magnNPs by NOM (which can lead to increased NPs mobility (Baalhousa et al., 2013)) might also have been lowered in the magnNPs-Cu soil, thereby favoring the retention of magnNPs and adsorbed Cu in the columns. Most magnNPs were probably bound to clays and NOM in the soil because of their high affinity to each other (Theng and Yuan, 2008). For most fine texture soil, leaching of trace elements and nanoparticulate compounds is limited because of the strong binding of these elements with soil colloids and especially clays, which display high surface areas (Reith and Cornelis, 2017; Sagee et al., 2012). In addition, the contributions of smaller pore sizes and larger surface area in soil columns likely increased both electrostatic interactions and physical straining, and thus reduced the mobility of magnNPs in the mediums. Eventually, since Cu was not transferred to plant roots and aerial parts in the same extent than it did in Cu plants, it is concluded that magnNPs also reduced the bioavailability of Cu to the plants. In terms of phytoremediation, the concentration of Cu was probably too high for magnNPs to absorb enough Cu to prevent any Cu accumulation into the plant tissues.

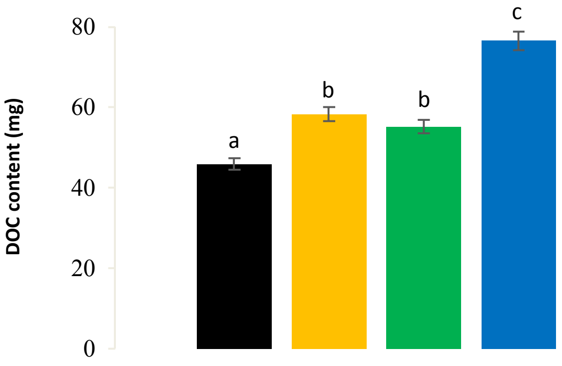

Figure 4: Total DOC amounts (mg) in the soil solution released from each soil column: control (black), magnNPs (yellow), Cu (green) and magnNPsCu (blue). Data represent means ± standard error of the mean (n=4). Different letters above bars indicate statistical significance ($p < 0.05$) at each condition.

IV.3.2. Responses of plants to magnNPs in the context of Fe deficiency

IV.3.2.1. Impacts of magnNPs on growth

Germination (short-term) and hydroponic culture (mid-term) experiments highlighted that sunflower fresh weights increased with magnNPs concentrations in Fe-deficient cultures (**Figure 5**). The responses to Fe deficiency usually include decreased plant weight, changes in root morphology, and up-regulation of genes involved in Fe uptake (Morissey et al., 2009; Salama et al., 2009). In both germination and hydroponic culture, Fe deficiency in the absence of magnNPs was characterized by lower weights of plants as compared to plants without Fe-deficiency. The occurrence of magnNPs in Fe-deficient cultures prevented any Fe-deficiency symptoms, particularly in hydroponic experiments, by raising the weights of the plants at least as high as that of non-Fe-deficient control plants. In Fe-deficient hydroponic cultures, the small (5 mg L^{-1}) and the high (1000 mg L^{-1}) concentrations of magnNPs were effective on both the roots and the shoots as compared to Fe-deficient control plants. Thus, magnNPs were able to complement the need of Fe to Fe-deficient cultures. On another hand, the effect of magnNPs on the growth of plants from Fe-bearing cultures did not show any significant

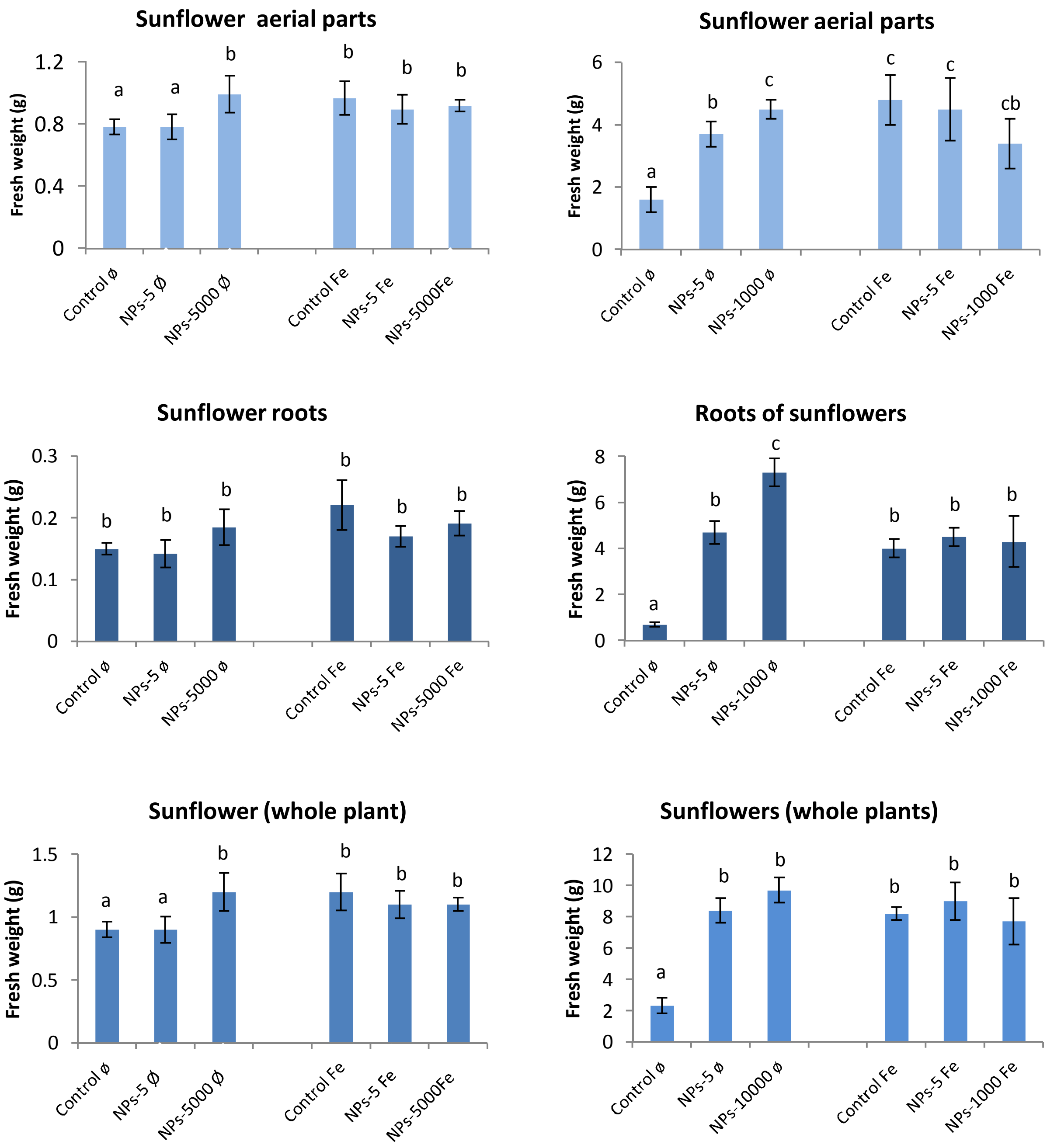

Figure 5: Fresh weights of plants measured after 7 day germination (left side) and 18 days in hydroponic culture (right side) (with n= 5 or 4). The analyses were made on six treatments investigated in germination (Fe-deficient (ø) Hoagland (0.5x) control; Fe-deficient (ø) Hoagland (0.5x) with 5mg L^{-1}magnNPs; Fe-deficient (ø) Hoagland (0.5x) with 5000 mg L^{-1}; Hoagland (0.5x) control; Hoagland (0.5x M) with 5mg L^{-1} magnNPs; magnNPs; Hoagland (0.5x) with 5000 mg L^{-1} magnNPs) and hydroponic cultures (Fe-deficient (ø) Hoagland (0.5x) control; Fe-deficient (ø) Hoagland (0.5x) with 5mg L^{-1}magnNPs; Fe-deficient (ø) Hoagland (0.5x) with 1000 mg L^{-1}magnNPs; Hoagland (0.5x) control; Hoagland (0.5x M) with 5mg L^{-1} magnNPs; Hoagland (0.5x) with 1000 mg L^{-1} magnNPs). Data represent means ± standard error of the mean. Different letters above bars indicate statistical significance ($p < 0.05$) at each condition.

growth improvement or decreased root growth. It was observed that 25 mg L^{-1} and, 50 and 100 mg L^{-1} iron oxide F_2O_3 NPs induced noticeable root growth decrease of *Arabidopsis* *thaliana* (Bombin et al., 2015) and *Zea mays* respectively (Li et al, 2016). However, in both germination and hydroponic experiences of the present studyneither, the low nor, the highconcentration of magnNPs decreasedthe growth of sunflower roots. These results were also observed for bean, maize and wheat (S.I. - A., **Figure S1**) in the germination experiences. For a longer exposure time (18 days), Fe-deficiency was more pronounced against which small magnNPs content (5 mg L^{-1}) was more effective than on the 7-day germination plantlets. Thus, the amount of magnNPs translocated may be important regards to the impacts on the growth of the aerial parts

IV.3.2.2. Pigment contents

The contents of chlorophyll *a*, chlorophyll *b* and carotenoid (xanthophylls and carotenes) pigments were determined in sunflower leaves of plants grown in hydroponic conditions (**Figure 6**). As for all vascular plants, the pigment composition of sunflower includes chlorophyll *a* and chlorophyll *b,* which are light collectors, and carotenoids, which have multiple functions in light capture and photoreception and in many other processes (participation in (i) the dissipation of oxidative stress from excess light, (ii) the synthesis of abscisic acid, (iii) the mechanism of stomatal closure and (iv) the regulation of gene expression through their oxidation products) (Esteban et al., 2015). The responses of the photosynthetic pigment composition thus, likely reflect changes in environmental conditions (Yudina et al., 2017). Different reports notably, evidenced that the nanoparticles influence the photosynthetic pigment concentration and its activity in plants (Qian et al., 2013; Perrault et al., 2013; Tripathi et al., 2017).

In our study, pigment contents in sunflower leaves were the lowest in plants grown without iron (Fe-deficient Hoagland), thus highlighting that iron deficiency has a notable impact on the pigment composition (**Figure 6**). In plants, iron is involved in the synthesis of chlorophyll, and it is essential for the maintenance of chloroplast structure and function (Rout et al., 2015). Fe deficiency primary affects structure and function of the chloroplasts, which generally results in the decrease of leaf Fe content and a marked reduction of chlorophyll level (Briat et al., 2007; Salama et al., 2009). On another hand, it was observed, from this study, that magnNPs increase goes hand in hand with an increase in pigment contents. In particular, in the case of Fe-deficiency, both small and (chiefly) high concentration of magnNPs raised the pigment contents close to that of Fe-bearing cultures. Chlorophyll a /b ratio were the highest for plants with available Fe and/or plants exposed to magnNPs. Thus, magnNPs contributed to maintain the plant photosynthetic machinery under Fe deficiency and they likely provided iron to Fe-deficient plants to raise their pigment contents in amounts comparable to that of non-deficient Fe controls. Last, sunflowers exposed to both iron and 1000 mg L^{-1} magnNPs displayed the highest pigment contents (C*a*, C*b*, C+K), which were increased as compared to Fe-control and plants exposed to low magnNPs concentrations.

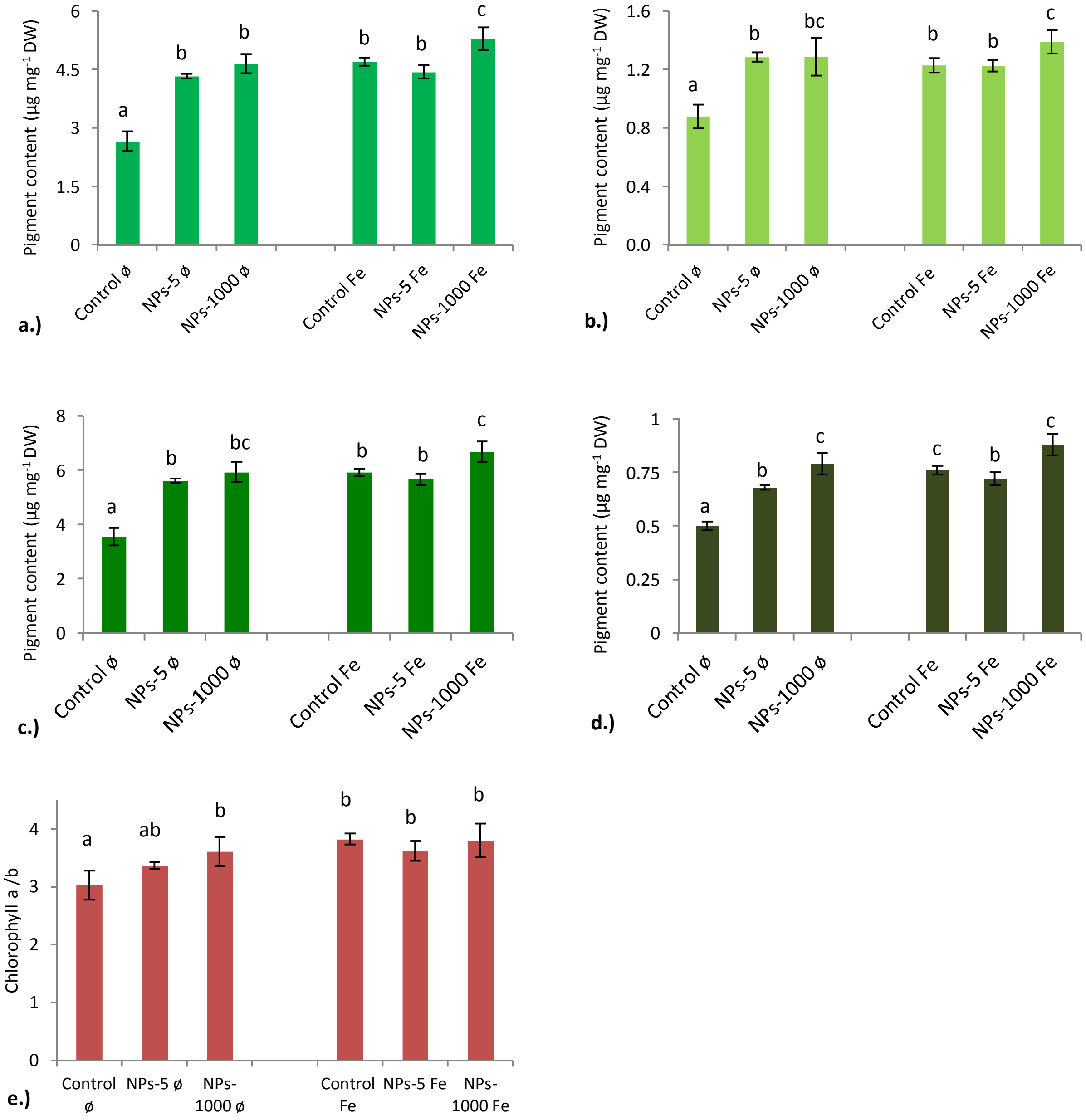

Figure 6: Pigment contents (µg mg^{-1} DW) measured in sunflower leaves: a.) Chlorophylls a; b.) Chlorophylls b; c.) Chlorophylls a + b, d.) carotenoids and e.) Chlorophylls a / b. Data represent mean ± standard error of the mean. Different letters above bars indicate statistical significance ($p < 0.05$) at each condition.

IV.3.2.3. Oxidative stress and antioxidant response

The main cellular components of plants susceptible to be damaged by free radicals are lipids, proteins, carbohydrates and nucleic acids (Blokhina et al., 2003). Lipid peroxidation stems from the production of extra free radicals. When ROS levels exceed the capacity of the plant to scavenge them, lipid peroxidation increases in biological membranes, impacting the physiological processes of the cell. Thiobarbituric acid reactant species (TBARS), including malondialdehyde (MDA), which is one of the main ending products of oxidative modification of lipids, are commonly used as indicators of lipid peroxidation. MDA is further responsible for cell membrane damage resulting from the decomposition of lipid peroxides, which are highly reactive and unstable. Cell membrane damages include changes in the intrinsic properties of the membrane such as, membrane fluidity, ion transport, loss of enzyme activity and protein cross-linking (Labudda, 2013). These changes are critical as they could ultimately cause cell death (Sharma et al., 2012). In the present study, highest TBARS were measured in the controls compared to NPs-Fe exposed plants (**Figure 7a**). Moreover, decreased MDA with increasing magnNPs concentrations were observed and the availability of iron in the Hoagland solution did not affect the dose dependent-trend (**Figure 7a**). The positive effect of iron oxide nanoparticles on lipid peroxydation was recently highlighted by several authors on other plant species (Iannone et al., 2016; Palmquist et al., 2017; Praveen et al., 2018). According Praveen et al. (2017), iron oxide NPs could act as nanozymes, improving growth and ROS tolerance. Antioxidant response obtained from guaiacol peroxidase (POD) brought further clues regards to the previous hypothesis. In Fe-deficient plants (leaves), POD activity was decreased with increasing magnNPs concentrations and in non-deficient cultures, POD was decreased in the same extent at 5 and 1000 mg L^{-1} magnNPs (**Figure 7b**). The guaiacol peroxidases are widely recognized as stress enzymes and their activation has been reported under many stressful conditions, including trace metal exposure (Gzyl and Gwóźdź, 2009); therefore, in the present study, POD increases would rather be related to iron deficiency than magnNPs exposure. On the other hand, SOD activity was also decreased with magnNPs exposure. Previous studies evidence the simultaneous induction and decline of SOD with certain enzymatic activities, likely resulting from their co-regulation (Shigeoka et al., 2002). Thus, additional work is required to determine if the observed decrease in POD and SOD activities with increasing magnNPs concentrations might be caused by magnNPs induced-modified cell functioning (**Figure 7c**).

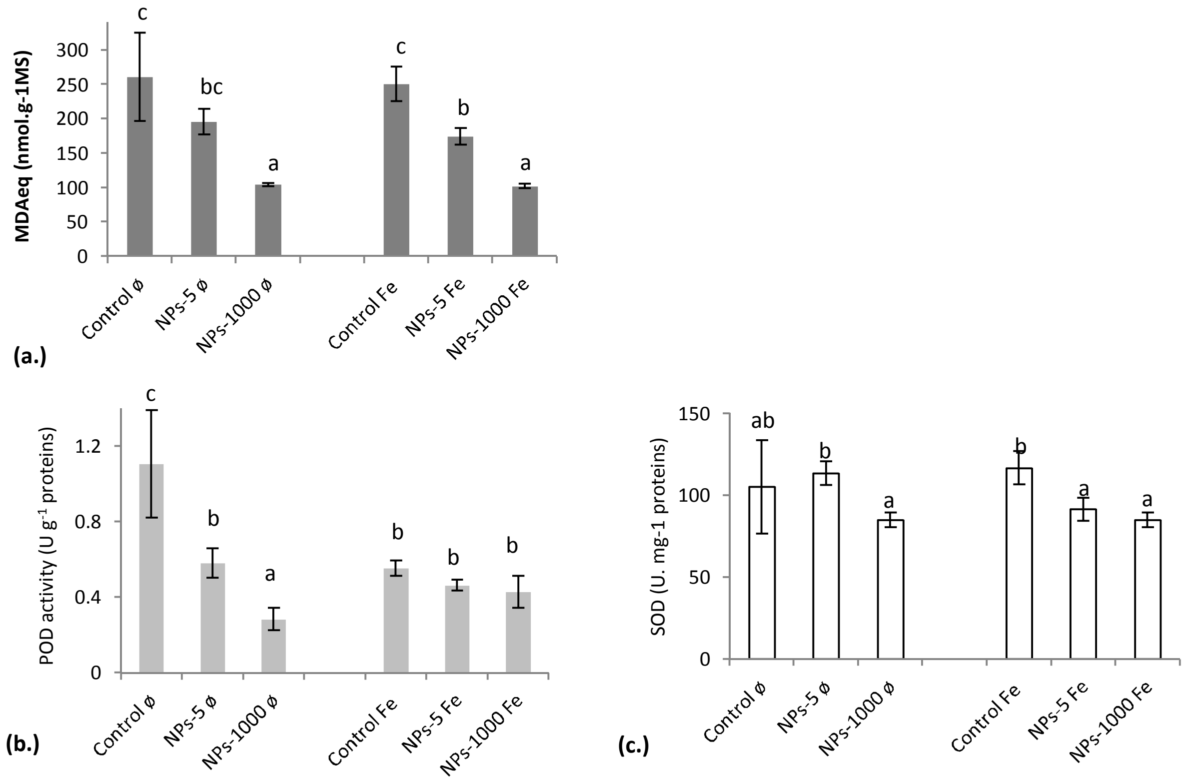

Figure 7: (a.) MDA content (nmol g^{-1} DW), (b.) POD activity (U. mg^{-1} proteins) (c.) SOD activity (U. mg^{-1} proteins) measured in the leaves of sunflowers grown in hydroponic cultures under the six treatments (Fe-deficient (ø) Hoagland (0.5x) control; Fe-deficient (ø) Hoagland (0.5x) with 5mg L^{-1} magnNPs; Fe-deficient (ø) Hoagland (0.5x) with 5000 mg L^{-1}magnNPs; Hoagland (0.5x) control; Hoagland (0.5x M) with 5mg L^{-1} magnNPs; Hoagland (0.5x) with 5000 mg L^{-1} magnNPs). Different letters above bars indicate statistical significance (p< 0.05) at each condition.

IV.3.3. Effects of magnNPs on plants in a Cu contaminated-soil

IV.3.3.1. Impacts of magnNPs and Cu on the growth parameters

According to fresh weight measurements, magnNPs had few effects on sunflower growth in the soil medium, respective to the fresh weights measured for control plants on aerial parts and total plants (**Figure 8**), although the fresh weight of flowers was decreased. Sunflower grown on Cu polluted soils displayed significant size reduction of the aerial parts and flowers as compared both to control and magnNPs plants. The fresh weights measurements of the flowers alone might highlight growth retardation. On the other hand, the impact of copper on sunflowers aerial parts growth was significant, as sunflower are very sensitive to Cu concentration (Lin et al., 2003). Cu toxicity has already been reported to reduce the growth of different plants species in addition to inducing chlorosis and necrosis of the leaves (Adrees et al., 2015). These symptoms were also observed in this study, on plants grown on Cu contaminated soils (S.I.). In conclusion, magnNPs are expected to have only a very little impact on sunflower growth, whereas copper pollution, either alone or with magnNPs, considerably reduce the plant growth.

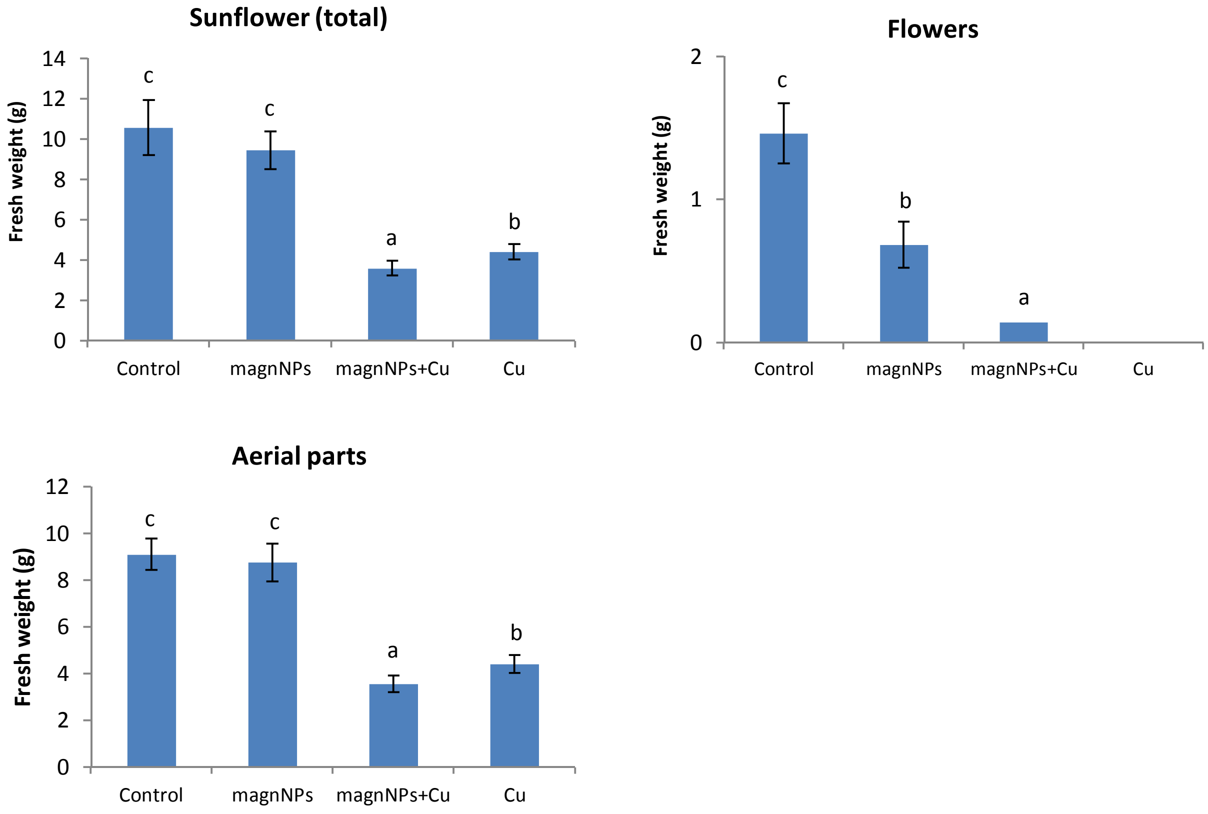

Figure 8: Fresh weights measured on the aerial parts (stems and leaves) and flowers of sunflowers, separately, and fresh weights calculated from the sum of the different parts of the plants (aerial parts and flower). Data were measured after 57 days growth on 4 different soils (control soil, soil with 1%wgt magnNPs, soil with copper (500 ppm) and soil with both copper and magnNPs). Data represent means ± standard error of the mean (n=4). Different letters above bars indicate statistical significance (p< 0.05) at each condition.

IV.3.3.2. Pigment contents

Pigment contents measured in the different plants highlighted that plants from control soil columns displayed the higher amount of pigments, whereas the three other treatments studied affected the pigment composition relative to the control plants (**Figure 9**). Treatment with magnNPs alone decreased the pigment content (especially the carotenoid content) although not in the extent that Cu and magnNPs-Cu did. A lower content of chlorophyll, inactivation of enzymes and proteins linked to photosynthesis process and, modificationof thylakoid membranes have been reported in several studies resulting from Cu toxicity (Dey et al., 2014, Ouzoudinou, 1994). In most of the plants Cu is found associated with plastocyanin, an important component of the electron transport chain between cvt bf6 and PSI in the chloroplast. According to Baszynski et al. (1988), copper deficiency reduces PSI electron transport due to a decreased formation of plastocyanin. Binding of metals to the various sensitive sites of the photosynthetic apparatus can also directly affect the photosynthetic machinery. Furthermore, the excess of Cu has been demonstrated to strongly affect the chloroplast structure with degradation of grana stacks and stroma lamellae (Baszynski et al., 1988). Cu excess usually induces chlorosis and necrosis of leaves, which was observed in our study, resulting from the inhibition of pigment accumulation and the decrease in the chlorophyll integration into photosystems (Dey et al., 2014). Thus, Cu toxicity not only, induced decreased pigments contents but also, decreased the photosynthetic activity (**Table 5**). On the other hand, Cu and NPs-Cu pigment contents, were not significantly different. Therefore, it is thus suggested that although it is capable of reducing Cu contamination (ICP-MS measurements evidenced lower Cu content in plant tissues (**section 2.1.**)), magnNPs did not prevent any Cu toxicity.

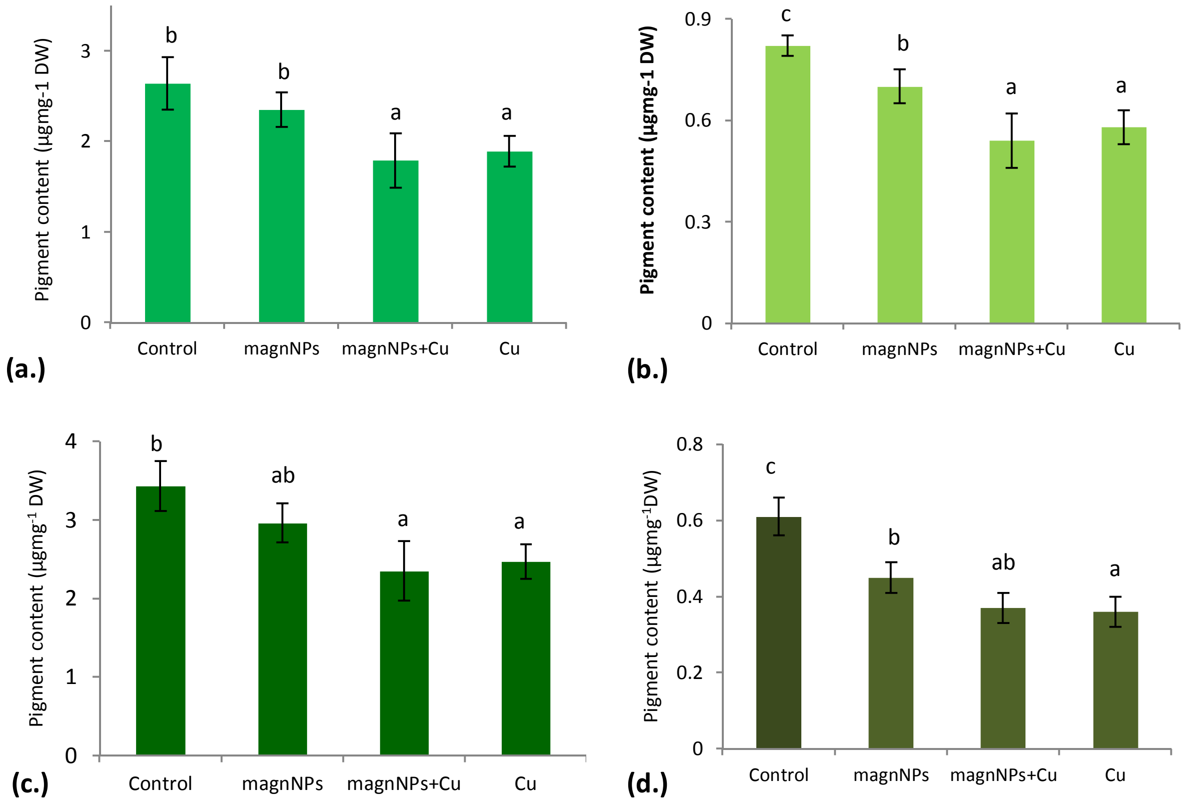

Figure 9: Pigments contents (µg mg^{-1} DW) measured in the leaves of control plants, magnNPs, magnNPsCu and Cu-treated plants from soil columns experiments on sunflowers: a.) Chlorophyll a; b.) Chlorophyll b; c.) Chlorophyll a + b; d.) carotenoids (xanthophylls + carotenes). Data represent means ± standard error of the mean (n=4). Different letters above bars indicate statistical significance ($p < 0.05$) at each condition.

Table 5: Quantum efficiencies (QY) measured on the leaves of sunflowers (Control, magnNPs, magnNPsCu, Cu columns) after 18 days growth.

	Control	magnNPs	magnNPsCu	Cu
QY	0.83	0.83	0.80	0.76

IV.3.3.3. Oxidative stress and antioxidant response

From lipid peroxidation measurements, it was observed that the presence of magnNPs decreased the MDA content relative to the other treatments (**Figure 10**). As compared to magnNPs alone, when both Cu and magnNPs were present in the soil, the MDA content increased. Eventually, Cu alone induced higher oxidative damage than the previous treatments, meaning that Cu has a higher negative impact on lipid peroxidation than Cu with magnNPs does. Oxidative stress is generally due to enhanced accumulation of ROS, particularly $O_2^{\cdot}$ and $H_2O_2^{\cdot}$ in chloroplasts, mitochondria, and peroxisomes (Abedi and Pakniyat, 2010). In the presence of transmission metals such as Fe^{2+} and Cu^{2+}, $H_2O_2^{\cdot}$ can breakdown to $OH^{\cdot}$ in the succession of reactions called Haber-Weiss and Fenton reactions (Birben et al., 2012). Generation of reactive radicals can cause cellular damage via depletion of enzyme activities through lipid peroxidation and reaction with nuclear proteins and DNA. Oxidative stress can also cause the impairment of macromolecules, which leads to the enhancement of the protection mechanism against ROS (Praveen et al., 2018). Amongst the antioxidant enzymes, superoxide dismutase is an important enzyme in protecting cells against oxidative stress (Alscher et al., 2002). $H_2O_2^{\cdot}$, which also results from the action of SOD, is toxic to cells and can be considered as a key agent in decomposing $H_2O_2^{\cdot}$. In the present study, results indicate that SOD was decreased with Cu contamination as Cu toxicity likely increased the activity of H_2O_2-scavenging enzymes (**Figure 10**). Furthermore, based on the analyses of antioxidant enzymes activities POD, it was observed that magnNPs, magnNPs-Cu and Cu treatments increased POD activity and MDA in a consistent way. Higher POD activity was induced in response to increased oxidative damage. In fact, peroxidase is deeply involved in all physiological events related to reduced growth in plants (such as lignification, cross-connection of cell wall polysaccharides), oxidation of indole-3-acetic acid (IAA), cell elongation, and phenol oxidation (Li et al., 2013). Therefore, changes in peroxidase activity are likely indicative of a change in metabolic activity of physiological events (respiration, photosynthesis, transpiration, gas exchange). POD activity from control plants was not increased as no such metabolic changes occurred.

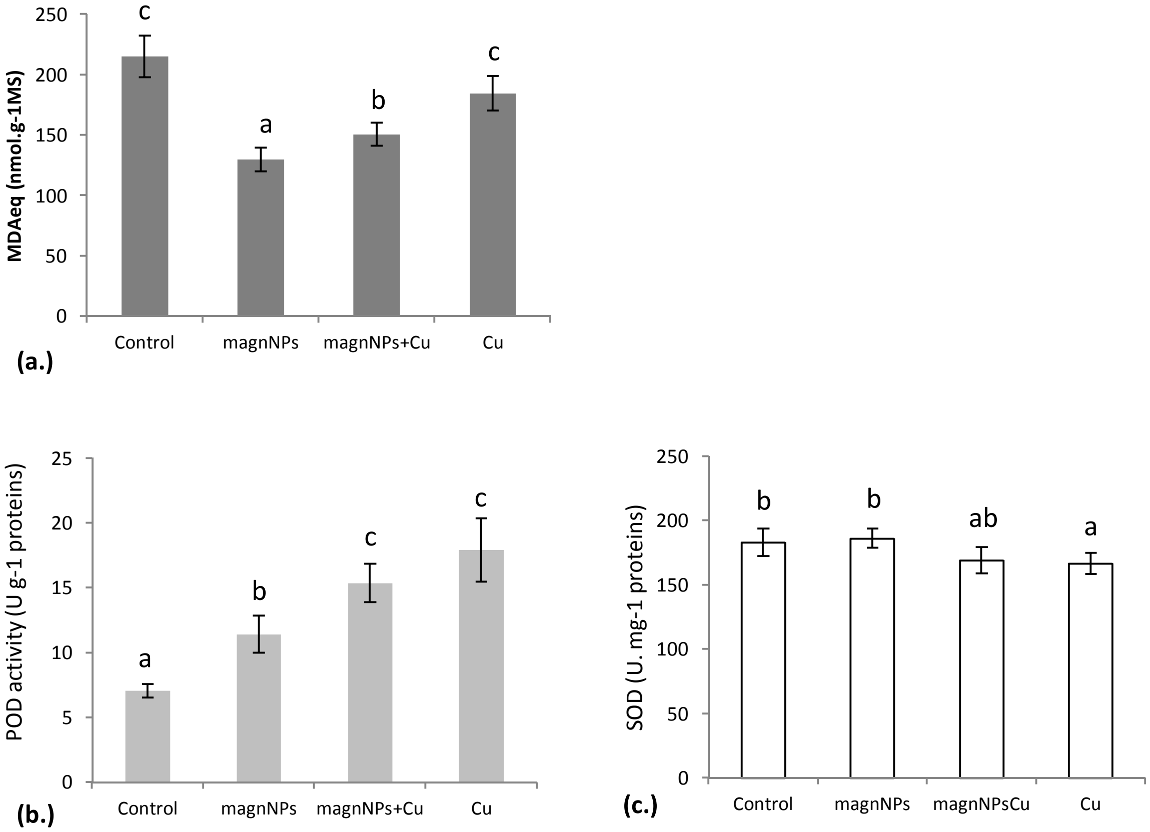

Figure 10: (a.) MDA content (nmol g^{-1} DW), (b.) POD activity (U mg^{-1} proteins) and (c.) SOD activity (U mg^{-1} proteins) measured in the leaves of sunflowers from soil column experiment (57 days growth) under the four treatments (control soil, soil with 1%wgt magnNPs, soil with copper (500 ppm) and soil with both copper (500 ppm) and magnNPs (1% wgt)).Data represent means ± standard error of the mean (n=4). Different letters above bars indicate statistical significance ($p < 0.05$) at each condition.

IV.4. Conclusions

The characteristics of magnNPs, together with those of the growth medium, are critical parameters to understand the fate and behavior of magnNPs with plants. In particular, it was evidenced that magnNPs uptake was improved in hydroponic cultures, from its aggregation at roots surfaces to its entering and accumulation in the stems and, less significantly, in the plant leaves. MagnNPs translocations in plants was highly decreased in plants grown in magnNPs-contaminated soils, not to occur in the aerial parts of the plants. In addition to soil matrix influence, compounds interacting with magnNPs, such as copper, also turned out to be critical in determining the fate and behavior of magnNPs within sunflower plants. In particular, Cu contamination decreased both magnNPs uptake by plants and its mobility in the medium. In turn, magnNPs also decreased Cu uptake and accumulation in the plants.

According to growth parameters and lipid peroxidation responses, magnNPs were not harmful to sunflower, even at high concentrations (1000 and 5000 mg L^{-1}) in hydroponics. MagnNPs were also able to provide Fe so that neither, growth retardation nor, decrease in chlorophyll content (Fe deficiency symptoms) was observed in Fe-deficient plants. MagnNPs further reduced the oxidative damage and triggered a higher antioxidant response than controls in both hydroponic cultures and soil column experiment. In Cu-contaminated soils, magnNPs tended to decrease Cu toxicity and it is thus, expected that magnNPs could help in phytoremediation, although Cu contamination was likely too high in this study for allowing magnNPs to scavenge enough Cu and prevent Cu toxicity.

Acknowledgments

We are thankful to L. Joanny for performing SEM analyses at the CMEBA (University of Rennes). This study was funded by both the CNRS-INSU/INEE EC2CO and the Interdisciplinary Mission programs through 'NanoOrgaTraces' and ALIEN projects, respectively both awarded to M. Pédrot and the University of Rennes through 'Défis Scientifiques Emergents' program awarded to A. Dia.

References:

T. Abedi and H. Pakniyat, 2010. Antioxidant Enzyme Changes in Response to Drought Stress in Ten Cultivars of Oilseed Rape (*Brassica napus* L.). Czech Journal of Genetic Plant Breeding, 46 (1), 27-34.

M. Adrees, S. Ali, A. Rizwan, M. Ibrahim, F. Abbas, M. Farid, M. Zia-ur-Rehman, M. Kashif Irshad, S. Aslam Bharwana, 2012. The effect of excess copper on growth and physiology of important food crops: a review. EnvironmentalScience Pollution Research, 22, 8148-8162.

G. R. Aïken, H. Hsu-Kim and J. N. Ryan, 2011. Influence of dissolved organic matter on the environmental fate of metals, nanoparticles and colloids. Environmental Science and Technology, 45, 3196-3201.

R.G. Alscher, N. Erturk and L.S. Heath, 2002. Role of superoxide dismutases (SODs) in controlling oxidative stress. Journal of Experimental Botany, 5, 31331-1341.

M. Amde, J.- F. Liu, Z.-Q. Tan and D. Bekana, 2017. Transformation and bioavailability of metal oxide nanoparticles in aquatic and terrestrial environments. A review. Environmental Pollution, 230, 250-267.

N. A. Anjum, M. A. Merios Rodrigo, A. Moulick, Z. Heger, P. Kopel, O. Zitka, V. Adam, A. S. Lukatkin, A. C. Duarte, E. Pereira and R. Kizek, 2016. Transport phenomena of nanoparticles in plants and animals/humans. Environmental Research, 151, 233-243.

M. Baalhousha, Y. Nur, I. Römer, M. Tejmaya, J.R. Lead, 2013. Effect of monovalent and divalent cations, anions and fulvic acid on aggregation of citrate-coated silver nanoparticles. Science of the Total Environment, 454-455, 119-131.

L. Barhoumi and D.Dewez, 2013. Toxicity of superparamagnetic iron oxide nanoparticles on green Alga *Chlorella vulgari.* BioMed Research International, 2013, Article ID 647974, 11 p.

R. Barrena, E. Casals, J. Colon, X. Font, A. Sanchez and V. Puntes, 2009. Evaluation of the ecotoxicity of model nanoparticles. Chemosphere, 75, 850-857.

T. Baszynsk, A. Tukendorf, M. Ruszkowska, E. Skorzynska, and W. Maksymiec, 1988. Characteristics of the photosynthetic apparatus of copper non tolerant spinach exposed to excess copper. Journal of plant physiology, 132, 708-713.

G. Batley, J. K. Kirbyand M. J. McLaughlin, 2013. Fate and Risks of nanomaterials in aquatic and terrestrial environments. Accounts of chemical research, 46(3), 854-862.

O. Blokhina, E. Virolainen and K. Fagerstedt, 2003. Antioxydants, Oxidative Damage and Oxygen Deprivation Stress: a Review. Annals of Botany (91), 179-194

S. Bombin, M. Lefebvre, J. Sherwood, Y. Xu, Y. Bao, and K. M. Ramonell, 2015. Development and Reproductive effects of Iron Oxide Nanoparticles in *Arabidopsis thaliana.* International Journal of Molecular Sciences, 16, 24174-24193.

J.F. Briat, C. Curie and F. Gaymard, 2007. Iron utilization and metabolism in plants.Current Opinion in Plant Biology, 10, 276-282.

E. Birben, U. M. Sahiner, C. Sackesen, S. Erzurum and O. Kalayci, 2012. Oxidative Stress and Antioxidant Defense. WAO Journal (5), 9-19.

Bradford M., 1976. A rapid and sensitive method for the quantitation of microgram quantities of protein utilizing the principle of protein-dye binding. Analytical Biochemistry, 72, 248-254.

I. Cakmak and H. Marschner, 1992. Magnesium deficiency and high light intensity enhance activities of super oxide dismutase, ascorbate peroxidase and gluthatione reductase in bean leaves. Plant Physiology, 98, 1222-1227.

Z. Cifuentes, L. Custardoy, J.M. de la fuente, C. Marquina, M. R. Ibarra, D. Rubiales and A. Peres-de-Luque, 2010. Absorption and translocation to the aerial part of magnetic carbon–coated nanoparticles through the root of different crop plants. Journal of Nanobiotechnology, 8, 26.

C. Claudio, E. di lorio, Q. Liu, Z. Jiang, and V. Barron, 2017. Iron Oxide Nanoparticles in Soils: Environmental and Agronomic Importance. Journal of Nanoscience and Nanotechnology 17, 4449-4460.

C. Colombo, G. Palumbo, J.-Z. He and S. Cesco, 2014. Review on iron availability in soil: interaction of Fe minerals, plants, and microbes. Journal of Soil and Sediments, 14(3), 538-548.

R. M. Cornell and U. Schwertmann, 2003. The iron oxides : structure, properties, reactions, occurrences and uses. 2nd edition, *http://trove.nla.gov.au/version/36973177*, Edited by Wiley-VCH, 664p.

E. Demangeat, M. Pédrot, A. Dia, M. Bouhnik-Le-Coz, F. Grasset, K. Hanna, M. Kamagate and F.Cabello-Hurtado, 2018. Colloidal and chemical stabilities of iron oxide nanoparticles in aqueous solution: the interplay of structural, chemical and environmental drivers. Environmental Science: Nano, 5, 992-1001.

S. Dey, P.B. Mazumder and S.B. Paul, 2014. Effect of copper on growth and chlorophyll content in tea plants (CAMELLIA SINENSIS (L.) O. KUNTZE). International Journal of Research in Applied, Natural and Social Sciences (IMPACT: IJRANSS), 2(5), 223-230.

R. Esteban, O. Barruia, U. Artetxe, B. Fernandez-Marin, A. Hernandez and J. I. Garcia-Plazaola, 2015. Internal and external factors affecting photosynthetic pigment composition in plants: a meta-analytical approach. New physiologist, 206, 268-280.

C. H. Foyer and S. Shigeoka, 2010. Understanding Oxidative Stress and Antioxydant Functions to Enhance Photosynthesis. Update on Oxidative Stress and Photosynthesis, 155, 93-100.

C.N. Giannopolis and S.K. Ries, 1977. Superoxide Dismutases: I. Occurrence in higher plants. Plant Physiology, 59(2), 309-314.

L. Goswani, K.-H. Kim, A. Deep, P. Das, S. S. Bhattacharya, S. Kumar and A. A. Adelodun, 2017. Engineered nanoparticles:Nature, behavior and effects on the environment. Journal of Environmental Management, 196, 297-315.

J. Gzyl, K.Rymer and E. A. Gwóźdź, 2009. Differential response of antioxidant enzymes to cadmium stress in tolerant and sensitive cell line of cucumber (*Cucumis sativus L.*), 56(4), 723-727.

A. Hadju, E. Illés, E. Tombacz and I. Borbath, 2009. Surface charging, polyanionic coating and colloid stability of magnetite nanoparticles. Colloids and Surfaces A: Physicochemical and Engineering Aspects 347, 104-108.

T. Hiemstra and W.H. Van Riemsdijk, 2006. On the relationship between charge distribution, surface hydration and the structure of the interface of metal hydroxides. Journal of Colloid and Interface Science, 301, 1-18.

D.R. Hoagland and D.I. Arnon, 1950. The water-culture method for growing plants without soil. California Agricultural Experiment Station, Circular 347, 32p.

M. F. Hochella Jr., S. K. Lower, P. A. Maurice, R. Lee Penn, N. Sahai, D. L. Sparks, B. S. Twining, 2008. Nanominerals, Mineral Nanoparticles, and Earth Systems. Science 319, 1631-1635

D. M. Hodges, J. M. DeLong, C. F. Forney and R. K. Prange, 1999.Improving the thiobarbituric acid-reactive-substances assay for estimating lipid peroxidation in plant tissues containing anthocyanin and other interfering compounds. Planta, 207, 604-611.

Hu, H. Li, J. Li, G. Zhao, W. Wu, L. Liu, Q. Wang, and Y. Guo, 2018. Absorption and bio-transformation of selenium nanoparticles by wheat seedlings (Triticum aestivum L.). Frontiers in Plant Science, 9, 597-607.

M.F. Iannone, M. D. Groppa, M.E. de Sousa, M. Beatriz Fernandez van Raap and M.P. Benavides, 2016. Impact of Magnetite Iron Oxide nanoparticles on wheat (*Triticum aestivum L.*) development: evaluation of oxidative damage. Environmental and Experimental Botany. 131, 77-88.

S. H. Joo and D. Zhao, 2017. Environmental dynamics of metal oxide nanoparticles in heterogeneous systems: a review. Journal of Hazardous Materials, 322, 29-47.

M. Kah, S. Beulke, K. Tiede and T. Hofmann, 2013. Nanopesticides: state of knowledge, environmental fate, and exposure modeling. Critical Reviews Environmental Science Technology, 43(16), 1823-1867.

S. E. Khalafalla and G. W. Reimers, 1980. Preparation of dilution-stable aqueous magnetic fluids. IEEE Transactions on Magnetics, 16(2), 178-183.

L.R. Khot, S. Sankaran, J.M. Maja, R. Ehsani and E.W. Schuster, 2012. Applications of nanomaterials in agricultural production and crop protection: a review. Crop Protection 35, 64-70.

J.-H. Kim, Y. Lee, E.-J. Kim, S. Gu, E.-J. Sohn and Y.-S. Seo, 2014. Exposure of iron nanoparticles to Arabidopsis thaliana enhances root elongation by triggering cell wall loosening. Environmental Science and Technology, 48 (6), 3477-3485.

M. Labudda, 2013. Lipid peroxidation as a biochemical marker for oxidative stress during drought. An effective tool for plant breeding, E-wydawnictwo, Poland. 1-12.

J. Li, P.R. Chang, J. Huang, Y. Wang, H. Yuan and H. Ren, 2013. Physiological effects of magnetic iron oxide nanoparticles towards watermelon. Journal of Nanoscience and Nanotechnology, 13, 5516-5567.

C.L. Li, F. Ji, S. Wang, J.J. Zhang, Q. Gao, J.G. Wu, L.P. Zhao, L.C. Wang and L.R. Zheng, 2015. Adsorption of Cu(II) on humic acids derived from different organic materials, Journal of Integrative Agriculture 14(1), 168-177.

J. Lin, W. Jiang, D. Liu, 2003. Accumulation of copper by roots, hypocotyls cotyledons and leaves of sunflower (*Helianthus annuus* L.). Bioresource Technology 86, 151-155.

Lichtenthaler HK, Wellburn AR,1983. Determination of total carotenoids and chlorophyll *a* and *b* of leaf extract in different solvents. Biochemical Society Transactions, 11, 591–592.

J.-F. Liu, Z.-S. Zhao, and G.-B. Jiang, 2008. Coating Fe_3O_4 Magnetic Nanoparticles with Humic Acid for High efficient Removal of Heavy Metals in water. Environmental Science and Technology (42), 6949-6954.

R. Liu, H. Zhang and R. Lal, 2016. Effects of stabilized Nanoparticles of copper, zinc, manganese and iron oxides in low concentration on lettuce (*Lactuca sativa*) seed germination: nanotoxicants or nanonutrients? Water Air Soil Pollution, 227, 42.

S. Legros, P. Chaurand, J. Rose, A. Masion, V. Briois, J.H. Ferrasse, H.S. Macary, J.Y. Bottero and E. Doelsch, 2010. Investgation of copper speciation in pig slurry by a multipletechnique approach. Environmental Science and Technology, 44, 6926-6932.

H. Marschner, 1995. Mineral nutrition of higher plants, 2nd edition. Academic, San Diego.

H. Marschner, V. Römheld, and M. Kissel, 1986. Different strategies in higher plants in mobilization and uptake of iron. Journal of Plant Nutrition, 9 (3-7), 695-713.

R. Massart, 1981. Preparation of aqueous magnetic liquids in alkaline and acidic media. IEEE Transactions on Magnetics, 17,1247-1248.

D.P. Maxbauer, J.M. Feinberg, D.L. Fox and Edward A. Nater, 2017.Response of pedogenic magnetite to changing vegetation in soils developed under uniform climate, topography, and parent material. Scientific Reports,7, 17575-17785.

A. Michaud, M. Bravin, M. Galleguillos and P. Hinsinger, 2007. Copper uptake and phytotoxicity as assessed in situ for durum wheat (*Triticum turgidum*, durum L.) cultivated in Cu-contaminated, former vineyard soils. Plant Soil, 298 (1-2), 99-111.

P. Miralles, T. L. Church and A. T. Harris Toxicity, Uptake, and Translocation of Engineered Nanomaterials in Vascular plants, 2012. Environmental Science and Technology, 46, 9224-9239.

J. Morrissey and M. L. Guerinot, 2009. Iron uptake and transport in plants: the good, the bad, and the ionome. Chem Rev 109 (10), 4553-4567.

E. Navarro, A. Baun, R. Behra, N. B. Hartman, J. Filser, A-J. Miao, A.Qigg, P. H. Santschi and L. Sigg, 2008. Environmental behavior and ecotoxicity of engineered nanoparticles to algae, plants and fungi. Ecotoxicology, 17, 372-386.

B. Nowack, T. Bucheli, 2007. Occurrence, behavior and effects of nanoparticles in the environment. Environmental Pollution, 150, 5-22.

G. Ouzounidou , 1994. Copper induced changes on growth, metal content and photosynthetic function of *Alyssum montanum L.* plants. Environmental and experimental Botany 34 (2), 165-172.

M.G.M. Palmqvist, G.A. Seisenbaeva, P. Svedlindh and V. G. Kessler, 2017. Maghemite Nanoparticles Act as Nanoenzymes, Improving Growth and Abiotic Stress Tolerance in Brassica napus. Nanoscale Research Letters, 12, 631-640.

C. Peng, D. Duan, C. Xu, Y. Chen, L. Sun, H. Zhang, X. Yuan, L. Zheng, Y. Yang, J. Yang, X. Zhen and Y. Chen, 2015. Translocation and biotransformation of CuO nanoparticles in rice (Oryza sativa L.) plants. Environmental Pollution, 197, 99-107.

F. Perrault, M. Samadaniand D. Dewez, 2013. Effect of soluble copper released from copper oxide nanoparticles solubilization on growth and photosynthetic processes of *Lemnagibba* L. Nanotoxicology, 1-9.

R. Podila and J. M. Brown, 2013. Toxicity of engineered nanomaterials: a physic-chemicalperspective. Journal of Biochemical and Molecular Toxicology,27(1), 50-55.

S. R. Pouran, A. A. Abdul Raman and W. M. A.W.Daud, 2014.Review on the application of modified iron oxides as heterogeneous catalysts in Fenton reactions. Journal of Cleaner Production (64), 24-45.

A. Praveen, E. Khan, S. Ngiimei D., M. Perwez, M. Sadar andM. Gupta, 2018. Iron Oxide Nanoparticles as Nano-adsorbents: A Possible Way to Reduce Arsenic Phytotoxicity in Indian Mustard Plant (*Brassica juncea* L.). Journal of Plant Growth Regulation, 37(2), 612-624.

J. Putter, 1974. Peroxidase. In: Bergmeyer, H.U., Ed.., Methods of enzymatic analysis, Verlag Chemie, Weinham, 685-690.

H. Qian, X. Peng, X. Han, J. Ren, L. Sun andZ. Fu,2013. Comparison of the toxicity of silver nanoparticles and silver ions on the growth of terrestrial plant model *Arabidopsis thaliana*. Journal of Environmental Sciences, 25,1947–1956.

A. Rastogi, M. Zivcak, O. Sytar, H. M. Kalaji, X. He, S. Mbarki and M. Brestic, 2017. Impact of metal and metal oxide nanoparticles on plant: a critical review. Frontiers in Chemistry, 5, 78-94.

F. Reith and G. Cornelis, 2017. Effect of soil properties on gold- and platinum nanoparticle mobility, Chemical Geology, 466, 446-453.

C. M. Rico, S. Majumdar, M. Duarte-Gardea, J. R. Peralta-Videa and J. L. Gardea-Torresdey,2011. Interaction of nanoparticles with edible plants and their possible implications in the food chain. Journal of Agricultural and Food Chemistry, 59, 3485–3498.

G.R.Rout and S. Sahoo, 2015. Role of iron in plant growth and metabolism. Reviews in Agricultural Science (3), 1-24.

O. Sagee, I.H. Dror and B. Berkowitz, 2012. Transport of silver nanoparticles (AgNPs) in soil. Chemosphere, 88, 670-675.

Z. Salama and H. El-Beltagi, 2009. Effect of Fe deficiency on antioxidant system in leaves of three flax cultivars. NotulaeBotanicaeHortiAgrobotanici Cluj-Napoca 37 (1), 122-128.

V.K. Sharma, J. Filip, J. Zboril and R.S. Varma, 2015. Natural inorganic nanoparticles – formation, fate and toxicity in the environment. Chemical Society Reviews, 44(23), 8410-8423.

S. Shigeoka, T. Ishikawa, M. Tamoi, Y. Miyagawa, T. Takeda, Y. Yabuta, K. Yoshimura, 2002. Regulation and function of ascorbate peroxidase isoenzymes. Journal of Experimental Botany, 53, 1305-1319.

P. Solanki, A. Bhargava, H. Chhipa, N. Jain and J. Panwar, 2015. Nano-fertilizers and their smart delivery system. Nanotechnologies in food and agriculture. Springer Internationl Publishing Cham, 81-101.

S. de Souza Pinto, A. E. de Souza, M. A. Oliva and E. Gusmao Pereira, 2016. Oxidative damage and photosynthetic impairment in tropical rice cultivars upon exposure to excess iron. Scientia Agricola 73 (3), 217-226.

W. H. Suh, K. Suslick, G. D. Stucky and Y.-H. Suh, 2009. Nanotechnology, nanotoxicology, and neuroscience. Progress in Neurobiology, 87, 133-170.

B.K.G. Theng and G. Yuan, 2007. Nanoparticles in the soil environment. Elements, 4, 395-399.

D. K. Tripathi, Shweta, S. Singh, S. Singh, R. Pandey, V. P. Singh, N. C. Sharma, S. M. Prasad, N. K. Dubey and D. K. Chauhan, 2017. An overview on manufactured nanoparticles in plants: Uptake, translocation, accumulation and phytoxicity. Plant physiology and Biochemistry, 110, 2-12.

N.C. Uren, 1984. Forms, reactions and availability of iron in soils. Journal of Plant Nutrition, 7 (1-5), 165-176.

A. M. Vindedahl, J. H. Strehlau, W. A. Arnold and R. L. Penn, 2016. Organic matter and iron oxide nanoparticles: aggregation, interactions and reactivity. Environmental Science: Nano., 3, 494-505.

L. Wang, J. Li, Q. Jiang and L. Zhao, 2012. Water-soluble Fe_3O_4 nanoparticles with high solubility for removal of heavy-metal ions from waste water. Dalton Transactions 41, 4544-4551.

D. Yeghicheyan, C. Bossy, M. Bouhnik Le Coz, C. Douchet, G. Granier, A. Heimburger, F. Lacan, A. Lanzanova, T. C. C. Rousseau, J.L. Seidel, M. Tharaud, F. Candaudap, J. Chmeleff, C. Cloquet, S. Delpoux, M. Labatut, R. Losno, C. Pradoux Y. Sivry and J. E. Sonke, , 2013. Geostandards and Geoanalytical Research, 37(4),449.

P.K. Yudina, L.A. Ivanova, D.A. Rhondina, N. V. Zolotareva, and L.A. Ivanov, 2017. Variation of leaf traits and pigment content in three species of steppe plants depending on climate aridity. Russian Journal of Plant Physiology, 64 (3), 410-422.

H.Zhu, J. Han, J.Q. Xiao and Y. Jin, 2008. Uptake, translocation, and accumulation of manufactured iron oxide nanoparticles by pumpkin plants. Journal of Environmental Monitoring,10, 713–717.

Supporting Information

A. Germination experiments

Germination experiments have also been conducted on maize, bean and wheat following the same treatments than in the study for sunflower: Fe-deficient (ø) Hoagland (0.5x) control; Fe-deficient (ø) Hoagland (0.5x) with 5mg L^{-1} magnNPs; Fe-deficient (ø) Hoagland (0.5x) with 5000 mg L^{-1}; Hoagland (0.5x) control; Hoagland (0.5x M) with 5 mg L^{-1} magnNPs; magnNPs; Hoagland (0.5x) with 5000 mg L^{-1} magnNPs).

Fresh weight measurements (g) are here after displayed:

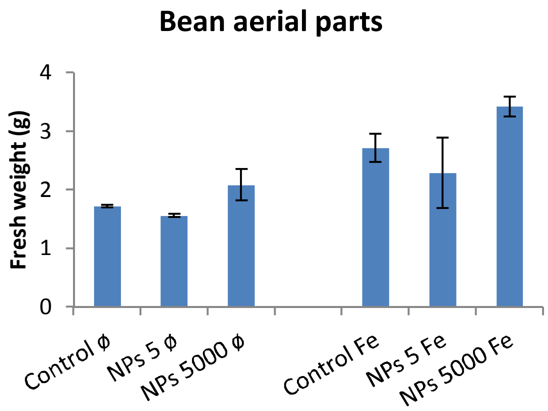

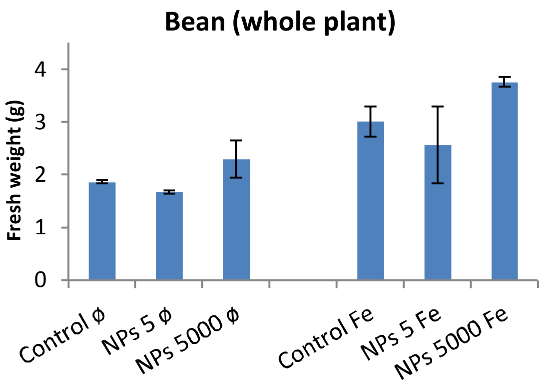

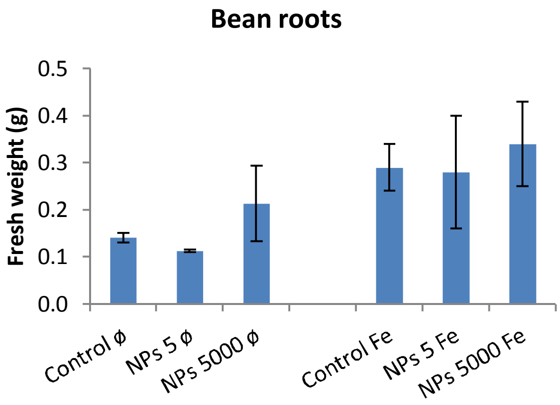

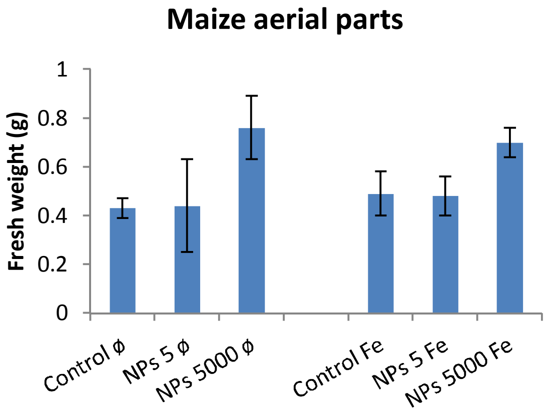
Maize aerial parts
Fresh weight (g)
1
0.8
0.6
0.4
0.2
0
Control ø
NPs 5 ø
NPs 5000 ø
Control Fe
NPs 5 Fe
NPs 5000 Fe

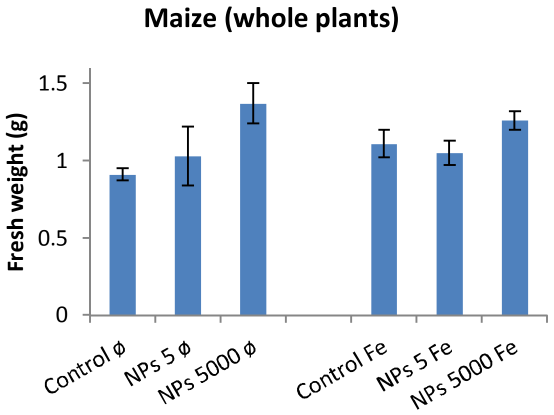
Maize (whole plants)
Fresh weight (g)
1.5
1
0.5
0
Control ø
NPs 5 ø
NPs 5000 ø
Control Fe
NPs 5 Fe
NPs 5000 Fe

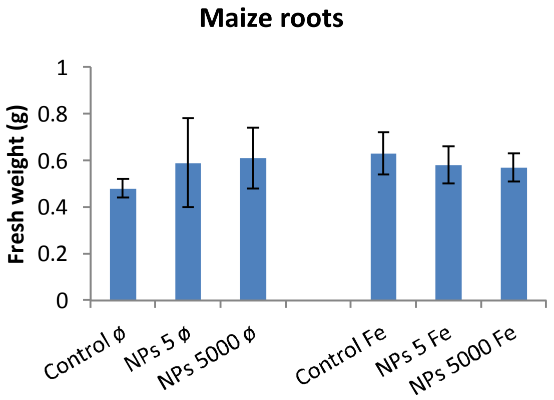
Maize roots
Fresh weight (g)
1
0.8
0.6
0.4
0.2
0
Control ø
NPs 5 ø
NPs 5000 ø
Control Fe
NPs 5 Fe
NPs 5000 Fe

Figure S1: Fresh weights of plants measured after 7 day germination testing. Bean, maize and wheat seeds were exposed to six different treatments: Control ø (Fe-deficient Hoagland (0.5x)); NPs 5 ø (Fe-deficient Hoagland (0.5x) with 5 mg L^{-1} magnNPs); NPs 5000 ø (Fe-deficient Hoagland (0.5x) with 5000 mg L^{-1} magNPs); Control Fe (Hoagland (0.5x)); NPs 5 Fe (Hoagland (0.5x) with 5 mg L^{-1} magnNPs); NPs 5000 Fe (Hoagland (0.5x) with 5000 mg L^{-1} magnNPs). Data represent mean ± standard error of the mean of three independent experiments (n=6).

B. Hydroponic experiments

Hydroponic experiments have also been conducted on maize and bean following the same treatments than in the sunflower study: Fe-deficient (ø) Hoagland (0.5x) control; Fe-deficient (ø) Hoagland (0.5x) with 5mg L^{-1}magnNPs; Fe-deficient (ø) Hoagland (0.5x) with 1000 mg L^{-1}magnNPs; Hoagland (0.5x) control; Hoagland (0.5x M) with 5mg L^{-1} magnNPs; Hoagland (0.5x) with 1000 mg L^{-1} magnNPs

- Fresh weight measurements (g) are displayed here after:

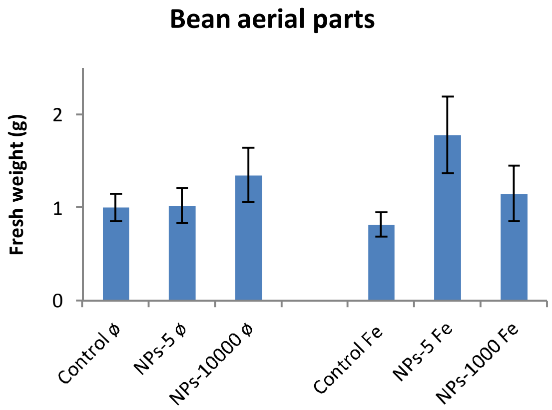
Bean aerial parts

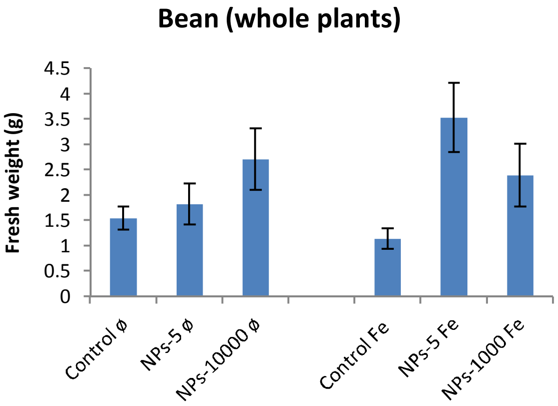
Bean (whole plants)

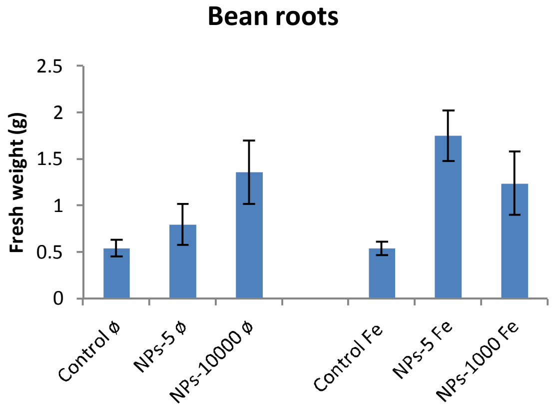
Bean roots

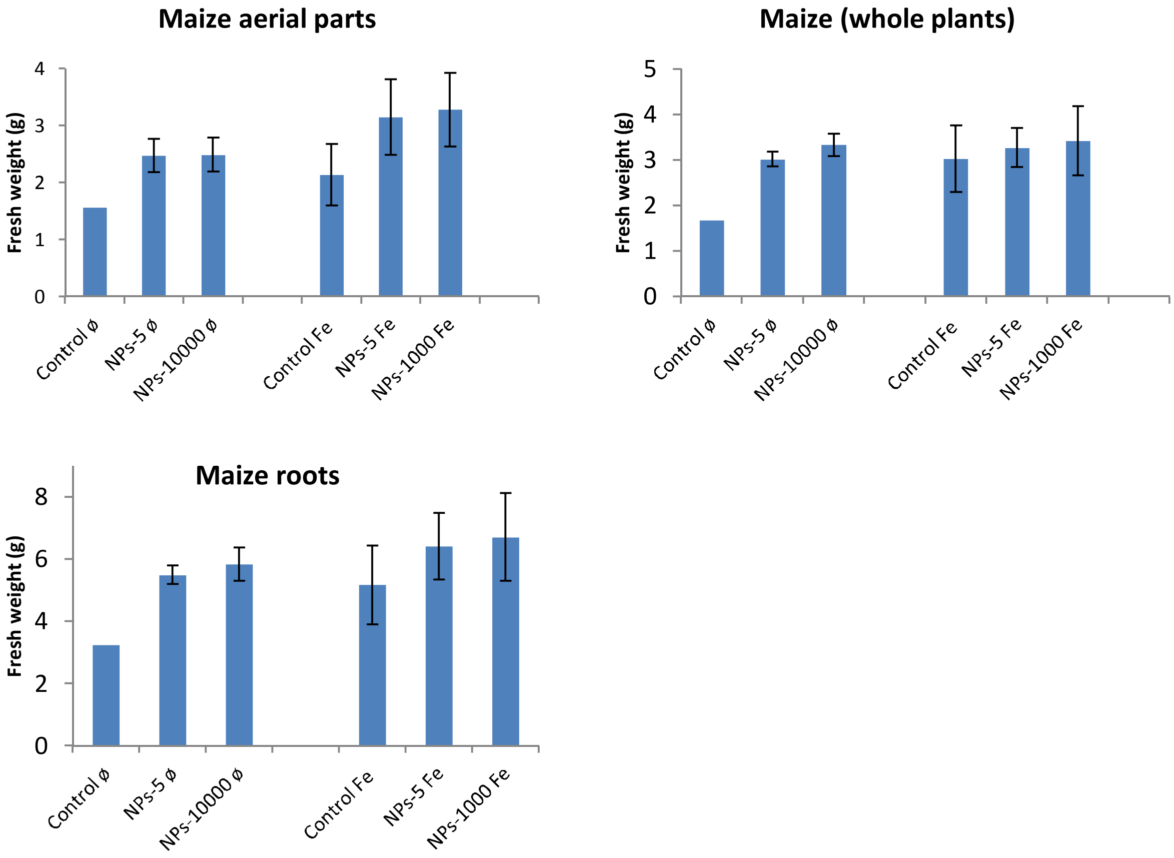

Figure S2: Fresh weights of plants measured after 18 days in hydroponic culture. Seven-days-old seedlings were exposed to six different treatments: Control ø (Fe-deficient Hoagland (0.5x)); NPs 5 ø (Fe-deficient Hoagland (0.5x) with 5 mg L^{-1} magnNPs); NPs 1000 ø (Fe-deficient Hoagland (0.5x) with 1000 mg L^{-1} magNPs); Control Fe (Hoagland (0.5x)); NPs 5 Fe (Hoagland (0.5x) with 5 mg L^{-1} magnNPs); NPs 1000 Fe (Hoagland (0.5x) with 1000 mg L^{-1} magnNPs). Data represent mean ± standard error of the mean of two independent experiments.

C. Soil columns: experimental set up

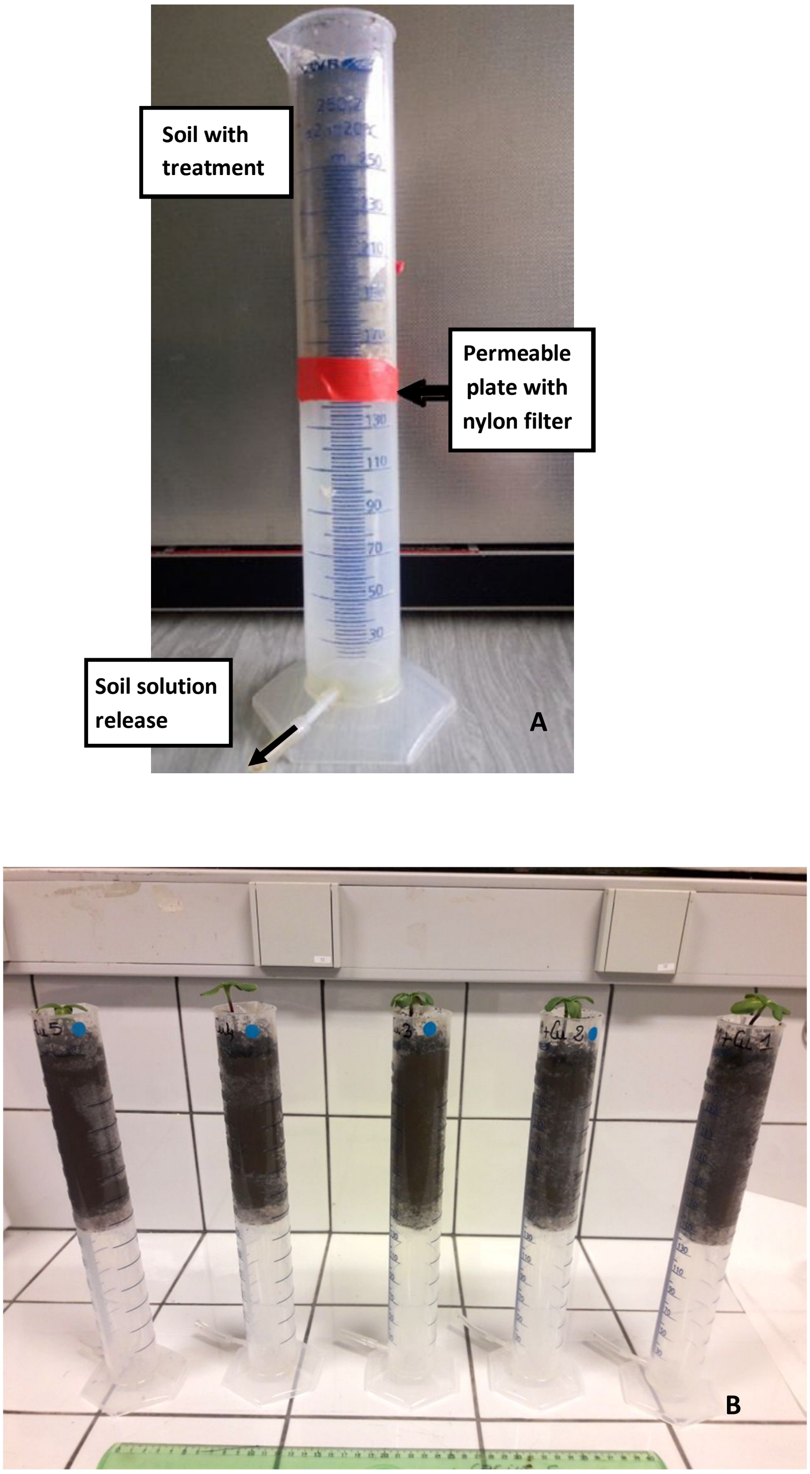

Figure S3: Soil column experiments. (A) Soil column design, before introducing sunflower seeds; (B) After 5 days growth, sunflowers with magnNPs-Cu treatment.

D. SEM and EDS analyses

EDS analyses were acquiredalong with SEM pictures, at the surface of root fragments.

- SEM image with mineralized depositsare supposed to be aggregated magnNPs (the photo shows another spot – (but from the same sample) than the one displayed in the study). At point 43, the EDS spectrum is marked by high iron (Fe) and oxygen (O) peaks.These elementary peaks only slightly decreased farther from point 43 (point 45) but, still evidenced magnNPs occurrence close to that point (still high Fe concentration).

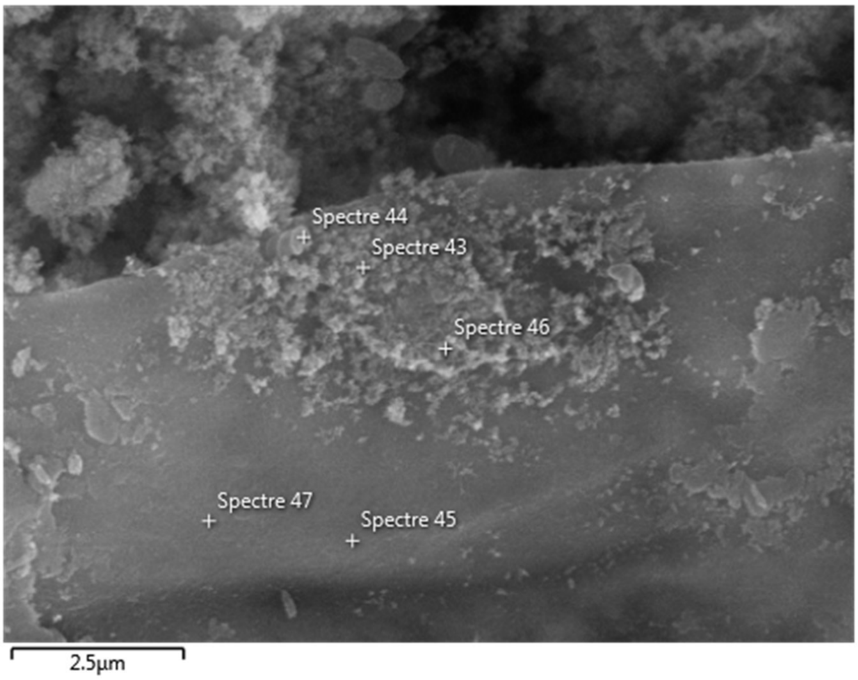

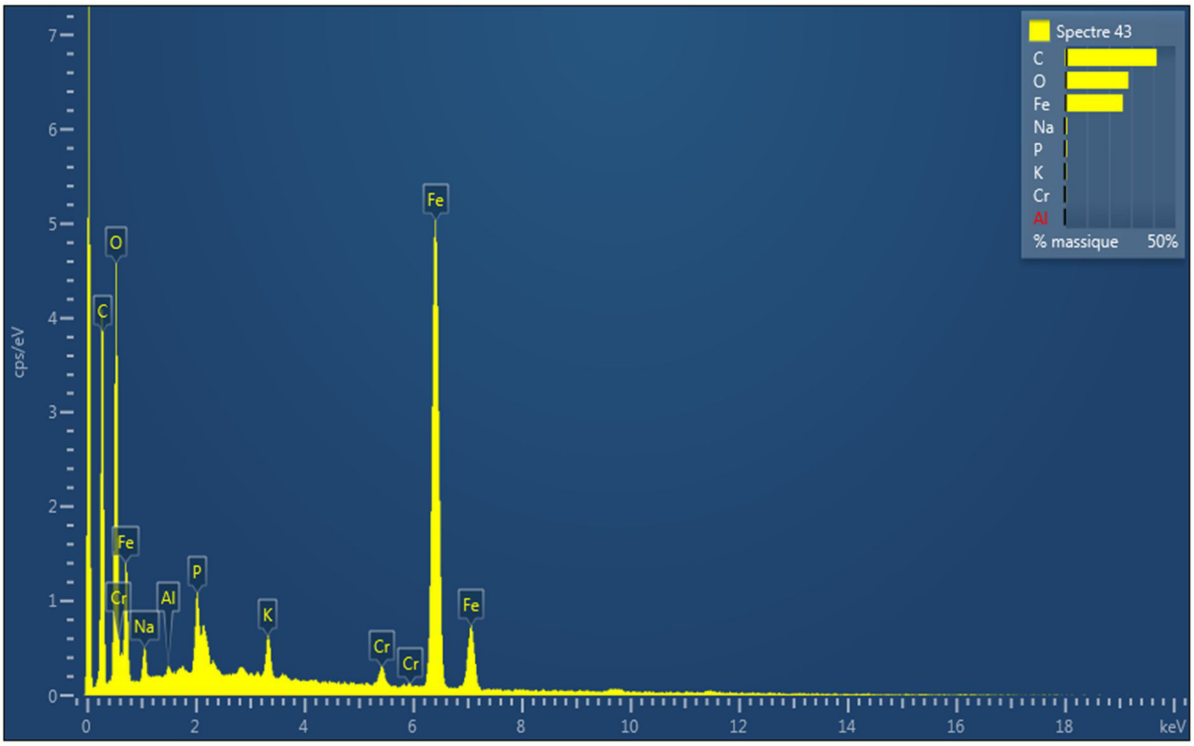

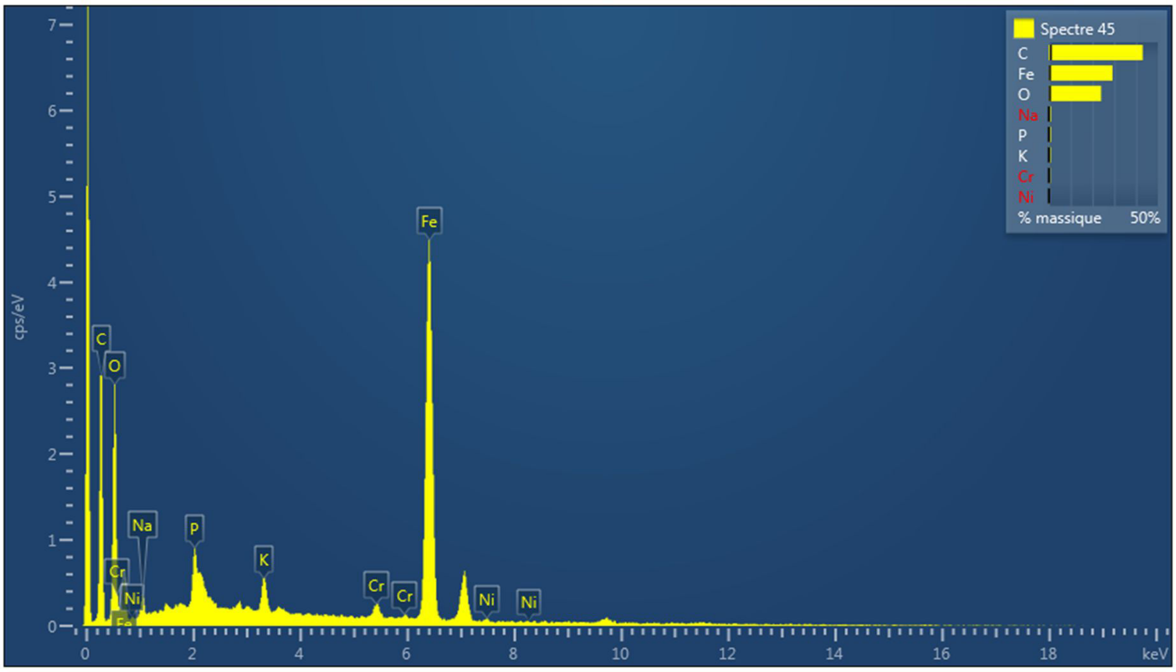

Figure S4: EDS spectrums (from SEM analysis) ofthe deposits observed at the surface of a plant root fragment exposed to high concentration (2500 mg L^{-1}) of magnNPs.

- SEM image at higher distance from magnNPs. EDS analyses exhibit lower iron (Fe) and oxygen (O) preaks as magnNPs are further (e.g.EDS spectrum of point 49).

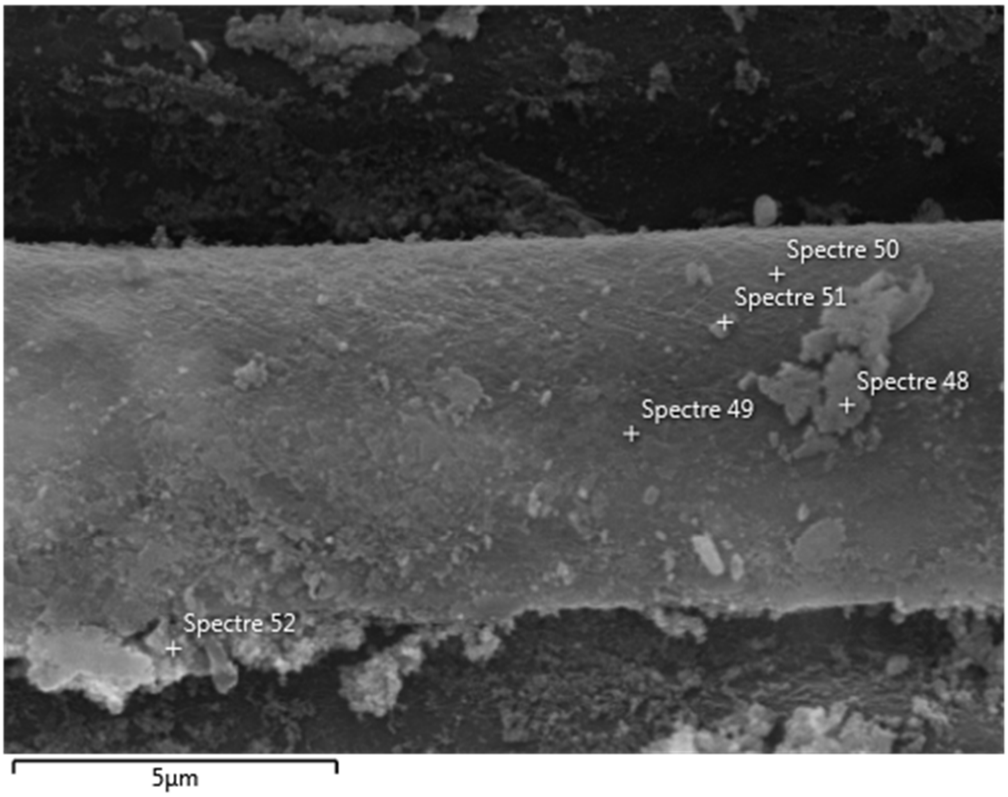

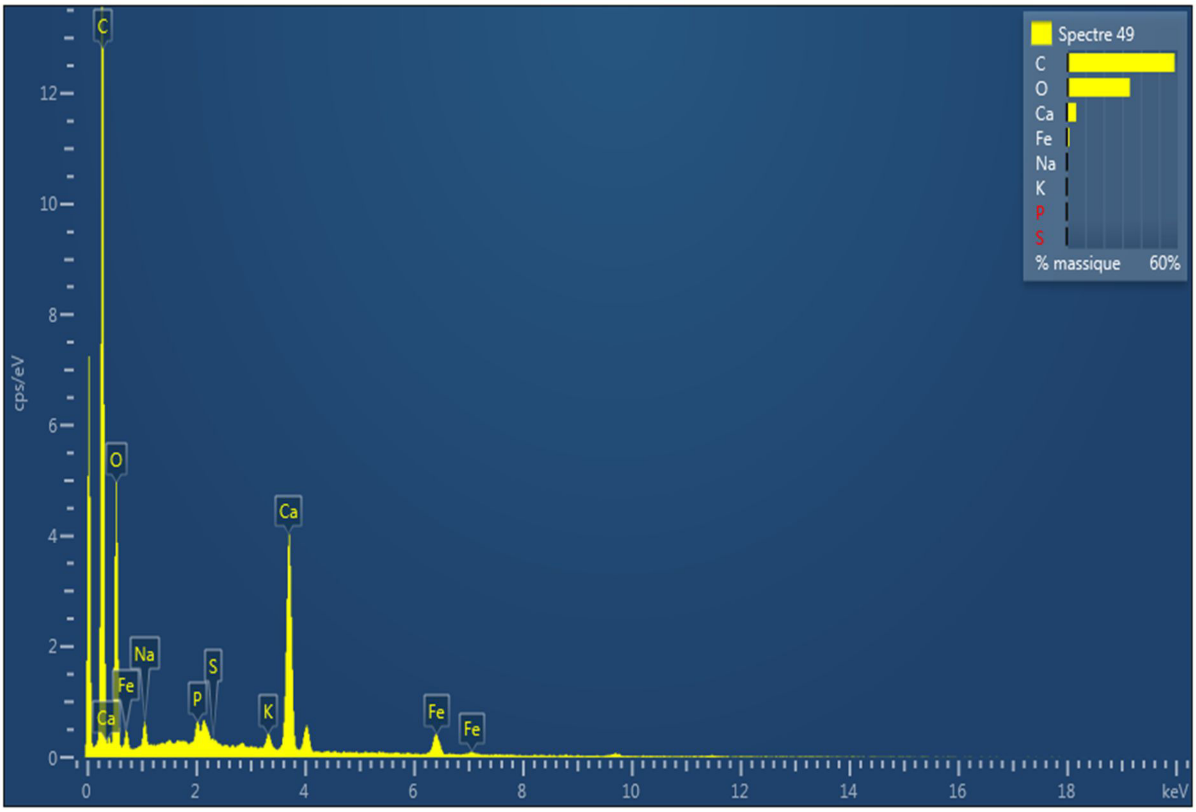

Figure S5: EDS spectrums from SEM analysis on the root surface, showing only few iron in the tissue.

- EDS spectrum obtained for magnNPs alone (TEM, Au grid). EDS displays high iron (Fe) and oxygen (O).

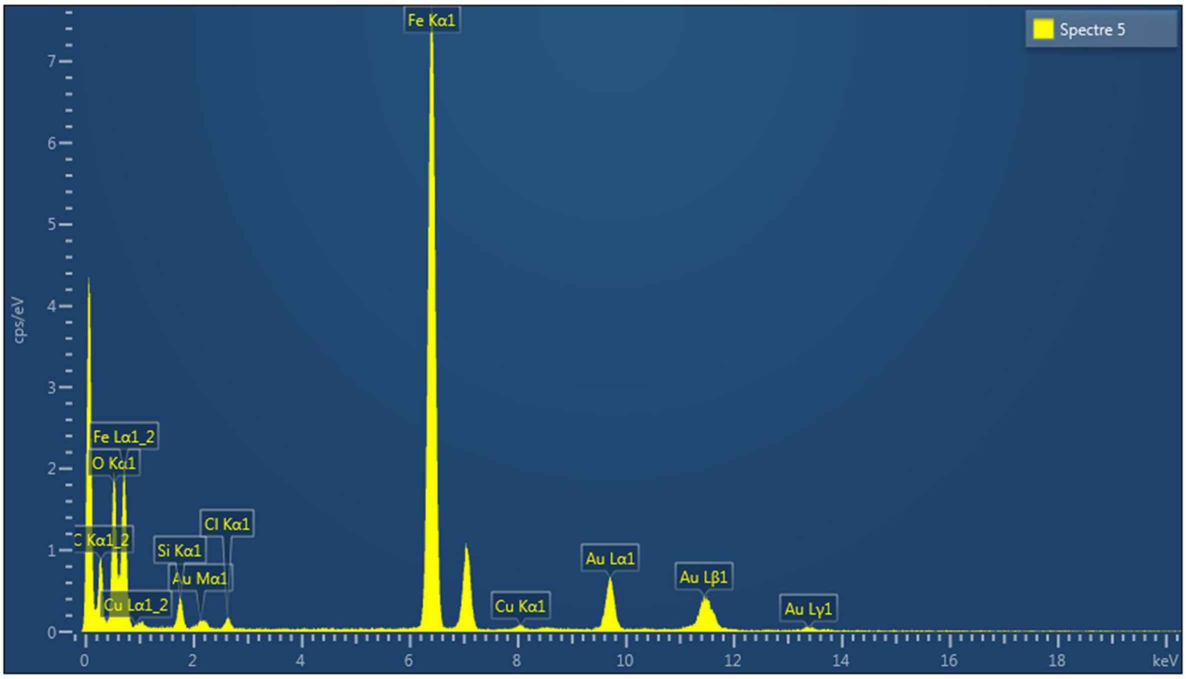

Figure S6: EDS spectra obtained from TEM analysis of magnNPs alone (without any previous contact with plants).

Chapitre 5 :

Discussion générale

La forte utilisation des NPs-Fe dans de multiples domaines, toujours plus diversifiés, est à l'origine de leur libération et diffusion dans les différents compartiments de l'environnement sans que les conséquences environnementales ne soient encore réellement connues. Mais, avant qu'elles n'entrent en contact avec les organismes vivants, les NPs-Fe arborent une réactivité de surface considérable. Celle-ci est responsable d'une part, des interactions mutuelles NPs-Fe/NPs-Fe, qui définissent leur comportement en solution (1^{er} volet de la thèse), et d'autre part, des interactions avec les multiples composants organiques et inorganiques du sol et des eaux naturelles, susceptibles de modifier leurs propriétés intrinsèques (propriétés chimiques et propriétés structurales) et d'affecter la dynamique des éléments traces (ETs) (deuxième volet de la thèse). Enfin, les conséquences de ces transformations étant susceptibles d'affecter d'une part, le comportement des NPs-Fe et la composition élémentaire des solutions de sol, et d'autre part, la biodisponibilité et toxicité des NPs-Fe pour les plantes, l'étude des interactions entre les NPs-Fe et les plantes constitue l'objet du troisième volet de cette thèse.

V.1. Comportement, interactions et devenir des NPs-Fe dans l'environnement

V.1.1. Comment évoluent les propriétés des NPs-Fe avec leur milieu ?

D'un côté, les conditions du milieu (pH, Eh, température, O_2) affectent leurs propriétés intrinsèques, telle que la cristallochimie des NPs-Fe. Nous avons notamment mis en évidence dans cette étude, la transformation progressive et rapide (5 jours) de la magnétite en maghémite par oxydation (cf. Chap.2). Celle-ci se caractérise par une diminution du rapport Fe(II)/Fe(III) et s'opère généralement de la surface vers le cœur de l'oxyde (Frison et al., 2013 ; Löhr et al., 2017), formant au fil du temps, une couche oxydée de plus en plus épaisse (sans changer la taille de la particule) vers le centre de la nanoparticule de magnétite/maghémite. Cette transformation minéralogique est fondamentale car en modifiant rapidement ses propriétés de surface, la magnétite se comportera plutôt comme une maghémite avec les constituants interagissant à sa surface. Les NPs de maghémite ont une surface spécifique généralement plus élevée que les NPs de magnétite de même taille (dans cette étude, augmentation de 115 à 130 $m^2 g^{-1}$ après oxydation) et un point de charge nul (pHzpc), également supérieur à celui de la magnétite (6.3 pour la magnétite contre environ 7 pour une maghémite de même taille). Par ailleurs, l'oxydation de Fe^{2+} en Fe^{3+} génère des lacunes au sein de la structure cristalline de la maghémite ce qui a des conséquences majeures sur la réactivité chimique de la maghémite.

D'un autre côté, les bactéries, les substances organiques et inorganique du sol et de la solution de sol (macromolécules organiques, débris cellulaires…) sont autant d'agents capables de former un revêtement autour des NPs ou des'adsorber à leur surface en patchs, mono- ou multi-couche(s) (selon leur quantité et selon les propriétés du milieu). En enrobant les NPs d'acides humiques (AH) et de phospholipides (PC), molécules fréquemment rencontrées dans la plupart des milieux naturels (issues de la dégradation d'organismes vivants), nous avons ainsi observé l'ancrage de groupements fonctionnels spécifiques - principalement, les groupements carboxyliques pour les acides humiques, et les groupements phosphates pour les phospholipides - à la surface des NPs de magnétite.

Ces modifications sont cruciales car elles sont fortement impliquées dans les réactions de surfaceavec d'autres constituants (comme les métaux) de l'environnement et dans les interactions mutuelles entre NPs. En termes de **stabilité colloïdale**, nous avons ainsi observé que les NPs de maghémite formaient des agrégats de plus grandes tailles (> 400 nm), notamment à pH acides (pH de 3 à 5), comparés à ceux générés par les NPs de magnétite (80% <100 nm). L'oxydation de la magnétite en maghémite, qui est attendue dans la plupart des eaux naturelles de surface et les sols sains, affecte donc considérablement l'état d'agrégation des NPs de magnétite. L'oxydation de la magnétite, qui se produit spontanément de manière abiotique en condition aérobie (milieu dans lequel l'oxygène fonctionne comme un accepteur d'électrons), peut également être catalysée dans des conditions hypoxiques par l'action des bactéries, qui, en oxydant le Fe^{2+} en Fe^{3+}, contribuent aussi à la corrosion des particules (biodégradation) (Lei et al., 2017). Lorsque les NPs sont enrobées de molécules organiques, leur comportement colloïdal est également modifié. Les acides humiques favorisent la stabilité colloïdale des NPs par lasuspension de petits agrégats et NPs individuelles (<100 nm) avec une très faible dispersion de tailles sur une large gamme de pH.Les interactions à la surface des NPs-Fe enrobées ne sont plus seulement électrostatiques, elles sont dites « électro-stériques », car les molécules adsorbées forment une couchephysique à la surface des NPs-Fe. Les phospholipides, même s'ils mettent en jeu le même type d'interactions que celles qui se produisent en surface des NPs-Fe enrobées d'AH, modifient peu la distribution de taille des NPs de magnétite. L'état d'agrégation des NPs-Fe (qui résulte de la somme des forces attractives et répulsives), est une caractéristique déterminante quant à leur devenir dans les sols. Selon plusieurs études, la formation d'agrégats affecte la **mobilité des NPs dans les sols** (transfert àtravers les pores du sol, efficacité de collage avec les autres particules du sol) ainsi que le transport (mouvement brownien, mécanique, sédimentation différentielle…) et le taux de sédimentation des NPs présentes en suspension dans les eaux de surface (Ollivier et Labille, 2016 ; Bhatt et Tripathi, 2011). L'état d'agrégation est également important vis-à-vis de la **biodégradation** des NPs dans l'environnement. Les NPs agrégées, qui forment des suspensions de plus grosses particules, ont une énergie de surface plus faible et une surface réduite en contact avec la solution et les bactéries, ce qui les rend moins solubles (Mudunkotuwa et Grassian, 2011). En termes de solubilité, nous avons observé que les NPs de magnétite enrobées d'acides humiques et celles enrobées de phospholipides diminuaient la quantité de fer dissous issu des NPs. Cette constatation suppose l'implication de plusieurs mécanismes. D'un côté, le fer solubilisé pourrait s'adsorber à la surface des oxydes enrobés de molécules organiques. D'un autre côté, les deux enrobages induisent chacun une « protection » contre la dissolution des NPs-Fe (cf. Chap.2). La « barrière » formée en surface des NPs enrobées d'acides humiques ou de phospholipides n'impacte donc pas seulement la stabilité colloïdale des NPs (interactions stériques), elle empêche également la dissolution des NPs-Fe et pourrait, selon certaines études (Hao et al., 2006), protéger de l'oxydation. Bien que ces transformations, essentiellement surfaciques, aient un impact crucial sur les phénomènes (agrégation, dissolution) qui régissent leur devenir dans l'environnement (**Figure 1**), il est toutefois important de remarquer que les molécules adsorbées en surface des NPs ont une « durée de vie » contrainte par les conditions du milieu. Lors d'un changement de pH, ou par adsorption compétitive avec d'autres ions ou molécules, les matériaux peuvent se désorber de la surface à laquelle ils étaient attachés. Ils peuvent aussi être dégradés par oxydation sous l'action de l'ozone ou de la lumière (Katsumata et al., 2008) ou, biodégradés par les (micro-)organismes présents dans le milieu.

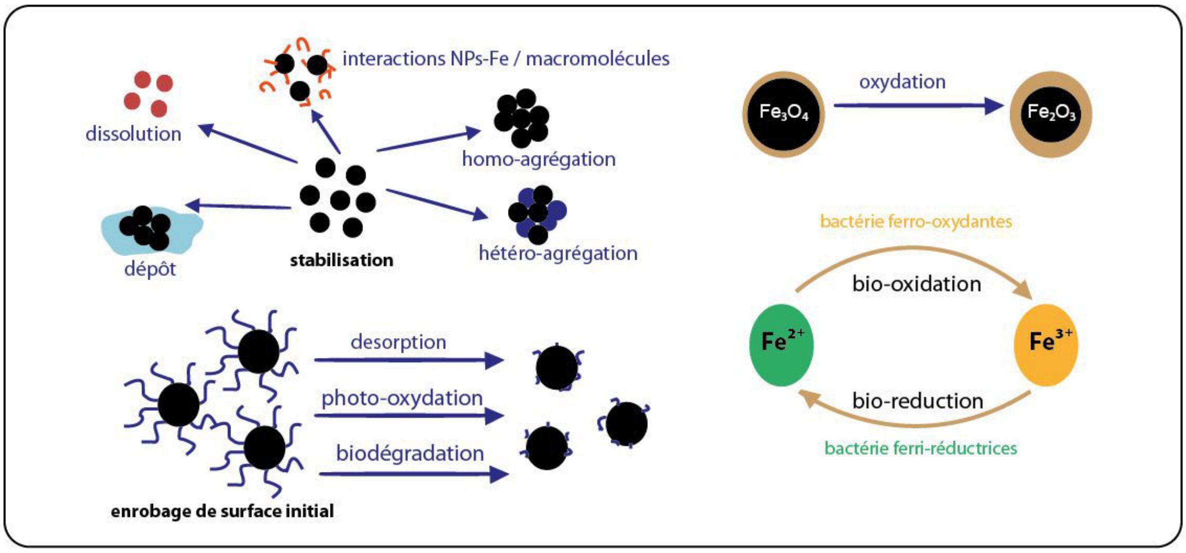

Figure 1 : Principales transformations des NPs-Fe dans l'environnement (modifié d'après Lei et al., 2017).

V.1.2. Quels sont les impacts de ces transformations sur la réactivité des NPs-Fe avec les éléments traces ?

L'interface à laquelle se produisent ces changements est aussi le siège de réactions avec d'autres constituants organiques et inorganiques dont le devenir dans les eaux et les sols représente un enjeu majeur pour les écosystèmes. A cet égard, les NPs de magnétite et de maghémite constituent d'importants piégeurs de métaux dans les drainages acides miniers (DAM) et dans certains environnements contaminés (par exemple, dans les zones humides polluées en arsenic) (Mukherjee et al., 2006). Au-delà de leur grande réactivité avec les ETs, les NPs de magnétite et de maghémite ont des propriétés magnétiques, qui leur permettent d'être facilement séparées et récupérées du milieu dans lequel elles avaient été introduites (Lingamdinne et al., 2017). A la surface des NPs-Fe, les métaux sont piégés par différents processus (complexation, co-précipitation…) qui dépendent de la concentration en métal, de leur spéciation, des propriétés physico-chimiques de la solution (pH, Eh, force ionique, température), de la concentration en NPs et de leurs propriétés intrinsèques (taille, surface spécifique, pHzpc) ainsi que des modifications surfaciques pouvant être induites par le milieu. Dans nos travaux, nous nous sommes intéressés à la réactivité des NPs-Fe, avec un élément trace métallique modèle (le cuivre) d'abord en milieu aqueux puis dans un sol en présence de tournesol. Afin de tenir compte des possibles modifications induites par le milieu sur les NPs-Fe, l'adsorption du Cu a également été étudiée sur des NPs de magnétite transformées-oxydées (maghémite), enrobées d'AH ou de PC (cf. Chap. 3).

Les résultats indiquent que l'adsorption du Cu à la surface des NPs est initialement contrôlée par le pH. En effet, au-delà du pHzpc des NPs-Fe, leur surface devient négativement chargée ce qui favorise la complexation de Cu^{2+} avec les surfaces des NPs-Fe hydroxylées. Ainsi, la proportion de Cu adsorbée aux NPs de magnétite augmente considérablement à partir de pH 6 pour atteindre 100% à pH8. Au contraire, lorsqu'elles sont enrobées d'AH, les NPs-Fe adsorbent le Cu dès pH 4, car les groupements fonctionnels acides ancrés à la surface des NPs-Fe (principalement des groupements carboxyliques et phénoliques) abaissent le point de charge nul des NPs-Fe à une valeur proche de pH 3 (Liu et al., 2008). En plus d'abaisser le pHzpc des NPs-Fe (favorisant en conséquence l'adsorption du Cu sur une large gamme de pH), les groupements fonctionnels des AH procurent de nouveaux de sites d'adsorption pour le cuivre. Nous avons d'une part, observé qu'en augmentant les concentrations de cuivre en solution, la proportion de cuivre adsorbée atteignait environ 100% aux pH favorables ($pH > 4$). Ces résultats indiquent que la saturation des sites de surface observée pour les NPs-Fe non enrobées d'AH n'avait plus lieu après cette modification surfacique. De plus, en calculant les isothermes d'adsorption de Freundlich, nous avons également montré que l'adsorption du cuivre à la surface des NPs enrobées d'AH repose sur la formation de complexes hétérogènes, probablement « multi-sites » (diversité des groupements fonctionnels) et/ou multi-dendates (cf. Chap. 3). Les paramètres d'adsorption « n » et « K » associés à l'isotherme de Freundlich, indiquent en effet un processus de sorption hétérogène (nous avons observé, en traçant l'isotherme, que le paramètre « n » était fortement dévié de n=1). L'enrobage des NPs-Fe avec des AH favorise donc considérablement l'adsorption du Cu, en plus de favoriser leur stabilité colloïdale aux $pH > 4$. Ces effets ne sont toutefois pas toujours observés dans la mesure où ils dépendent des conditions environnementales. Par exemple, la concentration en acides humiques dans le milieu joue un rôle majeur sur la réactivité des NPs-Fe car elle conditionne la quantité d'AH potentiellement adsorbée à la surface des NPs-Fe et donc à la fois, la charge globale de surface et la conformation des AH en surface. D'après Hadju et al. (2009), les AH présents en « patchs » à la surface des NPs favorisent l'agrégation des NPs aux pH acides car les NPs montrent alors des charges opposées (charges négatives liées auxacides humiques et charges positives propres aux NPs) et s'attirent. La présence de Ca^{2+} en solution est aussi susceptible de favoriser l'agrégation des NPs en formant des ponts cationiques entre NPs (Joo et Zhao, 2017). En outre, si les conditions du milieu influencent les propriétés d'agrégation des NPs-Fe, nous n'avons pas observé dans cette étude (adsorption du Cu aux NPs-Fe à différents pH), d'effets qui prouvent une relation entre l'état d'agrégation des NPs-Fe et leur capacité d'adsorption. Cette observation pourrait néanmoins permettre de préciser que le processus d'agrégation observé initialement avec le pH est un phénomène réversible qui repose sur la cohésion non fusionnelle du matériel agrégé (Gilbert et al., 2009).

Les caractéristiques de stabilité colloïdale et de celles de réactivité avec les constituants de l'environnement sont toutes deux fondamentales à l'étude des interactions NPs-Fe/plantes. Ces caractéristiques sont impliquées dans des processus de biodégradabilité, d'agrégation et de transport d'éléments ou molécules réactives qui s'avèrent cruciales vis-à-vis des problématiques de biodisponibilité et toxicité induites dans les interactions NPs-Fe-plantes.

V.2. Etude des interactions NPs-Fe/plantes : enjeux agronomiques et impacts environnementaux

Plusieurs études ont été récemment conduites au regard de possibles nouvelles utilisations des NPs-Fe en agriculture (Kah et al., 2013; Khot et al., 2012 ; Solanki et al., 2015). Leur réactivité avec les ETs et certaines molécules organiques (pesticides), leurs biodégradabilité et devenir dans l'environnement, leurs biodisponibilité et biocompatibilité sont parmi les principales thématiques de recherche étudiées pour utiliser les NPs de fer à des fins agronomiques. Plusieurs questions importantes nécessitent en effet encore des réponses pour permettre une utilisation suffisamment raisonnée des NPs-Fe sur les plantes.

Ces questions se posent d'abord concernant :

- **le devenir des NPs dans l'environnement** : quel est l'impact des plantes sur les NPs-Fe ? Celui des NPs-Fe sur leur milieu ? Comment répondent, en retour, les NPs-Fe aux modifications physico-chimiques du milieu (rétroactions) ?
- **la valorisation des NPs-Fe par les plantes** : les plantes peuvent-elles utiliser le fer des NPs ou des éléments qu'elles pourraient transporter?
- **la biocompatibilité NPs/plantes :** comment les NPs-Fe interfèrent-elles avec les plantes vasculaires et quels sont les impacts physiologiques sur les plantes? Existe-t-il un seuil de tolérance (concentration appliquée) des plantes aux NPs-Fe et ce seuil est-il fonction de la plante (espèce, stade de développement) auquel sont appliquées les NPs-Fe? Quel est le rôle du milieu vis-à-vis de ces interactions?

Dans cette étude, nous avons tenté d'apporter des éléments de réponse à plusieurs de ces questions.

V.2.1. Valorisation des NPs de magnétite par les plantes

Le fer est un élément essentiel pour les plantes. C'est un élément redox sensible constitutif de nombreuses métallo-enzymes, faisant partie des cofacteurs transporteurs d'électrons, et jouant en rôle majeur dans la biosynthèse de chlorophylles.Les conséquences d'une carence en fer sur le végétal vont de la chlorose à la nécrose des tissus de la plante (Briat et al., 2007). Si le fer est rarement insuffisant dans les sols, les conditions du milieu rendent la solubilisation des oxydes et hydroxydes de fer parfois difficile ou le fer moins biodisponible en raison de la présence d'éléments compétiteurs (Vose, 1982). De ce point de vue, l'utilisation des NPs comme nano-nutriments (Fe) serait une pratique envisageable. Aucun effet négatif en lien avec la présence de NPs-Fe n'a en effet été observé sur la biomasse végétale dans les expériences de germination, après 7 jours d'exposition. De plus, en introduisant des concentrations précises de NPs-Fe à différentes espèces végétales (tournesol, maïs, haricot) en hydroponie, nous avons montré que les NPs-Fe permettaient aux plantes d'obtenir du fer et qu'elles empêchaient les effets induits lors d'une carence en fer (observés sur les plantes témoins ayant été cultivées sans fer disponible) (Salama, 2009). Nous avons également constaté que la concentration des NPs-Fe dans le milieu nécessitait d'être prise en compte comme cela a été démontré précédemment (Li et al., 2016). En cas de carence en fer, une faible concentration en NPs-Fe (5 mg L^{-1}) suffit à réduire notablement les principaux symptômes de carence induits par l'absence de fer dissous dans le milieu. En outre, une augmentation de la concentration en NPs-Fe (d'un facteur 200) permet non seulement, à la plante de parer à la carence en fer mais aussi, d'augmenter la biomasse végétale par rapport aux plantes témoins disposants de fer dissout (non exposées aux NPs). Par ailleurs, lorsque le fer dissout est présent dans le milieu hydroponique, aucune amélioration notable liée à la présence de NPs n'est constatée sur la croissance des plantes. Enfin, si cette étude met en évidence l'utilisation des NPs-Fe par les plantes, la question de leur biodisponibilité dans un milieu sol pour les plantes ne s'est toutefois pas encore posée. Les sols sont en effet des milieux complexes qui tendent à retenir les NPs en particulier, s'ils contiennent une proportion importante d'argiles (Theng et Yuan, 2007). Si de faibles concentrations en NPs-Fe suffisent à compenser une carence en fer en milieu hydroponique, elles pourraient s'avérer insuffisantes pour parer à une telle carence dans un milieu solide (non étudié ici). Enfin, la biodisponibilité des NPs-Fe dans les sols est fonction de nombreux paramètres qui incluent les propriétés du sol (composition minérale, texture, CEC, pH, teneur en matière organique, ETs), leur mode d'introduction dans le milieu (concentration introduite, formulation) et l'action de la biomasse (enrobages, biodégradation) qui ensemble affectent : a) la stabilité (colloïdale et chimique) des NPs-Fe dans le milieu, b) leur réactivité avec les constituants en présence, et c.) leur mobilité dans le milieu.

V.2.2. Impacts des NPs-Fe sur la physiologie des plantes

L'analyse des impacts des NPs sur les plantes nécessite de prendre en compte le rôle joué par de nombreux paramètres. Dans cette étude les effets des NPs-Fe ont été étudiés en fonction de la durée d'exposition, du stade de développement de la plante, de l'espèce étudié, de la concentration en NPs appliquées et des propriétés du milieu (composition) (**Tableau 1**). Les impacts des NPs-Fe sur les plantes ont été étudiés au regard des paramètres de croissance, de la production de chlorophylles, de la performance photosynthétique, de la peroxidation lipidique, et des réponses enzymatiques des plantes. Les analyses biologiques ont été conduites sur les plantes cultivées : a) en hydroponie (carencées et non carencées en fer - avec deux concentrations d'exposition aux NPs-Fe) et b) sur sol (colonnes de sol, contaminées ou non-contaminées en cuivre et NPs-Fe). En hydroponie, l'exposition des plantes aux NPs-Fe n'a pas montré d'impact négatif sur la croissance des plantes et a permis d'augmenter la biomasseavec l'augmentation des concentrations de NPs-Fe en cas de carence en fer. Les plantes peuvent donc utiliser les NPs-Fe pour obtenir fer favorablement à leur croissance, mais, aucune augmentation supplémentaire de la biomasse n'est constatée lorsque le fer dissous est présent dans le milieu. Les plantes sont donc capables de réguler l'absorption du fer des NPs-Fe relativement à leur croissance. Les teneurs en chlorophylles *a*, *b* et en caroténoïdes ont aussi été augmentées en hydroponie en lien avec l'exposition de NPs-Fe, et cet effet a été observé à la fois, dans les plantes carencées (exposées à une faible et à une forte concentration de NPs-Fe (5 mg L^{-1} et 1000 mg L^{-1}) et dans les plantes non carencées en fer exposées à une forte concentration de NPs-Fe (1000 mg L^{-1}). Ces résultats ont déjà été observés en hydroponie sur le maïs (Racuciu et Creanga, 2007) et le soja (Ghafariyan et al., 2013) avec des NPs de magnétite. Il a toutefois aussi été observé que l'application d'une forte concentration de maghémite ne diminuait pas la production de chlorophylles du maïs (utilisant 50 et 100 mg L^{-1}) (Li et al., 2016). D'un autre côté, la présence des NPs-Fe, et l'augmentation des concentrations, ont diminué la peroxidation lipidique (à la fois par rapport aux plantes témoins carencées et aux plantes témoins non carencées en fer). Les NPs-Fe n'ont donc pas d'impact négatif sur la peroxidation lipidique et pourraient même peut-être permettre d'apporter une certaine protection aux plantes contre les agents oxydants impliqués dans cette altération ; ce qui a déjà été observé auparavant (Ianonne et al., 2016). Nous avons de plus observé (via des observations au microscope électronique à balayage) que les NPs s'agrégeaient en formant parfois des dépôts très étendus sur les surfaces racinaires en milieu hydroponique. Cette répartition pourrait altérer les mécanismes d'échanges au niveau des racines et pourrait provoquer des blessures aux tissus (Martinez-Fernandez et al., 2016). Dans l'expérience de culture sur sol, la présence de NPs n'a pas impacté la croissance des plantes, suggérant une diminution de l'interaction des NPs-Fe avec les plantes, en lien avec le milieu (rétention des NPs-Fe dans le sol). Cette décroissance de la biodisponibilité résulte probablement de la présence de minéraux à forte surface d'adsorption et de matières organiques capables de former des complexes stables. D'un autre côté, la présence de cuivre dans le milieu a fortement diminué la croissance des plantes. La toxicité du cuivre a également été observée au niveau de la production de pigments avec une diminution significative des teneurs en chlorophylles et caroténoïdes dans les plantes exposées au cuivre (avec ou sans NPs-Fe). Ces plantes ont aussi montré les symptômes d'une chlorose qui pourrait résulter de la réduction de l'absorption du fer induite par celle du cuivre (le cuivre ayant un comportement antagoniste avec le fer lors de leur absorption (Vose, 1982)). En termes de peroxydation lipidique et de réponse antioxydante, la présence des NPs-Fe dans le milieu diminue la peroxydation lipidique comparée à celle mesurée pour lesplantes témoins alors qu'elle tend à augmenter l'activité POD. En activant ce mécanisme de protection, les NPs-Fe favorisent donc d'elles-mêmes la réponse à un possible stress oxydatif, permettant notamment de contrer la peroxydation lipidique. Nous avons par ailleurs, constaté que les NPs-Fe n'empêchaient pas la toxicité du cuivre envers les plantes mais, pourraient en réduire les effets. Ainsi, nous pouvons supposer que si les concentrations en cuivre dans un milieu pollué sont légèrement inférieures à 500 mg kg^{-1} (comme c'est le cas dans certains sols agricoles encore fortement contaminés - de 100 à 300 mg kg^{-1}), les NPs-Fe pourraient réduire drastiquement leur absorption par les plantes (Martinez-Fernandez et al., 2015). Il est à noter que les conditions du milieu, et notamment les propriétés du sol (composition, texture ou présence de pesticides) seraient sans doute un facteur crucial à prendre en compte dans une telle hypothèse en impactant la mobilité des NPs-Fe (Theng et Yuan, 2007) et celle du cuivre et/ou des autres éléments associés.

Tableau 1 : Principaux résultats obtenus durant les différentes expériences de culture avec les NPs-Fe.

Nanoparticules	Concentrations	Espèce végétale	Culture	Durée	Effets
8 nm Fe_3O_4	5 et 5000 mg L^{-1}	*Helianthus annuus, Zea mays, Phaseolus vulgaris, Triticum aestivum*	germination	7 jours	Pas d'effets significatifs
8 nm Fe_3O_4	5 et 1000 mg L^{-1}	*Helianthus annuus, Zea mays, Phaseolus vulgaris*	croissance en hydroponie	18 jours	- Augmentent la biomasse en cas de carence en fer - Augmentent la production de chlorophylles - Augmentent la réponse antioxydante et diminuent la peroxidation lipidique
8 nm Fe_3O_4 (ajout $CuSO_4$)	1,2 g kg^{-1} (500 mg kg^{-1})	*Helianthus annuus*	colonne de sol	57 jours	- Pas d'effets significatifs des NPs-Fe (seules) sur les plantes - Diminuent l'absorption du cuivre par les plantes - Augmentent la réponse antioxydante et diminuent la peroxidation lipidique

V.2.3. Mobilité, translocation et devenir des NPs-Fe et des éléments traces associés

Du fait de leurs propriétés magnétiques, les NPs-Fe - en particulier, les NPs de magnétite - peuvent être identifiées par le signal magnétique caractéristique qu'elles génèrent par mesure de l'aimantation rémanente et/ou de la susceptibilité magnétique de l'échantillon dans lequel elles sont présentes. A travers cette méthode (dans notre cas, la mesure de susceptibilité magnétique), nous avons mis en évidence non seulement, la translocation des NPs-Fe dans les plantes mais aussi, l'impact de la composition du milieu sur la mobilité des NPs-Fe dans un système sol - plante (soit, non-contaminé soit, contaminé en cuivre). En regard des mesures effectuées, nous avons d'abord constaté que la translocation des NPs-Fe était favorisée en culture hydroponique : les mesures de susceptibilité magnétiques sont en effet, plus élevées dans les différents tissus - en particulier dans les parties aériennes - des plantes cultivées en milieu hydroponique que dans ceux des plantes cultivées sur sol pour des durées d'exposition et concentrations en NPs-Fe comparables. Par ailleurs, les mesures de susceptibilité magnétiques ont mis en évidence une relation existant entre la concentration d'exposition de NPs-Fe aux plantes et la concentration finale transloquée dans la plante. En effet, une faible concentration de NPs exposée induit une plus faible quantité de NPs-Fe transloquées dans la plante qu'avec une exposition de concentration plus élevée. Cette dernière observation montre aussi que la plante n'a pas de système régulateur capable de limiter l'entrée des NPs-Fe, comme c'est le cas pour certaines substancesà partir d'une certaine concentration d'exposition. Les mesures de susceptibilité magnétique effectuées sur les différents tissus de la plante ont de plus montré que les NPs-Fe s'introduisaient progressivement des racines vers les parties aériennes les plus extrêmes de la plante avec des quantités de NPs-Fe transloquées de plus en plus faibles. Il est donc suggéré que les NPs-Fe parviennent à traverser les parois cellulaires au niveau des racines et à emprunter le système vasculaire (phloème) qui permet aux substances nutritives d'être distribuées dans les différents organes des plantes, des parties les plus basses vers les plus hautes. Dans le même milieu contaminé en cuivre, la transolocation des NPs est restreinte par la présence de cuivre. En termes nutritifs, le cuivre est un élément antagoniste du fer et sa présence a pu impacter l'absorption des NPs-Fe. En outre, les analyses ICP-MS des tissus végétaux montrent que la concentration en cuivre dans ces tissus est, elle, aussi réduite. Les NPs-Fe, ont donc pu contribuer à séquestrer une partie du cuivre à leur surface dans le sol. Les NPs-Fe ont donc un impact sur le transfert et la mobilité des autres éléments du sol et elles affectent leur biodisponibilité. Enfin, dans le sol, les mesures magnétiques ont confirmé la présence des NPs-Fe selon une répartition homogène (comme lors de leur introduction) qui montre que les NPs-Fe sont relativement immobiles dans le milieu (colonne de sol), en dépit des lessivages du sol.

Références :

I. Bhatt et B. N. Tripathi, 2011. Interaction of engineered nanoparticles with various components of the environment and possible strategies for their risk assessment, Chemosphere 82, 308-317.

J.F. Briat, C. Curie et F. Gaymard, 2007. Iron utilization and metabolism in plants.Current Opinion in Plant Biology, 10, 276-282.

R. Frison, G. Cernuto, A. Cervellino, O. Zaaharko, G. M. Colonna, A. Guagliardi et N. Masciocchi, 2013. Magnetite-Maghemite Nanoparticles in the 5-15 nm range: correlating the core-shell composition and surface structure to the magnetic properties. A total scattering study, Chemistry of Materials, 25, 4820-4828.

M.H. Ghafariyan, M.J. Malakouti, M.R. Dadpour, P. Stroeve, M. Mahmoudi, 2013. Effects of magnetite nanoparticles on soybean chlorophyll. Environmental Science and Technology, 47(18) , 10645-10642.

B. Gilbert, R. K. Ono, K. A. Ching et C. S. Kim, 2009. The effects of nanoparticles aggregation processes on aggregates structure and metal uptake, Journal of Colloids and Interface Science, 339, 285-295.

A. Hadju, E. Illés, E. Tombacz et I. Borbath, 2009. Surface charging, polyanionic coating and colloid stability of magnetite nanoparticles. Colloids and Surfaces A: Physicochemical and Engineering Aspects, 347, 104-108.

J. Hao, C. Cleveland, E. Lim, D. R. Strongin et M. A. A. Schoonen, 2006. The effect of adsorbed lipid on pyrite oxidation under biotic conditions. Geochemical Transactions, 7:8.

M.F. Iannone, M. D. Groppa, M.E. de Sousa, M. Beatriz Fernandez van Raapet M.P. Benavides, 2016. Impact of Magnetite Iron Oxide nanoparticles on wheat (*Triticumaestivum L.*) development: evaluation of oxidative damage. Environmental and Experimental Botany. 131, 77-88.

S.H. Joo et D. Zhao, 2017. Environmental dynamics of metal oxide nanoparticles in heterogeneous systems: a review. Journal of Hazardous Materials, 322, 29-47.

M. Kah, S. Beulke, K. Tiedeet T. Hofmann, 2013. Nanopesticides: state of knowledge, environmental fate, and exposure modeling. Critical Reviews of Environmental Science and Technolology, 43, 1823-1867.

H. Katsumata, M. Sada, S. Kaneco, T. Suzuki, K. Ohaet Y. Yobiko, 2008. Humic acid degradation in aqueous solution by the photo-Fenton process. Chemical Engineering Journal 137, 225-230.

L.R. Khot, S. Sankaran, J.M. Maja, R. Ehsaniet E.W. Schuster, 2012. Applications of nanomaterials in agricultural production and crop protection: a review. Crop Protection 35, 64-70.

C. Lei, Y. Sun, D.C.W. Tsanget D. Lin, 2017. Environmental transformations and ecological effects of iron-based nanoparticles. Environmental Pollution, 232, 10-30.

J. Li, P.R. Chang, J. Huang, Y. Wang, H. Yuan et H. Ren, 2013. Physiological effects of magnetic iron oxide nanoparticles towards watermelon. Journal of Nanoscience and Nanotechnology, 13, 5516-5567.

J. Li, J. Hu, C. Ma, Y. Wang, C. Wu, J. Huang et B. Xing, 2016. Uptake, translocation and physiological effects of magnetic iron oxide (γ-Fe_2O_3) nanoparticles in corn (*Zea mays* L.). Chemosphere 159, 326-334.

L.P. Lingamdinne, Y-Y. Chang, J.-K. Yang, J. Singh, E.-H.Choi, M. Shiratani, J.R. Koduru et P.Attri, 2017. Biogenic reductive preparation of magnetic inverse spinel iron oxide nanoparticles for the adsorption removal of heavy metals. Chemical Engineering Journal 307, 74-84.

J.-F. Liu, Z.-S. Zhao et G.-B. Jiang, 2008. Coating Fe_3O_4 Magnetic Nanoparticles with Humic Acid for high efficient Removal of Heavy Metals in water. Environmental Science and Technology, 42, 6949-6954.

S. C. Löhr, D. T. Murphy, L. D. Nothdurft, R. Bohlar, S. Piazolo et C. Siegel, 2017. Maghemite soil nodules reveal the impact of fire on mineralogical and geochemical differentiation at the Earth’s surface, Geochimica et Cosmochimica Acta, 200, 25-41.

D. Martínez-Fernández, M. Vítková, M.P. Bernal, M. Komárek, 2015. Effects of Nano-maghemite on Trace Element Accumulation and Drought Response of Helianthus annuus L. in a Contaminated Mine Soil. Water, Air, &Soil Pollution 226: 101.

D. Martínez-Fernández, D. Barroso, M. Komárek, 2016. Root water transport of *Helianthus annuus* L. under iron oxide nanoparticle exposure. Environmental Science and Pollution Research23: 1732-1741

I. A. Mudunkotuwa et V. H. Grassian, 2011. The devil is in the details (or the surface): impact of surface structure and surface energetics on understanding the behavior of nanomaterials in the environment, Journal of Environmental Monitoring, 13, 1135-1144.

A. Mukherjee, M.K. Sengupta, M.A. Hossain, S. Ahamed, B. Das, B. Nayak, D. Lodh, M.M. Rahman et D. Chakraborti, 2006. Arsenic contamination in groundwater: a global perspective with emphasis on the Asian scenario. Journal of Health Populationand Nutrition, 24, 142-163.

E. Navarro, A. Baun, R. Behra, N. B. Hartman, J. Filser, A-J. Miao, A. Qigg, P. H. Santschi et L. Sigg, 2008. Environmental behavior and ecotoxicity of engineered nanoparticles to algae, plants and fungi. Ecotoxicology, 17, 372-386.

P. Ollivier et J. Labille, 2016. Les NPs manufacturées: innovation et devenir dans l'environnement. Géosciences, 20, 66-73.

M. Racuciu et D.-E. Creanga, 2007. TMA-OH coated magnetic nanoparticles internalized in vegetal tissue. Romanian Journal of Physics, 52 (3-4), 395-402.

Z. Salama et H. El-Beltagi, 2009. Effect of Fe deficiency on antioxidant system in leaves of three flax cultivars. NotulaeBotanicaeHortiAgrobotanici Cluj-Napoca 37 (1), 122-128.

P. Solanki, A. Bhargava, H. Chhipa, N. Jain, J. Panwar, 2015. Nano-fertilizers and their smart delivery system. In: Rai M., Ribeiro C., Mattoso L., Duran N., (eds) Nanotechnologies in food and agriculture. Springer International Publishing Cham, 81-101.

B.K.G. Theng, G. Yuan, 2007. Nanoparticles in the soil environment. Elements, 4, 395-399.

P. B. Vose, 1982. Iron nutrition in plants: A world overview, Journal of Plant Nutrition, 5:4-7, 233-249.

Conclusions et perspectives

Conclusions

Le premier volet de cette thèse, centré sur l'étude des propriétés intrinsèques des NPs-Fe, nous a permis d'apporter des réponses concernant les stabilités colloïdale et chimique et la réactivité des NPs-Fe avec leur milieu. Plus précisément, nous avons pu identifier les paramètres physico-chimiques impliqués dans les interactions NPs-Fe / NPs-Fe et dans les interactions NPs-Fe / cuivre (Cu). Celles-ci sont essentiellement dépendantes des propriétés extrinsèques (notamment le pH) et des propriétés intrinsèques des NPs (pHzpc, surface spécifique), mettant en évidence le comportement dynamique des NPs-Fe avec les conditions du milieu. Dans nos expérimentations, les propriétés des NPs-Fe (taille, forme, composition, cristallinité) et celles de la solution (force ionique, température, salinité, composition) ont été contrôlées afin de mieux comprendre la nature des interactions impliquées dans ces systèmes. De plus, les environnements naturels qui sont des milieux dynamiques, chimiquement riches et complexes, sont susceptibles d'évoluer dans le temps, modifiant le comportement des NPs-Fe dans le milieu et leurs interactions (entre elles et avec le milieu). L'oxydation de la magnétite est une modification commune qui se produit spontanément en milieu aérobie. Nous avons observé qu'en plus de suivre une cinétique rapide, la maghémite présente un comportement colloïdal bien distinct des NPs de magnétite. L'enrobage des NPs-Fe par diverses matières organiques est un phénomène attendu en conditions naturelles que nous avons aussi envisagé en enrobant les NPs-Fe d'acides humiques ou de phospholipides. Les impacts de ces modifications surfaciques sont conséquents, en particulier avec les acides humiques, qui améliorent la stabilité colloïdale des NPs de magnétite et augmentent considérablement leur réactivité chimique (adsorption du cuivre). Afin de préciser les impacts du milieu sur le comportement des NPs-Fe, l'introduction de NPs dans des milieux abritant la vie végétale a été effectuée. D'un côté, les expériences en milieu hydroponique ont mis en évidence leur oxydation, leur agrégation à la surface des racines et leur absorption par les plantes (translocation). D'un autre côté, des expériences en colonne, montrent que le sol affecte considérablement la mobilité des NPs-Fe dans le milieu et leur disponibilité aux plantes. Les interactions avec certains constituants du sol (matière organique, argiles) pourraient diminuer la mise en contact des NPs-Fe avec les plantes. Au-delà de l'impact du milieu sur les NPs-Fe, nous avons étudié l'impact des NPs-Fe elles-mêmes sur leur milieu. En termes de dynamique géochimique du milieu, l'impact des NPs-Fe a été étudié dans un sol pollué en cuivre. Nous avons observé qu'à forte concentration dans le milieu (500 mg.kg^{-1}), les NPs-Fe absorbaient une partie de ce cuivre à leur surface, ce qui diminuait sa biodisponibilité pour les plantes (rétention dans le sol). A une telle concentration de cuivre, les NPs-Fe (1% en masse du sol) n'ont pas empêché les symptômes induits par la toxicité du cuivre. Par ailleurs, en termes de toxicité des NPs-Fe *sensu stricto*, aucun symptôme n'a été observé ; ni sur les plantes exposées aux NPs-Fe dans le sol, ni sur les plantes exposées aux NPs-Fe dans les milieux de culture hydroponiques (quelles que soient les concentrations d'exposition et les stades de croissance des plantes). En outre, les NPs-Fe ont permis de compléter les apports en fer des plantes en empêchant les symptômes de carence observés dans les conditions de carence en fer étudiées. La présence des NPs-Fe a induit une augmentation de la biomasse végétale et des teneurs en chlorophylles avec l'augmentation de concentration d'exposition des NPs-Fe. Les plantes (tournesol) exposées aux NPs-Fe présentent également une moindre peroxydation lipidique et une activité antioxydante plus importante que les plantes témoins (non exposées) ; ce qui suppose un effet bénéfique des NPs-Fe (protection contre l'activité antioxydante) mais, qui suggère également une modification de l'activité cellulaire, qui pourrait résulter d'un dérèglement physiologique lié à l'internalisation des NPs-Fe.

Perspectives

Outre les contraintes évoquées précédemment et mises en évidence via notre démarche expérimentale sur la caractérisation (a) des NPs-Fe et de leurs modifications, (b) les interactions NPs-Fe/Cu et (c) les interactions NPs-Fe/plantes/Cu, ces travaux nous suggèrent de nombreuses perspectives d'étude.

Concernant l'étude de la stabilité colloïdale des NPs-Fe, si l'étude des distributions de tailles des NPs-Fe a été déterminée par granulométrie laser, la détermination du diamètre hydrodynamique des NPs-Fe via DLS apporterait sans doute une information cruciale à l'égard de leur comportement avec le vivant (processus d'internalisation). Bien que cette analyse soit rendue difficile, justement par l'agrégation des NPs-Fe, un enrobage (de type surfactant) pourrait être employé pour approfondir cette problématique de caractérisation (résolution plus fine de la fraction < 100 nm). Il apparaîtrait de plus nécessaire de préciser le rôle de la concentration en NPs-Fe et de la force ionique de la solution sur leur état d’agrégation, car chacun d’entre eux joue un rôle sur la stabilité colloïdale des NPs-Fe en milieu aqueux qu’il est possible de contrôler.

En ce qui concerne les modifications de surface induites aux NPs, les informations quantitatives et qualitatives associées aux enrobages de surface nécessiteraient d’être précisées. Il s’agirait en particulier de déterminer à la fois la quantité de matériel (dans notre cas ; acides humiques et phospholipides) présente autour des NPs (une expérience de désorption pourrait par exemple, être envisagée) ainsi que la caractérisation de leur conformation. Cette dernière problématique nous permettrait par exemple de préciser si plusieurs NPs sont enrobées dans une matrice organique complexe, ou, si un enrobage continu est présent autour de chaque nanoparticule, ou encore, si un enrobage discontinu enrobe plus globalement les NPs.

En termes de réactivité chimique, nous avons étudié l’adsorption du cuivre sur des NPs-Fe nues et enrobées d’acides humiques et de phospholipides et avons observé une augmentation des proportions de cuivre adsorbé en lien avec ces enrobages (notamment, les NPs-Fe enrobées d’acides humiques). Afin d’évaluer l’impact des NPs-Fe sur leur milieu, il serait probablement nécessaire d’étudier les interactions cuivre / molécules organiques seules (non enrobées aux NPs-Fe). Par ailleurs, si nous avons mis en évidence la faible solubilisation des NPs-Fe enrobées, nous n’avons pas pu écarter complètement l’hypothèse de la ré-adsorption du fer dissous aux NPs-Fe enrobées d’acides humiques et de phospholipides. Il serait donc intéressant d’évaluer si le fer non solubilisé est effectivement présent à la surface des NPs-Fe enrobées (des analyses FTIR pourraient être envisagées).

Enfin, concernant les interactions NPs-Fe/plantes, plusieurs perspectives de travaux pourraient être explorées. Ayant constaté le fort impact du sol sur la mobilité des NPs, il serait intéressant d’approfondir cette observation en étudiant leur capacité de transfert dans différents types de sols (en modifiant la composition et donc la texture du sol - par exemple, moins argileux et plus sableux - ainsi que la proportion de matière organique), afin de mieux comprendre les paramètres contrôlant leur mobilité dans ces milieux. De plus, si les NPs retiennent une partie du cuivre ajoutée dans le sol, elles pourraient aussi modifier son transport et sa biodisponibilité/toxicité. L’impact des NPs-Fe sur la dynamique géochimique du sol pourrait donc être précisé aussi bien par rapport à la composition et texture du sol que par rapport à la charge métallique (et en NPs-Fe) présente. Enfin, si la valorisation des NPs-

Fe a été démontrée dans les cultures hydroponiques (en permettant de parer à une éventuelle carence en fer), il serait sans doute nécessaire de vérifier si l'impact est le même dans une culture sur sol. En outre, des analyses protéomiques pourraient aussi nous permettre de discerner des effets physiologiques ou moléculaires non visibles avec les indicateurs étudiés.

Dans un stade ultime de réflexion, on pourrait sans doute imaginer, en travaillant en collaboration avec des modélisateurs du transport des NPs en milieu poreux (et plus spécifiquement du transport réactif), être capable de prédire quel pourrait être l'impact de l'adjonction intentionnelle ou non de NPs-Fe sur la dynamique chimique d'un sol ou sur la croissance d'éventuelles plantes associées. Ceci suppose comme préalable d'étudier à l'échelle moléculaire les processus physico-chimiques susceptibles de contrôler le devenir et le transport des NPs-Fe afin d'être en mesure de paramétrer, calibrer et valider ces modèles (avec des données expérimentales ou de terrain). L'inclusion graduelle dans ces modèles de l'ensemble des processus de transformation possibles de ces NPs-Fe au cours du temps pourrait aboutir à des modèles certes complexes mais, qui seraient seuls garants de la réalité de la complexité des trajectoires environnementales.

Annexes :

Autres travaux

Journal of Colloid and Interface Science 470 (2016) 153–161

Contents lists available at ScienceDirect

Journal of Colloid and Interface Science

journal homepage: www.elsevier.com/locate/jcis

Does As(III) interact with Fe(II), Fe(III) and organic matter through ternary complexes?

Charlotte Catrouillet *, Mélanie Davranche, Aline Dia, Martine Bouhnik-Le Coz, Edwige Demangeat, Gérard Gruau

Géosciences Rennes UMR 6118, Université Rennes 1, CNRS, 35042 Rennes cedex, France

GRAPHICAL ABSTRACT

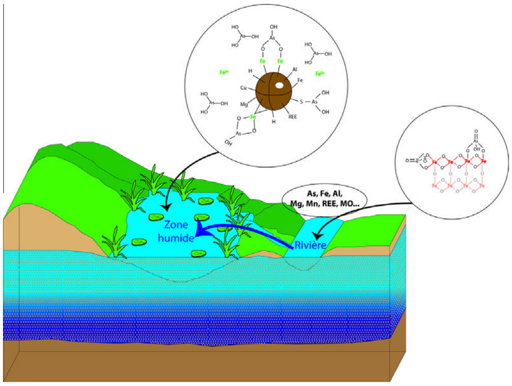

ARTICLE INFO

Article history:
Received 8 January 2016
Revised 18 February 2016
Accepted 18 February 2016
Available online 20 February 2016

Keywords:
Arsenic(III)
Iron(II, III)
Humic substances
Binding
Sorption
PHREEQC–Model VI
PHREEPLOT
Ternary complex

ABSTRACT

Up until now, only a small number of studies have been dedicated to the binding processes of As(III) with organic matter (OM) via ionic Fe(III) bridges; none was interested in Fe (II). Complexation isotherms were carried out with As(III), Fe(II) or Fe(III) and Leonardite humic acid (HA). Although PHREEQC/Model VI, implemented with OM thiol groups, reproduced the experimental datasets with Fe(III), the poor fit between the experimental and modeled Fe(II) data suggested another binding mechanism for As(III) to OM. PHREEQC/Model VI was modified to take various possible As(III)–Fe(II)–OM ternary complex conformations into account. The complexation of As(III) as a mononuclear bidentate complex to a bidentate Fe (II)–HA complex was evidenced. However, the model needed to be improved since the distribution of the bidentate sites appeared to be unrealistic with regards to the published XAS data. In the presence of Fe (III), As(III) was bound to thiol groups which are more competitive with regards to the low density of formed Fe(III)–HA complexes. Based on the new data and previously published results, we propose a general scheme describing the various As(III)–Fe–MO complexes that are able to form in Fe and OM-rich waters.

---

* Corresponding author.

E-mail address: charlotte.catrouillet@univ-rennes1.fr (C. Catrouillet).

http://dx.doi.org/10.1016/j.jcis.2016.02.047

1. Introduction

Arsenic (As) is a strong contaminant of water and soil worldwide (Word Health organization), mainly as arsenite – As(III) – or arsenate – As(V) – depending on the redox conditions [1]. Iron (Fe) speciation exerts a strong control on the As fate in the environment, as oxidized Fe species are known for their capacity to bind high concentrations of As(III, V) [2,3]. Organic matter (OM) seems to be an important direct and indirect controlling factor, especially in floodplains and wetlands where As concentrations can be high [4–6]. Organic matter act (i) as a source of C for bacterial metabolic activity, especially Fe(III) and As(V) reducing-bacteria, (ii) as a sorbent of Fe(III, II)/Fe(III)-oxyhydroxides [7–11], and as an As(III, V) competitor for its binding to Fe(III)-oxyhydroxides [12–16]. More recently, several studies demonstrated that OM may directly bind As(III, V). Different mechanisms were put forward to describe As-OM binding, including As(III, V) complexation with OM carboxylic and phenolic groups [17,18], or As(III) binding with OM thiol groups [19–21]. However, most of the As bound to OM generally occurs as As–Fe–OM ternary complexes in several systems, such as peatland, riparian wetlands, streams, groundwaters [13,22–27]. The high affinity of As for Fe(III)-oxyhydroxides and of Fe (III)/Fe(III)-oxyhydroxides for OM explains this behavior [14,23,25,28–31]. These studies were predominantly performed under oxidizing conditions and therefore concerned As(V). The situation is much less clear regarding the possible predominance of As(III)–Fe–OM ternary complexes. Using SEC-ICP-MS coupling and ultrafiltration, some authors provided evidence that As(III) could also form ternary complexes with OM via Fe(III) bridges, even though they failed to identify the nature of the Fe(III) bridges: Fe(III) ions or Fe(III)-oxyhydroxides [31]. Hoffmann et al. [26] who studied the As(III) binding to natural peat via ionic Fe(III) showed an increasing binding with increasing Fe(III) concentrations. Using EXAFS records, they suggested that As(III) binding could occur either through mononuclear bidentate or binuclear monodentate complexes with Fe(III). They argued that the stability constants for ternary complexes were probably lower than those for the direct As(III) binding to peat thiol groups. However, the high experimental concentrations required for the XAS measurements were quite far off from those generally expected in the environment, especially ionic Fe(III) concentrations which generally precipitate in such conditions. Finally, no study were interested in potential As(III) binding to OM via Fe(II), although these bridges are expected to be dominant in anoxic conditions, notably in wetlands and floodplains where OM, Fe and As concentrations are high [32].

The aim of this study was to evaluate the potentiality to form As (III)–Fe–OM ternary complexes via ionic Fe(II) and Fe(III) bridges at concentrations prevailing in natural waters. As a result, we developed a combined experimental and modeling approach to (i) discriminate between the controlling binding mechanisms involved in the formation of As(III)–Fe–OM ternary complexes and (ii) provide stability constants to quantify which of these mechanisms are likely to be dominant in natural waters. The major advantage of the modeling approach is to test mechanisms at lower Fe amounts than those required by spectroscopic methodologies.

2. Experimental section

2.1. Experimental setup

All of the aqueous solutions were prepared with analytical grade Milli-Q water. The As(III), Fe(II) and Fe(III) stock solutions were prepared with sodium arsenite ($NaAsO_2$), iron chloride tetrahydrate ($FeCl_2{\cdot}4H_2O$) and iron nitrate nonahydrate ($Fe(NO_3)_3{\cdot}9H_2O$), respectively. The used humic acid (HA) was the standard HA Leonardite from the International Humic Substance Society. It was purified by removing the HA molecules <10 kDa using a Labscale TFF system equipped with a Pellicon XL membrane. The composition of the purified HA could be probably slightly modified by this purification as compared to the initial HA. All binding experiments (except Fe(III), see below) were conducted in a Jacomex isolator glove box (<5 ppm of O_2) to prevent the oxidation of As(III) and Fe(II). The ionic strength was fixed at 0.05 M with NaCl for all experiments.

2.1.1. As(III)–Fe(II)–HA experiments

Three adsorption isotherm experiments were carried out at 50 mg L^{-1} DOC (dissolved organic carbon). The first adsorption isotherm was performed at pH 6 with 50 μg L^{-1} of As(III) and 0.8–12 mg L^{-1} of Fe(II). The second and third isotherms were carried out at pH 6 and 5, respectively, with 5–50 μg L^{-1} of As(III) and 5–6 mg L^{-1} of Fe(II). Arsenic and Fe(II) solutions were added simultaneously to humic acid solution, and were then stirred for 48 h to reach equilibrium.

2.1.2. As(III)–Fe(III)–HA experiments

Three standard batch equilibrium experiments were carried out with DOC and Fe^{3+} concentrations of 50 and 0.5 mg L^{-1}, respectively. The Fe(III) stock solution was prepared at pH 1.5 and the Fe^{3+} concentration used was adjusted to prevent oxyhydroxide precipitation. Using PHREEQC–Model VI and the minteq.v4 database modified with respect to Fe(III)–HA binding [9,33], the model showed that precipitation was only expected to occur for Fe(III) concentrations >1.2 mg L^{-1}. The pH was fixed at 4, 5 and 6 with sub boiling HCl and NaOH for the three isotherms, respectively. Experimental solutions were stirred for 24 h to reach equilibrium between Fe^{3+} and HA. Arsenic(III) was added at concentrations ranging from 5 to 50 μg L^{-1} in a glove box to prevent oxidation. Experimental solutions were then stirred for 48 h to reach equilibrium.

2.1.3. Sampling

For all experiments, 15 mL of solution was sampled and ultrafiltrated at 5 kDa (Vivaspin VS15RH12, Sartorius) under N_2 atmosphere. Ultracentrifugation cells were previously washed with Milli-Q water until DOC concentration in the ultrafiltrate was <1 mg L^{-1}. All experiments were conducted in duplicate.

2.2. Chemical analyses

All measurements were performed at Géosciences Rennes, France. DOC concentrations were measured using an organic carbon analyzer (Shimadzu TOC-V CSH). Arsenic and Fe concentrations were determined using an ICP-MS. Instrumental and data acquisition parameters can be found in Supporting Information 1 (SI). To ensure that no oxidation occurred during the experiments, the concentrations of As(III) and As(V) were monitored using a HPLC-Agilent 1260 Infinity coupled to an Agilent G3154-65001 and Fe_{TOT} was compared to the Fe(II) measured in the ultrafiltrate ($(Fe(II)_{UF})$) using the 1.10-phenanthroline colorimetric method (AFNOR, 1982). Because the absorbance of Leonardite at 50 mg L^{-1} is high, the Fe(II) concentration in the Fe(II)–HA solution was not checked. Arsenic(III) and Fe in the ultrafiltrates were assumed to be inorganic whereas As(III) and Fe bound to HA were considered to be in the fraction >5 kDa.

2.3. Modeling

2.3.1. Model description

Because As(III) can bind to OM thiol groups, the modeling calculations were performed using a modified version of the PHREEQC/

Model VI allowing this particular binding to be taken into account [21]. In the modified PHREEQC–Model VI, the ions complexation occurs through 12 discrete sites: four carboxylic groups (sites A), four phenolic groups (sites B) and four thiol groups (sites S). The abundances, intrinsic acidity constant for A, B and S sites and their distribution term are denoted as n_A, n_B, n_S, pK_A, pK_B, pK_S, ΔpK_A, ΔpK_B and ΔpK_S, respectively. Only monodentate complexes of As(III) with thiols are defined [21]. The fraction of proton sites that can form bidentate and tridentate complexes are named f_B and f_T, respectively [34]. All values of the parameters used for modeling calculations are given in supporting information Table S7. The strength of the interaction between one site and one ion is defined by the complexation constant $\log K$. Considering the 12 sites that can generate bidentates and tridentates, 84 equations are needed to describe the interaction between one ion and the 84 HA sites (further information is given in Section 2.2 of supporting information). The specific complexation parameters for the carboxylic, phenolic and thiol groups are $\log K_{MA}$, $\log K_{MB}$ and $\log K_{MS}$, respectively. The CCM model was used to model the electrostatic interactions. Ion accumulation in the vicinity of HA is calculated with the Donnan model. Further information can be found elsewhere [21].

2.3.2. Binding parameters and modeling strategy

2.3.2.1. Binary complexes. The binding parameters describing As(III) complexation by HA were previously determined using modified PHREEQC/Model VI including As(III)-thiol complexes [21]. The binding parameters used for the Fe(II)–HA binary complexes were determined using an earlier PHREEQC/Model VI version without thiol groups implementation [7]. These parameters therefore had to be re-evaluated using the present dataset and the new model version. To keep same proportions of monodentates, bidentates and tridentates the ΔLK_2 value used and the relationship between $\log K_{MA}$ and $\log K_{MB}$ were the same as those previously used [7], $\Delta LK_2 = 3.90$ and $\log K_{MA} = 0.49 * \log K_{MB}$. All binding parameters calculated here are presented in supporting information Table S8. All equations describing Fe(II) binding with each OM site were described in a previous study [7].

2.3.2.2. Ternary complexes. The experimental data were fitted using the PHREEPLOT program coupled with the modified version of PHREEQC/Model VI [7]. The 84 sites, their acidity constants and the binding parameters for Fe(II) and As(III) were added into the "minteq.v4" database. No previous study exists on the binding of As(III) to Fe(II)–HA complexes. The nature of the complexes formed had to be deduced from our experimental dataset and/or literature data. Only one study was dedicated to the characterization of the binding mechanisms of As(III) to Fe(III) as ion bound to peat [26]. Using EXAFS records, this study showed that for low Fe(III) concentrations, As(III) bound with Fe(III) as mononuclear bidentate complexes, whereas for high Fe(III) concentrations, As(III) bound with Fe(III) either as mononuclear bidentate complexes or as binuclear monodentate complexes. Jönsson and Sherman [35] suggested the formation of binuclear monodentate complexes for As(III) binding to green rust, fougerite and magnetite. However, Ona-Nguema et al. [36] rejected this hypothesis and proposed the formation of As(III) polymers. Thoral et al. [37] suggested that As(III) might form binuclear monodentate complexes with $Fe(OH)_2$ oxides under anoxic conditions. With respect to Fe(II), the modeling calculations performed earlier showed that Fe(II) bound with OM mainly through bidentate complexes [7], confirming this spectroscopic data [26].

Based on these proposed mechanisms, the modified PHREEQC/Model VI was first tested without Fe ternary complexes. They were implemented only when the model failed to reproduce the experimental datasets. From the spectroscopic data, six O atoms are bound to both Fe(II) and Fe(III) as FeO_6 octahedra [36,38]. Furthermore, the distance between As(III) and Fe(III) when As(III) is bound to Fe(III) oxides as corner-sharing bidentate complexes is between $d_{As(III)–Fe(III)} = 3.4–3.58$ Å and $d_{As(III)–Fe(II)} = 3.51$ Å for $Fe(OH)_2$ [36,38]. All the complex conformations for As(III)–Fe(II) were thus deduced from the As(III)–Fe(III) spectroscopic datasets. The complexation of As(III) to monodentate Fe(II)–OM complexes was described either as mononuclear bidentate complexes (Eq. (1)) or as binuclear bidentate complexes (Eq. (2)). With regards to the As(III) binding to bidentate Fe(II)–OM complexes, As(III) complexation was described either as mononuclear bidentate complexes (Eq. (3)) or as binuclear bidentate complexes (Eq. (4)). Although Fe(III)–OM tridentate complexes were calculated in Model VI, the possibility to form complexes with As(III) was low considering their negative charge.

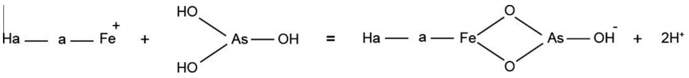

(1)

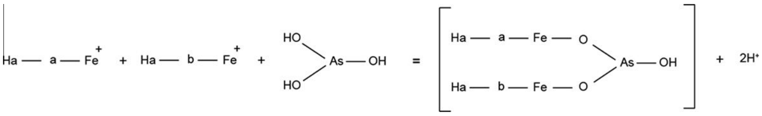

(2)

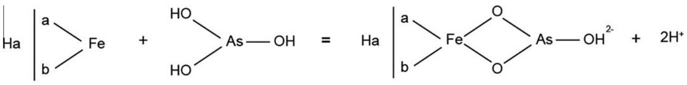

(3)

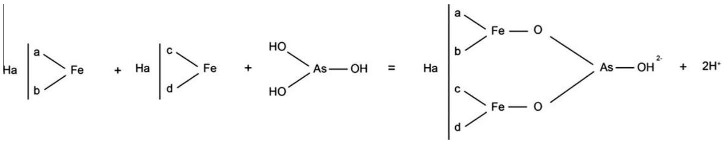

(4)

All of these equations were first tested separately, then by pairs (i.e. Eqs. (1) + (2), or Eqs. (3) + (4)), and last all together. All runs were finally compared to each other using their RMSE (Root Mean Square Deviation) calculated as $\sqrt{\text{mean}((\log\mu(\text{exp}) - \log\mu(\text{cal}))^2}$, with $\log\mu$(exp) and $\log\mu$(cal) representing the logarithm of the measured and modeled As(III) bound concentrations, respectively.

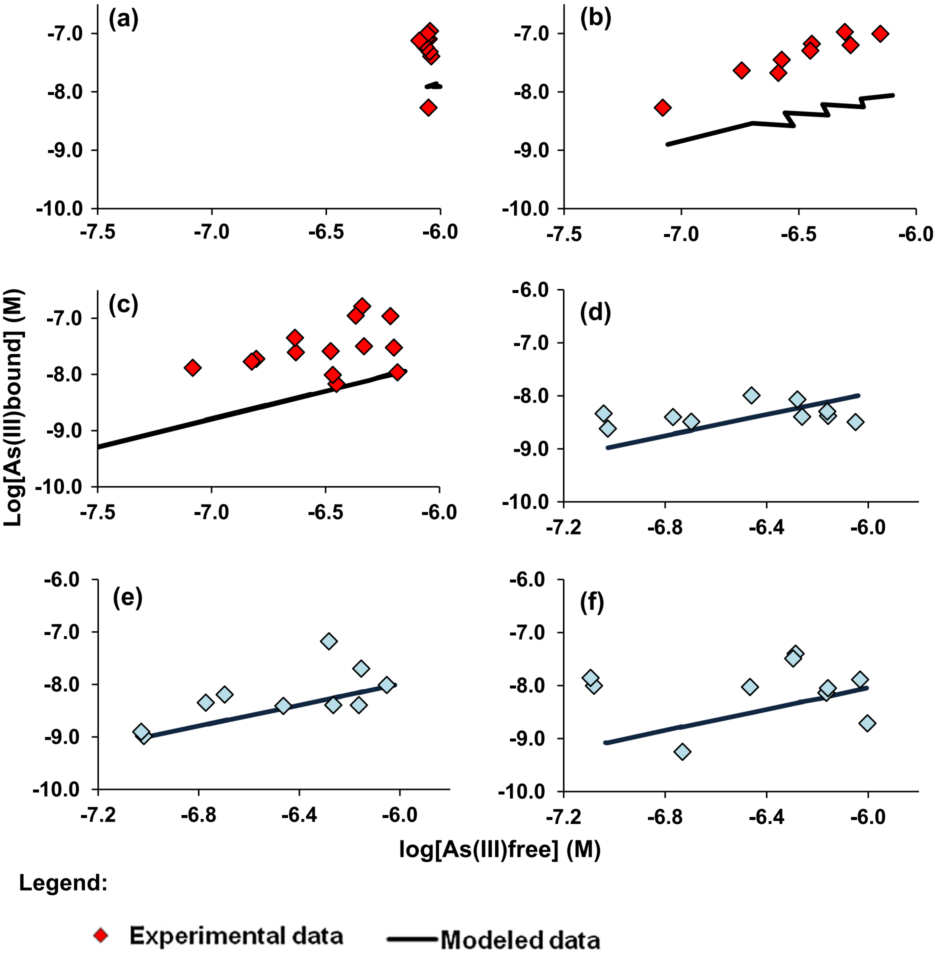

Fig. 1. (a) As(III)–Fe(II)–HA binding experiments and modeled data using only the thiol binding parameters according to the [Fe(II)] concentration, (b) at pH 6, (c) pH 5, (d) As(III)–Fe(III)–HA binding experiments and modeled data using only the thiol binding parameters at pH 4, (e) pH 5, and (f) pH 6.

3. Results

3.1. As(III)–Fe(II)–HA experimental and modeling data

No Fe(II) and As(III) oxidation occurred in the experiments. The binding parameters $\log K_{MA}$ (2.34) and $\log K_{MB}$ (4.78) for Fe(II) binding to HA, determined by fitting the experimental datasets using the modified PHREEQC/Model VI, were close to the $\log K_{MA}$ (2.19) and $\log K_{MB}$ (4.46) determined without the thiol sites implementation [7]. Since the relationship between $\log K_{MA}$, $\log K_{MB}$ and ΔLK_2 was kept, the same proportions of monodentate, bidentate and tridentate complexes were calculated than previously [7]. Bidentates were the most abundant complexes formed between Fe(II) and HA. The experimental and modeled adsorption isotherm of Fe(II) binding to HA are presented in supporting information Fig. S1.

The adsorption isotherms of As(III) by Fe(II)–HA (log[As(III)–HA] relative to $\log[As(III)_{UF}]$) are displayed in Fig. 1a–c. Fig. 1a showed that, for the same As(III) concentrations but increasing Fe(II) concentrations, the amount of bound As(III) increased. For adsorption isotherms at pH 5 and 6, no plateau was reached, i.e. no saturation was obtained (Fig. 1b and c). The model that did not take ternary complexes into account (e.g. As(III)–S–HA complexes) could not reproduce the experimental datasets (RMSE = 0.87). Therefore, the presence of Fe(II) modified the binding behavior of As(III) to HA and had to be taken into account in the model hypothesis. No Fe(II) oxides precipitated as evidenced by the saturation index calculated using PHREEQC/Model VI. Therefore, As(III) speciation was mainly controlled by direct As(III)–S–HA and indirect As(III)–Fe(II)–HA complexes.

Model fits obtained using one or more of the four equations described in Section 2.3.2 are displayed in supporting information Figs. S9–13. When only one equation was used, Eqs. (3) and (4) were the most reliable as shown by the low RMSE (RMSE = 0.18 and 0.19 respectively, Table 1 and Figs. S5, 6). When a pair of equations were used (Eq. (1) + Eq. (2) or Eq. (3) + Eq. (4)), the equation that yielded the smallest RMSE obtained in the single model (i.e. one equation) dominated the binding mechanism (Table 1). This result can be explained by the fact that the fitting program works based on the smallest statistical parameters. When Fe(II) binding to HA was considered to occur via monodentate complexes, Eq. (1) dominated over Eq. (2), leading to a comparatively much higher $\log K$: $\log K = 4.15$ for Eq. (3) versus −1.33 for Eq. (2). Note that the $\log K$ obtained for Eq. (1) was similar to the one obtained with

Table 1
Binding parameters and RMSE for the different tested mechanisms.

Mechanism	Log *k*				RMSE
Eq. (1)	4.15				0.38
Eq. (2)	4.33				0.58
Eq. (3)	3.39				0.18
Eq. (4)	2.27				0.19
Eq. (1) + Eq. (2)	4.15		−1.33		0.38
Eq. (3) + Eq. (4)	3.39		−1.94		0.18
Eq. (1) + Eq. (2) + Eq. (3) + Eq. (4)	−1.56	−1.32	3.39	−2.09	0.18

Eq. (1) only (Table 1). For the models that used both Eqs (3) and (4) (RMSE = 0.18, Table 1) and all equations together (supporting information Fig. S8), the dominant equation was Eq. (3) (mononuclear bidentate complexation of As(III) with bidentate Fe(II)–HA complexes), with RMSE = 0.18.

3.2. As(III)–Fe(III)–HA experimental data

The adsorption isotherms of As(III) to Fe(III)–HA (log[As(III)–HA] relative to log[As(III)$_{UF}$]) are displayed in Fig. 1d–f. No plateau was reached at pH 5 and 6 (Fig. 1e and f), by contrast with pH 4 (Fig. 1d). The proportion of bound As(III) at the different pH was similar, suggesting a minor role of pH in As(III) binding. The model that only considered the binding of As(III) to thiol groups correctly reproduced the experimental data (Fig. 1d–f and total RMSE = 0.52). The high RMSE was due to the dispersion of the experimental points. In our experimental conditions, Fe(III) did not seem to influence the binding of As(III) to HA.

4. Discussion

4.1. Monodentate or bidentate Fe(II)–HA sites: which ones complex As(III) most efficiently?

As shown by their lowest RMSE, Eqs. (3) and (4) better fit the experimental dataset (RMSE = 0.18 and 0.19, Table 1). However in PHREEQC/Model VI, the fraction of sites that can make bidentate Fe(II)–OM complexes was determined from the geometry of the OM molecules. The minimal distance between two sites was fixed at 0.3 nm for a sphere with a radius of 0.8 nm. If the distance between two sites ranged between 0.3 and 0.45 nm, the sites were defined as bidentate sites [39]. In our simulations, Eq. (4) represents the binding of As(III) to two Fe atoms, each forming bidentate complexes with OM. The distance between each Fe atom was $d_{Fe-Fe} \approx (0.3–0.45) * 2 = 0.6–0.9\ \text{nm} = 6–9\ \text{Å}$ (Fig. 2a). Spectroscopic data demonstrated that the distance between As and the neighbor O (d_{As-O}) varied from 1.70 to 1.79 Å [26,36,37,40]. The distance between Fe(III) and O atoms (d_{Fe-O}) varied from 1.94 to 1.99 Å [26,40] and from 1.99 to 2.14 Å for Fe(II)–O and Fe(II)–As(III) systems [36,37,41]. The maximal distance between As and Fe bound via an O ($d_{As-O-Fe}$) was therefore equal to $d_{As-O-Fe}\text{max} = d_{As-O}\text{max} + d_{Fe-O}\text{max} = 1.79 + 2.14 = 3.93\ \text{Å}$ which was $\ll 6–9\ \text{Å}$ (d_{Fe-Fe} for two bidentate sites). Thus, the binding of As to Fe through O with distances of 6–9 Å between two Fe atoms seemed impossible (Fig. 2a). Therefore, although PHREEQC/Model VI allowed the binding of As(III) to HA through Fe(II) bidentate sites, for geometrical reasons, in experimental and natural conditions, this possibility was expected only when Fe dimer and trimer appeared [25,26,42,43].

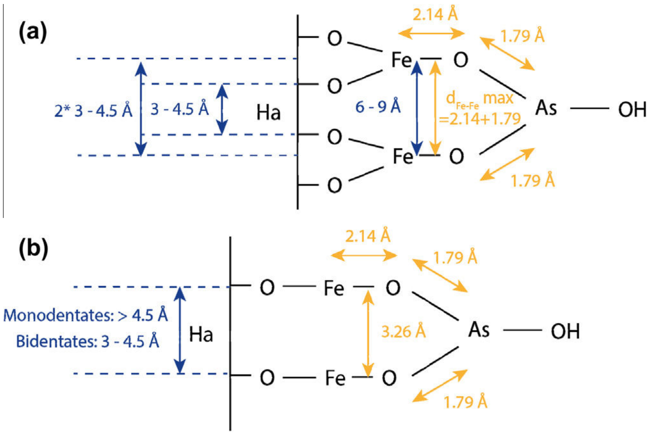

Fig. 2. Complexes formed with (a) Eq. (6) and (b) Eq. (4). Fe–O and As–O distances (in orange) were determined from the Fe(OH)$_2$ oxides and As(OH)$_3$, respectively [36]. The distances in blue are defined in PHREEQC–Model VI [34]. (For interpretation of the references to colour in this figure legend, the reader is referred to the web version of this article.)

Eq. (2), which assumed the As(III) binding to two Fe(II)–MO monodentates, poorly reproduced the experimental datasets (RMSE = 0.58, Table 1). The fit was poor (RMSE = 0.71, supporting information Fig. S3) for the isotherm at pH 5. According to PHREEQC–Model VI, the abundance of the Fe(II)–OM monodentate complexes would be quite low, ranging between 0.02 and 18% versus 74 and 83% for the Fe(II)–OM monodentate and bidentate complexes, respectively. This low abundance of the Fe(II)–OM monodentate complexes likely explained why Eq. (2) failed to satisfactorily reproduce the experimental data. A critical point was that in PHREEQC–Model VI, monodentate sites were assumed to be separated from each other by more than 4.5 Å whereas in the Fe(OH)$_2$ oxides, when As(III) was bound to Fe, d_{Fe-Fe} was smaller at 3.26 Å (Fig. 2b). Therefore, Eq. (2) was impossible with the common hypothesis used in PHREEQC/Model VI. Hoffmann et al. [26] showed that As(III) could form binuclear monodentates with Fe(III) complexed to HA. As discussed above, the complexation of As(III) by bidentate Fe(II)–OM complexes was not reliable for geometrical reasons and as a result, only Fe(II)–OM monodentate could bind As(III). These observations suggested that a part of the bidentate sites, defined in the model as spaced apart by 3–4.5 Å, possibly bound Fe(II) in a monodentate mode (e.g. Ha-ab(Fe)$_2$ versus Ha-abFe).

Hoffmann et al. [26] showed that As(III) was bound as binuclear monodentate complexed to Fe(III)–OM. Using PHREEQC/Model VI and their experimental conditions, we calculated that Fe(III) was able to recover between 0.75% and 5.95% of the HA sites. The coupling of the spectroscopic [26] and modeled datasets demonstrated that As(III) binuclear monodentate complexes were formed from a recovery of 5.95%. In our experiments, the surface recovery by Fe(II) ranged between 5% and 38% which support our hypothesis that As(III) binding to HA mainly occurred through binuclear monodentate Fe(II)–HA complexes.

Although Eq. (1) better reproduced the experimental datasets than Eq. (2), the calculated RMSE was higher than for Eqs. (3) and (4) (Table 1). Considering only the atomic distances, the binding of As(III) to only one Fe(II)–HA complex is thought to be plausible, but in addition, for example, to Eq. (3).

As seen previously, when several equations were used together, the model chose the equation that provided the smallest RMSE and attributed a negative log K to the other equations. With regards to the Fe(II) recovery on HA, and the spectroscopic data in the literature, mononuclear bidentate and binuclear monodentate complexes seemed to be the most reliable mechanisms involved in As(III) binding by Fe(II)–HA. Used together Eqs. (1) and (2) described the As(III) binding to Fe(II)–HA monodentate complexes. Regarding the low density of Fe(II)–HA monodentates, the model should be able to determine the log K for both equations. When Eqs. (3) and (4) were used together, enough Fe(II) bidentate complexes were formed. However, none of these coupled equations reasonably fit the experimental datasets. In fact, the model was not able to assess the respective weight of each equation. Some constraints had to be implemented in PHREEQC/Model VI to improve the quantification of each equation relative to the other ones. PHREEQC/Model VI was able to accurately discriminate the binding of one ion to the carboxylic and phenolic sites and to determine the corresponding binding parameters. In this case, the constraints were imposed by the acidity constants which control the density of each site relative to the pH and by the imposed linear relationship between the $\log K_{MA}$ and $\log K_{MB}$ values ($\log K_{MB} = 3.39 * \log K_{MA}$) [34].

4.2. Instructions to better model As(III)–Fe(II)–HA interactions

To improve the modeling of the data using Eq. (2) – the most probable equation with regards to the spectroscopic data [26] – we modified PHREEQC/Model VI by identifying the proportion of bidentate sites that can potentially bind two Fe (2-monodentate mode). In Model VI, the bidentate Fe(II) sites are distributed between weak, strong, and very strong bidentate sites. The differences between each site are defined by the site abundance and the ion binding parameters ($\log K_{MA}$, $\log K_{MB}$ and ΔLK_2). The strong and very strong bidentate sites are 10.01 and 100.11 times less abundant, respectively, than the weak bidentate site. The $\log K$ value for the strong bidentate sites is equal to that of the weak bidentate sites plus ΔLK_2, the distribution term that modified the strength of the bidentate and tridentate sites. $\log K$ for the very strong bidentate sites are equal to those for weak bidentate sites plus $2 * \Delta LK_2$. In a bidentate complex, two sites bind one Fe, whereas in the 2-monodentate mode, for each monodentate site, one site binds Fe. In the 2-monodentate mode, $\log K$ will be lower than the bidentate $\log K$. Therefore, the 2-monodentate could only be developed from the weak bidentate group, as strong and very strong bidentate sites have higher binding constants. In PHREEQC/Model VI, the binding constant for the weak bidentate group was defined as the sum of two monodentate sites; however, the mechanism had to be modified to correspond to the required 2-monodentate mode. Eq. (5) corresponds to the classical equation and Eq. (6) to the equation for the 2-monodentate mode.

$$\mathrm{Ha\_ab}^{2-} + \mathrm{Fe}^{2+} = \mathrm{Ha\_abFe} \quad \log k = \log k(a) + \log k(b) \tag{5}$$

$$\mathrm{Ha\_ab}^{2-} + 2\mathrm{Fe}^{2+} = \mathrm{Ha\_abFe}_2^{+2} \quad \log k = \log k(a) + \log k(b) \tag{6}$$

With regards to the abundance of the sites, it cannot be assumed that all of the weak bidentate sites are involved in the 2-monodentate mode. It was also difficult to quantify the exact proportion of weak bidentate sites that could bind Fe(II) in the 2-monodentate mode. Consequently, tests were performed with a proportion of these weak bidentate sites varying from 5% to 90%. When the proportion was 5%, 5% of the weak bidentate sites bound Fe following Eq. (2) and 95% following Eq. (3) when fitting the experimental data (supporting information Table S13). This procedure was applied to Eqs. (2) and (3) simultaneously, which corresponded to a new modeling configuration. The model was not able to determine the $\log K$ for the proportions ranging from 5% to 80%. However, for 90% of the bidentate sites that used Eq. (3), the fitted $\log K$ were equal to 2.86 and 3.95, respectively. Because As(III) was only bound to one Fe following this equation versus two Fe in Eq. (2), the $\log K$ for Eq. (2) should be lower than for Eq. (3); 90% of the bidentate sites that used the 2-monodentate mode were therefore too large. Thus, it is necessary to experimentally/analytically determine the proportions of Fe(II) among the bidentate sites that could possibly be involved in the 2-monodentate mode (e.g. using spectroscopy). Then, $\log K$ between As(III) and the Fe(II)–HA complexes should be determined using both binding mechanisms.

4.3. Interpretation of the As(III)–Fe(III)–HA data

The model using thiol groups only reproduced our experimental datasets reasonably well. The presence of Fe(III) did not seem to influence the binding of As(III) to the thiol groups, suggesting that (i) no competition for thiol groups occurred and (ii) no or negligible ternary complexes were formed. However, for their experimental conditions, Hoffmann et al. [26] clearly observed this type of ternary associations between As(III), Fe(III) and peat. The reason was that the concentrations used were much higher (in [26] 13 g L^{-1}, 20–200 mg L^{-1} and 22.5 mg L^{-1} of DOC, Fe(III) and As(III), respectively versus here, 50 mg L^{-1}, 0.6 mg L^{-1} and 5–50 μg L^{-1} of DOC, Fe(III) and As(III), respectively), and the pH was different (pH 7, 8.4 and 8.8 [26] versus 4, 5 and 6 here). At pH 8.4 and 8.8, As(III) occurred as $H_2AsO_3^-$ implying the formation of new complex. The negative charge caused by the higher pH increased the binding of As(III) as ternary complexes via Fe(III) bridges as shown by the comparison of the isotherms performed for similar Fe(III) and As (III) concentrations but different pH in Hoffmann et al. (Fig. 2A in [26]). Although the DOC/Fe ratios were equivalent (65–650 for [26] and 83 here), the As/Fe ratios were different (1.1–0.11 for [26] versus 0.0083–0.001 here). Moreover, the Fe(III) concentrations used here were chosen to avoid any Fe(III) precipitation. The S content of the peat used by Hoffmann et al. [26] was also very low and did not allow the binding of As(III) to peat through thiol sites, by contrast, with the here used HA as previously shown [21]. Thus, the thiol sites were able to compete with the Fe(III)–HA complexes, in low amounts, for As(III) binding. At circumneutral pH and intermediate As/C ratio, Hoffmann et al. [26] observed that the $\log Kd$ (distribution coefficient of As(III) on organic carbon) was higher for As(III) bound to peat thiol sites than for As(III) bound to Fe(III)-peat complexes. In our experiments, As(III) bound to Fe(III)–HA was probably not present in high enough amounts to be detected, particularly in comparison with As(III) bound to S–HA. However, higher concentrations of Fe(III) should induce precipitation and the mechanism would be then performed with particulate or colloidal Fe(III) oxyhydroxides, which was not the purpose of the present study. It is important to note that the experimental conditions used by Hoffmann et al. [26] were developed to specifically promote the formation of ternary complexes via ionic Fe(III) and to allow the detection of As(III) and Fe(III) using the XAS technique.

4.4. Environmental implications

In floodplains and wetlands, the speciation of the elements depends strongly on the redox conditions. In such environments, when the soils are flooded and become water saturated, O_2 is consumed by bacteria, creating anoxic conditions, whereas when the soils are not saturated, oxic conditions prevailed. Under reducing conditions, As is mainly as As(III) and Fe as Fe(II), while under moderately reducing conditions As(III), As(V), Fe(II) and Fe(III) species can coexist. The speciation of Fe(III) depends on the amount of Fe(III) and on the physico-chemical conditions (pH, Eh, OM, competitors, etc.). For high Fe(III) concentrations, Fe occurs mostly as particulate or colloidal oxyhydroxides (lepidocrocite, ferrihydrite, goethite, etc.) generally bound to OM in organic-rich environments [44]. Iron(III) oxyhydroxides are the main sorbent of As(III) and As (V) in the environment. These systems are well documented and $\log K$ estimates can be found ($Hfo\_sOH + H_3AsO_3 = Hfo\_sH_2AsO_3 + H_2O$, $\log k = 5.41$, 5.74 or 4.02 [2,3,45]). In organic-rich environments, As(III) is expected to either compete with OM molecules for its binding to Fe(III) oxyhydroxydes, which could strongly limit its complexation [13], or to be complexed by Fe(III) oxyhydroxides which are themselves bound to OM (Fig. 3) [13,23,30,31]. For low Fe(III) concentrations, no precipitation occurred and Fe occurs as Fe^{3+}, $Fe(OH)^{2+}$ and $Fe(OH)_2^+$, depending on the pH. In organic-rich environments, Fe(III) as ion can be bound by the carboxylic and phenolic groups of OM [8–10,43], mostly as bidentate complexes. Hoffmann et al. [26] showed that at high concentrations of Fe (III), As(III) and OM, ternary complexes can be produced via ionic Fe(III) (Fig. 3). However, these results were strongly dependent on their experimental conditions performed to specifically

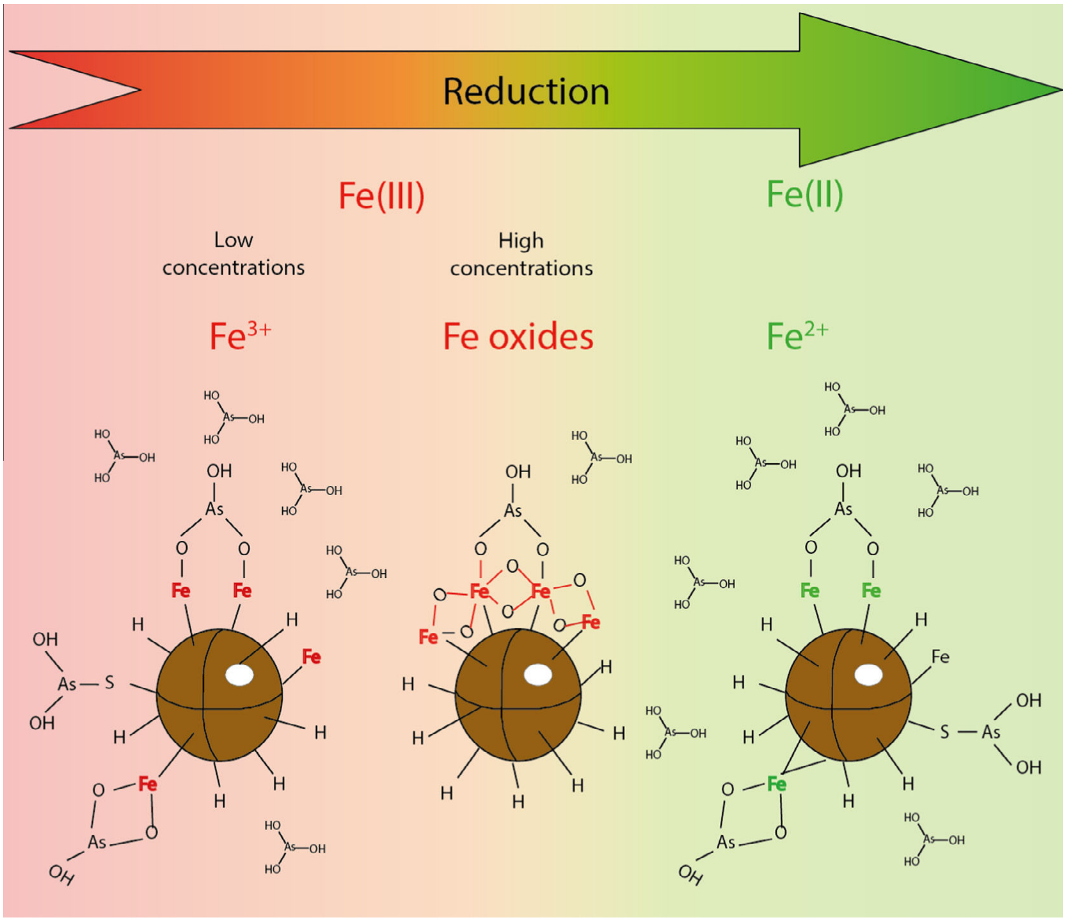

Fig. 3. Schematic model describing the complexes that may form between As(III) Fe(II) and/or Fe(III) and dissolved organic matter (DOM), with regards to the redox status of Fe, and Fe and the DOM concentrations. This scheme may apply to what happens in floodplain and wetland waters [21,25,26].

promote this binding mechanism. In environmental conditions, for high amounts of Fe(III) such as those used by Hoffmann et al. [26], Fe(III) precipitated as Fe(III) oxyhydroxides and thus sorbed As(III) (high log$K$). In this case, we can consider that the ternary complex occurred through Fe(III) oxides or nano-oxides. In our studies, for higher OM thiol amounts and low Fe(III) concentrations, As(III)–Fe(III)–OM ternary complexes via ionic Fe(III) were not detected. Therefore, for an environmental level of Fe(III), ternary complexes via ionic Fe(III) does not seem possible even in organic-rich waters [44,46–48], notably when there is a sufficient number of thiol sites on OM to bind As(III) [19,21]. If the S% in OM does not totally correspond to thiol, much of the dissolved OM should contain a sufficiently high number of thiol groups to efficiently outcompete As(III) complexation by ternary Fe(III)–HA complexes. The competition between thiol binding and ternary complexes via ionic Fe(III) probably always occurs in natural OM-mediated interactions.

In waterlogged floodplains and wetlands, ferric-reducing bacteria reductively dissolved Fe(III) oxyhydroxides, thereby releasing Fe(II) into the solution. In such environments, high OM concentrations are produced. Catrouillet et al. [7] demonstrated that OM can strongly bind Fe^{2+} and $Fe(OH)^+$, especially at neutral and basic pH. Here, we showed that As(III) might be indirectly bound as ternary complexes to OM via ionic Fe(II) (Fig. 3) and directly bound through OM thiol sites. The dynamics of the As(III) bound to OM is therefore controlled by the own OM dynamic. However, in the present work, we estimated that As(III) bound to OM by direct and indirect mechanisms could vary from 5% to 26% of the total As(III). We performed speciation calculations to test the studied mechanism in reduced water produced by the anoxic incubation of an organic-rich wetland soil (unpublished data). Arsenic(III), Fe(II) and DOC concentrations were measured in the colloidal fraction which corresponded to the concentrations measured by ultrafiltration in the >3 kDa fraction, and the truly dissolved concentrations which corresponded to the concentrations measured by HPLC–ICP-MS in the <3 kDa fraction. In these calculations, we considered that the As(III) measured by HPLC–ICP-MS occurred as free species. This experimental dataset was used to test the present model using the following assumptions: DOC was only composed of HA (for which the proportion of reactive and non-reactive DOM was not known), the thiol groups concentration was equal to that of the Leonardite (0.13 mmol g^{-1}) and the binding of As(III) to Fe(II)–HA complexes was calculated using only Eq. (2), with log$K$ = 3.39. We calculated that 1.2% of As(III) was bound to S–OM and 22.7% to Fe(II)–OM. These calculations were close to the proportion determined from the analytical techniques, i.e. 32% of As(III) bound to OM. The experimental proportions corresponded to the difference between As_{TOT} (determined by ICP-MS) and free As(III) concentrations (determined by HPLC–ICP-MS). Therefore, the binding of As(III) with OM as ternary complexes via ionic Fe(II) seemed to be potentially important in anoxic environments such as floodplains and wetlands, even if the mechanisms and binding constants used for this calculation had to be improved. As long as reducing conditions prevail, a large proportion (this study >24–32%) of As(III) was in the solution as labile species, possibly transferred to the underlying aquifers.

Note that all of these complex conformations investigated in this study were described for the $As(OH)_3$ species. However, for pH > 8, As(III) is expected to occur as a negatively charged species, namely $As(OH)_3O$. Hoffmann et al. showed that with increasing pH, As(III) speciation change should result in a higher proportion of As(III) bound to OM through ternary complexes [26]. However, although the binding of ternary complexes seems to be favored for $As(OH)_2O^-$, few natural waters have $pH > 8$ and high enough OM and Fe concentrations. This is why these mechanisms were not presented in Fig. 3.

5. Conclusion and perspectives

We provided experimental datasets for As(III) binding to HA as ionic Fe(II) and Fe(III) occurred. Arsenic(III) was bound to HA as ternary complexes via ionic Fe(II) and through HA thiol sites (4–26% of total As(III)). No ternary complexes seem to be formed with Fe(III) in our experimental conditions chosen to mimic natural waters Fe(III) and DOM concentrations. However, Hoffmann et al. [26], demonstrated the formation of such a complex. As assessed by EXAFS record, they showed that As(III) formed mononuclear bidentate and binuclear monodentate complexes, Fe(III) being itself bound to peat. The differences outlined in between both studies is explained by the lower Fe(III) concentrations and the higher amount of HA thiol groups in our experimental conditions. It appeared that Fe(III)-HA complex was not enough competitive regards to thiol functional group to succeed in As(III) binding at low Fe(III) concentrations. Various complex conformations were indeed tested with PHREEPLOT–PHREEQC/Model VI: (i) mononuclear bidentate of As(III) bound to monodentate of Fe(II) with OM, (ii) binuclear monodentate of As(III) bound to monodentate of Fe(II) with OM, (iii) mononuclear bidentate of As(III) bound to bidentate of Fe(II) to OM (iv) monodentate binuclear of As(III) to bidentate of Fe(II) to OM. The complex conformation involving binuclear monodentate of As(III) bound to bidentate of Fe(II) with OM was not possible regards to the atomic distances, deduced from the spectroscopic data available in literature and to their abundances. The complex conformation involving mononuclear bidentate of As(III) bound to bidentate of Fe(II) with OM was possible and fitted well the experimental datasets. The binding conformation based on binuclear monodentate of As(III) bound to monodentate of Fe(II) with OM was impossible in its current form with PHREEQC/Model VI. The atomic distances required a new binding mode for the bidentate sites described by Tipping [34], namely the formation of Fe(II) 2-monodentate complexes in the group of weak bidentates sites. PHREEQC/Model VI was not able actually to correctly model ternary complexes. Finally, the binding conformation involving mononuclear bidentate of As(III) bound to monodentate of Fe(II) with OM was possible but, unfortunately did not correctly fit the experimental data. Even if ternary complexes were possible using ionic Fe(III, II), the percentage of As(III) bound to OM remained low. Most part of As(III) stayed labile and therefore is easily transferable to environment. The amount of As(III) bound to OM is however less mobile and its ability to be transferred in environment will depend on which in between particulate or colloidal OM this species is bound to. These results raise now the crucial question of the fate of this As(III) either labile or bound to OM when the conditions become oxidizing?

Acknowledgments

We are thankful to Dr. Rémi Marsac and Christian le Carlier de Veslud for advice regarding the modeling. Patrice Petitjean is acknowledged for ensuring the maintenance of the glove box during the experiments. Dr. Sara Mullin is thanked for post-editing the English style. This study was funded by the French ANR, through the "Programme Jeunes Chercheurs": ARSENORG.

Appendix A. Supplementary material

Supplementary data associated with this article can be found, in the online version, at http://dx.doi.org/10.1016/j.jcis.2016.02.047.

References

[1] J.A. Plant, D.G. Kinniburgh, P.L. Smedley, F.M. Fordyce, Arsenic and selenium, in: Treatise Geochem, Elsevier, 2004, pp. 17–66.

[2] S. Dixit, J.G. Hering, Comparison of Arsenic(V) and Arsenic(III) sorption onto iron oxide minerals: implications for arsenic mobility, Environ. Sci. Technol. 37 (2003) 4182–4189, http://dx.doi.org/10.1021/es030309t.

[3] D.A. Dzombak, F.M.M. Morel, Surface Complexation Modeling: Hydrous Ferric Oxide, John Wiley & Sons, New York, 1990, p. 393.

[4] W.P. Tseng, H.M. Chu, S.W. How, J.M. Fong, C.S. Lin, S. Yeh, Prevalence of skin cancer in an endemic area of chronic arsenicism in Taiwan, J. Natl Cancer Inst. 40 (1968) 453.

[5] K. Kalbitz, R. Wennrich, Mobilization of heavy metals and arsenic in polluted wetland soils and its dependence on dissolved matter, Sci. Total Environ. 209 (1998) 27–39.

[6] H.M. Anawar, J. Akai, K. Komaki, H. Terao, T. Yoshioka, T. Ishizuka, et al., Geochemical occurrence of arsenic in groundwater of Bangladesh: sources and mobilization processes, J. Geochem. Explor. 77 (2003) 109–131, http://dx.doi.org/10.1016/S0375-6742(02)00273-X.

[7] C. Catrouillet, M. Davranche, A. Dia, M. Bouhnik-Le Coz, R. Marsac, O. Pourret, et al., Geochemical modeling of Fe(II) binding to humic and fulvic acids, Chem. Geol. 372 (2014) 109–118, http://dx.doi.org/10.1016/j.chemgeo.2014.02.019.

[8] T. Karlsson, P. Persson, Coordination chemistry and hydrolysis of Fe(III) in a peat humic acid studied by X-ray absorption spectroscopy, Geochim. Cosmochim. Acta 74 (2010) 30–40, http://dx.doi.org/10.1016/j.gca.2009.09.023.

[9] R. Marsac, M. Davranche, G. Gruau, A. Dia, M. Pédrot, M. Le Coz-Bouhnik, et al., Effects of Fe competition on REE binding to humic acid: origin of REE pattern variability in organic waters, Chem. Geol. 342 (2013) 119–127, http://dx.doi.org/10.1016/j.chemgeo.2013.01.020.

[10] C. Sjöstedt, I. Persson, D. Hesterberg, D.B. Kleja, H. Borg, J.P. Gustafsson, Iron speciation in soft-water lakes and soils as determined by EXAFS spectroscopy and geochemical modelling, Geochim. Cosmochim. Acta 105 (2013) 172–186, http://dx.doi.org/10.1016/j.gca.2012.11.035.

[11] H. Van Dijk, Cation binding of humic acids, Geoderma 5 (1971) 53–67.

[12] H.J. Shipley, S. Yean, A.T. Kan, M.B. Tomson, A sorption kinetics model for arsenic adsorption to magnetite nanoparticles, Environ. Sci. Pollut. Res. 17 (2010) 1053–1062, http://dx.doi.org/10.1007/s11356-009-0259-5.

[13] M. Grafe, M.J. Eick, P.R. Grossl, Adsorption of arsenate (V) and arsenite (III) on goethite in the presence and absence of dissolved organic carbon, Soil Sci. Soc. Am. J. 65 (2001) 1680–1687.

[14] M. Bauer, C. Blodau, Mobilization of arsenic by dissolved organic matter from iron oxides, soils and sediments, Sci. Total Environ. 354 (2006) 179–190, http://dx.doi.org/10.1016/j.scitotenv.2005.01.027.

[15] S. Wang, C.N. Mulligan, Speciation and surface structure of inorganic arsenic in solid phases: a review, Environ. Int. 34 (2008) 867–879, http://dx.doi.org/10.1016/j.envint.2007.11.005.

[16] M. Martin, L. Celi, E. Barberis, A. Violante, L.M. Kozak, P.M. Huang, Effect of humic acid coating on arsenic adsorption on ferrihydrite-kaolinite mixed systems, Can. J. Soil Sci. 89 (2009) 421–434.

[17] J. Buschmann, A. Kappeler, U. Lindauer, D. Kistler, M. Berg, L. Sigg, Arsenite and arsenate binding to dissolved humic acids: influence of pH, type of humic acid, and aluminum, Environ. Sci. Technol. 40 (2006) 6015–6020.

[18] V. Lenoble, D.H. Dang, M. Loustau Cazalet, S. Mounier, H.-R. Pfeifer, C. Garnier, Evaluation and modelling of dissolved organic matter reactivity toward AsIII and AsV – implication in environmental arsenic speciation, Talanta 134 (2015) 530–537, http://dx.doi.org/10.1016/j.talanta.2014.11.053.

[19] M. Hoffmann, C. Mikutta, R. Kretzschmar, Bisulfide reaction with natural organic matter enhances arsenite sorption: insights from X-ray absorption spectroscopy, Environ. Sci. Technol. 46 (2012) 11788–11797, http://dx.doi.org/10.1021/es302590x.

[20] P. Langner, C. Mikutta, R. Kretzschmar, Arsenic sequestration by organic sulphur in peat, Nat. Geosci. 5 (2011) 66–73, http://dx.doi.org/10.1038/ngeo1329.

[21] C. Catrouillet, M. Davranche, A. Dia, M. Bouhnik-Le Coz, M. Pédrot, R. Marsac, et al., Thiol groups controls on arsenite binding by organic matter: new experimental and modeling evidence, J. Colloid Interface Sci. 460 (2015) 310–320, http://dx.doi.org/10.1016/j.jcis.2015.08.045.

[22] M. Bauer, C. Blodau, Arsenic distribution in the dissolved, colloidal and particulate size fraction of experimental solutions rich in dissolved organic matter and ferric iron, Geochim. Cosmochim. Acta 73 (2009) 529–542, http://dx.doi.org/10.1016/j.gca.2008.10.030.

[23] I. Ko, J.-Y. Kim, K.-W. Kim, Arsenic speciation and sorption kinetics in the As–hematite–humic acid system, Colloids Surf. Physicochem. Eng. Asp. 234 (2004) 43–50, http://dx.doi.org/10.1016/j.colsurfa.2003.12.001.

[24] A.D. Redman, D.L. Macalady, D. Ahmann, Natural organic matter affects arsenic speciation and sorption onto hematite, Environ. Sci. Technol. 36 (2002) 2889–2896, http://dx.doi.org/10.1021/es0112801.

[25] C. Mikutta, R. Kretzschmar, Spectroscopic evidence for ternary complex formation between arsenate and ferric iron complexes of humic substances, Environ. Sci. Technol. 45 (2011) 9550–9557, http://dx.doi.org/10.1021/es202300w.

[26] M. Hoffmann, C. Mikutta, R. Kretzschmar, Arsenite binding to natural organic matter: spectroscopic evidence for ligand exchange and ternary complex formation, Environ. Sci. Technol. 47 (2013) 12165–12173, http://dx.doi.org/10.1021/es4023317.

[27] E. Neubauer, F. von der Kammer, K.-H. Knorr, S. Peiffer, M. Reichert, T. Hofmann, Colloid-associated export of arsenic in stream water during stormflow events, Chem. Geol. 352 (2013) 81–91, http://dx.doi.org/10.1016/j.chemgeo.2013.05.017.

[28] H.-T. Lin, M. Wang, G.-C. Li, Complexation of arsenate with humic substance in water extract of compost, Chemosphere 56 (2004) 1105–1112, http://dx.doi.org/10.1016/j.chemosphere.2004.05.018.

[29] K. Ritter, G.R. Aiken, J.F. Ranville, M. Bauer, D.L. Macalady, Evidence for the aquatic binding of arsenate by natural organic matter−suspended Fe(III), Environ. Sci. Technol. 40 (2006) 5380–5387, http://dx.doi.org/10.1021/es0519334.

[30] P. Sharma, M. Rolle, B. Kocar, S. Fendorf, A. Kappler, Influence of natural organic matter on as transport and retention, Environ. Sci. Technol. 45 (2011) 546–553, http://dx.doi.org/10.1021/es1026008.

[31] G. Liu, A. Fernandez, Y. Cai, Complexation of arsenite with humic acid in the presence of ferric iron, Environ. Sci. Technol. 45 (2011) 3210–3216, http://dx.doi.org/10.1021/es102931p.

[32] M. Davranche, A. Dia, M. Fakih, B. Nowack, G. Gruau, G. Ona-nguema, et al., Organic matter control on the reactivity of Fe(III)-oxyhydroxides and associated As in wetland soils: a kinetic modeling study, Chem. Geol. 335 (2013) 24–35, http://dx.doi.org/10.1016/j.chemgeo.2012.10.040.

[33] R. Marsac, M. Davranche, G. Gruau, M. Bouhnik-Le Coz, A. Dia, An improved description of the interactions between rare earth elements and humic acids by modeling: PHREEQC-Model VI coupling, Geochim. Cosmochim. Acta 75 (2011) 5625–5637, http://dx.doi.org/10.1016/j.gca.2011.07.009.

[34] E. Tipping, Humic ion-binding model VI: an improved description of the interactions of protons and metal ions with humic substances, Aquat. Geochem. 4 (1998) 3–47.

[35] J. Jönsson, D.M. Sherman, Sorption of As(III) and As(V) to siderite, green rust (fougerite) and magnetite: implications for arsenic release in anoxic groundwaters, Chem. Geol. 255 (2008) 173–181, http://dx.doi.org/10.1016/j.chemgeo.2008.06.036.

[36] G. Ona-Nguema, G. Morin, Y. Wang, N. Menguy, F. Juillot, L. Olivi, et al., Arsenite sequestration at the surface of nano-Fe(OH)2, ferrous-carbonate hydroxide, and green-rust after bioreduction of arsenic-sorbed lepidocrocite by Shewanella putrefaciens, Geochim. Cosmochim. Acta 73 (2009) 1359–1381, http://dx.doi.org/10.1016/j.gca.2008.12.005.

[37] S. Thoral, J. Rose, J.M. Garnier, A. Van Geen, P. Refait, A. Traverse, et al., XAS study of iron and arsenic speciation during Fe (II) oxidation in the presence of As (III), Environ. Sci. Technol. 39 (2005) 9478–9485.

[38] G. Ona-Nguema, G. Morin, F. Juillot, G. Calas, G.E. Brown, EXAFS analysis of arsenite adsorption onto two-line ferrihydrite, hematite, goethite, and lepidocrocite, Environ. Sci. Technol. 39 (2005) 9147–9155, http://dx.doi.org/10.1021/es050889p.

[39] E. Tipping, M.A. Hurley, A unifying model of cation binding by humic substances, Geochim. Cosmochim. Acta 56 (1992) 3627–3641.

[40] L.K. ThomasArrigo, C. Mikutta, J. Byrne, K. Barmettler, A. Kappler, R. Kretzschmar, Iron and arsenic speciation and distribution in organic flocs from streambeds of an arsenic-enriched peatland, Environ. Sci. Technol. 48 (2014) 13218–13228, http://dx.doi.org/10.1021/es503550g.

[41] T. Echigo, M. Kimata, Single-crystal X-ray diffraction and spectroscopic studies on humboldtine and lindbergite: weak Jahn-Teller effect of Fe2+ ion, Phys. Chem. Miner. 35 (2008) 467–475, http://dx.doi.org/10.1007/s00269-008-0241-7.

[42] J.W.J. van Schaik, I. Persson, D.B. Kleja, J.P. Gustafsson, EXAFS Study on the reactions between iron and fulvic acid in acid aqueous solutions, Environ. Sci. Technol. 42 (2008) 2367–2373, http://dx.doi.org/10.1021/es072092z.

[43] A. Vilgé-Ritter, J. Rose, A. Masion, J.-Y. Bottero, J.-M. Lainé, Chemistry and structure of aggregates formed with Fe-salts and natural organic matter, Colloids Surf. Physicochem. Eng. Asp. 147 (1999) 297–308.

[44] M. Pédrot, A.L. Boudec, M. Davranche, A. Dia, O. Henin, How does organic matter constrain the nature, size and availability of Fe nanoparticles for biological reduction?, J Colloid Interface Sci. 359 (2011) 75–85, http://dx.doi.org/10.1016/j.jcis.2011.03.067.

[45] P.J. Swedlund, J.G. Webster, Adsorption and polymerisation of silicic acid on ferrihydrite, and its effect on arsenic adsorption, Water Res. 33 (1999) 3413–3422.

[46] T. Allard, N. Menguy, J. Salomon, T. Calligaro, T. Weber, G. Calas, et al., Revealing forms of iron in river-borne material from major tropical rivers of the Amazon Basin (Brazil), Geochim. Cosmochim. Acta 68 (2004) 3079–3094.

[47] G. Olivie-Lauquet, T. Allard, M. Benedetti, J.-P. Muller, Chemical distribution of trivalent iron in riverine material from a tropical ecosystem: a quantitative EPR study, Water Res. 33 (1999) 2726–2734.

[48] O.S. Pokrovsky, J. Schott, B. Dupré, Trace element fractionation and transport in boreal rivers and soil porewaters of permafrost-dominated basaltic terrain in Central Siberia, Geochim. Cosmochim. Acta 70 (2005) 3239–3260.

Available online at www.sciencedirect.com

ScienceDirect

Geochimica et Cosmochimica Acta 203 (2017) 284–302

Geochimica et Cosmochimica Acta

www.elsevier.com/locate/gca

Highlighting the wide variability in arsenic speciation in wetlands: A new insight into the control of the behavior of arsenic

Hélène Guénet [a,b,c], Mélanie Davranche [a,*], Delphine Vantelon [b],
Martine Bouhnik-Le Coz [a], Emilie Jardé [a], Vincent Dorcet [c],
Edwige Demangeat [e], Jacques Jestin [d]

[a] *Géosciences Rennes, UMR 6118, Univ. Rennes 1, Campus de Beaulieu, 35042, Rennes Cedex, France*
[b] *Synchrotron SOLEIL, L'orme des merisiers, Saint Aubin BP48, 91192, Gif sur Yvette Cedex, France*
[c] *Univ Rennes 1, UMR CNRS 6226, Inst Sci Chim Rennes, Ctr Diffractometrie Rayons 10, F-35042 Rennes, France*
[d] *Laboratoire Léon Brillouin, CEA Saclay 91191 Gif/Yvette Cedex, France*
[e] *Géosciences Rennes, BAT 15 P321, Univ. Rennes 1, Campus de Beaulieu, 35042, Rennes Cedex, France*

Received 21 September 2016; accepted in revised form 7 January 2017; available online 17 January 2017

Abstract

Although the behavior of Arsenic (As) under reducing conditions in periods of high water levels in wetlands is well understood and documented, there is a lack of information under oxidizing conditions when the water level decreases. In this study, we were interested in the first stage of the oxidizing period, when oxidation products are still in suspension. A soil sample from the Naizin Kervidy wetland (France) was incubated in the laboratory to produce a reduced soil solution. The reduced solution was subsequently oxidized, filtered and ultrafiltered using decreasing pore size membranes (5 μm, 3 μm, 0.2 μm, 30 kDa and 5 kDa). The distribution of As and Fe was investigated in each size fraction of the oxidized solution and their speciations were studied using XAS, HPLC and SEC-ICP-MS. Organic matter was characterized using thermally assisted hydrolysis and methylation gas chromatography–mass spectrometry (THM-GC–MS) and fluorescence spectroscopy. The majority of the As was present as As(V) but a small amount of As(III) still remained despite the advanced oxidized conditions. In the >0.2 μm fractions, the XAS analyses showed that As was associated, in the second shell, with Fe (As–Fe = 3.35 Å) as bidentate binuclear complexes and C (As–C = 2.90 Å), suggesting the integration of As in biological objects. In the <30 kDa fraction, As was directly bound to C (As–C = 1.96 Å) in the first shell indicating the presence of organic As species. In the second shell, an As–Fe distance of 3.35 Å was found showing that part of the As was still complexed with Fe. The 0.2 μm–30 kDa fraction was a transitional fraction in terms of the Fe species and OM composition. In this fraction, organic matter exhibited a more humic character (aromatic molecules) inducing an increasing cation binding capacity. As a consequence, in this fraction and in the smallest one, As, Fe and OM seemed to form ternary complexes in which the Fe or nano-oxides in the >30 kDa fraction and as monomer, or cluster in <30 kDa fraction acted as a bridge. In all of the fractions, a proportion of As(V) was present as organic methylated species. These organic species might be produced by several organisms (animal or plant) via a detoxification process. They seemed to be bound to the particulate and colloidal Fe/OM phases as well as integrated in the remains of the organisms. Mass calculations provided evidence that 90% of the As was contained in the >5 μm particulate fraction and thus was hardly mobile. This study showed that although wetlands have been identified as a potential source of As, a number of biological and geochemical trapping mechanisms also favor As stabilization in wetlands.

Keywords: Arsenic; Nanoparticles; Iron; Neutrons; SAXS; XAS; Organic matter; THM-GC–MS; Colloids

---

* Corresponding author.
E-mail address: melanie.davranche@univ-rennes1.fr (M. Davranche).

http://dx.doi.org/10.1016/j.gca.2017.01.013
0016-7037/

1. INTRODUCTION

Arsenic is a toxic element, and groundwater has been identified as the source of contamination (Smedley and Kinniburgh, 2001). Several mechanisms have been proposed to explain the As contamination of aquifers. Among them, riparian wetlands and floodplains appeared to play a potential role in the As solubilization process (Kocar et al., 2008; Fendorf, 2010). Arsenic enrichment has been identified in many wetland soils (e.g. Anawar et al., 2003; Du Laing et al., 2009). Riparian wetlands and floodplains are organic matter (OM)-enriched zones, adjacent to streams or rivers and are characterized by seasonal flooding. They receive water from three different sources: (i) groundwater discharge, (ii) subsurface flow and (iii) flow from an adjacent surface-water body (Lewis, 1995). During high water levels subsequent to flooding, anaerobic conditions are established and favor the reductive dissolution of wetland soil Fe(III)-oxyhydroxides and associated elements such as As and OM (Olivié-Lauquet et al., 2001; Grybos et al., 2007, 2009; Davranche et al., 2011; Dia et al., 2015). Following its solubilization, As(V) is reduced to As(III), generally by autochthonous bacteria through detoxification or metabolism processes (Dia et al., 2015). When the water table decreases, the soil solution is reoxidized and newly formed Fe(III)-oxyhydroxides are associated with OM precipitate as colloidal aggregates that are able to trap As (Aström and Corin, 2000; Bauer and Blodau, 2009; Sharma et al., 2011; ThomasArrigo et al., 2014). In these aggregates, colloidal or ionic Fe was shown to act as a bridge between As and OM, thus forming ternary complexes (Ritter et al., 2006; Mikutta and Kretzschmar, 2011). These colloidal aggregates represent a first step in the agglomeration process. The formed solids are expected to settle in the soil porosity following the increase of evapotranspiration and the decrease of the water level. Al-Sid-Cheikh et al. (2015) and Guénet et al. (2016) studied similar agglomerates that were collected directly in a wetland soil matrix (Naizin Kervidy, France). They demonstrated that As was heterogeneously distributed in both Fe-enriched zones and OM-enriched/Fe depleted zones. Al-Sid-Cheikh et al. (2015) used NanoSIMS observations to suggest that As in an OM-enriched/Fe-depleted zone could be associated with OM via thiol (SH) binding sites. However, they showed using X-ray absorption spectroscopy that As was mainly bound to OM via Fe(III)-oxyhydroxides, Fe monomers or small clusters occurring as bridges in the ternary system. As a result, the speciation of As in OM-enriched/Fe-depleted zones is still unknown. However, in order to identify the control exerted by wetlands on As solubilization and dynamics, it is essential to understand and explain all of the processes that are able to solubilize or trap As in this type of environment.

Natural oxidized solids, collected in the wetland soil porosity, result from the agglomeration of colloidal aggregates. Therefore, the objective of the present study was to determine the As speciation in these entities. To make it easier to take samples and quantify the analysis, colloidal aggregates were produced in the laboratory subsequent to anoxic incubations of wetland soil. After the soil solution was sampled and oxidized, the formed aggregates were size-fractionated using filtration and ultra-filtration. A study of the distribution of As, Fe and OM in each size fraction of the oxidized solution was combined with the investigation of As and Fe speciation and OM characterization using multiple techniques. The OM was characterized using THM-GC–MS and fluorescence spectroscopy in each size fraction where the As and Fe speciation was determined by K-edge X-ray absorption spectroscopy (XAS) analysis. The smallest size fractions were investigated using size exclusion chromatography (SEC) combined with an inductive coupled plasma mass spectrometer (ICP-MS) and high-performance liquid chromatography (HPLC) combined with an ICP-MS.

2. MATERIALS AND METHODS

2.1. Site description and soil sampling

Soil was taken from the Mercy riparian wetland in the Kervidy-Naizin sub-catchment located in Brittany in western France. This sub-catchment has been monitored since 1991 to investigate the effects of intensive agriculture (corn cultures and livestock) on water quality. The hydrological, pedological and geochemical contexts are therefore well documented (Bourrié et al., 1999; Dia et al., 2000; Olivié-Lauquet et al., 2001; Gruau et al., 2004). The sampled uppermost soil horizon was defined as the organo-mineral horizon (Ah) of a planosol (according to the WRB international classification) which contained (wt%; anhydrous basis) OM (15%), clay (42%), quartz (30%) and Fe(III)-oxyhydroxides (3.5%) (Grybos et al., 2007). The dissolved OM (DOM), Fe(II) and trace metal concentrations in the soil solution were found to increase during flooding periods, from 0.83 to 2.5 mmol L^{-1} (DOM), from 0 to 0.21 mmol L^{-1} (Fe(II)) and from 0.01 to 0.025 μmol L^{-1} (As), respectively (Dia et al., 2000; Grybos et al., 2007).

Approximately 5 kg of soil was collected in March 2015 from the surface layer, sieved at 2 mm and stored in the dark at 4 °C to minimize latent biological activity.

2.2. Production of colloidal aggregates

To reproduce the reducing conditions observed in wetland soils, a soil suspension was prepared under anoxic conditions in a Jacomex anaerobic chamber. The soil suspension was prepared in triplicate following the protocol given in Grybos et al. (2007). Approximately 130 g of the sieved soil was mixed with 1.8 L of a synthetic solution containing 0.48 mmol L^{-1} of $NaNO_3$ and NaCl, and 0.1 mmol L^{-1} of Na_2SO_4. The synthetic solution was adjusted to mimic the anionic composition of the soil solution during autumn (the time period when the water table rises) in the Mercy wetland system. The solution was continuously stirred throughout the duration of the anaerobic experiment. The experiments were performed in triplicate with an anhydrous soil/solution ratio of 1/20 (soil moisture = 44 wt%). The extended reduction was followed by monitoring the increase in the pH, Eh and Fe^{2+} and trace element concentration subsequent to the reductive dissolution of the Fe-oxyhydroxides in the soil. After one month under anoxic conditions, the pH, Eh and Fe^{2+} values reached 7.2, −130 mV and 20 mg L^{-1} respectively (see Supplementary information Figs. S1 and S2). The soil suspensions were then filtered using 5 µm cellulose nitrate filters (Sartorius). The three soil solutions were removed from the anaerobic chambers and allowed to oxidize at ambient air in the dark at room temperature and under air extraction during two weeks. Previous kinetic experiments (see Supplementary information Figure S3) revealed that an equilibrium in the elemental size distribution was reached after two weeks of oxidation. The triplicates were then size-fractionated using a series of filtration units at 5, 3 and 0.2 µm and ultrafiltrations at 30 and 5 kDa. First, two sequential filtrations using cellulose nitrate membrane filters at 3 µm and 0.2 µm (from Sartorius) were performed and samples were recovered on filters. Then, the 0.2 µm-filtered solutions were ultrafiltered at 30 kDa and then 5 kDa using a Labscale TFF system equipped with two Pellicon XL membranes (PXC030C50 and PXC05C50). An aliquot of each liquid fraction was stored in the dark at 4 °C and the remaining suspensions were freeze-dried.

2.3. As, Fe and OC concentration measurements

The organic carbon (OC) concentrations in the soil solutions were measured using an organic carbon analyzer (Shimmadzu TOC-V CSH). The accuracy of the dissolved organic carbon (DOC) measurements was estimated to be ±5% by using a standard solution of potassium hydrogen phthalate. The organic carbon (OC) content in the freeze-dried samples was determined at the INRA SAS laboratory in Rennes, France, using a dry combustion method with a CN Analyzer (Flash EA-1112). The concentration of the Fe(II) from aliquots collected during the reduction of the soil solution were determined with the 1.10-phenantroline colorimetric method (AFNOR, 1982) at 510 nm using a UV–visible spectrometer (UV/VIS Spectrometer "Lambda 25" from Perkin Elmer). The Fe and As concentrations were determined by ICP-MS using an Agilent technologies 7700× at the University of Rennes 1. The samples were pre-digested twice with 14.6 N HNO_3 at 90 °C, evaporated to complete dryness and then resolubilized with HNO_3 at 0.37 mol L^{-1} to avoid any interference with the DOC during the analysis. A flux of He was injected into a collision cell to remove interference from $^{40}Ar^{35}Cl/^{75}As$ and $^{40}Ar^{16}O/^{56}Fe$. Quantitative analyses were performed using a conventional external calibration procedure (seven external standard multi-element solutions, Inorganic Venture, USA). Rhodium-Rhenium was added online as an internal standard at a concentration level of 300 mg L^{-1} to correct for instrumental drift and possible matrix effects. Calibration curves were calculated from the intensity ratios of the internal standard and analyzed elements. The international geostandard SLRS-4 was used to control the accuracy and reproducibility of the measurement procedure. The instrumental error on the As and Fe analysis was below 3%. Given that the chemical As and Fe blanks were below the detection limits (respectively 0.003 and 0.07 µg L^{-1}), no correction was needed.

2.4. Transmission electron microscopy (TEM) observations

A drop of each size fraction of the oxidized solution (i.e. 3–0.2 µm, <0.2 µm, <30 kDa, <5 kDa) was deposited onto a 300 mesh copper grid coated with a lacey carbon film (Oxford Instruments, S166-3) and dried at room temperature. High-Resolution Electron Microscopy (HREM) investigations were performed on a TEM with a JEOL 100CXII instrument (voltage 100 kV) (THEMIS Analytical Facility at the University of Rennes 1). The elemental composition of the different structures was determined with a JEOL 2100F (voltage 200 kV) equipped with an X-ray energy dispersive spectroscopy (XEDS) detector (Kevex detector with an ultrathin window).

2.5. Organic matter characterization

2.5.1. THM-Gas chromatography-mass spectrometry (THM-GC–MS)

Approximately 2 mg of each freeze-dried sample was introduced into an 80 µL aluminum reactor with an excess of solid tetramethylammonium hydroxide (TMAH – ca. 10 mg). The thermally assisted hydrolysis and methylation (THM) reaction was performed inline using a vertical micro-furnace pyrolyser PZ-2020D (Frontier Laboratories, Japan) operating at 400 °C for 1 min. The products of this reaction were injected into a gas chromatograph (GC) GC-2010 (Shimadzu, Japan) equipped with a SLB 5MS capillary column in split mode (60 m × 0.25 mm ID, 0.25 µm film thickness). The split ratio was adapted according to the sample and ranged from 15 to 30. The temperature of the transfer line was 321 °C and the temperature of the injection port was 310 °C. The oven was programmed to maintain an initial temperature of 50 °C for 2 min, then rise to 150 °C at 15 °C min^{-1} and then rise to 310 °C at 3 °C min^{-1}, where it stayed for 14 min. Helium was used as the carrier gas, with a flow rate of 1.0 mL min^{-1}. Compounds were detected using a QP2010+ mass spectrometer (MS) (Shimadzu, Japan) operating in the full-scan mode. The temperature of the transfer line was set at 280 °C, the ionization source at 200 °C and the molecules were ionized by electron impact using an energy of 70 eV. Compounds were identified on the basis of their full-scan mass spectra by comparison with the NIST library and with published data (Nierop and Verstraten, 2004; Nierop et al., 2005). They were classified into three categories: lignin and tannin markers, carbohydrates and fatty acids. The peak area of the selected *m*/*z* for each compound was integrated and corrected by a mass spectra factor calculated as the reciprocal of the proportion of the fragment used for the integration and the entire fragmentogram provided by the NIST library. The proportion of each compound class was calculated by dividing the sum of the areas of the compounds in this class by the sum of the peak areas of all of the analyzed compounds expressed as a percentage. The presented data are an average of the triplicates. We also investigated the presence of organic As species using the arsenobetaine reference compound ($C_5H_{11}AsO_2$ (AB) from Sigma Aldrich).

2.5.2. *Fluorescence spectral analysis*

At each fractionation step, we collected filtrate suspensions. The fractions below 5 µm, 3 µm, 30 kDa and 5 kDa and between 0.2 µm and 30 kDa were analyzed using a spectrofluorometer Perkin–Elmer LS 45 in a 10 mm quartz cuvette (at the Ecole de Chimie de Rennes, France). The three dimensional excitation-emission fluorescence spectra were acquired by collecting individual emission spectra (290–600 nm) over a range of excitation ranging from 240 to 550 nm, with an increment of 5 nm, at a scan speed of 1500 nm/min. The slits were set to 5 nm for both the excitation and emission monochromators. The spectra obtained using this technique were treated PROGMEEF software in Matlab language (Luciani et al., 2008). Since Fe can potentially affect DOM absorbance in the UV region (Poulin et al., 2014; Weishaar et al., 2003), the raw absorbance of the sample at 254 nm was corrected by taking into account the molar absorptivities of Fe(III) (Poulin et al., 2014). We calculated three indices to characterize the OM. The fluorescence index (FI) (McKnight et al., 2001) is the ratio between the emission intensity at λ_{Em} 450 nm and λ_{Em} 500 nm using a fixed excitation of λ_{Ex} 370 nm. The Biological index (BIX) (Huguet et al., 2009) is calculated from the ratio between the emission intensities at λ_{Em} 380 nm and λ_{Em} 430 nm using a fixed excitation of λ_{Ex} 310 nm. Finally, the Fluorescence Humification index (HIX) (Zsolnay et al., 1999) is calculated as the ratio of λ_{Em} 435–480 nm divided by λ_{Em} 300–345 nm at 254 nm at a fixed excitation of 254 nm.

2.6. XAS analysis

2.6.1. *Data collection*

All size fractions of the oxidized solution were freeze-dried. The obtained powders were pressed into 6 mm pellets and fixed to the support using double-sided adhesive tape. The Arsenic K-edge spectra were collected on the DiffAbs beamline and the Fe K-edge spectra on the LUCIA beamline (Flank et al., 2006) of the SOLEIL Synchrotron (SOLEIL, St Aubin, France). On both beamlines, the monochromators were Si(111) double crystals. The 2nd crystal was bendable on DiffAbs for sagittal focusing. The beam size used for the As K-edge on the sample was 286 × 228 µm. The beam size for the Fe K-edge was 2 × 2 mm. Spectra were collected in fluorescence mode using a 4-element silicon drift diode detector. To prevent beam-induced redox changes, the samples were maintained under vacuum at 70 K using a liquid nitrogen cryostat. Spectra were calibrated using sodium arsenate dibasic heptahydrate (Sigma Aldrich).

2.6.2. *XAS data analysis*

Arsenic and iron XAS spectra were extracted using the Athena software (Ravel and Newville, 2005) including the Autbk algorithm (Rbkb = 1, k-weight = 3). Normalized spectra were obtained by fitting the pre-edge region with a linear function and the post-edge region with a quadratic polynomial function. The Fourier transform of the k^3-weighted EXAFS spectra was calculated over a range of 2–10.5 $\mathrm{\AA}^{-1}$ using a Hanning apodization window (window parameter = 1). Back Fourier filters were extracted over the 1–3.5 Å R-range, using the same apodization window shape.

The EXAFS data were analyzed by shell fitting using the software code Artemis (Ravel and Newville, 2005). Theoretical back scattering paths for the fits were calculated from the various crystal structures using FEFF6. Scorodite (Kitahama et al., 1975), tooeleite (Morin et al., 2007) and 4-Hydroxy-3-nitrobenzenearsonic acid (Nuttall and Hunter, 1995) structures were used to extract paths from the backscatters of the As(V), As(III) and organic As species, respectively. Goethite (Hazemann et al., 1991) and Fe-carboxylate (Horcajada et al., 2007) structures were used to obtain the backscattering paths for Fe. Shell-fit analyses were performed within the 1–3.5 Å R-range for As and 1.1–3.5 Å for Fe. The best fit was chosen by minimizing the reduced χ^2 which depends on the number of independent parameters, the number of fitted parameters and the uncertainty of the data points. For As, the addition of multiple scattering tends to improve the quality of the fit (Morin et al., 2002; Voegelin et al., 2007). In the 5–3 µm and 3–0.2 µm fractions, the triangular As–O–O (MS1, degeneracy = 12), collinear As–O–As–O (MS2 degeneracy = 4) and non-collinear As–O–As–O (MS3, degeneracy = 12) paths were added for the fit of the $\mathrm{As^{(V)}O_4}$-tetraedron. The MS1 path was constrained by an interatomic distance set to $(1 + (2/3)^{(1/2)}) \times \mathrm{R_{As\text{-}O}}$ and a Debye–Waller parameter of $\sigma^2_{\mathrm{As\text{-}O}}$. The MS2 path was constrained by an interatomic distance of $2\mathrm{R_{As\text{-}O}}$ and its Debye–Waller parameter was calculated as $\sigma^2_{MS2} = 4 \times \sigma^2_{\mathrm{As-O}}$. The interatomic distance of MS3 was defined as 2× $\mathrm{R_{As\text{-}O}}$ and its Debye–Waller parameter as $2 \times \sigma^2_{\mathrm{As-O}}$ (Voegelin et al., 2007).

2.7. Arsenic in the <30 kDa and <5 kDa fractions

2.7.1. *SEC-ICP-MS*

The distribution of Fe, OM and As in the fractions below 30 kDa and 5 kDa was investigated using a separation method via the SEC-ICP-MS technique. The separation was achieved using two online SEC NUCLEOSIL® 50 columns (250 mm × 4.6 mm) composed of unmodified spherical silica (50 Å pore size) from Macherey–Nagel, attached to an Agilent 1260 Infinity HPLC system (Agilent Technologies France) fitted with an autosampler. The columns were equipped with a prefilter/guard column (UltraShield UHPLC Trident Direct) with a cutoff of 0.45 µm (Restek Corporation). The mobile phase consisted of a sodium dodecyl sulfate (SDS, purity ⩾98.5%), sodium nitrate ($\mathrm{NaNO_3}$, purity ⩾99.5%), and sodium citrate tribasic dehydrate (SC, purity ⩾98%), with a pH of 6.5. The three products were purchased from Sigma–Aldrich. Stock solutions of 0.1 mol $\mathrm{L^{-1}}$ SDS, 0.1 mol $\mathrm{L^{-1}}$ $\mathrm{NaNO_3}$ and 0.1 mol $\mathrm{L^{-1}}$ SC were prepared in ultrapure water (Milli-Q-water, Millipore system) and filtered at 0.2 µm (with cellulose acetate filters from Sartorius, Germany). The mobile phase composition was obtained by mixing 5% SDS, 10% $\mathrm{NaNO_3}$ and 5% SC using an Agilent quaternary pumping system. The injection volume was 50 µL. The mobile phase flow rate was 0.9 mL $\mathrm{min^{-1}}$, and the pressure was constant at around 235 bars. The SEC columns were followed by an Agilent UV detector from a 1260 Infinity system (excitation $\lambda = 254$ nm, emission $\lambda = 410$ nm) for organic molecules and an Agilent 7700 ICP-MS (Agilent Technologies, France) for the other elements. A similar volume of 100 µL was injected for all of the samples. Before entering the ICP-MS, the effluent passed through an interface in which tellurium was mixed in as an internal standard. This set-up allows the elemental composition to be determined as a function of particle size.

In order to investigate the potentially present dissolved As species, the relevant As(III) and As(V) standards were used. They included (i) two inorganic As species: sodium arsenite (Fluka Analytical) at 37 µg L^{-1} and sodium arsenate dibasic heptahydrate (Inorganic Ventures) at 28 µg L^{-1}, and (ii) three organic methylated species at approximately 18 µg L^{-1}: disodium methylarsenate hexahydrate, $CH_3AsNa_2O_3$ (MMA), dimethylarsenate, $C_2H_7AsO_4$ (DMA) and trimethylarsonio acetate or arsenobetaine, $C_5H_{11}AsO_2$ (AB) from Sigma Aldrich.

2.7.2. HPLC-ICP-MS

High-performance liquid chromatography (HPLC) paired with inductively coupled plasma mass spectrometry (ICP-MS) has previously been used to characterize As compounds in <30 kDa and <5 kDa fractions (Geiszinger et al., 2002; Dobran and Zagury, 2006; Ronkart et al., 2007; Huang and Matzner, 2007). The mobile phase consisted of NaH_2PO_4 (PBS, 2 mmol L^{-1}), $NaNO_3$ (3 mmol L^{-1}), CH_3COONa (10 mmol L^{-1}), EDTA-2Na (0.2 mmol L^{-1}) and CH_3OH (1%) (Sigma–Aldrich) at pH 11 and filtered at 0.2 µm (using cellulose acetate filters from Sartorius, Germany). The injection volume was 50 µL with a mobile phase flow rate of 0.9 mL min^{-1}. An anionic column G3154A from Agilent Technologies 1100 Series (Tokyo, Japon) equipped with a guard column was used. The sample was injected with an autosampler (Agilent Technologies 1100 Series), using a 100 µL aliquot. In order to interpret the chromatograms, the same relevant reference materials previously used for the SEC-ICP-MS experiment were analyzed with an injection volume of 30 µL.

3. RESULTS

3.1. Chemical composition of the soil solution

The Fe, As and OC concentrations in the different size fractions are plotted in Fig. 1. In all of the fractions, OC was the most abundant varying between 102 and 129 mg g^{-1} in the first three fractions and increasing to 320 mg g^{-1} and 340 mg g^{-1} in the 0.2 µm–30 kDa and <30 kDa fractions, respectively. In the <5 kDa fraction, the OC concentration decreased to 132 mg g^{-1}. The Fe distribution varied compared to the OC. The Fe concentrations increased from 23 mg g^{-1} in the >5 µm fraction to 69 mg g^{-1} in the 0.2 µm–30 kDa fraction. The 0.2 µm–30 kDa fraction was the richest Fe and OM fraction. In the <30 kDa and <5 kDa fractions, the Fe concentration dropped significantly to 13 mg g^{-1} and 1 mg g^{-1}, respectively. Therefore, most of the Fe was present as particles (>0.2 µm) and large size colloids (between 0.2 µm and 30 kDa) where the Fe/OC ratio was the highest. The smaller fractions (<30 kDa) were Fe-depleted and OC-enriched and the Fe/OC ratio was the lowest.

Above the 30 kDa fraction, the As distribution followed that of Fe. The As concentration increased from 5 µg g^{-1} in the <5 µm fraction, to 30 µg g^{-1} in the 0.2 µm–30 kDa fraction, via a plateau at 15 mg g^{-1} in the 5–3 µm and 3–0.2 µm fractions. Approximately 20% of the As was in the <30 kDa fraction. Below this threshold, As decreased less drastically than Fe and their concentrations were weakly correlated, indicating that small-size Fe species might not affect As partitioning. No apparent correlation was observed between the distributions of As and OC.

The concentrations of As, Fe and OC were calculated relative to the total dry mass recovered for each fraction. The results are given in% in Fig. 2. The calculations showed that 88% of the total As, 94% of the total Fe and 92% of the total OC were present in the >5 µm fraction since this fraction was the largest in terms of mass. The second fraction in terms of mass for the three elements was the 0.2 µm–30 kDa fraction which was composed of 6% of the total As and 4% of the total Fe and OC.

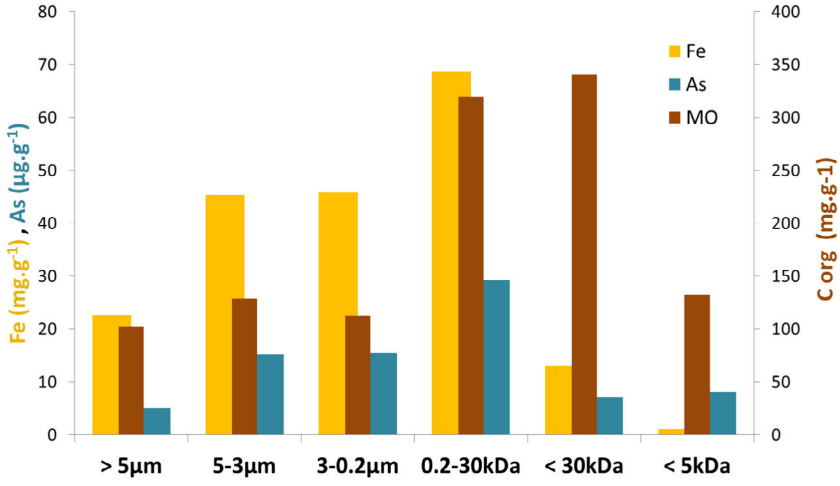

Fig. 1. Concentrations of Fe, As and organic carbon (C org) in each size fraction of the oxidized solutions.

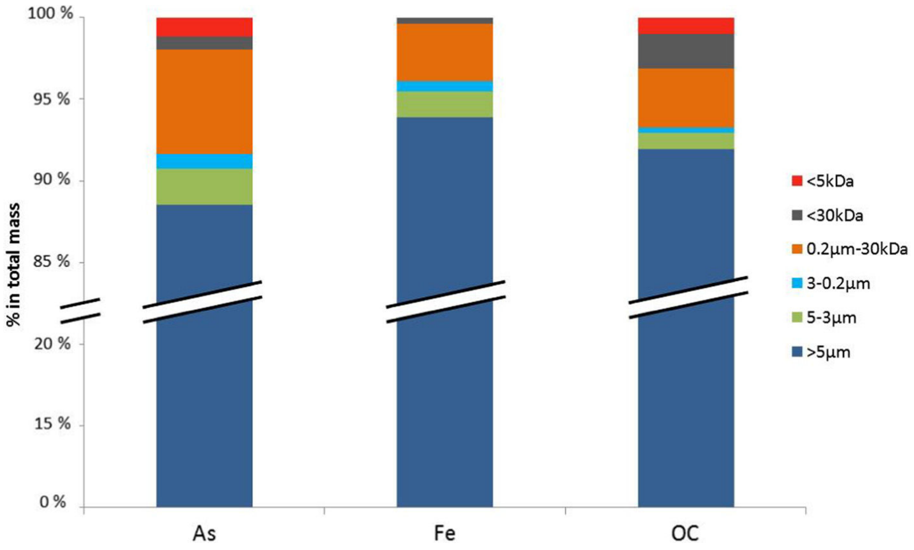

Fig. 2. Repartition of As, Fe and OC in the size fractions of the oxidized solution considering the total dry mass recovered for each fraction.

3.2. High resolution TEM observations of the different fractions

Representative transmission electron micrographs are presented for each fraction in Fig. 3. The overall sample was heterogeneous as revealed by the micrographs of the largest fraction (Fig. 3A). Micrometric organic compounds such as diatoms and silicate plant (e.g. horsetail) remains were observed (supplementary information Figure S5). The Fe phases were detected through their higher electron density and composition using EDS (Energy dispersive spectrometry) analysis. Goethite-like macro crystals

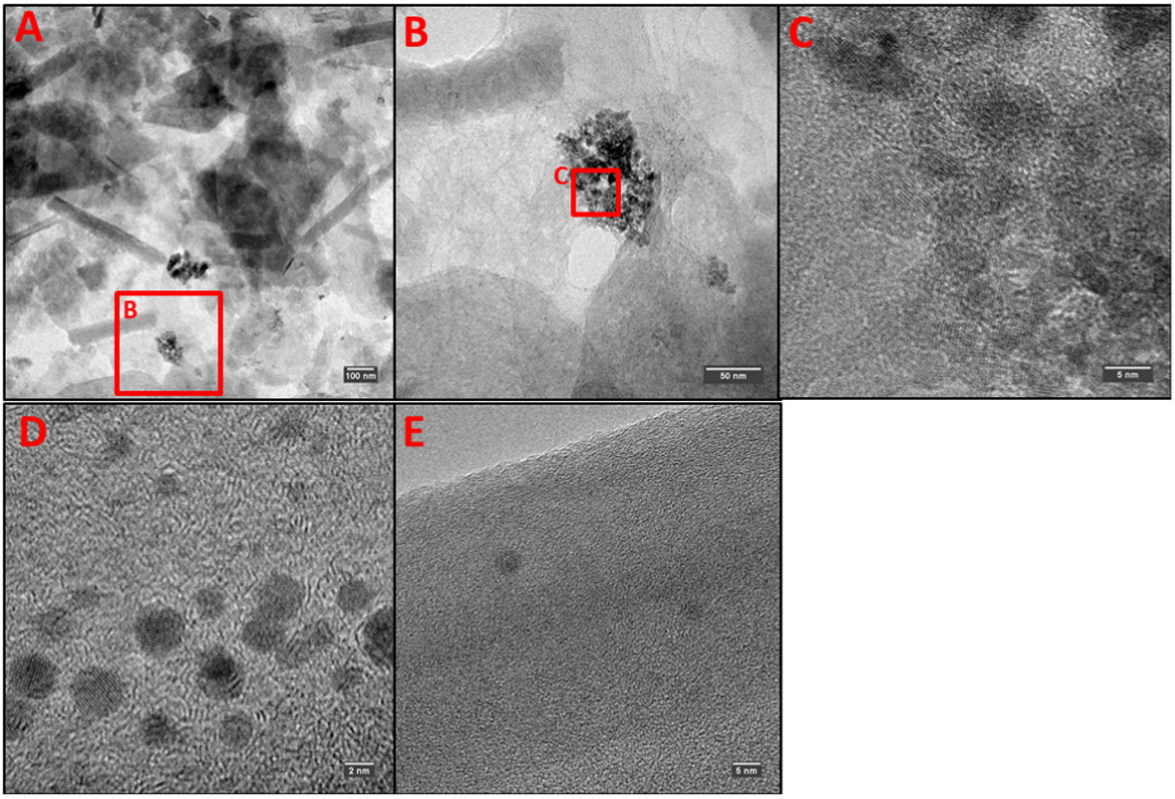

Fig. 3. Representative TEM micrographs of different size fractions. (A) Large view of 3–0.2 µm fraction. (B) Close-up on a Fe aggregate corresponding to the red square from micrograph (A), (C) high resolution micrograph of Fe nanoparticles from the red square of micrograph (B), (D) micrograph of 0.2 µm–30 kDa fraction and (E) micrograph of <30 kDa fraction. (For interpretation of the references to colour in this figure legend, the reader is referred to the web version of this article.)

(supplementary information Figure S5) and Fe(III)-oxyhydroxides aggregates (red squares in Figs. 3A and B) were observed. Fig. 3B shows a close-up of the Fe(III)-oxyhydroxide aggregates comprised of numerous spheroid nanoparticles, the apparent size of which, close to 4 nm, was visible at high resolution (Fig. 3C). With the increasing size fractionation, the large compounds were removed and only the dispersed Fe nanoparticles were observed for the 0.2 µm–30 kDa fraction (Fig. 3D). The analysis of the <30 kDa fraction revealed the presence of very scarce small aggregates without any crystal lattice visible (Fig. 3E). No aggregates were observed in the <5 kDa fraction.

3.3. Organic matter characterization

The organic molecular composition of each size fraction was investigated using THM-GC–MS. The different organic compounds, classified into fatty acids, lignin and tannin markers and carbohydrates, are presented in Fig. 4. Among the size fractions, two groups with similar compositions could be distinguished according to their size: larger or smaller than 0.2 µm. The larger size fractions were composed of more fatty acids than the smaller fractions (mean values of 61.1 vs. 11.5%) and contained fewer lignin and tannin markers (mean values of 27.4 vs. 81.7%). The increases in the lignin and tannin markers were concomitant with the increase in the OC concentration. The proportion of carbohydrates (or sugars) decreased between the first (mean value of 11.5%) and second group (mean value of 6.9%). Lignin and tannin markers were characteristic of OM derived from plant sources (Hedges and Parker, 1976), whereas carbohydrates and fatty acids were provided both by plant and microbial activities (Cranwell, 1974; Rumpel and Dignac, 2006). Low molecular weight (LMW) fatty acids are used as microbial indicators (Cranwell, 1974) while high molecular weight (HMW) fatty acids are used as plant indicators. The proportion of microbial fatty acids was calculated as the percentage of low molecular weight (LMW) fatty acids (<C19) by excluding C16:0 and C18:0, which can be either derived from plant or microbial input. In our samples, the proportion of high molecular weight (HMW) fatty acids in the >0.2 µm fractions was higher (from 55 to 58%) than the proportions of LMW fatty acids (from 42 to 45%), whereas the HMW fatty acids in the <0.2 µm fraction decreased and disappeared in the <30 kDa and <5 kDa fractions. A transition at the 0.2 µm threshold between a plant-derived fraction and a microbial-derived one clearly appeared in our samples.

The fragmentograms for all the size fractions displayed the presence of As methylated species. The distinction between AB and DMA was not possible as the THM-GC–MS analysis transformed the AB molecule into DMA. We calculated the distribution of these species in each size fraction as a percentage of the total methylated As detected using the THM-GC–MS technique (red full line in Fig. 4).

Indices deduced from the fluorescence analysis are displayed in Fig. 5. A mean value of 1.30 for the fluorescence index (FI) was calculated for the >5 kDa fractions, indicating a terrestrial origin for the OM. In contrast, the <5 kDa fraction showed a more microbial derived OM with a FI close to 1.49. The Humification index (HIX) increased from 6.25 for the largest fraction to 22 and 30.11 for the 0.2 µm–30 kDa and <30 kDa fractions, respectively. The HIX evolution showed that OM was more humified in the 0.2 µm-30 kDa and <30 kDa fractions, which also corresponded to the most OC-enriched fractions. The BIX index was constant with an average value of 0.4 indicating that the OM was not freshly produced.

In summary, the characterization of the OM suggested the fractions >0.2 µm were comprised of HMW organic molecules that primarily originated from plant residue. In contrast, the fractions <0.2 µm were composed of soil humic molecules (such as humic acids). The organic compounds in the <5 kDa fraction were smaller and were most probably produced by bacterial activities.

3.4. Characterization of the Fe phases using XAS

The Fe K-edge XANES analyses performed on each size fraction were fairly similar. The edge position at 7125 eV associated with a tiny pre-edge at 7114.2 eV and a broad

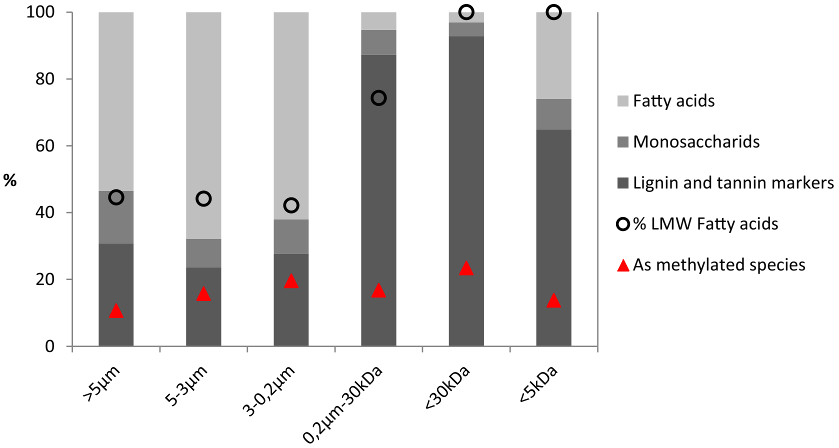

Fig. 4. Histogram of the recalculate proportions of fatty acids, monosaccharides and the markers for the lignin and the tannin in each fraction considering a sum of 100%. The superimposed dotted line represents the percentage of LMW of fatty acids and the full red line represents the repartition in% of the methylated arsenic species detected through GC analyses.

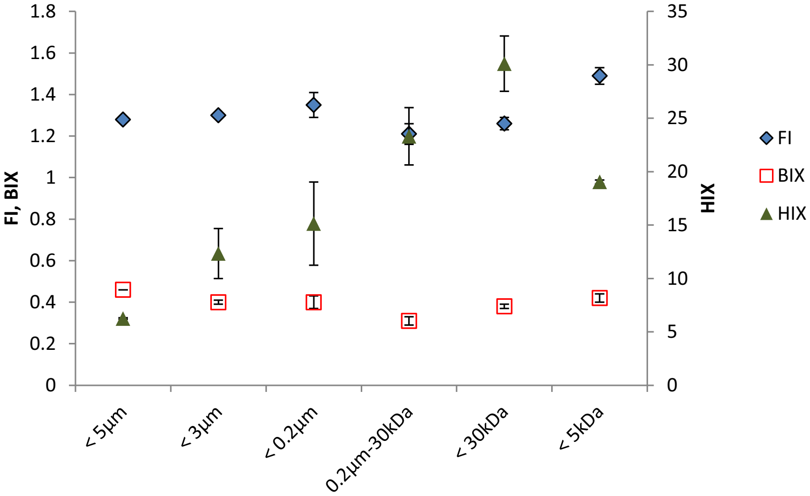

Fig. 5. Evolution of the three characterization indices. FI: fluorescence index; BIX: Biological index and HIX: Fluorescence humification index.

shoulder at 7148 eV reflected octahedral coordinated Fe (III) species in a poorly crystalline phase (see Supplementary information Figure S4). The EXAFS spectra and corresponding Fourier transforms (magnitude and imaginary part) of each size fraction as well as ferrihydrite (Fh) as a reference are reported in Fig. 6. The EXAFS spectra of the size fractions were fairly similar with three peaks at 4.1 Å, 6.3 Å and approximately 8.4 Å. A small peak close to 7.5 Å was observed in the 5–3 µm, 3–0.2 µm and 0.2 µm–30 kDa fractions and reference Fh, but not in the <30 kDa and <5 kDa fractions. Two peaks dominated the Fourier transform. The first peak, located at approximately 1.5 Å (R + ΔR), corresponded to the first shell of the neighboring atoms within the FeO_6 octahedra. The second peak at approximately 2.6 Å (R + ΔR) arose from the scattering of the Fe neighbors from the second coordination shell. Shell fits were performed within the 1.1–3.5 A range of the Fourier transformed k^3-weighted spectra over a k-range of 2–10.5 Å and are displayed in Fig. 6. The resulting EXAFS parameters of the fits are reported in Table 2.

3.4.1. First coordination shell

The first O shell was fitted with approximately six O at a mean distance of 2.00 Å, respectively. These distances corresponded to the Fe–O distances for the octahedra in the Fe(III)-oxyhydroxides (Waychunas et al., 1993). The number of O was later fixed to six to reduce parameter correlations.

3.4.2. Second coordination shell

The second peak at approximately 2.6 Å in the Fourier transforms (Fig. 6B) has a major contribution from the Fe neighbors. The spectra for the 5–3 µm, 3–0.2 µm and 0.2 µm-30 kDa fractions displayed a Fe-Fe_1 distance of 3.03–3.09 Å, which is characteristic of edge-sharing FeO_6 octahedra (Manceau and Combes, 1988; Manceau and Drits, 1993). A second Fe-Fe_2 distance of 3.38–3.49 Å was determined in all of the fractions, specific to double corner-sharing (Manceau and Combes, 1988; Combes et al., 1989; Waychunas et al., 1993; Bottero et al., 1994). In order to accurately model the spectra of the three smallest fractions, a Fe–C distance was added in the fit with 3.8 C at 2.95 Å for the 0.2 µm–30 kDa fraction, 2.4 C at 2.91 Å for the <30 kDa fraction and 3.3 C at 2.86 Å for the <5 kDa fraction. The highest OC/Fe concentration ratio was obtained for these three fractions, explaining why it was possible to observe the Fe–C distance. Karlsson and Persson (2010) obtained a similar Fe–C path in Fe bound to peat humic acid. They interpreted this result as the formation of small polynuclear Fe(III)–OM complexes. The 0.2 µm–30 kDa fraction could be considered as an intermediate fraction containing the two Fe–Fe distances (Fe–Fe1 and Fe–Fe2) and the Fe–C distance, while the first Fe-Fe1 distance disappeared in the <30 kDa and <5 kDa fractions. In agreement with Hoffmann et al. (2013), these distances provided evidence of the presence of small Fe clusters and/or Fe(III)-oxyhydroxide nanoparticles in the 0.2 µm–30 kDa fraction although only small clusters such as dimers or trimers were formed in the <30 kDa and <5 kDa fractions.

3.5. Speciation of arsenic by X-ray absorption spectroscopy

3.5.1. As K-edge XANES

The speciation of As in the different size fractions was determined by comparing the XANES sample with known references. The spectra for the fractions and inorganic As (III) and As(V) references are reported in Fig. 7. The white line energies observed for arsenite (11872.4 eV) and arsenate (11875.5 eV) corresponded to the literature (Smith et al., 2005). The white line peak positions were obtained from the point where the first derivative of the spectrum crossed zero. The fractions exhibited a peak maximum at 11875.6 eV for the 5–3 µm fraction, 11875.2 eV for the 3–0.2 µm fraction and 11874.8 eV for the 0.2 µm-30 kDa fraction, close to the white line value of arsenate. They exhibited a shoulder at lower energy (close to 11872.3 eV), the intensity for which increased with the size fractionation.

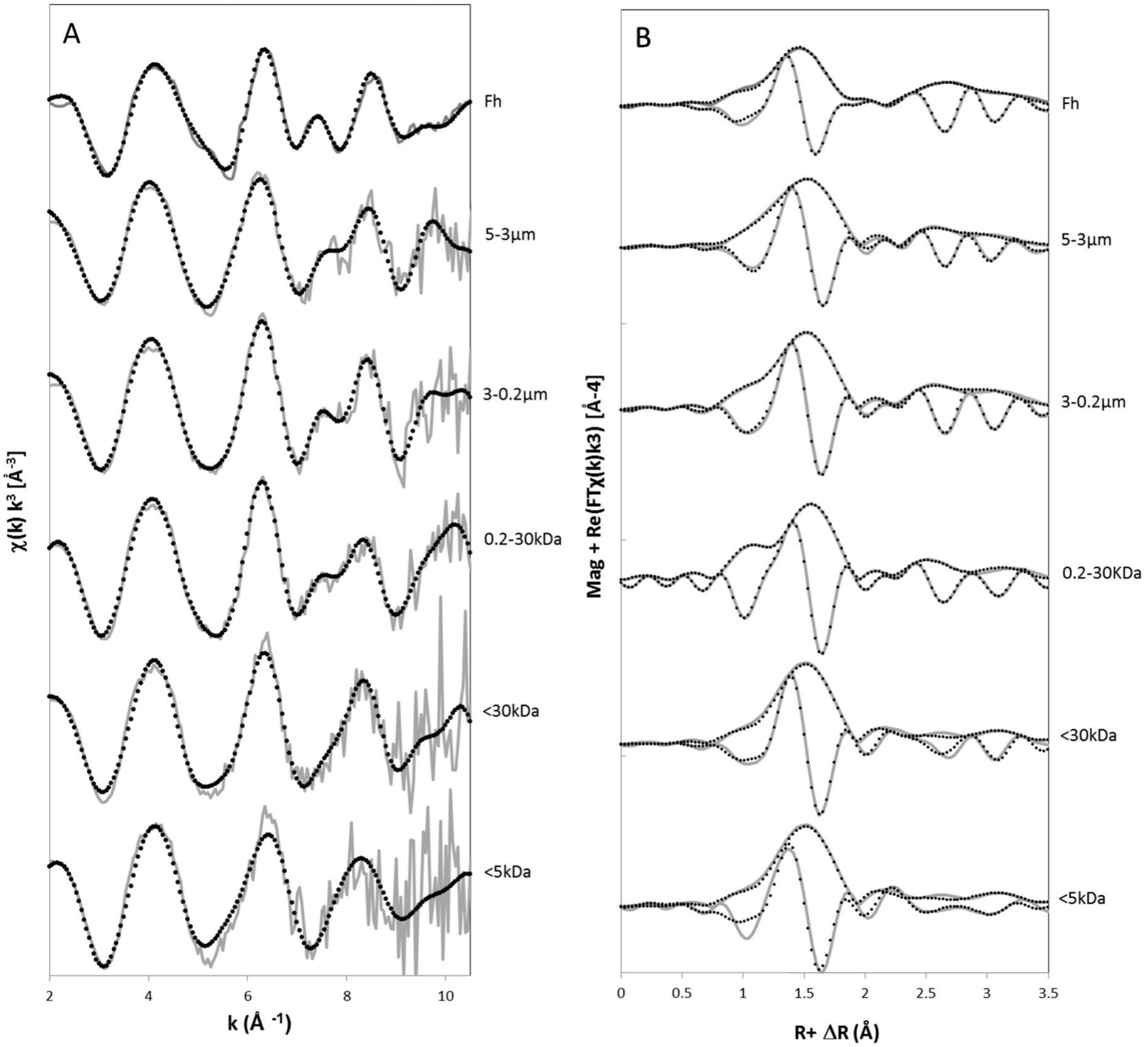

Fig. 6. (A) Iron K-edge EXAFS spectra of the different size fractions and ferrihydrite (Fh) and (B) magnitude and imaginary part of the associated Fourier transform (uncorrected for the phase shift). Solid lines are experimental data and dotted lines are the fit results.

The shoulder and white line positions corresponded to a mixture of inorganic As(III) and As(V) (Guénet et al., 2016). The spectra for the <30 kDa and <5 kDa fractions exhibited a single peak at 11874.0 and 11874.2 eV, respectively. These values did not correspond to inorganic species. Prior studies investigating the white line positions for multiple As compounds revealed that As(V) organic compounds such as AB, DMA and MMA have an intermediate white line position due to the difference in the electronegativities of O and C (Arčon et al., 2005; Smith et al., 2005; Lombi et al., 2009). The core electrons of the As atoms in an As–C bond are more easily photoionized than the 1s electrons of As in an As–O bond. The white line position observed for the <30 kDa and 5 kDa fractions could thus be attributed to As(V)-methylated compounds such as AB, DMA or MMA. The distinction between each species is prevented by the inability of XANES to discriminate between two aliphatic substituents on the C backbone (George and Pickering, 2007).

3.5.2. As K-edge EXAFS

The As K-edge EXAFS data and corresponding Fourier-Transform of each size fraction are reported in Fig. 8. Due to a lower concentration in As, the quality of the data for the <30 kDa and <5 kDa fractions had a poorer signal/noise ratio compared to the larger size fractions. However, the quality was good enough to extract information. From the 5–3 µm fraction to the 0.2 µm–30 kDa fraction, the EXAFS spectra exhibited a shoulder at 5.05 $Å^{-1}$. The second oscillation was characterized by a slight double-hump feature at approximately 6.55 and 7.55 $Å^{-1}$. The amplitude of the second hump decreased at the expense of the first one with the decreasing size fraction. The third oscillation was not well-defined for the <30 kDa and <5 kDa fractions but was composed of one peak at 9.05 $Å^{-1}$ for the 0.2 µm–30 kDa fraction, which exhibited an increasing shoulder with the increasing size fraction. The main peak in the Fourier transform was located at R + ΔR ~1.3 Å and corresponded to the first neighboring

Table 1

Fe K-edge EXAFS fits for the different fractions and the ferrihydrite reference.

Sample	Fe–O			Fe–C			Fe–Fe_1			Fe–Fe_2				
	N[a]	R[b] (Å)	σ^2[c]	N	R (Å)	σ^2	N	R (Å)	σ^2	N	R (Å)	σ^2	ΔE_0 [d]	R factor [e]
Fh	2.7 (1) 1.6 (2)	1.93 (1) 2.09 (1)	0.003 0.003				1.8 (10)	3.03 (2)	0.010	2.7 (11)	3.49 (2)	0.010	0.9 (1)	0.004
5–3 µm	6	2.01 (1)	0.009				2.4 (4)	3.07 (4)	0.013	0.9 (2)	3.38 (4)	0.005	-2.2 (9)	0.016
3–0.2 µm	6	1.99 (1)	0.008				1.8 (3)	3.03 (2)	0.009	1.2 (3)	3.42 (2)	0.005	-2.2 (5)	0.010
0.2 µm–30 kDa	6	2.02 (1)	0.009	3.8 (4)	2.95 (2)	0.005	0.7 (1)	3.09 (8)	0.004	1.1 (1)	3.49 (2)	0.005	2.1 (14)	0.003
<30 kDa	6	1.99 (1)	0.007	2.4 (9)	2.91 (6)	0.005				1.6 (6)	3.43 (3)	0.005	1.9 (8)	0.022
<5 kDa	6	1.99 (2)	0.008	3.3 (19)	2.86 (9)	0.005				0.7 (9)	3.39 (2)	0.005	2.2 (23)	0.050

[a] N, path degeneracy (coordination number).

[b] R(Å), interatomic distance.

[c] σ^2(Å), Debye–Waller factor.

[d] Energy-shift parameter.

[e] R-factor = Σi(datai-fiti)^2/Σidata. The amplitude reduction factor, S_0^2, was set to 0.75 from Fh fit. The reported errors were determined by the fitting procedure. The Debye–Waller of Fe–Fe_2 and Fe–C distances were determined from the <30 kDa fraction and then fixed to these values in all fractions. Parameter uncertainties are presented for the last significant figure and determined by the fitting.

Table 2

Shell-Fit parameters determined from the As K-edge EXAFS spectra of the size fractions.

	As–O			As–C			As–(O)–C			As–Fe_1			As–Fe_2				
Sample	N[a]	R[b] (Å)	σ^2[c]	N	R (Å)	σ^2	N	R (Å)	σ^2	N	R (Å)	σ^2	N	R (Å)	σ^2	ΔE_0 [d]	R factor [e]
5–3 µm	4.3 (4)	1.72 (1)	0.003				1.7 (5)	2.85 (3)	0.003				1.2 (2)	3.35 (1)	0.010	6.93	0.006
3–0.2 µm	3.7 (5)	1.73 (1)	0.007				2.1 (6)	2.86 (2)	0.004				1.0 (4)	3.33 (3)	0.009	8.62	0.013
0.2–30 KDa	3.6 (8)	1.77 (2)	0.003							1.2 (7)	2.8 (2)	0.004	0.8 (5)	3.40 (4)	0.004	10.4	0.013
<30 KDa	0.9 (1)	1.74 (6)	0.004	3.2 (4)	1.97 (4)	0.008							1.2 (2)	3.33 (4)	0.009	12.8	0.010
<5 KDa	0.8 (2)	1.66 (9)	0.003	4.4 (2)	1.92 (6)	0.006							0.5 (1)	3.34 (3)	0.005	10.7	0.015

The amplitude reduction factor, S_o^2, was set to 1.

[a] N, path degeneracy (coordination number).

[b] R(Å), interatomic distance.

[c] The Debye–Weller parameters were homogenized around a mean value.

[d] Energy-shift parameter.

[e] R-factor = Σi($data_i$-fit_i)^2/Σidata. The Debye–Weller for the Fe–Fe paths are covaried with σ^2As–Fe_1 = σ^2As–Fe_2. The reported errors are determined by the fitting procedure.

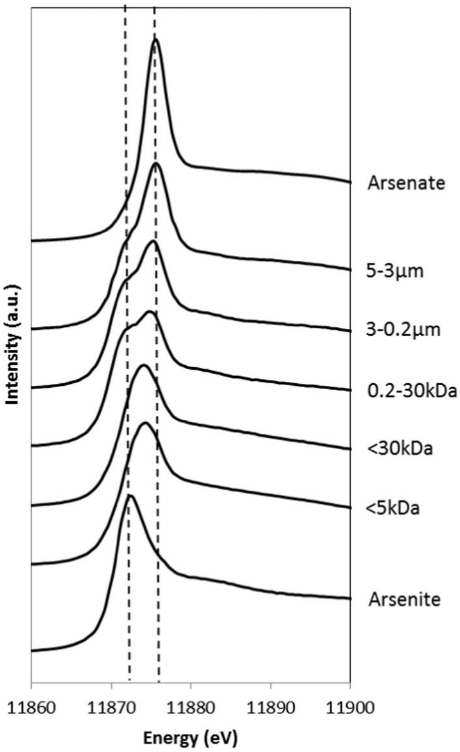

Fig. 7. As K-edge X-ray absorption near-edge structure (XANES) spectra of different fractions of the oxidized soil solution along with inorganic As(III) and As(V) references.

shell. With the decreasing size fraction, the width of the first peak increased until it formed two separate peaks in the <30 kDa and <5 kDa fractions at 1.07 and 1.56 Å, respectively. The 0.2 µm-30 kDa, <30 kDa and <5 kDa fractions exhibited two additional small peaks at R + ΔR ~2.4 Å and ~3.2 Å, accounted by for the second coordination shell neighbors, whereas the 5–3 µm and 3–0.2 µm fractions exhibited non-distinct peaks at R + ΔR ~2.2 Å, 2.5 Å and 3.0 Å. In order to explore the local As coordination, fits were performed within the 1–3.5 Å R-range (Fig. 8). The fitted parameters and constraints for the references and each size fraction are reported in Table 1.

3.5.3. First shell

The samples can be divided into two groups according to their first shell shape and fit. In the first group, made up of the largest fractions (i.e. 5–3 µm, 3–0.2 µm and 0.2 µm–30 kDa), between 3.6 and 4.3 O were needed to accurately fit the first shell at a distance of 1.72–1.73 Å for both the 5–3 µm and 3–0.2 µm fractions and 1.77 Å for the 0.2 µm–30 kDa fraction. In the second group, comprising the smallest fractions, the two peaks were successfully fitted using two paths. The first one was As–O with 0.9 O at 1.74 Å and 0.8 O at 1.66 Å for the <30 kDa and <5 kDa fractions, respectively. The second one was As–C with 4.4 C at 1.92 Å and 3.2 C at 1.97 Å for the <30 kDa and <5 kDa fractions, respectively. The values for the As–C distances were in agreement with Miot et al. (2008), who obtained an As–C distance of 1.91 Å, in the AB compound.

These EXAFS results refined the XANES observations by showing that the methylated As species were dominant in the <30 kDa and <5 kDa fractions but that inorganic As persisted.

3.5.4. Second coordination shell

An As–Fe distance was used to fit the second coordination shell for all of the fractions. These distances varied between 3.33 and 3.40 Å. They were in agreement with the distances reported for As(III) and As(V) monodentate binuclear corner-sharing complexes (^{2}C) where As(III) and/or As(V) were bound to the apical O atoms of two edge-sharing FeO_6 octahedra (Waychunas et al., 1993; Manceau, 1995; Ona-Nguema et al., 2005). For the 5–3 µm and 3–0.2 µm fractions, the residual between the fit and the spectra was high, suggesting the contribution of an additional neighbor in the second coordination shell. A path with an interatomic As–Fe distance of 2.89 Å, corresponding to As(III) edge-sharing complexes (E^2) (Ona-Nguema et al., 2005) was tested. However, the Debye-Weller value for the fit was negative thereby excluding this bonding. A second As–C path (via O binding) was tested. A better fit was obtained with a distance of 2.85 Å for the 5–3 µm fraction and 2.86 Å for the 3–0.2 µm fraction. The presence of other light atoms was also considered but finally ruled out because they would result in longer interatomic distances for Ca and Al (Arai et al., 2001; Bardelli et al., 2011) or a shorter interatomic distance for S (Hoffmann et al., 2014). For the 0.2–30 kDa size-fraction, the As–Fe distance at 2.89 Å, corresponding to As(III) in E^2 complexes (Ona-Nguema et al., 2005) was used to fit the data.

3.6. Arsenic speciation using SEC-ICP-MS and HPLC-ICP-MS

The size separation of the As reference materials is shown in Fig. 9A. The retention times for the As references were 4.8 min for dissolved As(V), 5.3 min for MMA, 7.1 min for DMA and 9.8 min for dissolved As(III). The retention times of OM, Fe and As in the <30 kDa and <5 kDa fractions are given in Fig. 9B and C. The Fe signal derived from the SEC-ICP-MS analysis was parallel to the UV signal corresponding to organic molecules. They were both comprised of a peak at 4.35 min and a shoulder at 4.80 min. This coelution indicated that Fe and OM are associated in two close sizes. No signals for the dissolved As(III), MMA or DMA were detected in either fraction. The As signal followed the Fe-OM association signal. For the <5 kDa fraction, a small peak matched the main peak of the Fe-OM signal but a higher peak matched the Fe-OM signal shoulder. For the <30 kDa fraction, two peaks that are quite similar in intensity were observed. The second peak at 4.8 min observed for As also matched that of the As (V) reference in the solution (Fig. 9A). Two hypotheses can be considered: (i) all of the As species were associated with Fe–OM aggregates, the size of which corresponded to the 4.8-min retention time or (ii) a portion of As(V) remained in the solution.

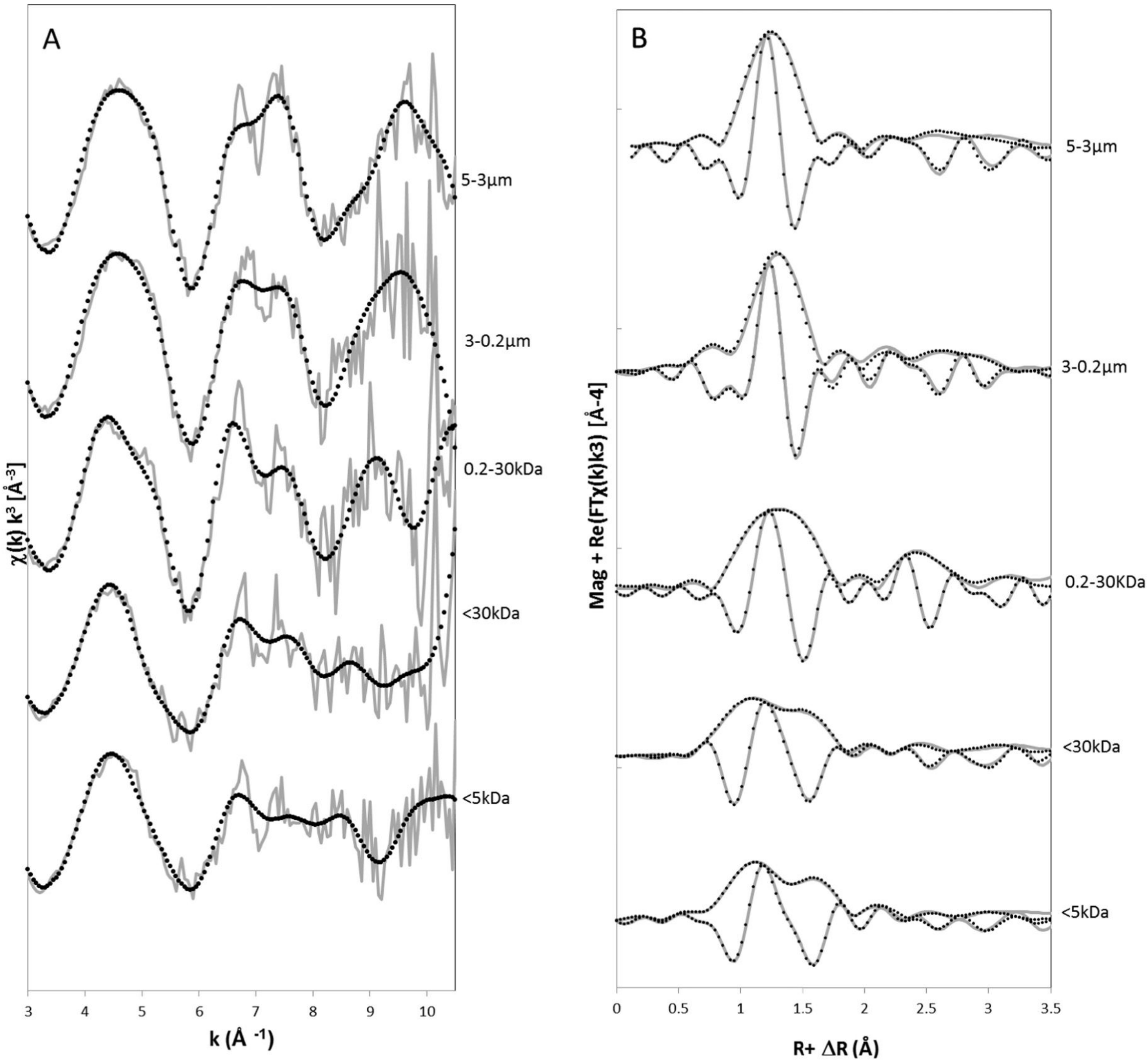

Fig. 8. As K-edge EXAFS spectra, magnitude and imaginary part of the Fourier transform (uncorrected from phase shift) of the different fractions (A) and (B) respectively. The fit results, given as dotted lines, are superimposed onto the data in solid grey lines.

Results from the HPLC-ICP-MS analysis are shown in Fig. 9D. The chromatograms revealed that As was mainly present as As(V) with a retention time of 7.6 min. Three other peaks were observed at 2.3, 2.9 and 3.3 min and were attributed to AB, DMA and As (III) dissolved in solution, respectively. The amount of As(III) was much lower in the <5 kDa fraction than in the <30 kDa fraction. Both of the organic As species were methylated As(V). A systematic shift of approximately 0.15 min was observed between the samples and each standard. This can be explained by the difference in the injected volume, which was 30 µL for the standard versus 100 µL for both fractions. Neubauer et al. (2013a, b) demonstrated that the retention time increases with the sample load. As the peaks were distant from each other, it was not possible to misidentify them; therefore the time shift was not corrected. The determination of the concentration of each As species was performed by injecting reference compounds at various concentrations. Recovery of each species was estimated by directly injecting the sample in the ICP-MS and comparing both concentrations. The total recovery of the injected standard solutions was close to 90%. However, the total recovery was only 65% for the <5 kDa fraction and 32% for the <30 kDa fraction, suggesting that a sample matrix effect through the column could have occurred.

It is important to note here that the HPLC-ICP-MS technique can only be used to detect dissolved species. However, the SEC-ICP-MS analysis showed that the As species was co-eluted with Fe/OM associations, i.e. As was bound to the Fe/OM associations. The detection of As species by HPLC-ICP-MS could result in a release of As species subsequent to a solubilization of Fe/OM favored by the presence of EDTA, which is a strong Fe complexing

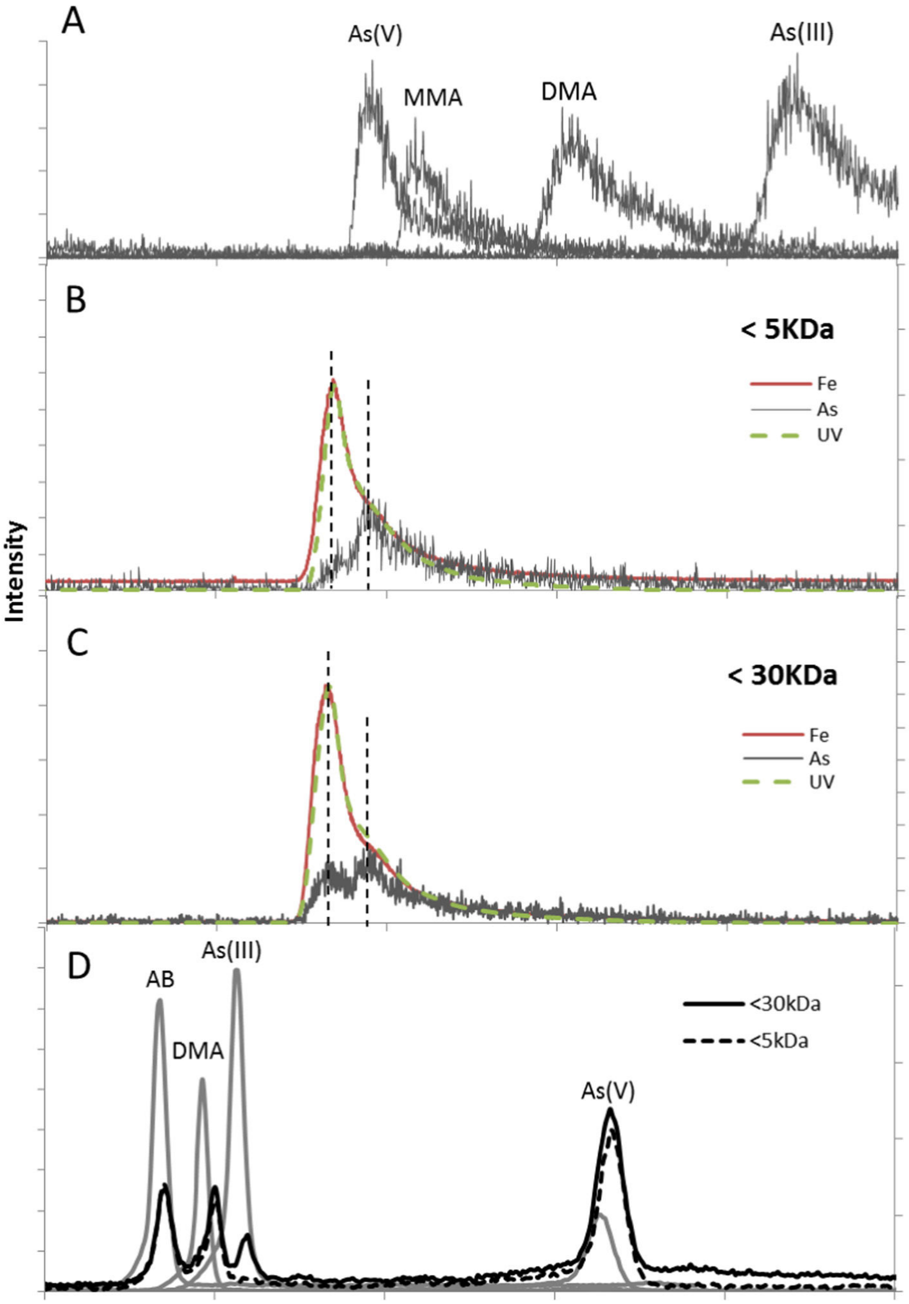

Fig. 9. (A) SEC-UV-ICP-MS chromatogram of reference As species, (B) and (C) chromatograms of OM (corresponding to the UV signal), Fe and As for <30 kDa and <5 kDa size fractions of the oxidized solution. Vertical dotted lines highlight the main features of the signals. (D) HPLC-ICP-MS chromatograms of As reference species used for peak identification (grey lines) and <30 kDa and <5 kDa size fractions (black lines) of the oxidized soil solution.

agent, in the mobile phase of the HPLC column. This hypothesis was confirmed by the detection of Fe in the column solution outlet via ICP-MS measurements. The EDTA seemed to impact the release of inorganic and organic As species differently. Therefore in our study, HPLC only provided information on the presence/absence and relative proportion between each detected As species in the <30 kDa and 5 kDa fractions.

4. DISCUSSION

4.1. As speciation as a function of the size fraction

Our results showed that the speciation and distribution of Fe and As, as well as the composition of the OM, varied according to the molecular size fractions in the oxidized soil solution.

4.1.1. 5–3 μm and 3–0.2 μm fractions

As revealed by the TEM images, the fractions were heterogeneous. Above 0.2 μm, a major mass fraction was composed of silicate, the remains of plant stems and diatoms. The OM in both the 5–3 μm and 3–0.2 μm fractions was composed of small degraded organic compounds that originated from plants (i.e. leaves and root remains) with a high proportion of fatty acids. Iron was present as aggregates of nanoparticles embedded in the OM (Table 2). The low degree of polymerization (i.e. crystal growth), evidenced by the TEM and XAS analyses, could be explained by the high amount of OM which impairs the crystal growth of the Fe(III)-oxyhydroxides (Cornell and Schwertmann, 2003; Pédrot et al., 2011). Scarce well-formed Fe crystals were assumed to have been inherited from the soil and therefore preserved from the reductive dissolution. Arsenic occurred mainly as As(V). A strong correlation existed between the As and Fe concentrations (Fig. 1A), indicating that most of the As was associated with Fe particles and aggregates. The specific surface of the nanoparticle aggregates was expected to be higher than the well crystallized Fe(III)-oxyhydroxides (Hiemstra and van Riemsdijk, 2007). Arsenic was therefore more likely to be bound as a bidentate complex to Fe nanoparticles aggregates (Ona-Nguema et al., 2009). The As K-edge EXAFS revealed the presence of an interatomic As–C distance of 2.85 Å suggesting the presence of As as organic compounds, probably inherited by the biological activities or matter. Several studies have hypothesized the binding of As to OM carboxylic or phenolic sites (Redman et al., 2002; Buschmann et al., 2006). Buschmann et al. (2006) suggested the formation of an As(V)-HA complex due to an additional chelation and stabilization effect. Dembitsky and Rezanka (2003) suggested that the inorganic As was complexed to carboxylic groups during the uptake by plants or fungi. The GC–MS analysis also revealed the presence of a small amount of arsenobetaine (AB); however the concentration for AB was so low that it could not be evidenced by XAS (no As–C distance observed at 1.98 Å), which is an averaging tool. The significant binding of As with the Fe phase meant that it was not possible to detect the As–C distance of 1.98 Å, which was masked by the presence of a large amount of stronger backscattering Fe neighbors in the EXAFS spectra (Table 2). Arsenobetaine was primarily found in marine environments but has also been shown to occur in terrestrial organisms such as mushrooms, earthworms, plants and soils (Huang and Matzner, 2007). Its formation was considered to be a detoxification mechanism used by organisms (Tamaki and Frankenberger, 1992). Arsenobetaine was probably adsorbed to Fe(III)-oxyhydroxides, as previously observed for other As methylated species (Bowell, 1994; Cox and Ghosh, 1994). Methylated As can also be taken up by plants which translocate the As from the soil to their tissues (Hiltbold, 1975; Geiszinger et al., 2002). Since, in the 5–3 μm and 3–0.2 μm fractions, the OM appeared to originate from plants, As methylated compounds could also be included in the plant remains.

4.1.2. 0.2 μm–30 kDa fraction

This size fraction represented the most concentrated fraction in the Fe and OM. These distributions were consistent with the ultrafiltration analysis of the shallow groundwater from the wetland in which the present soil was sampled (Pourret et al., 2007). Pourret et al. (2007) noticed that most of the Fe occurred as Fe–OM colloids, the size of which ranged from 0.2 μm to 30 kDa. Here, the Fe was identified as occurring as nanoparticles aggregated or dispersed in the OM matrix (Fig. 3). Compared to the high molecular size fractions, where carboxylic groups (within fatty acids) were dominant, the GC–MS analysis showed that the OM in this fraction was mainly composed of lignin and tannin markers which are more enriched in phenol groups. The complexation capacity of the phenolic groups is stronger than the carboxylic groups which implies a higher reactivity of this fraction toward metallic ions such as Fe (Tipping, 1998). Arsenic was present as a mixture of As(III) and As(V). Guénet et al. (2016) provided evidence that, in natural Fe-OM colloidal agglomerates, the OM prevents total As(III) oxidation by controlling the Fe species as Fe monomer/small clusters and weakly polymerized Fe(III) oxyhydroxides. The formation of these Fe species leads to the decrease of active adsorption sites for As oxidation. Arsenic reached its highest concentration and was strongly correlated with Fe in this fraction, indicating that the As was adsorbed by the Fe(III) phases (Fig. 1). These results were supported by the EXAFS measurements where As appeared as highly bound to Fe. However, the THM-GC–MS analysis also detected the presence of AB.

4.1.3. <30 kDa and <5 kDa fractions

Unlike the OC, the Fe concentration strongly decreased in these fractions. Fe was almost completely removed after this ultrafiltration step. The Fe formed small clusters as evidenced by the absence of an Fe–Fe distance at 3.03 Å and the fitting of the Fe–Fe distance at 3.44 Å, which corresponds to corner-sharing $Fe(O,OH)_6$ octahedra. The absence of a Fe(III)-oxyhydroxide phase was consistent with the TEM images where no Fe-nanoparticles were observed. The clusters were embedded in an OM matrix as revealed by the interatomic Fe–C distance of 2.9 Å. Organic matter is able to strongly bind Fe(II, III) through its carboxylic or phenolic groups (Liang et al., 1993; Tipping et al., 2002; Catrouillet et al., 2014). The stability constant of the Fe(III)-phenol complex, log K, is equal to 8.40 versus 4.01 for the Fe-acetate complex at an ionic strength of 0 (Sommer and Pliska, 1961; Desai and Milburn, 1969). Because the LMW OM was expected to contain more phenolic compounds, these fractions were highly reactive towards Fe.

A weak correlation between As and Fe was calculated for this LMW fraction which suggested that As was less associated with the Fe phases. The HPLC-ICP-MS and XAS analysis revealed the presence of As organic species where the oxidized As(V) was methylated as AB, MMA and DMA. In our experiment, the analysis of the soil solution before oxidation did not show any AB or DMA, which are therefore produced during the oxidation of the soil solution. Sohrin et al. (1997) observed, in a eutrophic lake, a seasonal variation in the concentration of the methylated As species produced under an oxidative condition and which decomposed to inorganic As under an anoxic condition. The presence of close to 30% of the methylated species combined with the presence of AsO_4 explained the weak As/Fe correlation. However, the As K-edge EXAFS spectra showed that part of the As was bound to Fe as monodentate binuclear corner-sharing complexes (^2C) on the small Fe clusters. Considering the Fe–C distance of 2.8 Å as well as the As–Fe distance of 3.43 Å, ternary complexes were possibly formed in the LMW fractions (Mikutta and Kretzschmar, 2011; Sharma et al., 2011; Hoffmann et al., 2013), which was confirmed by the coelution of Fe, As and OM in the SEC-ICP-MS analysis.

4.2. Implications for As dynamics in wetlands

In previous studies, Al-Sid-Cheikh et al. (2015) and Guénet et al. (2016), using a NanoSIMS analysis of agglomerate solids produced during the oxidizing period in our studied wetland, showed that the As distribution was highly heterogeneous with (i) As associated with Fe-enriched zones and (ii) As associated with OM-enriched/Fe-depleted hotspots. To explain this observed colocalization of As and OM, Al-Sid-Cheikh et al. (2015) suggested the binding of part of the As as As(III) to the OM thiol (SH-) functional groups. Unfortunately, the present results did not support this assumption; no As–S distances were detected in the EXAFS spectra for any size of the fractions, even in the lowest fraction. Therefore, the association between As and OM must be explained by a new mechanism. The present results demonstrated the presence of a significant amount of As as As(V) organic species, notably in the large size fractions (between 5 and 0.2 μm) (Fig. 2). These As(V) organic species, which came from plants and organisms, did not directly depend on the prevailing redox conditions. The detoxification processes for the organisms, activated by the production of dissolved As, was the mechanism that most probably controlled the production of these organic As(V) species (Dembitsky and Rezanka, 2003; Foster and Kim, 2014). A proportion of this organic As(V) species was scavenged in plants and organisms although a second part was probably excreted and subsequently adsorbed to the Fe phases. The organic As(V) species in the residue from the organisms might explain the colocalization of As and OM observed by the NanoSIMS in the OM-enriched/Fe-depleted hotspots (Al-Sid-Cheikh et al., 2015; Guénet et al., 2016).

Considering the wet mass of each size fraction, close to 92% of the As (inorganic and organic) was found in the >0.2 μm fractions, i.e. in the particulate fractions. With regards to these large sizes, these particles were not mobile since they could settle rapidly and easily. Larger particles can be regarded as the own particles of the soil that have been suspended in solution by the experimental design. Thus, the present results demonstrated that a large proportion of the As was i) involved in a biological mechanism and integrated in the particulate biological materials and ii) bound to non-mobile Fe particles (>0.2 μm particulate fractions). Both mechanisms favored the trapping of As in the wetland soil. The 0.2 μm–30 kDa fraction was the most Fe-enriched phase. In this size fraction, the As speciation was mainly controlled by its binding to poorly ordered Fe (III)-oxyhydroxides. Being in the colloidal size, this fraction might be considered as mobile and able to transport As up to rivers or aquifers along with the water movement. Close to 6% of the As was in this size-fraction, which was small with regards to the larger size fraction. Finally, below 30 kDa, the fractions were mainly comprised of organic colloids and/or molecules. In this smaller size fraction, As was present as inorganic species (arsenite and/or arsenate) and as organic As(V) species. Both seemed to be bound to the colloidal phases either via a direct interaction or via Fe monomers or small clusters, in a ternary system, with organic colloids. Stolpe and Hassellöv (2007) demonstrated that, in aquatic systems, organic-rich colloids are more mobile than Fe-rich colloids, which are subject to aggregation and sedimentation. For both the 0.2 μm–30 kDa and <30 kDa fractions, the mobility of As will be controlled by the ability of the colloids to be maintained in solution relative to their affinity with the soil components and water flux in the soil porosity where they were produced. However, it should be noted that the potential (bio)degradation of organic As(V) species as inorganic As(V) (Ritchie, 2004) should be considered although their binding to colloids should decrease their (bio)degradation.

These results shed new light on the control of the As dynamics by wetlands. Wetlands are often regarded as sources of As for groundwater and/or rivers (Kocar et al., 2008; Polizzotto et al., 2008; Fendorf, 2010; Neubauer et al., 2013a,b). However, these studies were mainly interested in the <0.2 μm fraction in the water sample. They demonstrated that the As was released in the solution as labile inorganic species or bound to Fe/OM colloids. The present work showed that the most removable As was the As that was bound, not only as inorganic species but also as organic species, to colloids with a size <0.2 μm. The proportion (8%) of this As was low with regards to the As contained in the higher size fractions, in which the As speciation seemed to be controlled by the biological activity and binding to particulate Fe-oxyhydroxides. Therefore, if riparian wetlands are able to produce labile As(III) under the reducing period (Takahashi et al., 2004; Fendorf, 2010), several mechanisms could interfere in its transfer to rivers and aquifers and therefore limit As mobility. The most studied As is the As bound to soil particulates or colloidal Fe(III)-oxyhydroxides; the latter, as shown here and elsewhere, is closely associated with OM (Pokrovsky and Schott, 2002; Stolpe and Hassellöv, 2007; Neubauer et al., 2013b). A second mechanism concerns the biological uptake of As (e.g. for the detoxification process), resulting in the production of organic As(V) species that can be scavenged by plants and organisms or bound to Fe(III) oxyhydroxides. This decrease in As mobility, subsequent to the establishment of oxidizing conditions, was previously discussed by Frohne et al. (2014) and Shaheen et al. (2016). The proposed mechanism was the precipitation of Fe(III)-oxyhydroxides and subsequent As binding. However, the present results provided evidence that this process was not the only one and is not be the most important in riparian wetlands.

5. CONCLUSION

In this study we provided new insight in the control of As behavior during the oxidation of a reduced wetland soil solution. We highlighted the large variation in As speciation in the various size compartments of a suspension provided by the reoxidation of a riparian wetland soil solution. In the oxidized solution, As is mostly bound to Fe and to OM via C. Three main products were evidenced: (i) particulate biological material inherited from soil biological activities, (ii) Fe-OM-rich colloids with a size ranging from 0.2 μm to 30 kDa and (iii) OM-rich colloids below 30 kDa in which Fe was present as monomers or small clusters. The characterization of the OM revealed that the fractions above 0.2 μm were mainly composed of fatty acids (with carboxyl groups) whereas the <0.2 μm fractions, lignin and tannin markers (with phenolic groups) were in the majority. The 0.2 μm-30 kDa fraction corresponded to a transition phase in terms of degradation and the composition of the main functional group. Fractions <30 kDa were enriched in phenolic groups suggesting a higher affinity for Fe as confirmed by the EXAFS records where Fe–C was detected in the <30 kDa fraction. Despite oxidizing conditions, a small amount of reduced inorganic As was still present in the sample. Arsenic occurred as As(III) or As(V) bound to Fe(III) as particulates, colloids or small clusters. Most surprisingly, methylated As(V) species were formed during the oxidation period and detected in all of the size fractions. These organic As(V) species are usually biologically produced and could be bound to Fe(III) as particulates, colloids or clusters, to colloidal OM or could remain integrated in the biological residual material found in the soil.

We provided evidence that As was primarily distributed in the high size fraction (>0.2 μm), i.e. in the non-transferable fractions of the suspension. Only 8% of the As was present in the smaller fractions that was expected to be removable.

ACKNOWLEDGEMENTS

We acknowledge the SOLEIL synchrotron for provision of synchrotron radiation facilities and we would like to thank the beamlines staff for their support, especially D. Thiaudière for his assistance on the DiffAbs beamline. Dr. S. Mullin is acknowledged for post-editing the English style (http://www.proz.com/profile/677614).

This study was funded by the French ANR through the "Programme Jeunes Chercheurs" (ANR-JC-11-JS56-0010, ARSENORG) and by the IUF (Institut Universitaire de France) allocation of Melanie Davranche.

APPENDIX A. SUPPLEMENTARY DATA

Supplementary data associated with this article can be found, in the online version, at http://dx.doi.org/10.1016/j.gca.2017.01.013.

REFERENCES

AFNOR (1982) Essais des eaux - Dosage du fer - Méthode spectrométrique à la phénantroline-1,10.

Al-Sid-Cheikh M., Pédrot M., Dia A., Guenet H., Vantelon D., Davranche M., Gruau G. and Delhaye T. (2015) Interactions between natural organic matter, sulfur, arsenic and iron oxides in re-oxidation compounds within riparian wetlands: NanoSIMS and X-ray adsorption spectroscopy evidences. *Sci. Total Environ.* **515–516**, 118–128.

Anawar H. M., Akai J., Komaki K., Terao H., Yoshioka T., Ishizuka T., Safiullah S. and Kato K. (2003) Geochemical occurrence of arsenic in groundwater of Bangladesh: sources and mobilization processes. *J. Geochem. Explor.* **77**, 109–131.

Arai Y., Elzinga E. J. and Sparks D. L. (2001) X-ray absorption spectroscopic investigation of arsenite and arsenate adsorption at the aluminum oxide-water interface. *J. Colloid Interface Sci.* **235**, 80–88.

Arčon I., van Elteren J. T., Glass H. J., Kodre A. and Šlejkovec Z. (2005) EXAFS and XANES study of arsenic in contaminated soil. *X-Ray Spectrom.* **34**, 435–438.

Aström M. and Corin N. (2000) Abundance, sources and speciation of trace elements in humus-rich streams affected by acid sulphate soils. *Aquat. Geochem.* **6**, 367–383.

Bardelli F., Benvenuti M., Costagliola P., Di Benedetto F., Lattanzi P., Meneghini C., Romanelli M. and Valenzano L. (2011) Arsenic uptake by natural calcite: an XAS study. *Geochim. Cosmochim. Acta* **75**, 3011–3023.

Bauer M. and Blodau C. (2009) Arsenic distribution in the dissolved, colloidal and particulate size fraction of experimental solutions rich in dissolved organic matter and ferric iron. *Geochim. Cosmochim. Acta* **73**, 529–542.

Bottero J. Y., Manceau A., Villieras F. and Tchoubar D. (1994) Structure and mechanisms of formation of FeOOH(Cl) polymers. Langmuir 10.

Bourrié G., Trolard F., Jaffrezic J.-M. R. G., Maître V. and Abdelmoula M. (1999) Iron control by equilibria between hydroxy-green rusts and solutions in hydromorphic soils. *Geochim. Cosmochim. Acta* **63**, 3417–3427.

Bowell R. J. (1994) Sorption of arsenic by iron oxides and oxyhydroxides in soils. *Appl. Geochem.* **9**, 279–286.

Buschmann J., Kappeler A., Lindauer U., Kistler D., Berg M. and Sigg L. (2006) Arsenite and arsenate binding to dissolved humic acids: influence of pH, type of humic acid, and aluminum. *Environ. Sci. Technol.* **40**, 6015–6020.

Catrouillet C., Davranche M., Dia A., Bouhnik-Le Coz M., Marsac R., Pourret O. and Gruau G. (2014) Geochemical modeling of Fe(II) binding to humic and fulvic acids. *Chem. Geol.* **372**, 109–118.

Combes J. M., Manceau A., Calas G. and Bottero J. Y. (1989) Formation of ferric oxides from aqueous solutions: a polyhedral approach by X-ray absorption spectroscopy: 1. Hydrolysis and formation of ferric gels. *Geochim. Cosmochim. Acta* **53**, 583–594.

Cornell R. M. and Schwertmann U. (2003) *The Iron Oxides: Structures, Properties, Reactions, Occurence and Uses*. VCH, Weinheim, Germany.

Cox C. D. and Ghosh M. M. (1994) Surface complexation of methylated arsenate by hydrous oxides. *Water Res.* **28**, 1181–1188.

Cranwell P. A. (1974) Monocarboxylic acids in lake sediments: indicators, derived from terrestrial and aquatic biota, of paleoenvironmental trophic levels. *Chem. Geol.* **14**, 1–14.

Davranche M., Grybos M., Gruau G., Pédrot M., Dia A. and Marsac R. (2011) Rare earth element patterns: a tool for identifying trace metal sources during wetland soil reduction. *Chem. Geol.* **284**, 127–137.

Dembitsky V. M. and Rezanka T. (2003) Natural occurrence of arseno compounds in plants, lichens, fungi, algal species, and microorganisms. *Plant Sci.* **165**, 1177–1192.

Desai A. G. and Milburn R. M. (1969) Iron(III)–phenol complexes. IV. Further thermodynamics studies of iron(III)–phenolate and proton–phenolate associations. *J. Am. Chem. Soc.* **91**, 1958–1961.

Dia A., Gruau G., Olivié-Lauquet G., Riou C., Molénat J. and Curmi P. (2000) The distribution of rare earth elements in groundwaters: assessing the role of source-rock composition, redox changes and colloidal particles. *Geochim. Cosmochim. Acta* **64**, 4131–4151.

Dia A., Lauga B., Davranche M., Fahy A., Duran R., Nowack B., Petitjean P., Henin O., Martin S., Marsac R. and Gruau G. (2015) Bacteria-mediated reduction of As(V)-doped lepidocrocite in a flooded soil sample. *Chem. Geol.* **406**, 34–44.

Dobran S. and Zagury G. J. (2006) Arsenic speciation and mobilization in CCA-contaminated soils: influence of organic matter content. *Sci. Total Environ.* **364**, 239–250.

Du Laing G., Rinklebe J., Vandecasteele B., Meers E. and Tack F. M. G. (2009) Trace metal behaviour in estuarine and riverine floodplain soils and sediments: a review. *Sci. Total Environ.* **407**, 3972–3985.

Fendorf S. (2010) Arsenic chemistry in soils and sediments. *Lawrence Berkeley Natl. Lab.* Available at: http://escholarship.org/uc/item/9jt907xz.pdf [Accessed September 23, 2015].

Flank A.-M., Cauchon G., Lagarde P., Bac S., Janousch M., Wetter R., Dubuisson J.-M., Idir M., Langlois F., Moreno T. and Vantelon D. (2006) LUCIA, a microfocus soft XAS beamline. *Nucl. Instrum. Methods Phys. Res. Sect. B Beam Interact. Mater. At.* **246**, 269–274.

Foster A. L. and Kim C. S. (2014) Arsenic speciation in solids using X-ray absorption spectroscopy. *Rev. Mineral. Geochem.* **79**, 257–369.

Frohne T., Rinklebe J. and Diaz-Bone R. A. (2014) Contamination of floodplain soils along the Wupper River, Germany, with As Co, Cu, Ni, Sb, and Zn and the impact of pre-definite redox variations on the mobility of these elements. *Soil Sediment Contam. Int. J.* **23**, 779–799.

Geiszinger A., Goessler W. and Kosmus W. (2002) Organoarsenic compounds in plants and soil on top of an ore vein. *Appl. Organomet. Chem.* **16**, 245–249.

George G. N. and Pickering I. J. (2007) X-ray absorption spectroscopy in biology and chemistry. In *Brilliant Light in Life and Material Sciences* Springer. pp. 97–119. Available at: http://link.springer.com/chapter/10.1007/978-1-4020-5724-3_9 [Accessed June 24, 2016].

Gruau G., Dia A., Olivié-Lauquet G., Davranche M. and Pinay G. (2004) Controls on the distribution of rare earth elements in shallow groundwaters. *Water Res.* **38**, 3576–3586.

Grybos M., Davranche M., Gruau G. and Petitjean P. (2007) Is trace metal release in wetland soils controlled by organic matter mobility or Fe-oxyhydroxides reduction? *J. Colloid Interface Sci.* **314**, 490–501.

Grybos M., Davranche M., Gruau G., Petitjean P. and Pédrot M. (2009) Increasing pH drives organic matter solubilization from wetland soils under reducing conditions. *Geoderma* **154**, 13–19.

Guénet H., Davranche M., Vantelon D., Pédrot M., Al-Sid-Cheikh M., Dia A. and Jestin J. (2016) Evidence of organic matter control on As oxidation by iron oxides in riparian wetlands. *Chem. Geol.* **439**, 161–172.

Hazemann J.-L., Bérar J. F. and Manceau A. (1991) Rietveld studies of the aluminium–iron substitution in synthetic goethite. *Mater. Sci. Forum* **79–82**, 821–826.

Hedges J. I. and Parker P. L. (1976) Land-derived organic matter in surface sediments from the Gulf of Mexico. *Geochim. Cosmochim. Acta* **40**, 1019–1029.

Hiemstra T. and van Riemsdijk W. H. (2007) Adsorption and surface oxidation of Fe(II) on metal (hydr)oxides. *Geochim. Cosmochim. Acta* **71**, 5913–5933.

Hiltbold A. E. (1975) Behavior of organoarsenicals in plants and soils. In *ACS Publications*. Available at: http://pubs.acs.org/doi/abs/10.1021/bk-1975-0007.ch004 [Accessed January 30, 2017].

Hoffmann M., Mikutta C. and Kretzschmar R. (2013) Arsenite binding to natural organic matter: spectroscopic evidence for ligand exchange and ternary complex formation. *Environ. Sci. Technol.* **47**, 12165–12173.

Hoffmann M., Mikutta C. and Kretzschmar R. (2014) Arsenite binding to sulfhydryl groups in the absence and presence of ferrihydrite: a model study. *Environ. Sci. Technol.* **48**, 3822–3831.

Horcajada P., Surble S., Serre C., Hong D.-Y., Seo Y. K., Chang J. S., Greneche J. M., Margiolaki I. and Ferey G. (2007) Synthesis and catalytic properties of MIL-100(Fe), an iron(iii) carboxylate with large pores. *Chem. Commun.*, 2820.

Huang J.-H. and Matzner E. (2007) Biogeochemistry of organic and inorganic arsenic species in a forested catchment in Germany. *Environ. Sci. Technol.* **41**, 1564–1569.

Huguet A., Vacher L., Relexans S., Saubusse S., Froidefond J. M. and Parlanti E. (2009) Properties of fluorescent dissolved organic matter in the Gironde Estuary. *Org. Geochem.* **40**, 706–719.

Karlsson T. and Persson P. (2010) Coordination chemistry and hydrolysis of Fe(III) in a peat humic acid studied by X-ray absorption spectroscopy. *Geochim. Cosmochim. Acta* **74**, 30–40.

Kitahama K., Kiriyama R. and Baba Y. (1975) Refinement of crystal-structure of scorodite. *Acta Crystallogr. Sect. B-Struct. Sci.* **31**, 322–324.

Kocar B. D., Polizzotto M. L., Benner S. G., Ying S. C., Ung M., Ouch K., Samreth S., Suy B., Phan K., Sampson M. and Fendorf S. (2008) Integrated biogeochemical and hydrologic processes driving arsenic release from shallow sediments to groundwaters of the Mekong delta. *Appl. Geochem.* **23**, 3059–3071.

Lewis W. M. (1995) *Wetlands: Characteristics and Boundaries*. Natl. Academy Press.

Liang L., McCarthy J. F., Jolley L. W., McNabb J. A. and Mehlhorn T. L. (1993) Iron dynamics: transformation of Fe (II)/Fe (III) during injection of natural organic matter in a sandy aquifer. *Geochim. Cosmochim. Acta* **57**, 1987–1999.

Lombi E., Scheckel K. G., Pallon J., Carey A. M., Zhu Y. G. and Meharg A. A. (2009) Speciation and distribution of arsenic and localization of nutrients in rice grains. *New Phytol.* **184**, 193–201.

Luciani X., Mounier S., Paraquetti H. H. M., Redon R., Lucas Y., Bois A., Lacerda L. D., Raynaud M. and Ripert M. (2008) Tracing of dissolved organic matter from the SEPETIBA Bay (Brazil) by PARAFAC analysis of total luminescence matrices. *Mar. Environ. Res.* **65**, 148–157.

Manceau A. (1995) The mechanism of anion adsorption on iron oxides: evidence for the bonding of arsenate tetrahedra on free Fe(O, OH)6 edges. *Geochim. Cosmochim. Acta* **59**, 3647–3653.

Manceau A. and Combes J. M. (1988) Structure of Mn and Fe oxides and oxyhydroxides: a topological approach by EXAFS. *Phys. Chem. Miner.* **15**, 283–295.

Manceau A. and Drits V. A. (1993) Local structure of ferrihydrite and feroxyhite by EXAFS spectroscopy. *Clay Miner.* **28**, 165–184.

McKnight D. M., Boyer E. W., Westerhoff P. K., Doran P. T., Kulbe T. and Andersen D. T. (2001) Spectrofluorometric characterization of dissolved organic matter for indication of precursor organic material and aromaticity. *Limnol. Oceanogr.* **46**, 38–48.

Mikutta C. and Kretzschmar R. (2011) Spectroscopic evidence for ternary complex formation between arsenate and ferric iron complexes of humic substances. *Environ. Sci. Technol.* **45**, 9550–9557.

Miot J., Morin G., Skouri-Panet F., Férard C., Aubry E., Briand J., Wang Y., Ona-Nguema G., Guyot F. and Brown G. E. (2008) XAS study of arsenic coordination in Euglena gracilis exposed to arsenite. *Environ. Sci. Technol.* **42**, 5342–5347.

Morin G., Lecocq D., Juillot F., Calas G., Ildefonse P., Belin S., Briois V., Dillmann P., Chevallier P. and Gauthier C. (2002) EXAFS evidence of sorbed arsenic (V) and pharmacosiderite in a soil overlying the Echassières geochemical anomaly, Allier. *France. Bull. Société Géologique Fr.* **173**, 281–291.

Morin G., Rousse G. and Elkaim E. (2007) Crystal structure of tooeleite, Fe6(AsO3)4SO4(OH)4{middle dot}4H2O, a new iron arsenite oxyhydroxy-sulfate mineral relevant to acid mine drainage. *Am. Mineral.* **92**, 193–197.

Neubauer E. v. d., Kammer F. and Hofmann T. (2013a) Using FLOWFFF and HPSEC to determine trace metal–colloid associations in wetland runoff. *Water Res.* **47**, 2757–2769.

Neubauer E., Köhler S. J., von der Kammer F., Laudon H. and Hofmann T. (2013b) Effect of pH and Stream Order on Iron and Arsenic Speciation in Boreal Catchments. *Environ. Sci. Technol.* **47**, 7120–7128.

Nierop K. G. J. and Verstraten J. M. (2004) Rapid molecular assessment of the bioturbation extent in sandy soil horizons under pine using ester-bound lipids by on-line thermally assisted hydrolysis and methylation-gas chromatography/mass spectrometry. *Rapid Commun. Mass Spectrom.* **18**, 1081–1088.

Nierop K. G. J., Preston C. M. and Kaal J. (2005) Thermally Assisted Hydrolysis and Methylation of Purified Tannins from Plants. *Anal. Chem.* **77**, 5604–5614.

Nuttall R. H. and Hunter W. N. (1995) Redetermination of 4-hydroxy-3-nitro-benzenearsonic Acid. *Acta Crystallogr. Sect. C-Org. Compd.* **51**, 2342–2344.

Olivié-Lauquet G., Gruau G., Dia A., Riou C., Jaffrezic A. and Henin O. (2001) Release of trace elements in wetlands: role of seasonal variability. *Water Res.* **35**, 943–952.

Ona-Nguema G., Morin G., Juillot F., Calas G. and Brown G. E. (2005) EXAFS analysis of arsenite adsorption onto two-line ferrihydrite, hematite, goethite, and lepidocrocite. *Environ. Sci. Technol.* **39**, 9147–9155.

Ona-Nguema G., Morin G., Wang Y., Menguy N., Juillot F., Olivi L., Aquilanti G., Abdelmoula M., Ruby C., Bargar J. R., Guyot F., Calas G. and Brown G. E. (2009) Arsenite sequestration at the surface of nano-Fe(OH)2, ferrous-carbonate hydroxide, and green-rust after bioreduction of arsenic-sorbed lepidocrocite by Shewanella putrefaciens. *Geochim. Cosmochim. Acta* **73**, 1359–1381.

Pédrot M., Boudec A. L., Davranche M., Dia A. and Henin O. (2011) How does organic matter constrain the nature, size and availability of Fe nanoparticles for biological reduction? *J. Colloid Interface Sci.* **359**, 75–85.

Pokrovsky O. S. and Schott J. (2002) Iron colloids/organic matter associated transport of major and trace elements in small boreal rivers and their estuaries (NW Russia). *Chem. Geol.* **190**, 141–179.

Polizzotto M. L., Kocar B. D., Benner S. G., Sampson M. and Fendorf S. (2008) Near-surface wetland sediments as a source of arsenic release to ground water in Asia. *Nature* **454**, 505–508.

Poulin B. A., Ryan J. N. and Aiken G. R. (2014) Effects of iron on optical properties of dissolved organic matter. *Environ. Sci. Technol.* **48**, 10098–10106.

Pourret O., Dia A., Davranche M., Gruau G., Hénin O. and Angée M. (2007) Organo-colloidal control on major- and trace-element partitioning in shallow groundwaters: confronting ultrafiltration and modelling. *Appl. Geochem.* **22**, 1568–1582.

Ravel B. and Newville M. (2005) ATHENA, ARTEMIS, HEPHAESTUS: data analysis for X-ray absorption spectroscopy using IFEFFIT. *J. Synchrotron Radiat.* **12**, 537–541.

Redman A. D., Macalady D. L. and Ahmann D. (2002) Natural organic matter affects arsenic speciation and sorption onto hematite. *Environ. Sci. Technol.* **36**, 2889–2896.

Ritchie A. (2004) An origin for arsenobetaine involving bacterial formation of an arsenic-Carbon bond. *FEMS Microbiol. Lett.* **235**, 95–99.

Ritter K., Aiken G. R., Ranville J. F., Bauer M. and Macalady D. L. (2006) Evidence for the aquatic binding of arsenate by natural organic matter−suspended Fe(III). *Environ. Sci. Technol.* **40**, 5380–5387.

Ronkart S. N., Laurent V., Carbonnelle P., Mabon N., Copin A. and Barthélemy J.-P. (2007) Speciation of five arsenic species (arsenite, arsenate, MMAAV, DMAAV and AsBet) in different kind of water by HPLC-ICP-MS. *Chemosphere* **66**, 738–745.

Rumpel C. and Dignac M.-F. (2006) Gas chromatographic analysis of monosaccharides in a forest soil profile: analysis by gas chromatography after trifluoroacetic acid hydrolysis and reduction–acetylation. *Soil Biol. Biochem.* **38**, 1478–1481.

Shaheen S. M., Rinklebe J., Frohne T., White J. R. and DeLaune R. D. (2016) Redox effects on release kinetics of arsenic, cadmium, cobalt, and vanadium in Wax Lake Deltaic freshwater marsh soils. *Chemosphere* **150**, 740–748.

Sharma P., Rolle M., Kocar B., Fendorf S. and Kappler A. (2011) Influence of natural organic matter on as transport and retention. *Environ. Sci. Technol.* **45**, 546–553.

Smedley P. L. and Kinniburgh D. G. (2001) A review of the source, behavior and distribution of arsenic in natural waters. *Appl. Geochem.* **17**, 517–568.

Smith P. G., Koch I., Gordon R. A., Mandoli D. F., Chapman B. D. and Reimer K. J. (2005) X-ray absorption near-edge structure analysis of arsenic species for application to biological environmental samples. *Environ. Sci. Technol.* **39**, 248–254.

Sommer L. and Pliska K. (1961) Eisen(III)-Acetatokomplexe. *Collect. Czechoslov. Chem. Commun.* **26**, 2754.

Stolpe B. and Hassellöv M. (2007) Changes in size distribution of fresh water nanoscale colloidal matter and associated elements on mixing with seawater. *Geochim. Cosmochim. Acta* **71**, 3292–3301.

Sohrin Y., Matsui M., Kawashima M., Hojo M. and Hasegawa H. (1997) Arsenic biogeochemistry affected by eutrophication in Lake Biwa. *Japan. Environ. Sci. Technol.* **31**, 2712–2720.

Takahashi Y., Minamikawa R., Hattori K. H., Kurishima K., Kihou N. and Yuita K. (2004) Arsenic behavior in paddy fields during the cycle of flooded and non-flooded periods. *Environ. Sci. Technol.* **38**, 1038–1044.

Tamaki S. and Frankenberger W. T. (1992) Environmental biochemistry of arsenic. *Rev. Environ. Contam. Toxicol.* **124**, 79–110.

ThomasArrigo L. K., Mikutta C., Byrne J., Barmettler K., Kappler A. and Kretzschmar R. (2014) Iron and arsenic speciation and distribution in organic flocs from streambeds of an arsenic-enriched peatland. *Environ. Sci. Technol.* **48**, 13218–13228.

Tipping E. (1998) Humic ion-binding model VI: an improved description of the interactions of protons and metal ions with humic substances. *Aquat. Geochem.* **4**, 3–47.

Tipping E., Rey-Castro C., Bryan S. E. and Hamilton-Taylor J. (2002) Al (III) and Fe (III) binding by humic substances in freshwaters, and implications for trace metal speciation. *Geochim. Cosmochim. Acta* **66**, 3211–3224.

Voegelin A., Weber F.-A. and Kretzschmar R. (2007) Distribution and speciation of arsenic around roots in a contaminated riparian floodplain soil: Micro-XRF element mapping and EXAFS spectroscopy. *Geochim. Cosmochim. Acta* **71**, 5804–5820.

Waychunas G. A., Rea B. A., Fuller C. C. and Davis J. A. (1993) Surface chemistry of ferrihydrite: Part1. EXAFS studies of the geometry of coprecipitated and adsorbed arsenate. *Geochim. Cosmochim. Acta* **57**, 2251–2269.

Weishaar J. L., Aiken G. R., Bergamaschi B. A., Fram M. S., Fujii R. and Mopper K. (2003) Evaluation of specific ultraviolet absorbance as an indicator of the chemical composition and reactivity of dissolved organic carbon. *Environ. Sci. Technol.* **37**, 4702–4708.

Zsolnay A., Baigar E., Jimenez M., Steinweg B. and Saccomandi F. (1999) Differentiating with fluorescence spectroscopy the sources of dissolved organic matter in soils subjected to drying. *Chemosphere* **38**, 45–50.

Associate editor: Mario Villalobos

Science of the Total Environment 631–632 (2018) 580–588

Contents lists available at ScienceDirect

Science of the Total Environment

journal homepage: www.elsevier.com/locate/scitotenv

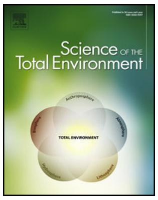

Experimental evidence of REE size fraction redistribution during redox variation in wetland soil

Hélène Guénet [a], Edwige Demangeat [a], Mélanie Davranche [a,*], Delphine Vantelon [b], Anne-Catherine Pierson-Wickmann [a], Emilie Jardé [a], Martine Bouhnik-Le Coz [a], Elaheh Lotfi [a], Aline Dia [a], Jacques Jestin [c,d]

[a] Univ. Rennes, CNRS, Géosciences Rennes, UMR 6118, Campus de Beaulieu, 35042, Rennes Cedex, France
[b] Synchrotron SOLEIL, L'orme des merisiers, Saint Aubin BP48, 91192 Gif sur Yvette Cedex, France
[c] Univ Rennes 1, UMR CNRS 6226, Inst Sci Chim Rennes, Ctr Diffractometrie Rayons 10, F-35042 Rennes, France
[d] Laboratoire Léon Brillouin, CEA Saclay, 91191 Gif/Yvette Cedex, France

HIGHLIGHTS

- Impact of reducing and oxidizing alternation on the REE speciation and patterns was investigated.
- Significant change occurred in the REEs-bearing fractions.
- Iron and organic matter play both a major role in the REEs scavenging.
- In wetland, Fe oxides are still present under reducing period and partially control REE speciation.

GRAPHICAL ABSTRACT

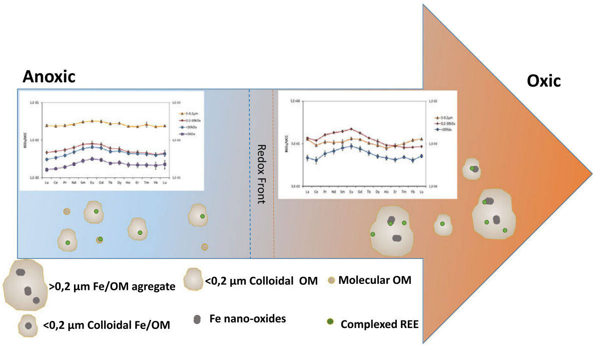

ARTICLE INFO

Article history:
Received 22 December 2017
Received in revised form 23 February 2018
Accepted 1 March 2018
Available online xxxx

Editor: F.M. Tack

Keywords:
Rare earth elements
Wetland
Redox alternation
Iron
Organic matter
Colloid
Nanoparticles

ABSTRACT

The evolution of rare earth element (REE) speciation between reducing and oxidizing conditions in a riparian wetland soil was studied relative to the size fractionation of the solution. In all size fractions obtained from the reduced and oxidized soil solutions, the following analyses were carried out: organic matter (OM) characterization, transmission electron microscopy (TEM) observations as well as major and trace element analyses. Significant REE redistribution and speciation evolution between the various size fractions were observed. Under reducing conditions, the REEs were bound to colloidal and dissolved OM (<2 µm size fractions). By contrast, under oxidizing conditions, they were distributed in particulate (>2 µm size fraction), colloidal (<2 µm size fraction), organic and Fe-enriched fractions. In the particulate size fraction, the REEs were bound to humic and bacterial OM embedding Fe nano-oxides. The resulting REE pattern showed a strong enrichment in heavy REEs (HREEs) in response to REE binding to specific bacterial OM functional groups. In the largest colloidal size fraction (0.2 µm–30 kDa), the REEs were bound to humic substances (HS). The lowest colloidal size fraction (<30 kDa) is poorly concentrated in the REEs and the REE pattern showed an increase in the middle REEs (MREEs) and heavy REEs (HREEs) corresponding to a low REE loading on HS. A comparison of the REE patterns in the present experimental and field measurements demonstrated that, in riparian wetlands, under a high-water level, reducing conditions are insufficient to allow for the dissolution of the entire Fe nano-oxide pool formed during the oxidative period. Therefore, even under reducing conditions, Fe(III) seems to remain a potential scavenger of REEs.

---

[*] Corresponding author.
E-mail address: melanie.davranche@univ-rennes1.fr (M. Davranche).

https://doi.org/10.1016/j.scitotenv.2018.03.005
0048-9697/

1. Introduction

A large number of processes and factors have been shown to control the behavior of rare earth elements (REEs) in solution. As an example, REE behavior is known to be strongly, directly or indirectly, controlled by pH, redox conditions and aqueous and surface complexation reactions (Koeppenkastrop and De Carlo, 1993; Tang and Johannesson, 2003; Quinn et al., 2004; Pourret et al., 2007; Marsac et al., 2010). REEs are commonly divided into three groups and will be referred in the following study as light REEs (LREE), middle REEs (MREE) and heavy REEs (HREE). LREE corresponds to those elements between lanthanum and samarium, HREE between holmium and lutetium and MREE are the lanthanides in between. Mineral and organic surfaces, such as clays, Fe and Mn oxyhydroxides or humic substances, can develop specific REE patterns in response to sorption processes and binding site heterogeneity (Koeppenkastrop and De Carlo, 1992; Coppin et al., 2002; Tang and Johannesson, 2003; Pourret et al., 2007; Marsac et al., 2013). In groundwater, many studies have shown a selective “oxidative scavenging” of cerium (Ce) by Fe and Mn oxyhydroxides resulting in Ce depletion in REE solution patterns (Koeppenkastrop and De Carlo, 1992; Bau, 1999; Ohta and Kawabe, 2001; Davranche et al., 2004, 2005; Pédrot et al., 2015). Furthermore, some bacteria are able to preferentially adsorb HREE, defined as holmium (Ho) through lutetium (Lu), which has an impact on the resulting REE pattern (Takahashi et al., 2005; Takahashi et al., 2010). In riparian wetland soils, seasonal flooding leads to variations in the redox conditions during which REEs are solubilized and mobilized. Several studies have reported the relationship between REEs and the organic colloidal pool from the soil solution (Viers et al., 1997; Tang and Johannesson, 2003; Dia et al., 2000; Pourret et al., 2007; Grybos et al., 2007; Davranche et al., 2011). Grybos et al. (2007) demonstrated that REEs are mostly bound to OM during the oxidative period and then released during the reducing period with dissolved organic matter (DOM) desorption, making OM the controlling phase of REE mobility in wetlands. Using ultrafiltration devices, Dia et al. (2000) did not find any variation between the REE patterns from the oxidized (low water level) and reduced (high water level) periods.

For the same riparian wetland soil, Pédrot et al. (2008) used leaching experiments under oxidizing conditions and Grybos et al. (2007) used anoxic incubations to obtain quite similar REE patterns exhibiting the specific OM binding feature, i.e. a MREE downward concavity specific to the binding of MREE to the OM carboxylic site (Pourret et al., 2007; Marsac et al., 2013) confirming that REE binding to OM dominates their speciation. However, some understated differences can be observed between the REE patterns obtained under experimental (oxic or anoxic) conditions and during field campaigns, such as a slight HREE enrichment and the presence of a slight Ce anomaly under field conditions (e.g. Dia et al., 2000; Pourret et al., 2010). With regards to the high sensitivity of the REE patterns to physico-chemical conditions and biogeochemical processes, these differences suggest that the previous conclusion establishing that OM has total control over REE speciation may be incorrect. The major discrepancy between field and experimental conditions is that REEs are submitted to redox alternations in the field; however, the anoxic experimental conditions were completely separate from the oxidizing leaching conditions under the experimental conditions. Therefore, no experimental studies were focus on the impact of the redox alternations on the evolution of the REE speciation and patterns, notably with regards to the impact of the reoxidation of Fe which is known to be a strong REE scavenger (Bau, 1999; Quinn et al., 2006). The question is now to explain why the difference observed experimentally is not observed in the field. Is OM the sole factor able to controlled REE speciation under reducing and oxidizing conditions? Or is there a significant REE speciation variation between reducing and oxidizing as suggested by the experiment?

In this study, we focused on the evolution of the REE patterns between reduced and oxidized soil solutions from a wetland soil. To overcome difficulties during field sampling, the soil solutions were obtained experimentally from the anoxic incubation of a wetland soil recovered from the Kervidy-Naizin catchment (Brittany, France). The reduced soil solution was then recovered and oxidized at ambient air. We chose to separate the solution from soil matrix to be able to evaluate the REE distribution between the various size fractions of the re-oxidation products (particle to solution). Reduced and oxidized solutions were filtered and ultrafiltered at different cut sizes. The different size fractions were studied using TEM and were chemically analyzed for major and trace elements; the organic matter (OM) composition was characterized using thermochemiolysis coupled to gas chromatography and mass spectrometry (THM-GC–MS) and fluorescence spectroscopy.

2. Material and methods

2.1. Site description and soil sampling

An organic-rich soil horizon was sampled in the Kervidy-Naizin subcatchment of the Mercy riparian wetland located in Brittany (France). This wetland seasonally undergoes drying (in the summer) and flooding periods (in the winter) and has been monitored since 1991 to investigate the effects of intensive agriculture (cultures and livestock) on water quality. Thus, the hydrological, pedological and geochemical contexts are well documented (Bourrié et al., 1999; Dia et al., 2000; Olivié-Lauquet et al., 2001). The sampled uppermost soil horizon was defined as the organo-mineral horizon (Ah) of a planosol (according to the WRB international classification) which contained (wt%; anhydrous basis) OM (15%), clay (42%), quartz (30%) and Fe-oxyhydroxides (3.5%) (Grybos et al., 2007). Approximately 5 kg of soil was collected in March 2015 from the surface layer, sieved at 2 mm and stored in the dark at 4 °C to minimize the latent biological activity during soil incubation.

2.2. Experimental simulation of the redox cycle

This method has been described in Guénet et al. (2017). To reproduce the reducing conditions observed in wetland soils, a soil suspension was prepared under anoxic conditions in a Jacomex anaerobic chamber. Approximately 130 g of the sieved soil was mixed with 1.8 L of a synthetic solution containing 0.48 mmol L^{-1} of $NaNO_3$ and NaCl, and 0.1 mmol L^{-1} of Na_2SO_4 which corresponded to an anhydrous soil/solution ratio of 1/20 (soil moisture = 44 wt%). The synthetic solution was adjusted to mimic the anionic composition of the soil solution during autumn (the time period when the water table rises) in the Mercy wetland system. The solution was continuously stirred throughout the duration of the anaerobic experiment. The experiments were performed in triplicate. The extended reduction was followed by monitoring the increase in the pH, Eh and Fe^{2+} concentration subsequent to the reductive dissolution of the soil Fe-oxyhydroxides.

2.3. Filtration procedure of the reduced and oxidized soil solutions

Note that to be able to study the oxidation by-product of the wetland soil (to avoid the mixing trapping of such product in the soil matrix). The reduced soil solutions, obtained subsequently to the soil incubation, were first separated from the soil solid phase using 5 μm cellulose nitrate filters from Sartorius. In a second strep, the soil solution was removed from the anaerobic chamber and allowed to oxidize at ambient air in the dark at room temperature.

An aliquot of this reduced solution was then filtered at 0.2 μm and sequentially ultrafiltered at 30 kDa and 3 kDa using ultrafiltration cells (Sartorius). The obtained size fractions (i.e. 5–0.2 μm, 0.2 μm–30 kDa, <30 kDa and <5 kDa) were analyzed for major and trace elements. The remaining 5 μm soil solutions of the triplicate were then removed from the anaerobic chambers and oxidized at ambient air in the dark at room temperature for two weeks. Triplicates were size-fractionated using a series of filtration units at 5 and 0.2 μm and ultrafiltration at 30 and 5 kDa. First, two sequential filtrations using cellulose nitrate membrane filters at 3 μm and 0.2 μm (from Sartorius) were performed and the samples were recovered on the filters. Then, the 0.2 μm filtered solutions were ultrafiltered at 30 kDa and then 5 kDa using a Labscale tangential flow filter system equipped with two Pellicon XL membranes (PXC030C50 and PXC05C50).

2.4. Chemical analysis

The organic carbon (OC) concentrations in the soil solutions were measured using an organic carbon analyzer (Shimmadzu TOC-V CSH). The accuracy of the dissolved organic carbon (DOC) measurements was estimated to be ±5% in the suspension filtered at 0.2 μm by using a standard solution of potassium hydrogen phthalate. Since this technique cannot be used to analyze particulate organic carbon, the samples larger than 0.2 μm in the oxidized soil solution were freeze-dried and the OC content was determined at the INRA SAS laboratory in Rennes, France using a dry combustion method with a CN Analyzer (Flash EA-1112). Unfortunately, with regards to the analytical limits, the amount of OC in the 5–0.2 μm size fraction in the reduced soil solution could not be determined. The concentration of the Fe(II) from aliquots collected during the reduction of the soil solution was determined with the 1.10-phenantroline colorimetric method (AFNOR, 1982) at 510 nm using a UV–visible spectrometer (UV/VIS Spectrometer "Lambda 25" from Perkin Elmer). The major and trace elements, including REE, were determined by Quadruple ICP-MS using an Agilent Technologies 7700×. All REEs with a mass greater than Sm were routinely corrected for isobaric interferences because Ba and light REEs are prone to form isobaric oxides during the analysis. The concentrations were determined using a conventional external calibration procedure with seven external standard multi-element solutions (from Inorganic Venture, USA). A mixed solution of Rhodium-Rhenium was used as an internal standard to correct the instrumental drift and potential matrix effects. The detection limit for the whole group of REEs is typically <0.25 ng L^{-1}. A SLRS-5 water certified reference material was used to check the accuracy of the measurement procedure, and the instrumental error on the REE analysis is <5%. The REE chemical blanks were below the detection limit and are thus negligible.

2.5. Transmission electron microscopy (TEM) observations

A drop of each size fraction of the oxidized solution for the 5–0.2 μm size fraction was deposited onto a 300 mesh copper grid coated with a lacey carbon film (Oxford Instruments, S166–3) and dried at room temperature. High-Resolution Electron Microscopy (HREM) investigations were performed on a TEM with a JEOL 100CXII instrument (voltage 100 kV) (THEMIS Analytical Facility at the University of Rennes 1). The elemental composition of the different structures was determined with a JEOL 2100F (voltage 200 kV) equipped with an X-ray energy dispersive spectroscopy (XEDS) detector (Kevex detector with an ultrathin window).

2.6. Organic matter molecular characterization

2.6.1. Fluorescence spectral analysis

The fluorescence measurements were done with a Perkin-Elmer LS 45 spectrofluometer using 10 mm quartz cells. The three-dimensional excitation-emission fluorescence spectra were acquired by collecting individual emission spectra (Em 290–600 nm) over a range of excitation Ex ranging from 240 to 550 nm, with an increment of 5 nm, at a scan speed of 1500 nm min^{-1}. The slits were set to 5 nm for both the excitation and emission monochromators. The spectra obtained using this technique were treated using the PROGMEEF software in Matlab language (Luciani et al., 2008). Since Fe can potentially affect DOM absorbance in the UV region (Weishaar et al., 2003; Poulin et al., 2014), the raw absorbance of the sample at 254 nm was corrected by taking the molar absorptivity of Fe(III) into account (Poulin et al., 2014). Each kind of organic substance has different excitation-emission wavelengths. Excitation-emission matrix (EEM) maps can be divided into five regions but only three of them are more likely to be represented in our sample and thus only the following three regions were considered: region I (Ex 200–250 nm, Em 380–500 nm) was related to fulvic acid-like organics, region II (Ex 250–280 nm, Em 200–380 nm) was related to soluble microbial by-product-like materials and region III (Ex 250–400 nm, Em 380–500 nm) was related to humic-like organics (Chen et al., 2003). The humification index (HIX), indicating the complexity and condensation (H/C ratios) of OM, was calculated as the ratio of the integrated fluorescence emission peak at longer wavelengths (435–480 nm) over shorter wavelengths (300–345 nm) at an excitation wavelength of 254 nm (Zsolnay et al., 1999). The fluorescence index (FI), calculated as the ratio of emission intensity at 450 and 500 nm at a fixed excitation wavelength of 370 nm (McKnight et al., 2001), is correlated with the structural conjugation and aromaticity and was used to differentiate the source of the DOM. The biological/freshness index (BIX), an indicator of the relative contribution of recently microbialproduced DOM, was calculated as the ratio of emission intensity at 380 and 430 nm for an excitation wavelength of 310 nm (Huguet et al., 2009).

2.6.2. THM-GC–MS

Approximately 2 mg of each freeze-dried sample was introduced into an 80 μL aluminum reactor with an excess of solid tetramethylammonium hydroxide (TMAH – ca. 10 mg). The thermally assisted hydrolysis and methylation (THM) reaction was performed inline using a vertical micro-furnace pyrolyser PZ-2020D (Frontier Laboratories, Japan) operating at 400 °C for 1 min. The products of this reaction were injected into a gas chromatograph (GC) GC-2010 (Shimadzu, Japan) equipped with a SLB 5MS capillary column in split mode (60 m × 0.25 mm ID, 0.25 μm film thickness). The split ratio was adapted according to the sample and ranged from 15 to 30. The temperature of the transfer line was 321 °C and the temperature of the injection port was 310 °C. The oven was programmed to maintain an initial temperature of 50 °C for 2 min, then rise to 150 °C at 15 °C min^{-1} and then rise to 310 °C at 3 °C min^{-1}, where it stayed for 14 min. Helium was used as the carrier gas, with a flow rate of 1.0 mL min^{-1}. Compounds were detected using a QP2010+ mass spectrometer (MS) (Shimadzu, Japan) operating in the full-scan mode. The temperature of the transfer line was set at 280 °C, the ionization source at 200 °C and the molecules were ionized by electron impact using an energy of 70 eV. Compounds were identified on the basis of their full-scan mass spectra by comparison with the NIST library and with published data (Nierop and Verstraten, 2004; Nierop et al., 2005; Denis et al., 2017). They were classified into three categories: lignin and tannin markers, carbohydrates and fatty acids. The peak area of the selected *m/z* for each compound was integrated and corrected by a mass spectra factor calculated as the reciprocal of the proportion of the fragment used for the integration and the entire fragmentogram provided by the NIST library. In this study, we present the compounds that are useful to interpret the REE patterns. The presented data are an average of the triplicates.

3. Results

After one month under anoxic conditions, the pH, Eh and Fe(II) values reached 7.2, −130 mV and 20 mg L^{-1}, respectively. Note that the TEM observation, EEM, and THM-GS–MS analyses were only performed on the oxidized solution, which is the condition of interest for this study.

3.1. Size distribution of the OM, Fe and REEs

The organic carbon (OC), total Fe and sum of the REE (ΣREE) concentrations in each size fraction of the reduced soil solution are presented in Fig. 2A. The amount of Fe was almost identical between the two largest size fractions, close to 0.9 μmol g^{-1}, and then increased to 6.3 μmol g^{-1} in the <5 kDa size fraction, following the trend observed for the OC concentration which rose to 2.1×10^{-4} mol g^{-1}. The highest Fe/OC ratio was calculated for the <30 kDa and <5 kDa size fractions and indicated that Fe was mainly present as ion bound to organic molecules (Davranche et al., 2013; Catrouillet et al., 2014). From the 0.2 μm–30 kDa to <30 kDa size fractions, ΣREE decreased from 1.3×10^{-2} to 2.7×10^{-3} μmol g^{-1}. In the <5 kDa size fraction, ΣREE decreases to reach the lowest ΣREE concentration at 2.7×10^{-3} μmol g^{-1}. These results provide evidence that ΣREE are mainly concentrated in the 5–0.2 μm, which are rich in OC and Fe.

As the oxidation experiment took place in ambient atmosphere, significant evaporation occurred leading to an increase in the bulk concentration between the reduced and oxidized conditions. The OC, Fe and ΣREE concentrations in each size fraction are presented in Fig. 1B. In all size fractions, OC was the most abundant, varying between 2×10^{-2} mol g^{-1} in the first size fraction and increasing to 2.7×10^{-2} mol g^{-1} and 2.7×10^{-2} mol g^{-1} in the 0.2 μm-30 kDa and <30 kDa size fractions, respectively. In the <5 kDa size fraction, the OC decreased to 1.1×10^{-2} mol g^{-1}. The iron distribution varied compared to the OC distribution. The Fe concentration decreased from 1.1×10^{-2} mol g^{-1} in the 5–0.2 μm size fraction to 8.8 10^{-3} mol g^{-1} in the 0.2 μm–30 kDa size fraction. In the <30 kDa and <5 kDa size fractions, the Fe concentration dropped significantly to 1.9×10^{-3} mol g^{-1} and 9.2×10^{-5} mol g^{-1}, respectively. Therefore, most of the Fe was present as particles (>0.2 μm) and large size colloids (between 0.2 μm and 30 kDa) where the Fe/OC ratio was the highest. The smaller size fractions (<30 kDa) were Fe-depleted and OC-enriched, and had the lowest Fe/OC ratio.

The REE concentration was higher in the largest size fraction, 5–0.2 μm (1 μmol g^{-1}). With decreasing pore size, the ΣREE seem to follow the trend of Fe, decreasing from 0,69 μmol g^{-1} in the 0.2–30 kDa size fraction to 1×10^{-4} μmol g^{-1} and 1.2×10^{-5} μmol g^{-1} in the <30 kDa and <5 kDa size fractions. No correlation was observed between the OC and ΣREE concentrations. This distribution suggested that the REEs were mainly bound to the particulate and colloidal fraction of the oxidized solution.

3.2. High resolution TEM observations

Representative transmission electron micrographs of the 5–0.2 μm size fraction are presented in Fig. 2. The largest view (i.e. Fig. 2A) showed that the natural sample was heterogeneous. Micrometric organic compounds such as diatoms and silicate plant (e.g. horsetail) remains were observed. The Fe phases were detected through their higher electron density and composition using EDS (Energy dispersive spectrometry) analysis. Fig. 2B shows a close-up of the Fe-oxyhydroxides aggregates comprising numerous spheroid nanoparticles. The organic and Fe particles are embedded in an organic matrix, probably a microbial biofilm, as observed in Fig. 2B and in the bottom right of Fig. 2A.

3.3. Organic matter characterization

3.3.1. Spectroscopic properties of the organic matter

Three-dimensional excitation-emission matrix (EEM) fluorescence spectroscopy gives information about the origin of the organic substances. Among the three distinct excitation-emission regions considered in the present study, the humic region (i.e. region III) was the most pronounced in all the samples (Fig. 3) and was correlated with the non-biodegradable compounds (Jimenez et al., 2014). No microbial-by-product-like substances were detected in the EEM of the oxidized solution. The fluorescence intensity in region III increased by 27% with decreasing size fractions. The fluorescence intensity decreased in region II.

A fluorescence index (FI) of 1.4 or less indicates OC of terrestrial origin, and values of 1.9 or higher correspond to microbial derived material (Birdwell and Engel, 2010). The calculated FI were 1.30 in the <5 μm size fraction and 1.49 in the <5 kDa size fraction. These results suggest that the OM in the largest size fraction had a terrestrial origin whereas the smallest size fraction had both terrestrial and microbial origins. The humification index (HIX) is an indicator of the OC bioavailability and is used to investigate the degree of humification. Highly humified organic material is expected to be less labile in comparison to lower humified organic substances (Zsolnay et al., 1999; Ohno, 2002; Singh et al., 2014). The here calculated HIX increased from 6.25 for the largest size fraction to 22 and 30.11 for the 0.2 μm–30 kDa and <30 kDa size fractions, respectively. The OM was more humified in the 0.2 μm–30 kDa and <30 kDa size fractions, which also corresponded to the most OC-enriched size fractions (Fig. 1B). The freshness index (BIX) was calculated constant with an average value of 0.4 indicating that the OC was not freshly produced.

3.3.2. Molecular composition of the organic matter in each size fraction

Low molecular weight (LMW) fatty acids are used as microbial indicators whereas high molecular weight (HMW) fatty acids are used as plant indicators (Cranwell, 1974; Denis et al., 2017). The proportion of microbial versus plant-derived fatty acids was calculated with the percentage of LMW fatty acids (<C19) by excluding C16:0 and C18:0, which can be derived from either plant or microbial input (Frostegard

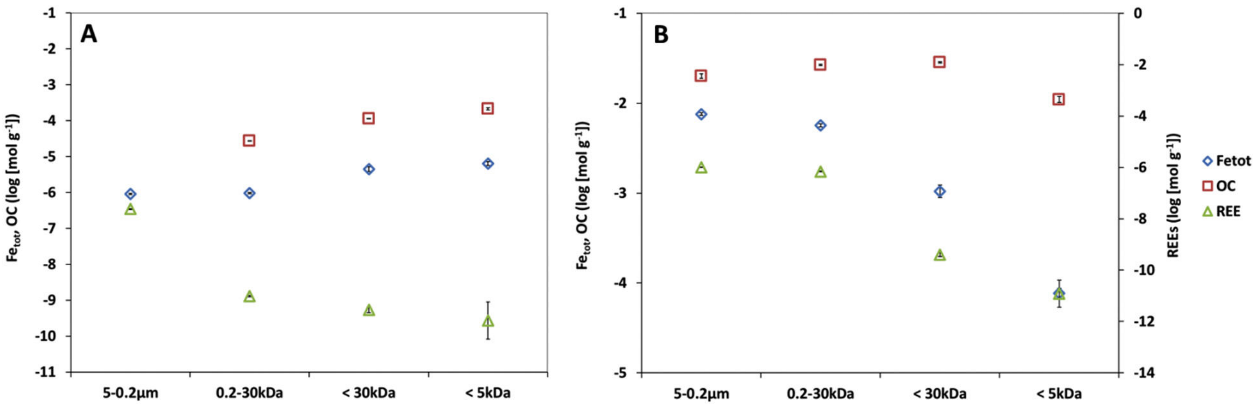

Fig. 1. Concentration of organic carbon (OC), Fe and REE (mol g^{-1}) in each size fraction of the A) reduced soil solution and B) oxidized soil solution. The error bars correspond to the standard deviation of the triplicates.

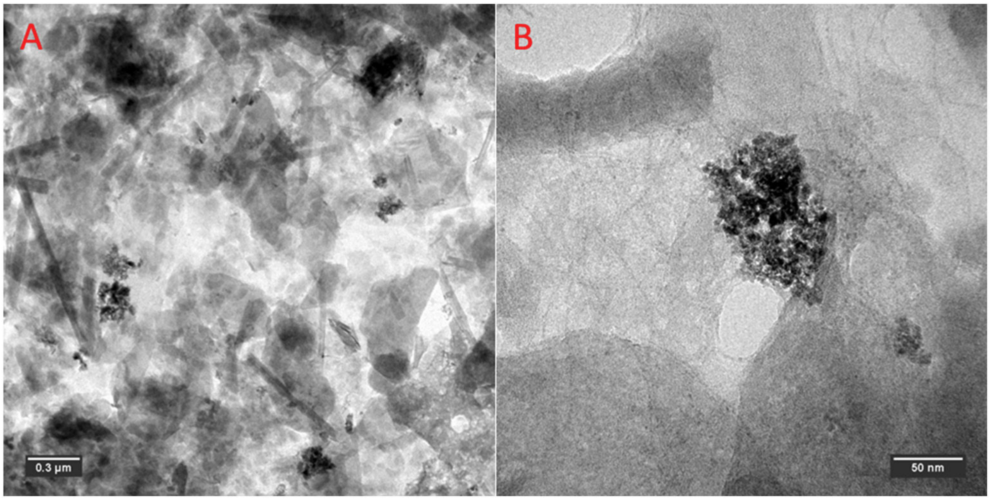

Fig. 2. Representative TEM micrographs of the 3–0.2 μm size fraction. A: magnified view of the sample. B: close-up on a Fe aggregate embedded in an organic matrix.

et al., 1993; Zelles, 1999), and the percentage of HMW fatty acids (>C19). The comparison of the fatty acids is shown in Fig. 4. In our samples, the proportion of HMW fatty acids in the >0.2 μm size fractions was higher (from 55 to 58%) than the proportions of LMW fatty acids (from 42 to 45%). On the contrary, the HMW fatty acids in the <0.2 μm size fractions decreased and disappeared in the <30 kDa and <5 kDa size fractions. A transition at the 0.2 μm threshold between a mixed plant and microbial-derived size fraction and a microbial-derived one clearly appeared in the oxidized soil solution. Among the fatty acids, branched-chain fatty acids such as iso or anteiso-C15 and iso or anteiso-C17 could be considered as tracers of living bacteria in the soil (Zelles, 1999). These fatty acids occur in many bacteria as major constituents of membrane lipids (Kaneda, 1991). As they are rapidly degraded upon cell death, these fatty acids can be considered as representative of the viable soil microbial community (Bardgett et al., 1999). In the >0.2 μm size fractions, approximately 25% of the LMW fatty acids were iso and anteiso C15 and C17. These results suggest that the largest size fractions included a living bacterial community.

Using THM-GC–MS, we detected phosphoric acid in all size fractions except for the <5 kDa size fraction. The value decreased from 1.1% ± 0.2% of the total detected compounds in the 5–0.2 μm size fraction, to 0.35% ± 0.04% in the 0.2–30 kDa size fraction increasing to 0.66% ± 0.10% in the <30 kDa size fraction.

3.4. Variability in the REE patterns

The rare earth element patterns normalized to the upper continental crust (UCC) (Taylor and McLennan, 1985) for each size fraction are displayed in Fig. 5A and B for the reduced and oxidized soil solutions, respectively. At the end of the reduction, the patterns exhibited a middle

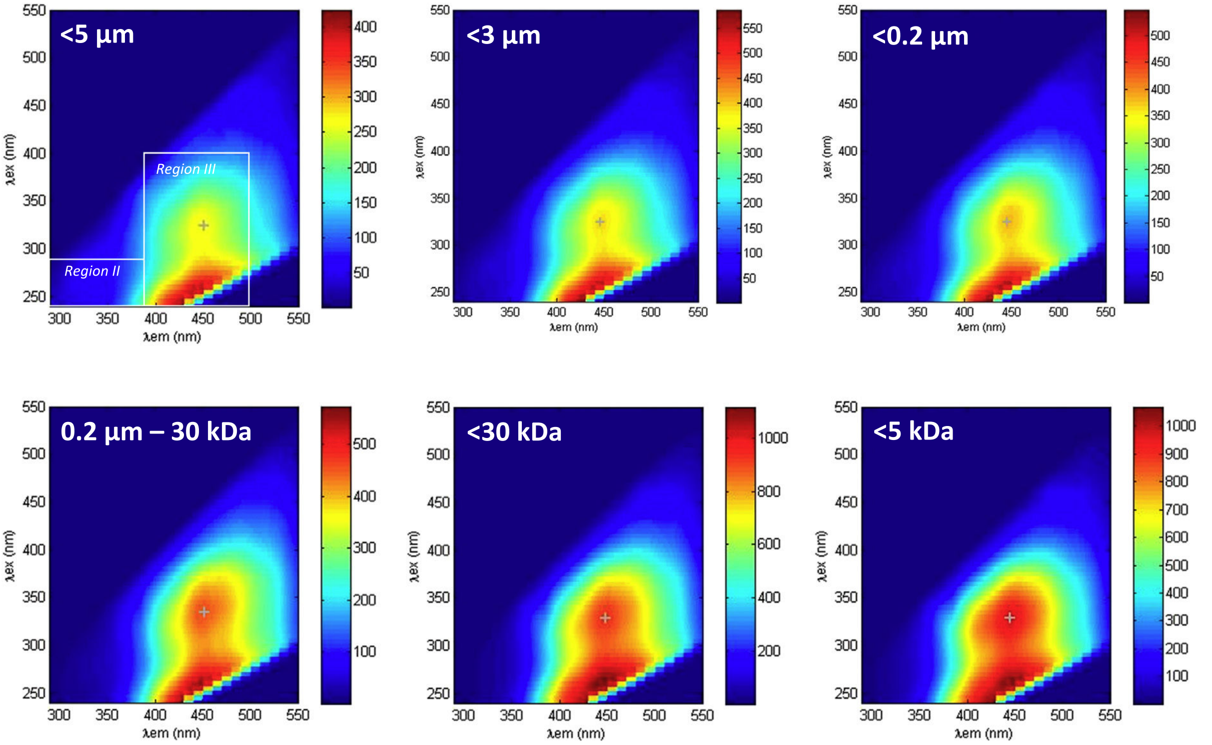

Fig. 3. The EEM spectra of DOM in the different size-fractions. The region II and III represent the microbial-by products-like materials and the humic-rich region, respectively.

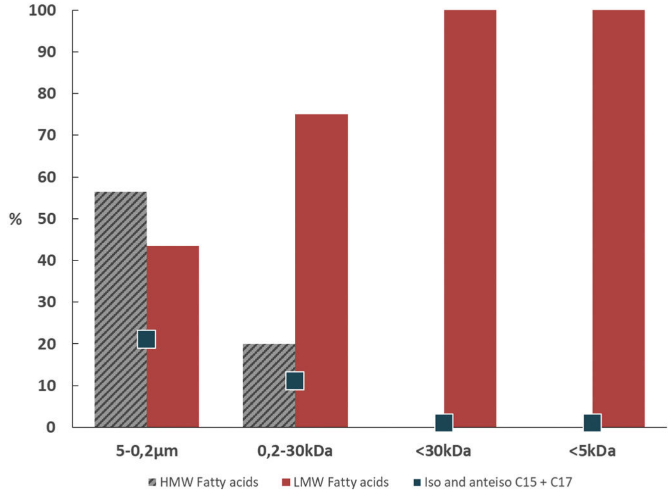

Fig. 4. Histogram of the percentage of high molecular weight (HMW) fatty acids compared to low molecular weight (LMW) fatty acids in each size fraction and the C15 and C17 (iso and anteiso) percentage of LMW fatty acids.

REE (MREE) downward concavity for each size fraction. The 5–0.2 μm pattern was nearly flat whereas the smaller size fractions exhibited a slight depletion in LREEs which increased with the size fractionation. This LREE depletion was traduced by a lower La/Yb ratio for the smaller size fraction (La/Yb = 0.93 and 1.02 for the 5–0.2 μm and 0.2 μm–30 kDa fractions, against 0.72 and 0.75 for the <30 kDa and the <3 kDa fraction, respectively). The <30 kDa and the <3 kDa patterns were broadly similar.

The REE patterns of the size fractionated oxidized soil solution were significantly different from those of the reduced period. Because the oxidation period took place in ambient atmosphere, evaporation occurred, leading to an increase in the ΣREE bulk concentration between the reduced and oxidized solutions. The REE pattern of the <5 kDa size fraction is not shown as the low REE concentrations resulted in an unrealistic normalized pattern. The size fractions over 0.2 μm were HREE-enriched compared to the 0.2–30 kDa and <30 kDa size fractions which were slightly depleted. The same MREE downward concavity as in the reduced fractions was observed in all the size fractions. A slight negative Ce anomaly seemed to have developed. The amplitude of this anomaly was calculated by the ratio $Ce/Ce^* = 2 * Ce_{UCC} / (La_{UCC} + Pr_{UCC})$ (Taylor and McLennan, 1985). Values higher than 1 indicate a positive Ce anomaly and values smaller than 1 indicate a negative Ce anomaly. The amplitude of the anomaly slightly increased from the largest size fraction to the smallest (i.e. from 0.87 to 0.75). However, this variation was very slight and, considering the logarithmic standard deviation (LSD) and amplitude, could be considered as nearly constant.

4. Discussion

4.1. Effect of oxidation on the REE size distribution and patterns

The REE data reported for the soil solution from the studied wetland changed between the reducing and oxidizing periods. While broadly similar in the reduced experiment, the REE patterns showed a significant REE fractionation between the different size fractions in the oxidized solution. Hereafter, the discussion focuses on the mechanisms and carrier phases responsible for REE fractionation during both periods.

During the establishment of reducing conditions, OM is solubilized with its REE loading (Grybos et al., 2007; Pédrot et al., 2008, 2015). Moreover, preexisting Fe-oxyhydroxides are biologically reduced during this period, leading to the increase of Fe(II) in the solution. Iron oxyhydroxides are able to strongly bind REE (Bau, 1999; Quinn et al., 2006; Schijf and Marshall, 2011). However, in an organic-rich environment such as wetland soil, Fe is mainly present as amorphous Fe(III) nanoparticles embedded in the OM and thus, are supposed to slightly sorb REEs (Grybos et al., 2007). Grybos et al. (2007) demonstrated that, under reducing conditions, REEs are mainly bound to dissolved OM released in the solution through its desorption from soil minerals subsequently to i) an increase in pH in response to H^+ consumption caused by the reducing reaction or ii) the reductive dissolution of Fe-oxyhydroxides. Thereby, the REEs are bound here to particulate and colloidal OM, as confirmed by the MREE downward concavity developed on the REE pattern for all the size fractions. This specific feature has been previously observed in OC-rich waters where organic-REE complexes dominate (Dia et al., 2000; Johannesson et al., 2004; Davranche et al., 2011; Pédrot et al., 2015). As seen in Fig. 6A, the normalization of REE$_{UCC}$ by the La concentrations in each size fraction highlighted the slight enrichment in HREE in the small size fractions (i.e. <30 kDa and <5 kDa). The decrease in the REE/OC ratio or "metal-loading", which is able to fractionate MREEs and HREEs (Yamamoto et al., 2010; Marsac et al., 2010), could explain this slight HREE enrichment (Fig. 1). Under low metal loading, the HREEs are preferentially bound to strong, but less abundant, binding sites, i.e. phenolic and/or multidentate sites. At high metal loading, the MREEs are preferentially bound to weak but more abundant carboxylic sites (Marsac et al., 2010).

During the reoxidation of the soil solution, the REEs were mainly concentrated in the 5–0.2 μm and 0.2–30 kDa size fractions, i.e. they were bound to the particulate and colloidal phase as observed in several studies for a similar environment (Dia et al., 2000; Tang and Johannesson, 2003; Pourret et al., 2007; Pédrot et al., 2008; Guénet et al., 2017). In the same wetland, Dia et al. (2000) used ultrafiltration to show that a major part of the REEs were distributed in the colloidal fraction of the soil solution. This fraction, which is considered mobile, is likely to be the major REE carriers as observed in our study. Leaching

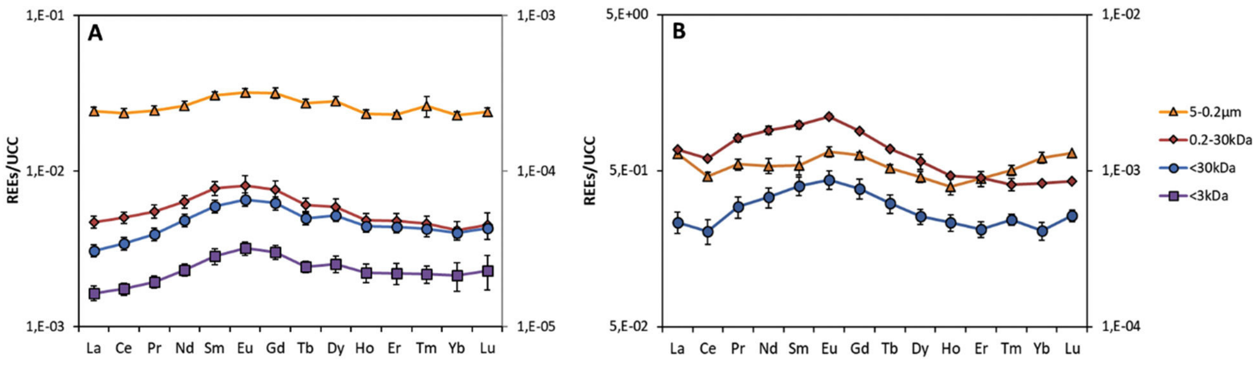

Fig. 5. UCC-normalized rare earth element (REE) patterns for the different size fractions of the A) reduced soil solution and the B) oxidized soil solution. The first vertical axis corresponds to the normalized concentrations for the 5–0.2 μm size fraction whereas the secondary vertical axis corresponds to the 0.2–30 kDa, <30 kDa and <5 kDa size fractions. The error bars correspond to the standard deviation of the triplicates.

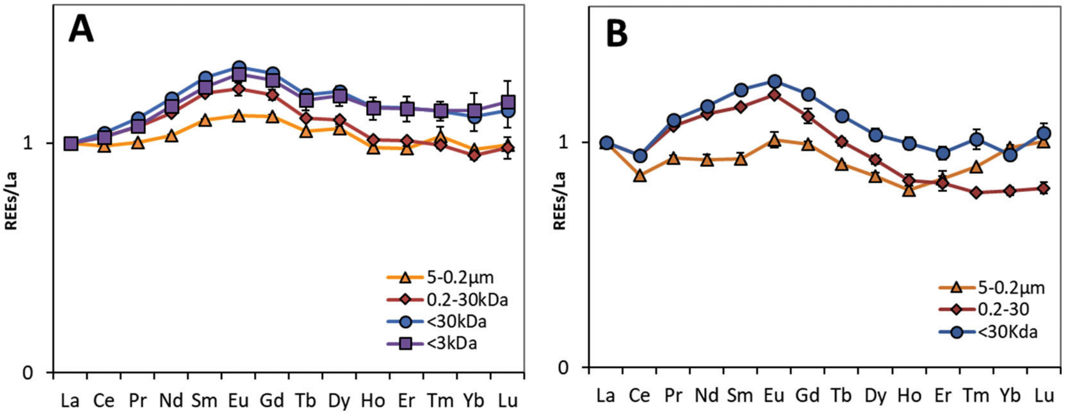

Fig. 6. Relative variations in the REE patterns in the A) reduced and B) oxidized soil solution fractions normalized by the La concentration.

experiments performed on soil sampled in the same site demonstrated that REE speciation is dominated by their binding with organic colloids under oxidizing as well as reducing conditions, as similar REE patterns were observed in both the reduced and oxidized <0.2 μm size fraction (Grybos et al., 2007; Pédrot et al., 2008). In our study, the oxidized REE patterns showed different degrees of HREE enrichments according to the size fraction. The correlation between the Fe and REE distribution in the 5–0.2 μm and 0.2 μm–30 kDa size fractions suggests that Fe might influence the REE distribution and patterns. The unique control of OM in REE speciation in wetland soils should thus be revised.

There could be several explanations for the HREE enrichment in the >0.2 μm size fractions (Fig. 6B). Firstly, the origin of the organic compounds might play an important role. Several authors have demonstrated the ability of the surface of the bacterial cells to bind REEs (Takahashi et al., 2005; Ngwenya et al., 2009; Ngwenya et al., 2010; Takahashi et al., 2010). The resulting pattern is a prominent enrichment in HREEs. Takahashi et al. (2010) used EXAFS measurements to demonstrate that carboxy-phosphate sites are responsible for REE binding and the specific pattern observed. The THM-GC–MS results showed that almost 50% of the fatty acids present in the large size fractions (i.e. >0.2 μm) were of low molecular weight, a sign of a bacterial origin. Moreover, living bacteria were present in these size fractions as demonstrated by the C15 and C17 anteiso and iso fatty acids. THM-GC–MS provided evidence that the organic compounds of these size fractions are phosphate-enriched. A significant amount of phosphate binding sites is generally found in fresh organic matter and bacteria cells but not in humic substances (Davis et al., 1999). Bacterial biofilms were also observed in the 3–0.2 μm size fraction on the MET micrographs (Fig. 2). The HREE enrichment observed in the REE pattern could therefore be attributed to the bacterial origin of the organic matter in the >0.2 μm size fractions. However, it is not clear why such an HREE enrichment was not observed in the >0.2 μm size fraction in the reducing experiment where reduction is bacterially driven. Two hypotheses exist. The bacteria lyse under alternating reducing and oxidizing conditions, which could lead to the release of the REE in solution and its readsorption to humic colloids. However, the more evident hypothesis is the high competition exerted by the high concentration of Fe(II) (and other cations) released under reducing conditions as compared to the REE low concentration, for the binding to the carboxy-phosphate sites of the organic matter.

The REE patterns of the small size fractions (<0.2 μm) are typical of REE-HS complexes, which are consistent with the fluorescence results showing an increase in the humification index with decreasing size fractions. Quinn et al. (2006) observed that the REE pattern for Fe oxyhydroxides exhibited a HREE enrichment. In our oxidized soil solution, the largest size fractions (>0.2 μm) exhibited a higher Fe/OC ratio compared with the smallest (<0.2 μm) size fraction, which is in line with the slight increase in the HREEs observed in Fig. 6B. The REE patterns in the largest size fraction could be the combination of the REE complexed to bacteria cells and the preferential re-adsorption of the HREEs to Fe(III) oxyhydroxides. Several authors have shown that particulate Fe oxyhydroxides are able to scavenge and oxidize Ce(III) into Ces (IV), leading to its removal from the soil solution (Byrne and Sholkovitz, 1996; Bau, 1999). A positive Ce anomaly is subsequently expected to develop on the REE pattern corresponding to the Fe-oxyhydroxides fraction (>0.2 μm size fractions) whereas a negative anomaly should appear in the solution (i.e. the <0.2 μm size fractions). Here, no positive Ce anomaly was observed. By contrast, the development of a slight negative Ce anomaly was observed on all the REE patterns. In the largest size fraction (i.e. 5–0.2 μm), the positive Ce anomaly that may have developed within the Fe compartment is assumed to be hidden in the broadly flat pattern. The negative Ce anomaly was so small in the solution that the positive anomaly developed on the Fe compartment should have been small as well. Guénet et al. (2016) demonstrated that the Fe oxyhydroxides that formed during the oxidation corresponded to amorphous Fe(III) nano-oxides, the size and reactivity of which are controlled by a high OM concentration. The presence of OM may have limited the oxidation of Ce(III) to Ce(IV) as Guénet et al. (2016) observed for As(III) and As(V). These authors showed that the nano-size limited the formation of As binding sites able to oxidize As (III). However, this point is only a hypothesis for Ce(III, IV) and must be confirmed by further studies.

4.2. Implication for the behavior and speciation of the REEs under alternating redox conditions in wetland soil

In the previous section, we questioned the statements made by Grybos et al. (2007) and Pédrot et al. (2008) concerning the dominance of OM in REE partitioning. To go further in the understanding of REE behavior during redox alternation in wetland soils, we compared our lab results with field results obtained from 2010 to 2017 (Davranche et al., 2013; Pédrot et al., 2015). The field datasets correspond to soil solution sampling using water traps situated in the soil organo-mineral horizon of the Mercy Wetland (Naizin, Brittany). The datasets correspond to a campaign carried out between November and May of each year during the field campaign, when the water level in the soil was high enough to allow water samples to be taken. Fig. 7 illustrates the variation range for the Eh and Fe(II) concentrations over the various campaigns. The highest Fe(II) measured concentrations corresponded to the intermediate Eh concentration in concordance with the alternation of the reducing/oxidizing conditions.

The REE patterns obtained in the <0.2 μm size fractions collected within the wetland soil were compared with the <0.2 μm size fractions obtained in both the soil reduction and subsequent soil solution oxidation experiments (Fig. 8). The REE field patterns exhibited a MREE downward concavity indicating that the soil solutions are MREE enriched. They were also depleted in HREE. A small and variable Ce

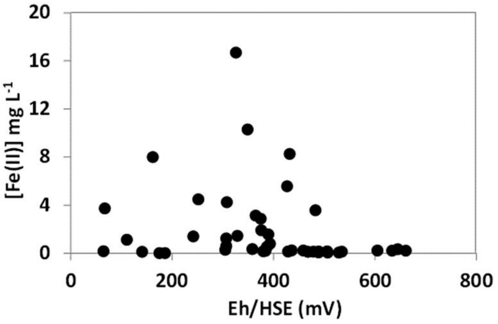

Fig. 7. Fe(II) and Eh concentration range for the field campaign. The Eh values were corrected relative to the hydrogen standard electrode (HSE).

anomaly developed, the value of which varied from 0.6 to 0.8. The field REE patterns are therefore quite similar to the REE patterns obtained for the oxidation experiment on the reduced soil solution where the Fe cluster and the nano-oxides dominate in solution as demonstrated by (Guénet et al., 2016; Guénet et al., 2017).

Fig. 9 reports the La/Sm and Gd/Yb ratios for the REE patterns obtained experimentally and recovered from the natural soil solution. The ratios calculated from the natural datasets (grey lines) are distributed between the ones of the reducing and oxidizing experiments (red and black lines). The results are interesting because while they confirm that the majority of the REE patterns corresponds to the oxidizing experiment patterns, they also demonstrate that they varied between a REE pattern close to a "reducing shape" and a REE pattern exhibiting an "oxidizing shape". This result highlights that Fe is a controlling factor of REE speciation in wetland soil irrespective of the redox conditions. In the field, even under reducing period, the presence of a Ce anomaly suggests the scavenging of Ce(IV) by Fe oxyhydroxides as previously discussed. Part of the Fe embedded in the organic matrix is not reductively dissolved under the reducing period and still complexes REEs. This REE pool partly dictates the REE pattern exhibited by the dissolved (<0.2 μm) fraction.

5. Conclusions

The oxidation experiment carried out subsequently to the wetland soil reduction highlights the significant redistribution and modification of the speciation in the REE pool during alternating redox conditions. Under reducing conditions, the REEs are bound to colloidal and dissolved OM. The oxidation of the soil solution involves then their redistribution in various ranges of particulate and colloidal organic and inorganic fractions. In the particulate fraction, the REEs seemed to be bound to humic and bacterial OM embedding Fe nano-oxides. The resulting REE pattern exhibited a strong enrichment of the last five HREEs in response to REE binding with the carboxy-phosphate site from the OM from a bacterial origin. This particulate fraction represented 34% of the total REEs. Rare earth elements were also largely redistributed in the highest colloidal fraction (0.2 μm–30 kDa) bound to humic substances and Fe nano-oxides. This size fraction represents 23% of the total REEs. In the lowest size fraction (<5 kDa), the REE concentrations were extremely low. The REE pattern exhibited an increase in MREEs and HREEs as compared to the 0.2 μm–30 kDa size fraction, probably in response to the decrease in the REE loading from OM. This REE redistribution between the particle and colloid fractions provided evidence that in wetlands, the decrease in the water level from the soil involves the scavenging and subsequent immobilization of a large amount of REEs.

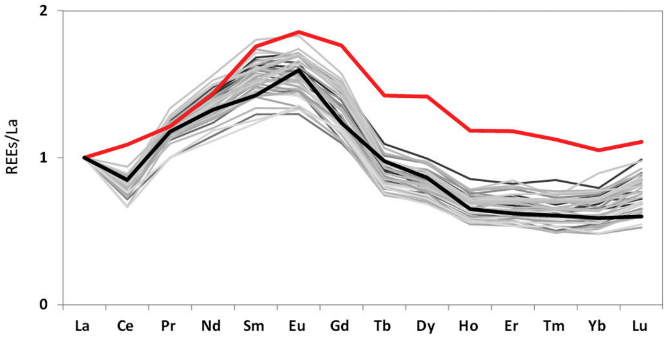

Fig. 8. Comparison of the REE pattern (normalized to La for comparison) obtained in the <0.2 size fractions recovered in the field (in grey), obtained for the reducing experiment (in red) and for the re-oxidation experiment (in black).

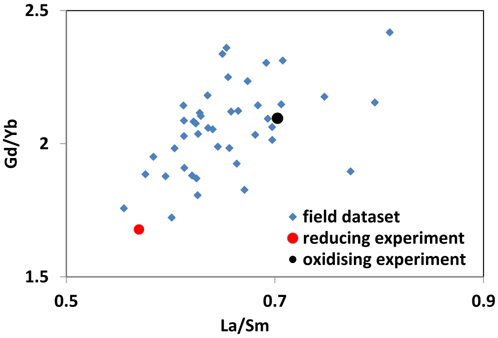

Fig. 9. Evolution of the La/Sm and Gd/Yb ratio for the REE pattern obtained from the field campaign and reducing and oxidizing experiments.

The comparison of the experimental REE patterns with the REE patterns of natural wetland soil solutions collected for the field campaign demonstrated that the reducing conditions in the riparian wetland were never sufficiently strong enough to involve the total dissolution of the Fe nano-oxides. Natural REE patterns are quite similar to the pattern obtained for the oxidizing experiment. However, the examination of the La/Sm and Gd/Yb ratio showed that the natural patterns varied between both of the REE patterns obtained for the reducing and oxidizing experiments. This evolution suggests that natural REE patterns depend on the amount and availability of the Fe nano-oxide binding sites as well as the REE loading of the organic compartment of the colloid fraction. These results provide a new insight into the control of REE speciation by Fe(III), even under reducing conditions in riparian wetlands.

Acknowledgments

We are grateful to Vincent Dorcet for acquiring the MET images. Dr. S. Mullin is acknowledged for post-editing the English style (http://www.proz.com/profile/677614). This study was funded by the French ANR through the "Programme Jeunes Chercheurs" (ANR-JC-11-JS56-0010, ARSENORG), by the IUF (Institut Universitaire de France) allocated to Melanie Davranche, and through a joint Brittany/SOLEIL/CEA Ph.D. allocation.

References

Bardgett, R.D., Lovell, R.D., Hobbs, P.J., Jarvis, S.C., 1999. Seasonal changes in soil microbial communities along a fertility gradient of temperate grasslands. Soil Biol. Biochem. 31, 1021–1030.

Bau, M., 1999. Scavenging of dissolved yttrium and rare earths by precipitating iron oxyhydroxide: experimental evidence for Ce oxidation, Y-Ho fractionation, and lanthanide tetrad effect. Geochim. Cosmochim. Acta 63, 67–77.

Birdwell, J.E., Engel, A.S., 2010. Characterization of dissolved organic matter in cave and spring waters using UV–Vis absorbance and fluorescence spectroscopy. Org. Geochem. 41, 270–280.

Bourrié, G., Trolard, F., Jaffrezic, J.-M.R.G., Maître, V., Abdelmoula, M., 1999. Iron control by equilibria between hydroxy-green rusts and solutions in hydromorphic soils. Geochim. Cosmochim. Acta 63, 3417–3427.

Byrne, R.H., Sholkovitz, E.R., 1996. Chapter 158 Marine chemistry and geochemistry of the lanthanides. Handb. Phys. Chem. Rare Earths 23, 497–593.

Catrouillet, C., Davranche, M., Dia, A., Bouhnik-Le Coz M., Marsac, R., Pourret, O., Gruau, G., 2014. Geochemical modeling of Fe(II) binding to humic and fulvic acids. Chem. Geol. 372, 109–118.

Chen, W., Westerhoff, P., Leenheer, J.A., Booksh, K., 2003. Fluorescence excitation−emission matrix regional integration to quantify spectra for dissolved organic matter. Environ. Sci. Technol. 37, 5701–5710.

Coppin, F., Berger, G., Bauer, A., Castet, S., Loubet, M., 2002. Sorption of lanthanides on smectite and kaolinite. Chem. Geol. 182, 57–68.

Cranwell, P.A., 1974. Monocarboxylic acids in lake sediments: indicators, derived from terrestrial and aquatic biota, of paleoenvironmental trophic levels. Chem. Geol. 14, 1–14.

Davis, W.M., Erickson, C., Johnston, C.T., Delfino, J.J., Porter, J.E., 1999. Quantitative Fourier transform infrared spectroscopic investigation of humic substance functional group composition. Chemosphere 38, 2913–2928.

Davranche, M., Pourret, O., Gruau, G., Dia, A., 2004. Impact of humate complexation on the adsorption of REE onto Fe oxyhydroxide. J. Colloid Interface Sci. 277, 271–279.

Davranche, M., Pourret, O., Gruau, G., Dia, A., Le Coz-Bouhnik, M., 2005. Adsorption of REE (III)-humate complexes onto MnO2: experimental evidence for cerium anomaly and lanthanide tetrad effect suppression. Geochim. Cosmochim. Acta 69, 4825–4835.

Davranche, M., Grybos, M., Gruau, G., Pédrot, M., Dia, A., Marsac, R., 2011. Rare earth element patterns: a tool for identifying trace metal sources during wetland soil reduction. Chem. Geol. 284, 127–137.

Davranche, M., Dia, A., Fakih, M., Nowack, B., Gruau, G., Ona-nguema, G., Petitjean, P., Martin, S., Hochreutener, R., 2013. Organic matter control on the reactivity of Fe (III)-oxyhydroxides and associated As in wetland soils: a kinetic modeling study. Chem. Geol. 335, 24–35.

Denis, M., Jeanneau, L., Petitjean, P., Murzeau, A., Liotaud, M., Yonnet, L., Gruau, G., 2017. New molecular evidence for surface and sub-surface soil erosion controls on the composition of stream DOM during storm events. Biogeosci. Discuss. 1–26.

Dia, A., Gruau, G., Olivié-Lauquet, G., Riou, C., Molénat, J., Curmi, P., 2000. The distribution of rare earth elements in groundwaters: assessing the role of source-rock composition, redox changes and colloidal particles. Geochim. Cosmochim. Acta 64, 4131–4151.

Frostegard, A., Tunlid, A., Baath, E., 1993. Phospholipid fatty acid composition, biomass, and activity of microbial communities from two soil types experimentally exposed to different heavy metals. Appl. Environ. Microbiol. 59 (11), 3605–3617.

Grybos, M., Davranche, M., Gruau, G., Petitjean, P., 2007. Is trace metal release in wetland soils controlled by organic matter mobility or Fe-oxyhydroxides reduction? J. Colloid Interface Sci. 314, 490–501.

Guénet, H., Davranche, M., Vantelon, D., Pédrot, M., Al-Sid-Cheikh, M., Dia, A., Jestin, J., 2016. Evidence of organic matter control on As oxidation by iron oxides in riparian wetlands. Chem. Geol. 439, 161–172.

Guénet, H., Davranche, M., Vantelon, D., Bouhnik-Le, Coz M., Jardé, E., Pierson-Wickmann, A.-C., Dorcet, V., Jestin, J., 2017. Highlighting the wide variability in arsenic speciation in wetlands: a new insight into the control of the behavior of arsenic. Geochim. Cosmochim. Acta 203, 284–302.

Huguet, A., Vacher, L., Relexans, S., Saubusse, S., Froidefond, J.M., Parlanti, E., 2009. Properties of fluorescent dissolved organic matter in the Gironde Estuary. Org. Geochem. 40, 706–719.

Jimenez, J., Gonidec, E., Rivero, J.A.C., Latrille, E., Vedrenne, F., Steyer, J.P., 2014. Prediction of anaerobic biodegradability and bioaccessibility of municipal sludge by coupling sequential extractions with fluorescence spectroscopy: towards ADM1 variables characterization. Water Res. 50, 359–372.

Johannesson, K.H., Tang, J., Daniels, J.M., Bounds, W.J., Burdige, D.J., 2004. Rare earth element concentrations and speciation in organic-rich blackwaters of the Great Dismal Swamp, Virginia, USA. Chem. Geol. 209, 271–294.

Kaneda, T.O.S.H.I., 1991. Iso-and anteiso-fatty acids in bacteria: biosynthesis, function, and taxonomic significance. Microbiol. Rev. 55 (2), 288–302.

Koeppenkastrop, D., De Carlo, E.H., 1992. Sorption of rare-earth elements from seawater onto synthetic mineral particles: an experimental approach. Chem. Geol. 95, 251–263.

Koeppenkastrop, D., De Carlo, E.H., 1993. Uptake of rare earth elements from solution by metal oxides. Environ. Sci. Technol. 27 (9), 1796–1802.

Luciani, X., Mounier, S., Paraquetti, H.H.M., Redon, R., Lucas, Y., Bois, A., Lacerda, L.D., Raynaud, M., Ripert, M., 2008. Tracing of dissolved organic matter from the SEPETIBA Bay (Brazil) by PARAFAC analysis of total luminescence matrices. Mar. Environ. Res. 65, 148–157.

Marsac, R., Davranche, M., Gruau, G., Dia, A., 2010. Metal loading effect on rare earth element binding to humic acid: experimental and modelling evidence. Geochim. Cosmochim. Acta 74, 1749–1761.

Marsac, R., Davranche, M., Gruau, G., Dia, A., Pédrot, M., Le Coz-Bouhnik, M., Briant, N., 2013. Effects of Fe competition on REE binding to humic acid: origin of REE pattern variability in organic waters. Chem. Geol. 342, 119–127.

McKnight, D.M., Boyer, E.W., Westerhoff, P.K., Doran, P.T., Kulbe, T., Andersen, D.T., 2001. Spectrofluorometric characterization of dissolved organic matter for indication of precursor organic material and aromaticity. Limnol. Oceanogr. 46, 38–48.

Ngwenya, B.T., Mosselmans, J.F.W., Magennis, M., Atkinson, K.D., Tourney, J., Olive, V., Ellam, R.M., 2009. Macroscopic and spectroscopic analysis of lanthanide adsorption to bacterial cells. Geochim. Cosmochim. Acta 73, 3134–3147.

Ngwenya, B.T., Magennis, M., Olive, V., Mosselmans, J.F.W., Ellam, R.M., 2010. Discrete site surface complexation constants for lanthanide adsorption to bacteria as determined by experiments and linear free energy relationships. Environ. Sci. Technol. 44, 650–656.

Nierop, K.G.J., Verstraten, J.M., 2004. Rapid molecular assessment of the bioturbation extent in sandy soil horizons under pine using ester-bound lipids by on-line thermally assisted hydrolysis and methylation-gas chromatography/mass spectrometry. Rapid Commun. Mass Spectrom. 18, 1081–1088.

Nierop, K.G.J., Preston, C.M., Kaal, J., 2005. Thermally assisted hydrolysis and methylation of purified tannins from plants. Anal. Chem. 77, 5604–5614.

Ohno, T., 2002. Response to comment on “Fluorescence inner-filtering correction for determining the humification index of dissolved organic matter”. Environ. Sci. Technol. 36 (4), 742–746.

Ohta, A., Kawabe, I., 2001. REE(III) adsorption onto Mn dioxide (δ-MnO2) and Fe oxyhydroxide: Ce(III) oxidation by δ-MnO2. Geochim. Cosmochim. Acta 65, 695–703.

Olivié-Lauquet, G., Gruau, G., Dia, A., Riou, C., Jaffrezic, A., Henin, O., 2001. Release of trace elements in wetlands: role of seasonal variability. Water Res. 35, 943–952.

Pédrot, M., Dia, A., Davranche, M., Bouhnik-Le Coz M., Henin, O., Gruau, G., 2008. Insights into colloid-mediated trace element release at the soil/water interface. J. Colloid Interface Sci. 325, 187–197.

Pédrot, M., Dia, A., Davranche, M., Gruau, G., 2015. Upper soil horizons control the rare earth element patterns in shallow groundwater. Geoderma 239–240, 84–96.

Poulin, B.A., Ryan, J.N., Aiken, G.R., 2014. Effects of iron on optical properties of dissolved organic matter. Environ. Sci. Technol. 48, 10,098–10,106.

Pourret, O., Dia, A., Davranche, M., Gruau, G., Hénin, O., Angée, M., 2007. Organo-colloidal control on major- and trace-element partitioning in shallow groundwaters: confronting ultrafiltration and modelling. Appl. Geochem. 22, 1568–1582.

Pourret, O., Gruau, G., Dia, A., Davranche, M., Molenat, J., 2010. Colloidal control on the distribution of rare earth elements in shallow groundwaters. Aquat. Geochem. 16 (1), 31.

Quinn, K.A., Byrne, R.H., Schijf, J., 2004. Comparative scavenging of yttrium and the rare earth elements in seawater: competitive influences of solution and surface chemistry. Aquat. Geochem. 10, 59–80.

Quinn, K.A., Byrne, R.H., Schijf, J., 2006. Sorption of yttrium and rare earth elements by amorphous ferric hydroxide: influence of solution complexation with carbonate. Geochim. Cosmochim. Acta 70, 4151–4165.

Schijf, J., Marshall, K.S., 2011. YREE sorption on hydrous ferric oxide in 0.5M NaCl solutions: a model extension. Mar. Chem. 123, 32–43.

Singh, S., Inamdar, S., Mitchell, M., McHale, P., 2014. Seasonal pattern of dissolved organic matter (DOM) in watershed sources: influence of hydrologic flow paths and autumn leaf fall. Biogeochemistry 118, 321–337.

Takahashi, Y., Châtellier, X., Hattori, K.H., Kato, K., Fortin, D., 2005. Adsorption of rare earth elements onto bacterial cell walls and its implication for REE sorption onto natural microbial mats. Chem. Geol. 219, 53–67.

Takahashi, Y., Yamamoto, M., Yamamoto, Y., Tanaka, K., 2010. EXAFS study on the cause of enrichment of heavy REEs on bacterial cell surfaces. Geochim. Cosmochim. Acta 74, 5443–5462.

Tang, J., Johannesson, K.H., 2003. Speciation of rare earth elements in natural terrestrial waters: assessing the role of dissolved organic matter from the modeling approach. Geochim. Cosmochim. Acta 67, 2321–2339.

Taylor, S.R., McLennan, S.M., 1985. The continental crust: Its composition and evolution. Blackwell Scientific, Oxford.

Viers, J., Dupré, B., Polvé, M., Schott, J., Dandurand, J.-L., Braun, J.-J., 1997. Chemical weathering in the drainage basin of a tropical watershed (Nsimi-Zoetele site, Cameroon): comparison between organic-poor and organic-rich waters. Chem. Geol. 140, 181–206.

Weishaar, J.L., Aiken, G.R., Bergamaschi, B.A., Fram, M.S., Fujii, R., Mopper, K., 2003. Evaluation of specific ultraviolet absorbance as an indicator of the chemical composition and reactivity of dissolved organic carbon. Environ. Sci. Technol. 37, 4702–4708.

Yamamoto, Y., Takahashi, Y., Shimizu, H., 2010. Systematic change in relative stabilities of REE-humic complexes at various metal loading levels. Geochem. J. 44, 39–63.

Zelles, L., 1999. Fatty acid patterns of phospholipids and lipopolysaccharides in the characterisation of microbial communities in soil: a review. Biol. Fertil. Soils 29, 111–129.

Zsolnay, A., Baigar, E., Jimenez, M., Steinweg, B., Saccomandi, F., 1999. Differentiating with fluorescence spectroscopy the sources of dissolved organic matter in soils subjected to drying. Chemosphere 38, 45–50.

UNIVERSITE ECOLOGIE
BRETAGNE GEOSCIENCES
LOIRE AGRONOMIE ALIMENTATION

UNIVERSITÉ DE RENNES 1

Titre : Devenir des nanoparticules de fer dans l'environnement : stabilité colloïdale, réactivité chimique et impacts sur le végétal

Mots clés : nanoparticules de fer, oxydation, agrégation, adsorption, métaux, plantes

Résumé : Les nanoparticules de fer manufacturées (NPs-Fe) sont des matériaux de taille nanométrique dont l'utilisation s'est, depuis peu, étendue à des domaines environnementaux. Leur dispersion dans les milieux aqueux et solides, et leurs interactions avec le vivant soulèvent toutefois encore de nombreuses questions. Dans la première partie de cette étude, nous conduisons un travail approfondi de caractérisation des NPs-Fe et précisons comment ces propriétés sont impliquées dans les processus contrôlant la stabilité colloïdale puis la réactivité chimique (capacité d'adsorption du cuivre) des NPs-Fe en solution aqueuse. Des modifications à la fois surfaciques et cristallochimiques sont appliquées afin de mettre en évidence le rôle clés de la chimie de surface des NPs-Fe. Dans cette étude, il est montré que les acides humiques limitent l'agrégation des NPs-Fe et procurent des sites d'adsorption pour les métaux. Les conditions physico-chimiques du milieu s'avèrent également jouer un rôle crucial. Le pH modifie notamment la charge de surface des NPs-Fe et les forces d'interactions électrostatiques qui en résultent. Dans un deuxième temps, nous étudions les interactions entre les NPs-Fe et les végétaux, en solution puis dans un sol. Après 63 et 57 jours, les mesures de susceptibilité magnétique montrent que les NPs-Fe s'accumulent au niveau des racines avant d'être détectées, en moindre quantité, dans les parties aériennes des plantes. L'exposition des plantes aux NPs-Fe se traduit par une augmentation de la biomasse végétale et des teneurs en chlorophylles et une diminution de la peroxydation lipidique.

Title : Fate and behavior of iron oxide nanoparticles in the environment: impacts on trace metal mobility and soil-plant systems

Keywords : iron oxide nanoparticles, oxidation, agregation, adsorption, element trace metals, plants

Abstract : Engineered Iron Oxide Nanoparticles (IONPs) are specific nanoscale materials that have recently been used into wide environmental applications. The dispersion of IONPs into soils and waters, as well as their interactions with living organisms, raise many scientific issues. The first part of this work is intended to provide a thorough characterization of IONPs in aqueous solution, from their intrinsic physico-chemical properties to their colloïdal behavior and chemical reactivity. Surface modifications are applied to evidence the key role of surface chemistry towards most interactions IONPs encounter. In particular, humic acid reduce NPs-Fe agregation and display a high adsorption capacity for trace metals, especially copper (Cu).On the other hand, the pH of the solution play a critical role towards NPs-Fe interactions. Depending on the pH, the surface charge of the particles are modified and hence pH is involved in the electrostatic forces that drive the particles agregation state and contribute to metal adsorption. The second part of the study is focused on the interactions occurring with IONPs in presence of plants. Several experiments are conducted in aqueous solution and in soil columns to precise the impacts of IONPs on the growth medium and to assess the effects of IONPs on plants. Results (magnetic susceptibility) show that IONPs manage to penetrate the roots of beans and sunflower plants (57 and 63 days-old) and that they are translocated to the aerial parts in very few amounts. Plants response to IONPs exposure results in increasing the plant biomass and the chlorophyll contents and by decreasing the lipid peroxidation.